



Universität Hamburg

DER FORSCHUNG | DER LEHRE | DER BILDUNG

# Ultra-High-Energy Cosmic Rays

## A Fireball Model to resolve the Deficit of Muons in Simulations of Extensive Air Showers

Dissertation zur Erlangung des Doktorgrades  
an der Fakultät für Mathematik, Informatik und Naturwissenschaften  
der Universität Hamburg

vorgelegt von

**Julien Pieter Jan Manshanden**

aus Amsterdam, den Niederlanden

Hamburg, 2021



Gutachter der Dissertation:

Prof. Dr. Günter Sigl

Prof. Dr. Dieter Horns

Gutachter der Disputation:

Prof. Dr. Erika Garutti

Prof. Dr. Dieter Horns

Prof. Dr. Jochen Liske

Prof. Dr. Géraldine Servant

Prof. Dr. Günter Sigl

Datum der Disputation: 24.02.2022

Vorsitzender der Prüfungsausschusses:

Prof. Dr. Jochen Liske

Vorsitzender der Promotionsausschusses:

Prof. Dr. Wolfgang Hansen

Dekan der Fakultät für Mathematik,

Informatik und Naturwissenschaften:

Prof. Dr. Heinrich Graener



© 2021 Julien Manshanden

Dieses Werk ist lizenziert unter einer

Creative Commons Namensnennung 4.0 International Lizenz:

<http://creativecommons.org/licenses/by/4.0/>

## Eidesstattliche Versicherung / Declaration on oath

Hiermit erkläre ich an Eides statt, dass ich die vorliegende Dissertationsschrift selbst verfasst und keine anderen als die angegebenen Quellen und Hilfsmittel benutzt habe.

*I hereby declare upon oath that I have written the present dissertation independently and have not used further resources and aids than those stated.*

Hamburg, den 12.12.2021

---

Ort, Datum | *Place, date*



---

Unterschrift | *Signature*

## Zusammenfassung

Experimentelle Beobachtungen von ausgedehnten Luftschauern haben ein Defizit des Myonengehalt im Vergleich zu theoretischen Simulationen aufgedeckt. Dies erschwert die genaue Bestimmung der Massenzusammensetzung ultra-hoch-energetischer kosmischer Strahlung. Wir untersuchen das Potential der Formation dichter Quark-Gluon Materiezuständen (sogenannte Feuerbälle) für die Auflösung dieses Myonendefizits, welche wir mit Daten des Pierre Auger Observatoriums über die Tiefe des Schauermaximums und die Zahl der Myonen auf dem Erdboden quantifizieren. Wir verwenden ein phänomenologisches Feuerballmodell, das die Formation eines Plasmas nachbildet und den Strange-Quark Gehalt im Vergleich zu aktuellen Standardmodellvorhersagen anreichert. Durch die Implementierung dieses Modells in bestehende Luftschauersimulationssoftware sehen wir, dass die Daten über die longitudinale Entwicklung der elektromagnetischen Schauerkomponente der Formation eines Plasmas widersprechen. Stattdessen beschränken wir das Feuerballmodell darauf, dass es ausschließlich eine Strangeness-Anreicherung der hadronischen Wechselwirkungen des Standardmodells darstellt. Für bestimmte Formen der Wahrscheinlichkeit der Feuerball-Formation, ermöglicht dies eine konsistente Interpretation der Daten hinsichtlich der Massenzusammensetzung der kosmischen Strahlung. Diese ersten Untersuchungen ergänzen wir mit einer analytischen Methode, die auf dem Heitler-Matthews Modell basiert. Hierdurch finden wir explizite Reihen von Feuerballparametern, die das Myonendefizit lösen. Einschränkungen basierend auf Daten über Schauer-zu-Schauer Schwankungen der Myonenzahl erfordern eine Strangeness-Anreicherung auch bei niedrigeren Energien. Bei Tevatron und LHC Energien quantifizieren wir dies als eine  $O(3-8)\%$  Steigerung des durchschnittlichen, in hadronischen Teilchen gehenden, Energieanteils im Vergleich zu Vorhersagen aktueller Modelle über die hadronische Wechselwirkung. Die direkte Interpretation der makroskopischen Auger Daten in Hinblick auf eine mikroskopische Wechselwirkungseigenschaft motiviert zu Experimenten der Vorwärtsphysik mit Beschleunigern der jetzigen Generation.

## Abstract

Experimental observations of extensive air showers have revealed a deficit of the muon content in their theoretical simulations. This hampers a precise determination of the ultra-high-energy cosmic ray mass composition. We investigate the potential of producing states of dense quark-gluon matter (so-called fireballs) to resolve this muon deficit, which we quantify with data from the Pierre Auger Observatory on the depth of the shower maximum and the number of muons at ground. We adopt a phenomenological fireball model that mimics the formation of a plasma and enhances the strange quark content with respect to current Standard Model predictions. When implementing this model into existing air shower simulation software we find that the formation of a plasma is in tension with data on the electromagnetic longitudinal shower development. Instead, we restrict the fireball model to only enhance the strangeness of Standard Model hadronic interactions. Then for specific forms of the fireball-production probability we obtain a consistent interpretation of the data in terms of the cosmic ray mass composition. Complementing these initial studies with an analytic approach based on the Heitler-Matthews model we find explicit sets of fireball parameters that resolve the muon deficit. Constraints from data on shower-to-shower fluctuations of the muon number require strangeness enhancements also at lower energies. At Tevatron and LHC energies we quantify this as an  $O(3 - 8)\%$  increase of the average fraction of energy going into hadronic particles compared to predictions from current hadronic interaction models. This direct interpretation of macroscopic Auger data in terms of a microscopic interaction property motivates forward physics experiments at current-generation accelerators.



# Contents

<b>1</b>	<b>Introduction</b>	<b>1</b>
<b>2</b>	<b>Cosmic Rays</b>	<b>5</b>
2.1	A Brief History of Cosmic Ray Physics . . . . .	5
2.2	Modern Subfields and Open Problems . . . . .	7
2.3	Extensive Air Showers . . . . .	12
2.3.1	Heitler Model: Electromagnetic Showers . . . . .	14
2.3.2	Heitler-Matthews Model: Hadronic Showers . . . . .	15
<b>3</b>	<b>The Pierre Auger Observatory</b>	<b>19</b>
3.1	Detectors . . . . .	19
3.1.1	Surface Detector . . . . .	21
3.1.2	Fluorescence Detector . . . . .	22
3.1.3	Other Detectors and AugerPrime . . . . .	23
3.2	Scientific Results . . . . .	24
3.2.1	Energy Spectrum . . . . .	24
3.2.2	Mass Composition . . . . .	25
3.2.3	Arrival Directions . . . . .	26
<b>4</b>	<b>Hadronic Interaction Models and Shower Simulations</b>	<b>29</b>
4.1	Hadronic Interactions . . . . .	29
4.1.1	High-Energy Hadronic Interaction Models . . . . .	30
4.1.2	Low-Energy Hadronic Interaction Models . . . . .	32
4.2	Air Shower Simulation Software . . . . .	32
4.2.1	CORSIKA . . . . .	33
4.2.2	CONEX . . . . .	34
4.2.3	CRMC . . . . .	34
<b>5</b>	<b>The Muon Deficit and the Fireball Model</b>	<b>37</b>
5.1	Experimental Evidence for the Muon Deficit . . . . .	37
5.1.1	Combining Measurements from Multiple Experiments . . . . .	40
5.2	Resolving the Muon Deficit . . . . .	41
5.3	A Phenomenological Fireball Model . . . . .	45

<b>6</b>	<b>Compatibility between <math>R_\mu</math> and <math>X_{\max}</math> in the Fireball Model</b>	<b>49</b>
6.1	Quantifying the Size of the Muon Deficit . . . . .	49
6.1.1	Calibration of $z_x$ . . . . .	49
6.1.2	Test Statistic $\Delta$ . . . . .	50
6.2	Fireball Simulations and the Effect on the Muon Deficit . . . . .	52
<b>7</b>	<b>Impact of the Fireball Model on Individual Observables</b>	<b>55</b>
7.1	Step-wise Constraining the Fireball Model . . . . .	55
7.2	Results and Discussion . . . . .	56
7.2.1	Range of Predictions . . . . .	57
7.2.2	Cross-Interpretation in terms of Composition . . . . .	60
<b>8</b>	<b>Extending the Heitler-Matthews Model of the Muon Number</b>	<b>65</b>
8.1	Muon Number in a Fireball-Extended Heitler Model . . . . .	65
8.1.1	The Effect of Discrete Interactions . . . . .	66
8.1.2	Resulting Muon Number . . . . .	68
8.2	Introducing an Energy-Dependent Multiplicity . . . . .	69
8.2.1	Power-law Dependence . . . . .	70
8.2.2	Generalized Dependence . . . . .	71
<b>9</b>	<b>Parameter Inference and Auger Data Interpretation</b>	<b>73</b>
9.1	Particle Interaction Parameters from CRMC . . . . .	73
9.1.1	Hadronic Energy Fraction . . . . .	73
9.1.2	Multiplicity . . . . .	75
9.1.3	Correlations . . . . .	78
9.2	Propagating Intrinsic Fluctuations to the Muon Number . . . . .	80
9.2.1	Average Muon Number $\langle N_\mu \rangle$ . . . . .	80
9.2.2	Relative Fluctuations of the Muon Number $\sigma(N_\mu)/\langle N_\mu \rangle$ . . . . .	86
9.3	Interpretation of Auger Data . . . . .	91
9.3.1	Mass Dependence and Effect on $X_{\max}$ . . . . .	91
9.3.2	Constraints on the Fireball Model . . . . .	93
<b>10</b>	<b>Conclusion</b>	<b>99</b>
	<b>Acknowledgements</b>	<b>101</b>
	<b>References</b>	<b>103</b>

---

<b>Appendices</b>	<b>121</b>
<b>A Effects of Mixed Compositions</b>	<b>121</b>
A.1 Effect of a Mixed Composition on the Calibration . . . . .	121
A.2 Extreme Values of $\sigma(X_{\max})$ and $\sigma(R_\mu)/\langle R_\mu \rangle$ . . . . .	123
A.3 Mapping Average Observables to Fluctuations and other Averages . . . . .	125
<b>B Additional Figures of <math>z_{\text{mass}}</math> in the Fireball Model</b>	<b>127</b>
B.1 Effect on Tension between $\langle \ln R_\mu \rangle$ and $\langle X_{\max} \rangle$ . . . . .	128
B.2 Effect on Tension between $\sigma(R_\mu)/\langle R_\mu \rangle$ and $\langle X_{\max} \rangle$ . . . . .	130
<b>C List of Symbols for Chapter 8</b>	<b>133</b>
<b>D Derivation of <math>N_\mu</math> in the Fireball-Extended Heitler-Matthews Model</b>	<b>135</b>
D.1 Fireball $N_\mu$ for a Constant Multiplicity . . . . .	135
D.2 Fireball $N_\mu$ for a Power-law Multiplicity . . . . .	136
<b>E Additional Figures of Fireball-Heitler-Matthews Fits</b>	<b>141</b>
E.1 Fireball-Heitler-Matthews Fits of $\langle N_\mu \rangle$ and $\sigma(N_\mu)/\langle N_\mu \rangle$ . . . . .	141
E.2 Fireball Mass Dependence of $\langle R_\mu \rangle$ . . . . .	145
E.3 Fireball Interpretation of Auger Data . . . . .	146

## List of Abbreviations

<b>AERA</b>	Auger Engineering Radio Array
<b>AGN</b>	Active galactic nucleus
<b>AMIGA</b>	Auger Muon and Infilled Ground Array
<b>BLS</b>	Balloon Launching Station
<b>CLF</b>	Central Laser Facility
<b>CMB</b>	Cosmic microwave background
<b>CR</b>	Cosmic ray
<b>DGLAP</b>	Dokshitzer-Gribov-Lipatov-Altarelli-Parisi (equations)
<b>EAS</b>	Extensive air shower
<b>EBL</b>	Extragalactic background light
<b>EM</b>	Electromagnetic
<b>FD</b>	Fluorescence detector
<b>GRFT</b>	Gribov-Regge Field Theory
<b>GZK</b>	Greisen-Zatsepin-Kuzmin (effect)
<b>HEAT</b>	High-Elevation Auger Telescopes
<b>ICRC</b>	International Cosmic Ray Conference
<b>LHC</b>	Large Hadron Collider
<b>PMT</b>	Photomultiplier tube
<b>QCD</b>	Quantum chromodynamics
<b>QED</b>	Quantum electrodynamics
<b>SBG</b>	Starburst galaxy
<b>SD</b>	Surface detector
<b>UHECR</b>	Ultra-high-energy cosmic ray
<b>UMD</b>	Underground Muon Detector
<b>VEM</b>	Vertical equivalent muon
<b>WCD</b>	Water Cherenkov detector
<b>WHISP</b>	Working group on Hadronic Interaction and Shower Physics
<b>XLF</b>	eXtreme Laser Facility

# 1 | Introduction

Microscopic particles – invisible to the naked eye – continuously bombard the Earth from outer space. Fortunately for life on Earth, we are well-shielded by the atmosphere. This shielding effect actually gave rise to their discovery in the first place: by taking electroscopes on balloon rides several kilometers up into the sky, it was shown in the early 20th century that the intensity of the radiation increases with altitude. This led to the inevitable conclusion that these rays are of cosmic origin, i.e., they are *cosmic rays* (CRs). Just like the arrival of CRs, the quest to unravel their nature continues to this day.

Nowadays we know that CRs are ionized nuclei that span a very wide range in energy, with the most energetic ones detected so far having energies up to a few  $10^{20}$  eV. For physicists, such macroscopic energies within microscopic particles are very intriguing. To provide a reference,  $10^{20}$  eV corresponds to 16 Joules, which is sufficient to accelerate from rest a typical association football of 430 grams to 8.6 m/s (!) – meaning that an inconveniently timed CR could score a goal and make you lose the championship. To also put this in a physics perspective; the most energetically human-accelerated particles are proton beams of 6.5 TeV<sup>1</sup>, which is almost 8 orders of magnitude lower than the most energetic observed CRs.

There is no need to worry about CRs ruining your football game because of the shielding of the atmosphere, but also because the highest-energetic CRs are extremely rare: at  $10^{20}$  eV on average only 1 particle arrives at Earth per square kilometer per century. This is a reflection of their very steep spectrum: for every order of magnitude higher in energy, there are 100 times fewer particles. Below  $10^{15}$  eV the rates are still high enough for CRs to be detected onboard of space stations or satellites, but above  $10^{15}$  eV one is forced to revert to ground-based experiments covering large areas to compensate for the low flux.

While the shielding of the atmosphere prevents the primary CR particles to reach the Earth's surface, their energies are large enough to leave observable physical imprints in the atmosphere. Upon the arrival of CRs at Earth they undergo hadronic interactions with atmospheric nuclei, which involves the production of many so-called secondary particles. These keep interacting and thereby induce a cascade of particles known as extensive air showers (EASs). It is these EASs that can be observed from the ground with a variety of techniques.

The properties of the original CR can then be inferred from the reconstruction of such EASs, which requires a solid understanding of the relevant particle physics processes. This includes regions of phase space inaccessible to current accelerators. In particular, the first interaction of ultra-high-energy cosmic rays (UHECRs,  $E > 10^{18}$  eV and reaching a few  $10^{20}$  eV) with atmospheric particles attain center of mass energies exceeding 450 TeV, which significantly surpasses the 13 TeV achieved at the Large Hadron Collider (LHC). Furthermore, most relevant for EASs

---

<sup>1</sup>1 TeV =  $10^{12}$  eV

are very forward interactions, which are generally not probed at collider<sup>2</sup> experiments. From this perspective, the study of UHECR-induced EASs constitutes a complementary particle physics laboratory. Simultaneously, the very existence of UHECRs gives rise to a plethora of intriguing questions regarding the responsible astrophysical processes and sources. This underlines the interdisciplinary nature of astroparticle physics in general, and CR physics in particular.

Detailed inferences of CR properties such as their energy spectrum, nuclear mass composition, and arrival direction are invaluable for testing astrophysical models on their origin, acceleration, and propagation. In particular, determining whether the composition at the highest energies tends to be light (i.e., proton) or heavy (i.e., iron) has the potential of ruling out many of such models [1]. Traditionally, the mass composition is inferred from EASs using the observable  $X_{\max}$ , which is the depth in the atmosphere where the shower development reaches its maximum. While proven to be a very powerful mass indicator,  $X_{\max}$  is typically measured with fluorescence telescopes that are limited by a 15% duty cycle. More statistics can be obtained from ground arrays measuring the footprint of these EASs with a 100% duty cycle. In this footprint, the number of muons  $N_{\mu}$  constitutes a complementary mass indicator, which also appears [2] to have a potentially larger mass separation power on a shower-by-shower basis [1].

The interpretation of data on these observables in terms of the nuclear mass  $A$  of the CR primary follows from comparisons to EAS Monte Carlo simulations. These simulations encode our understanding of the physics of air showers, including the relevant hadronic interactions. Due to the random nature of EASs, it is difficult to relate the observables to specific masses on a shower-by-shower basis. Therefore, current efforts focus on the interpretation of the first two statistical moments – averages  $\langle \cdot \rangle$  and fluctuations  $\sigma(\cdot)$  – of  $X_{\max}$  and  $N_{\mu}$ , with each being a unique mass indicator. It turns out that both moments of  $X_{\max}$  [3, 4] and, more recently, the fluctuations of the muon number [5] allow for a consistent composition interpretation of the data. In contrast, measurements of the average muon number significantly exceed predictions from simulations assuming the  $X_{\max}$ -inferred composition [1, 6]. This tension between theory and experiment is known as the *muon deficit*, i.e., there is a deficit of muons in simulations.

Several resolutions of the muon deficit have been proposed, ranging from the introduction of exotic new physics to small adjustments to current hadronic interaction models. All current proposals have in common that there is some effect suppressing the energy loss to the electromagnetic component of the EAS such that there is sufficient energy available to produce the observed number of muons at ground. As will be reviewed later in the thesis, the proposals differ in the origin of this suppression: string percolation [7], restoration of the chiral symmetry [8], production of a fireball state [9], presence of a core-corona effect [10], or a more conventional type of quark-gluon plasma [11, 12, 13]. Which, if any, of these proposals can solve the muon deficit is currently unclear.

Combining the muonic measurements from a variety of CR experiments, it was shown that the deficit starts at around 10 PeV CR primary energy [6]. This corresponds to 8 TeV in the center of mass frame of the first interaction<sup>3</sup>, and could therefore be probed at current collider experiments [1]. In fact, the ALICE collaboration reported on an enhanced production of multi-strange hadrons in high-multiplicity proton-proton collisions at  $\sqrt{s} = 7$  TeV [14]. Such

---

<sup>2</sup>Collider experiments refer to accelerator experiments where two beams are accelerated and collided. This in contrast to fixed-target experiments with only one energetic beam in the laboratory frame.

<sup>3</sup>Whereas [6] reports on a 10 PeV offset, [1] states it starts at 40 PeV. The latter corresponds through  $\sqrt{s} \approx \sqrt{2Em_p}$  to 8 TeV in the center of mass frame.

a strangeness enhancement is also proposed in the fireball model [9], which could therefore be taken as a hint that this fireball scenario constitutes a viable solution to the muon deficit [12].

With a detailed study of the effect of fireballs on UHECR-induced EASs, this thesis intends to assess that option. Particular emphasis will be put on high-level data of the reconstructed  $X_{\max}$  and  $N_{\mu}$  from air showers detected at the Pierre Auger Observatory, allowing for direct comparisons between theory and experiment. A complete exploration of the fireball parameter space in light of the muon deficit would either help exclude such exotic explanations, or give rise to concrete predictions for future forward-physics experiments.

In Chapter 2 follows a general introduction to CR-physics and EASs. Experimental data used in this thesis comes from the Pierre Auger Observatory, which is described in Chapter 3 along with its main scientific results. Chapter 4 reviews the relevant hadronic interaction models and simulation software. The muon deficit as well as the fireball model are then discussed in Chapter 5.

The remaining chapters contain the results of the three studies performed for this thesis. The first study, in Chapter 6, considers the general compatibility of  $R_{\mu}$ - and  $X_{\max}$ -data within the fireball model for a fraction of its parameter space. The second study, in Chapter 7, extends the parameter space and provides a systematic investigation of the impact of a fireball on the EAS observables. The last study consists of two parts: Chapter 8 derives a fireball-extended analytical framework – inspired by the Heitler-Matthews model – to predict the muon number, which is then used in Chapter 9 to find fireball parameters that would allow for a consistent interpretation of the data in terms of the CR mass composition, and therefore solve the muon deficit.



## 2 | Cosmic Rays

The physics of cosmic rays has been an active field of research for over a century. With in 1912 the first convincing evidence of the existence of invisible radiation originating from outer space [15], the field of cosmic ray physics preludes and even contributed to the birth of particle physics [16]. Despite this long history there are still various open questions about the CR properties and origin. Coupling this with humanity’s natural fascination for the cosmos provides both a historical and a practical case for the modern study of cosmic rays.

This chapter introduces the field by first providing a brief history of cosmic ray physics in Sec. 2.1. Then, the modern subfields along with some open problems are outlined in Sec. 2.2. Closing with an introduction to the phenomenon of extensive air showers in Sec. 2.3 we intend to provide a sufficient background for the thesis.

### 2.1 A Brief History of Cosmic Ray Physics

Despite the successes of the theory of electromagnetism – developed in the 18th and 19th century – one of the original observations made by C.A. de Coulomb in 1785 remained unexplained until the discovery of radioactivity by H. Becquerel in 1896 [16, 17]. This observation considered the spontaneous discharge of an electroscope, which first led to the conclusion that the air inside the isolated chamber was contaminated with conducting dust particles. Experiments in 1900 and 1901 by H. Geitel and J. Elster [18, 19] as well as C.T.R. Wilson [20] showed that the air itself possesses some conductivity, which was subsequently attributed to the ionization of air from radioactivity in the surrounding environment [16, 21]. Following experiments did not provide much clarity on the precise origin of the radioactivity, with in general the Earth’s crust being the assumed source [21, 22, 23].

Putting this assumption to the test, T. Wulf took in 1910 his improved electrometer to the top of the Eiffel Tower and found an insufficient decrease of the ionization rate with respect to the ground if the Earth’s crust was indeed responsible [16, 23, 24]. Around the same time, similar observations were made by A. Gockel from his three hot-air balloon flights above Switzerland up to a 4500 m height [16, 25, 26], and by D. Pacini from his measurements on the Tyrrhenian sea [23, 27, 28]. These observations indicated the presence of an additional atmospheric or extra-terrestrial component of the observed penetrating radiation.

The first convincing evidence for an extra-terrestrial origin is attributed to the seven balloon flights conducted by V.F. Hess in 1912 [15, 16, 23]. The measurements of the last (and most successful) flight – along with Hess himself – are shown in Fig. 2.1: after a slight initial decrease, there is a clear increase of the ionization rate with altitude. These results were subsequently confirmed and extended by W. Kolhörster in 1913 and 1914 with balloon flights of up to 9300 m

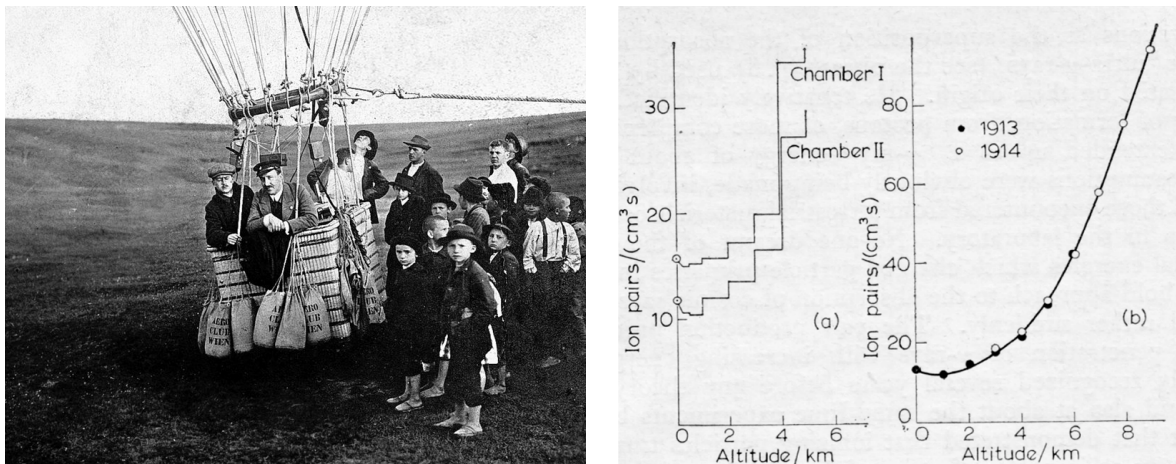


**Figure 2.1:** *Left:* V.F. Hess in 1912 before one of his balloon flights. Credits: VF Hess Society, Schloss Pöllau/Austria. *Right:* Measurements of the ionization rate as a function of altitude from Hess' seventh balloon flight in 1912 (left graph) and Kollhörster's confirmation flights in 1913 and 1914 (right graph). Figure from [29], reproduced with permission.

in altitude [30, 31], as also shown in Fig. 2.1. Despite the convincing evidence, it took another decade for a general consensus to be reached on the existence of these *cosmic rays* [16, 21].

The precise nature of these rays was still a mystery, with gamma rays (photons) – the most penetrating radiation known at the time – the main candidate [16, 21, 32]. During a series of voyages between Java and Amsterdam in 1927 and 1928, J. Clay observed a dependence of the ionization rate on geomagnetic latitude [33]. On top of their own coincidence measurements in 1929, W. Bothe and W. Kollhörster interpreted Clay's observations as further indications for a charged particle nature of cosmic rays due to deflections in Earth's magnetic field [32, 34]. Follow-up expeditions by Clay [35], A.H. Compton [36] and a world-wide collaborative effort [37] confirmed this picture [32].

Given that cosmic rays are charged particles deflected in Earth's magnetic field, B.B. Rossi realized in 1930 that an asymmetry in flux from the east and west would reveal the dominant charge [38, 39]. Three years later this effect was indeed observed by L. Alvarez and Compton [40], T.H. Johnson [41], and subsequently also by Rossi himself together with S. de Benedetti [42]. These measurements surprisingly indicated cosmic rays to be mostly positively charged, in contrast to the widespread assumption that they were electrons [38]. It, however, took until the early 1940s for proof of a predominantly proton composition (at energies of  $10^9 - 10^{12}$  eV) [43], and later also evidence for a subdominant fraction of heavier nuclei [38, 44]. Nowadays we understand cosmic rays to be the nuclei of ionized atoms, with their precise composition a current topic of research [45].

It is interesting to note that around the same time observations of cosmic rays with cloud chambers led C.D. Anderson to the discovery of the positron in 1932 [46] and the muon (together with S. Neddermeyer) in 1936 [47]. The use of cosmic rays to study subatomic particles continued until the first man-made accelerators in the 1950s [48]. Interestingly, with the detection of ultra-high energy cosmic rays modern cosmic-ray physics can again contribute to the field of particle physics (see, e.g., [49]).

The coincidence method of coupling multiple Geiger-Müller counters and looking at simul-

taneous signals – pioneered by Bothe in 1929 [50] and upgraded the following year by Rossi [51] – was an efficient technique to filter out background radiation in the laboratory and detect mostly cosmic rays. A subsequent shielding with up to 1 meter of lead, led Rossi in 1933 [52] to his transition curve. This curve showed that the coincidence rate first increased with absorber thickness before falling again, implying that cosmic rays produced showers of particles in lead [53]. The same phenomenon should also occur in air, as suggested by K. Schmeiser and Bothe in 1938 [54], which they subsequently measured to have sizes up to 40 cm. Similar measurements came independently from Kolhörster’s group [55], and it turns out that Rossi had observed coincidences between distant detectors already in 1934 [56], but he was unable to follow up on it [53]. Nevertheless, the final discovery of extensive air showers is attributed to P.V. Auger and his group in 1939 for not only measuring shower sizes of up to 300 m, but also for estimating the total energy of the primary particles to be  $O(10^{15})$  eV [53, 57] – many orders of magnitude above what was previously thought possible [58].

Since the discovery of extensive air showers their study has been used to infer properties of the primary CRs initiating such showers. Technological advances continually enabled the extension of the CR energy spectrum; from the initial high energies ( $> 10^{15}$  eV) towards ultra-high energies ( $> 10^{18}$  eV) and beyond. Further important properties include their mass composition and the arrival directions. Each property gives rise to a unique subfield of study, in addition to the subfield about their astrophysical interpretations. Ending the historical narrative here, we review the modern status of cosmic ray physics, the various subfields and some open problems in the next section.

## 2.2 Modern Subfields and Open Problems

A first subdivision of cosmic ray physics can be made according to the energies of the cosmic nuclei arriving at Earth. The corresponding energy spectrum  $J_{\text{LIS}}(E_{\text{kin}})$ <sup>1</sup>, i.e., the number of particles per unit energy, area, time and solid angle as a function of their (kinetic) energy  $E_{\text{kin}}$  is shown in Fig. 2.2.

The CR spectrum covers an astonishing 11(!) orders of magnitude in energy. Notice that it is the further multiplication by the energy to some power (2.6 in this case) that allows the vertical axis in this figure to span only a few orders of magnitude. This trick helps visualizing important spectral features. Simultaneously, it also implies that the differential flux itself falls by approximately 3 (for  $E_{\text{kin}} > 10^6$  GeV) orders of magnitude for every order of magnitude higher in energy. This makes higher-energetic cosmic rays rarer: while at 1 TeV a particle arrives each second in a square meter, at a few tens of PeV this becomes one per year for the same area, and at the end of the spectrum, around 100 EeV, we need to wait a century for a single particle to strike within one square kilometer<sup>2</sup>. In turn, the detection of these cosmic rays require ever larger experiments, such that at some point it is no longer feasible to build them in space. This marks the end of the experiments indicated by filled markers in Fig. 2.2 at a few  $10^5$  GeV<sup>3</sup>.

Fortunately, above energies of around  $10^6$  GeV, the EAS imprints left in the air and onto

<sup>1</sup>The subscript LIS refers to the local interstellar medium, implying that the relevant data ( $\lesssim 10$  GeV) has been corrected to account for the solar modulation due to solar activity [59].

<sup>2</sup>A brief reminder: 1 GeV =  $10^9$  eV, 1 TeV =  $10^{12}$  eV, 1 PeV =  $10^{15}$  eV, 1 EeV =  $10^{18}$  eV.

<sup>3</sup>With in the case of the ground-based H.E.S.S., this is because Cherenkov radiation from EASs becomes too bright compared to the Cherenkov radiation from the primary CR [62].

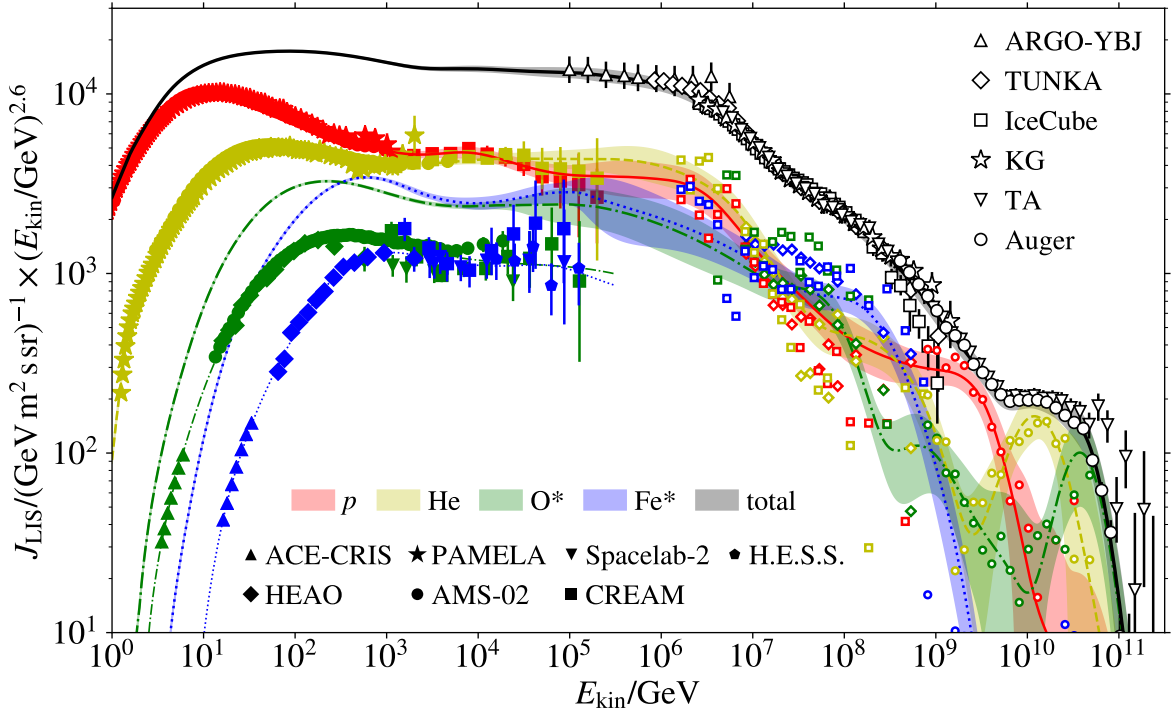


**Figure 2.2:** The energy spectrum of primary cosmic rays at Earth. Data is shown from both direct (solid markers) and indirect (open markers) experiments, along with corresponding global spline fits (lines). The nuclear masses (p: proton, He: helium, O: oxygen, and Fe: iron) are indicated by the colors, with black the all-particle spectrum. In the case of oxygen and iron the higher lines correspond to the mass groups lithium-neon and sodium-nickel, respectively. Figure from [60], which was updated from [61], reproduced with permission. See references therein for the experiments.

the ground are sufficiently large to be observed from the Earth's surface, as has been done by the experiments indicated by open markers. This, however, brings along an additional set of challenges. For example, both the nuclear mass and the energy of the cosmic rays can no longer be determined directly, but need to be inferred from characteristics of the induced EAS. While fluorescence telescopes enable calorimetric measurements of the energy deposit in the atmosphere, inferences of the primary mass rely on detailed particle physics models extrapolated beyond the phase-space accessible to accelerators [60]. Consequently, the mass measurements beyond  $10^6$  GeV are susceptible to larger uncertainties, with the bands in Fig. 2.2 corresponding to one standard deviation around the combined fit and the error bars from individual experiments suppressed for clarity.

In the following we will only consider high-energy CRs ( $E > 10^6$  GeV), and then mostly focus on the ultra-high-energy ones ( $E > 10^9$  GeV)<sup>4</sup>. Research related to lower-energetic CRs constitute its own field with associated open problems, but a description of these is beyond the scope of this thesis.

Measurements of both the mass composition and the spectral features are invaluable for

<sup>4</sup>At these energies the contribution of the rest mass to the total energy is negligible. Then with the kinetic energy approximately equal to the total energy we can drop the subscript.

testing astrophysical models: they contain information on the production, propagation and source distribution of CRs [60]. In particular, there are several famous features in the spectrum of high-energy CRs. The so-called ‘knee’ is a softening of the all-particle spectrum at around  $10^{6.6}$  GeV. A ‘second knee’ – i.e., a further softening of the all-particle spectrum – occurs at around  $10^8$  GeV. Then there is a hardening, known as the ‘ankle’ at around  $10^{9.7}$  GeV, before a strong suppression of the spectrum starts at around  $10^{10.7}$  GeV [60, 63].

Understanding CRs to be charged nuclei produced and accelerated in galactic and extragalactic sources, their production as well as their propagation to Earth are strongly influenced by the magnetic fields encountered along the way. In fact, the gyroradius  $r_g$  (also known as the Larmor radius) quantifies the deflection of charged particles in uniform magnetic fields [60]:

$$r_g = 1.1 \frac{1}{Z} \left( \frac{E}{10^9 \text{ GeV}} \right) \left( \frac{B}{\mu\text{G}} \right)^{-1} \text{ kpc}, \quad (2.1)$$

where we assumed the CR to be relativistic; with in particular the velocity component perpendicular to the magnetic field to be relativistic:  $v_{\perp} \approx c$ . The gyroradius corresponds to the radius of the circular trajectory of the CR, and is proportional to its rigidity  $R \equiv E/Z$  (i.e., energy per charge) and inversely proportional to the magnetic field strength  $B$ .

This length scale is very useful to get a qualitative understanding of the magnetic effects on CRs. For example, for CRs to be magnetically confined within an astrophysical object of size  $L$ , a minimal requirement is that the gyroradius is smaller than the object:  $r_g \leq L$  [60]. Inverting this, we find the maximum energy of CRs that can be confined within a source with a specified size and magnetic field strength:

$$E \leq E_{\text{max}} = 9.2 \cdot 10^8 Z \left( \frac{L}{\text{kpc}} \right) \left( \frac{B}{\mu\text{G}} \right) \text{ GeV}. \quad (2.2)$$

This is known as the Hillas criterion, and constitutes a rather optimistic upper limit on the CR energy since it does not consider the CR production. Taking into account the shock acceleration mechanism gives the more restrictive Lagage-Cesarsky limit [64], which contains another factor  $\beta = v_{\text{sh}}/c$  from the velocity of the shock [65]. Only for relativistic shocks does this relax to the Hillas criterion. A deviation from the Bohm limit – where the CR diffusion coefficient is well-approximated by the gyroradius – as well as energy-loss processes could introduce further suppression factors to this maximum energy [65, 66].

Nevertheless, this criterion provides a helpful assessment of potential CR sources, as is visualized in the famous Hillas plot shown in Fig. 2.3. Source classes above and to the right of the Hillas criterion (diagonal lines, corresponding to  $E_{\text{max}} = 10^{20}$  eV) are plausible candidates for these CRs. In particular, it can be seen that supernovae (SNe, brown), normal galaxies (lila) and Wolf-Rayet stars (gray) are not able to accelerate CRs to these energies, while the rest of the sources can [66]. One can continue such assessments by further requiring that these sources are luminous enough to reproduce the observed CR spectrum, see, e.g., Ref. [66] and references therein.

Returning to the features of the CR spectrum, their interpretations follow from considerations regarding both their acceleration and propagation. The knee at  $10^{6.6}$  GeV corresponds to a gyroradius of several parsecs for protons in typical galactic magnetic fields ( $B \sim O(\mu\text{G})$ ). This can be interpreted in terms of a propagation origin since the largest modes of the turbulent magnetic fields are of the some order of magnitude, implying that diffusion throughout the

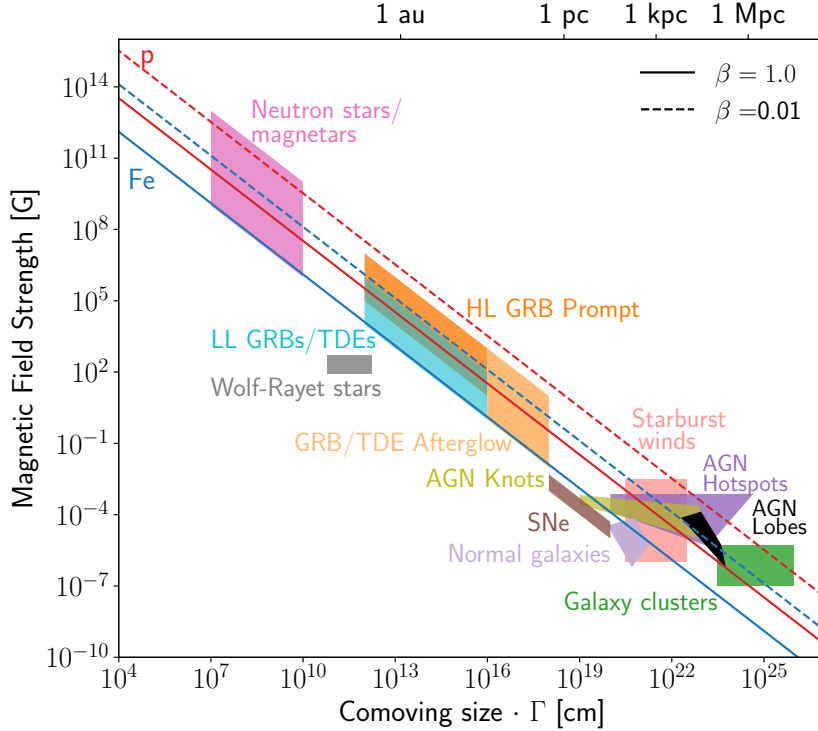


**Figure 2.3:** Hillas plot of UHECR source candidates. The colored geometric shapes represent the ranges in size ( $x$ -axis) and magnetic field strength ( $y$ -axis) of the indicated source classes. The diagonal lines are the Hillas bounds (Eq. 2.2, but with an additional factor  $\beta = v_{\text{sh}}/c$ ) for the acceleration of  $10^{11}$  GeV proton ( $Z=1$ , red) and iron ( $Z=26$ , blue) CRs, accelerated in non-relativistic ( $\beta = 0.01$ , dashed) and ultra-relativistic ( $\beta = 1$ , solid) shocks. Sources above and to the right of these lines satisfy the Hillas bound and thus are plausible candidates. Figure from [66], reproduced with permission. See this reference for more information on the source classes.

galactic disk becomes inefficient and thereby losing CRs from our galaxy that subsequently do not reach Earth [66]. An alternative explanation could be the violation of the implicit assumption that galactic sources can accelerate CRs up to the knee in the first place. In fact, supernova remnants ( $L \approx 10$  pc,  $B \sim O(\mu\text{G})$ ,  $\beta_{\text{sh}} \approx 0.01$ ) naively accelerate protons only up to the TeV-scale, but with sufficient magnetic field enhancements, the PeV-scale may be reached [66]. Despite the precise origin, it is interesting to note that the two knee features differ by a factor 25, indicating that the first knee might correspond to protons whereas the second knee is a reflection of iron nuclei (which contains 26 protons) [60]. Such a rigidity dependence follows directly from Eq. 2.2 and is also visible in the composition inferences of Fig. 2.2.

As it becomes harder to theoretically explain the acceleration of CRs up to the ankle with only galactic sources, a transition to extragalactic sources is expected between the knees and the ankle [65]. Also for the ankle itself there are various plausible explanations, with the most natural interpreting it as an effect due to photodisintegration of CR nuclei directly in the source environment [60, 67]. Only the highest energy nuclei can directly escape this environment, giving rise to a hard spectrum at Earth. The secondary nuclei from the photodisintegration then make up the lower-energetic soft spectrum, which together form the ankle.

While long-hypothesized, a strong suppression at the end of the spectrum is now firmly established [66, 68, 69]. The original hypothesis followed from expected interactions with photons of the cosmic microwave background (CMB). In particular, the production of pions<sup>5</sup> with typical CMB photons requires CR protons to have energies exceeding  $3.4 \cdot 10^{10}$  GeV [60, 65]. Combining this with the photon number density, the relevant cross-section and the typical energy loss per interaction of  $O(20\%)$  [65], one finds attenuation lengths – i.e., the distance over which the CR energy decreases by a factor  $e$  – of approximately 15 Mpc [60]. This constitutes a horizon beyond which sources cannot be responsible for the highest-energetic CRs observed on Earth. Given that sources are homogeneously distributed on cosmological scales, this mechanism induces a natural suppression to the CR flux, known as the Greisen-Zatsepin-Kuzmin (GZK) effect [70, 71]. Alternatively, the explanation for the observed suppression could again originate from a natural maximum energy that CRs can be accelerated to by their sources [66]. Looking at Fig. 2.3, this does not seem unreasonable.

Beyond measurements of the spectrum and composition, also arrival directions can provide valuable information on the CR origin. While magnetic fields deflect CR-trajectories and generally induce random walks and thus diffusive propagation, at sufficiently high rigidities the gyroradius (Eq. 2.1) becomes large enough such that over  $O(100)$  Mpc distances the deflection is only several degrees [66]. Such ballistic trajectories could then point directly back to the sources if the sources themselves are sufficiently close to Earth. Interactions with the CMB and the extragalactic background light (EBL) limit the distances to these sources to roughly the same value [66], below which the universe is also known to be inhomogeneous [72]. From these effects an anisotropic CR-sky can be expected at the highest energies. In fact, the Pierre Auger Collaboration found a dipole anisotropy above  $8 \cdot 10^9$  GeV. This dipole points away from the galactic plane and thus implies an extragalactic origin of these CRs [73]. While anisotropies on smaller angular scales are not yet statistically significant enough to claim their detection, interesting levels of significance were found from correlations of CR arrival directions with the locations of in particular starburst galaxies (SBGs) and active galactic nuclei (AGNs) [66, 74].

This interplay of detection on Earth and astrophysical interpretations in terms of both acceleration and propagation is typical for high-energy CR physics. With the main driving question of where CRs originate, each of these components can be regarded as subdisciplines due to their spatial separation: acceleration at the sources, propagation in the source environment and to Earth, and detection on Earth. Some open problems regarding the acceleration and propagation – e.g., the inconclusive interpretations of spectral features – were discussed above. A detailed and extensive listing of open problems in these subdisciplines is beyond the scope of this thesis, and the reader is referred to Ref. [66].

The detection on Earth mainly concerns the interpretation of observed EASs and the corresponding reconstruction of the properties of the primary CR. This involves the continuous development of experimental techniques to extract more information from EASs, and of hadronic interaction models to provide a better understanding of the EAS phenomenon itself. One intriguing open problem here is the so-called muon deficit, which leads to contradicting indications of the CR mass composition. A more elaborate discussion will follow in Sec. 5, whereas the phenomenon of EASs – due to its relevance for the thesis – is introduced in the next section.

---

<sup>5</sup>While the pair-production – i.e., the production of electron-positron pairs – threshold is lower due to the lighter electron mass, the CR suppression through this channel is not as significant: a CR loses only 0.1% of its energy per produced pair, with a comparable cross-section [65, 70].

## 2.3 Extensive Air Showers

Upon arrival of CRs at Earth they interact with the atmosphere. This involves many physical processes, but at a certain height the CR undergoes a hadronic interaction with the nucleus of an atom of an air molecule such as nitrogen. This is known as the first interaction and the associated center of mass energy  $\sqrt{s}_{\text{CR-air}}$  is given by

$$\sqrt{s}_{\text{CR-air}} \approx \sqrt{2m_{\text{air}}E} \approx 164 \left( \frac{m_{\text{air}}}{14.4 m_p} \right)^{1/2} \left( \frac{E}{10^{18} \text{ eV}} \right)^{1/2} \text{ TeV}, \quad (2.3)$$

which for UHECRs exceeds energies attainable at collider experiments of  $O(10 \text{ TeV})$ . Here the mass of an air nucleus  $m_{\text{air}}$  is approximated as 14.4 times the proton mass (80% nitrogen and 20% oxygen). Collisions with single air nucleons (e.g., from a proton CR primary) still results in energies exceeding  $164/\sqrt{14.4} \approx 43 \text{ TeV}$  for UHECRs.

The first interaction occurs high up in the atmosphere, at a height varying typically between 15 and 35 km [75], ultimately determined by the associated interaction length. This length depends on both the cross section of the interaction and the (number) density of air nuclei. Interestingly, the dependence on the cross section enables the study of EASs to measure this quantity at the aforementioned energies unavailable to collider experiments [75], with, e.g., the Pierre Auger Collaboration reporting the particle-production proton-air cross section at  $\sqrt{s} = 57 \text{ TeV}$  [76].

The secondary particles produced in the first interaction continue propagating down through the atmosphere and at some point decay or interact with further air nuclei, thereby triggering a cascade of particles known as an air shower. At this point it should be clear that these are stochastic processes, and that even for the same initial conditions the development in the atmosphere fluctuates from shower to shower.

Since the type of particle determines the interactions in which it can partake, an air shower is readily divided into components. The hadronic component – consisting of long-lived hadrons – forms the back-bone of the shower and feeds both the muonic and the electromagnetic (EM) component; mainly through the decay of charged and neutral pions, respectively [75]. The decay of muons provides a further channel connecting the muonic to the EM component, but due to the limited reactions in the reversed directions, the three components (hadronic, muonic, and EM) can be regarded as separate. Together, these components provide an intuitive picture of the dynamics of an air shower, which will be further outlined in the discussions of the Heitler and Heitler-Matthews models in Secs. 2.3.1 and 2.3.2.

Since the interaction length depends on the density of air  $\rho_{\text{air}}$  rather than the height  $h$ , it is convention to use the slant depth  $X$  when referring to the longitudinal development of an air shower:

$$X \equiv \int_h^\infty \rho_{\text{air}} ds, \quad (2.4)$$

which is simply the air density integrated along the shower axis, typically expressed in  $\text{g}/\text{cm}^2$ . The atmospheric depth traversed to reach the Earth's surface depends on the inclination of the shower (quantified by the zenith angle  $\theta$ ) as well as the height of the surface compared to sea level. For example, vertical showers ( $\theta = 0^\circ$ ) reach the Pierre Auger Observatory – located at

a mean altitude of 1400m – after traversing approximately  $875 \text{ g/cm}^2$  [77]. Taking into account the curvature of Earth, this can increase by a factor 40 for horizontal showers ( $\theta = 90^\circ$ ) [78].

In the initial stage of an air shower, the production of particles dominates over their losses to the environment. Therefore, the shower increases in size until this relationship is reversed. The depth in the atmosphere where the shower reaches its maximum size  $N_{\text{max}}$  is known as  $X_{\text{max}}$ , and turns out to be a very valuable mass indicator – i.e., an observable that provides a measure of the atomic mass of the primary CR.

This can be understood from the so-called *superposition principle*: motivated by a negligible nuclear binding energy of the primary CR with mass  $A$  and energy  $E$ , its resulting air shower can be represented as a superposition of  $A$  proton-induced showers each with energy  $E/A$  [45, 65, 75]. Since air showers initiated by lower-energetic CRs traverse, on average, a smaller depth to develop to their maximum size, the superposition principle implies that heavier nuclei tend to have smaller  $X_{\text{max}}$  values. A further implication is that the shower-to-shower fluctuations  $\sigma(X_{\text{max}})$  of heavier nuclei are statistically suppressed. Note that beyond the first two statistical moments of  $X_{\text{max}}$ , also its complete distribution provides information on the CR mass composition [4].

While the superposition principle ignores the fact that due to their larger cross section, heavier CRs interact higher up in the atmosphere, also not all nucleons partake in this first interaction. From detailed Glauber calculations [79] it turns out that the average interaction length of these nucleons correspond to the one for protons, which is known as the semi-superposition theorem [45]. Therefore, the naive superposition principle can still be applied to obtain the mass dependence of average observables, but some caution is required for dealing with shower-to-shower fluctuations due to a common depth of the first interaction [45].

Further valuable composition information can be obtained from studying the sizes of various shower components at specific depths, with the depth corresponding to the ground level  $X_{\text{ground}}$  of particular interest. For UHECRs the area of this footprint can be  $O(10) \text{ km}^2$  [80], giving rise to the name extensive air showers. As the shower develops and the hadronic and muonic components feed the EM component, EM particles become the most abundant. Therefore,  $X_{\text{max}}$  is determined by where this component reaches its maximum size  $N_{e,\text{max}}$ . While  $N_{e,\text{max}}$  is independent of the CR mass, the size of this component is strongly attenuated on its further development to the ground. Thereby, the depths  $X_{\text{max}}$  and  $X_{\text{ground}}$  respectively introduce a mass and an inclination dependence to the EM size on the ground  $N_e$ . Given a sufficient depth to attenuate, smaller EM footprints can thus be expected from showers induced by heavier CRs [45, 75, 81].

This relationship is inverted when considering the muonic footprint. Muons mainly originate from the decay of charged pions and kaons towards the end of the hadronic cascade [75]. Since this cascade takes longer to develop from higher-energetic CRs, more energy is lost to the EM component, leaving less for the production of muons. This gives rise to a less than linear scaling of the muon number with CR energy. With a subsequent application of the superposition principle, this deviation from linearity introduces the aforementioned mass dependence [45, 75, 81]. The attenuation of the muonic component, and therefore the correlation with  $X_{\text{max}}$ , plays only a minor role [81].

Beyond  $X_{\text{max}}$  and the shower sizes, mass sensitive observables include the steepness of the lateral distribution function (i.e., the decrease in particle density as a function of the distance from the shower core), the muon production depth, and the inclination dependence of a signal rise-time asymmetry in opposite regions of a detector array [45]. These observables are rather

involved and not of direct relevance to the thesis. Instead, we will focus mainly on the muon number at ground  $N_\mu$  and  $X_{\max}$ , whose main features are well-reproduced by the so-called Heitler and Heitler-Matthews analytic models of air showers. It is worthwhile to highlight these models in the following subsections.

### 2.3.1 Heitler Model: Electromagnetic Showers

The original Heitler model [82, 83] considers the development of purely EM air showers. The development of these showers rely on two branching processes: Bremsstrahlung (i.e. the emission of a photon from an electron or positron), and pair production (i.e. the production of an electron-positron pair from a photon). It turns out that in air these processes occur on similar atmospheric depth scales, quantified by the splitting length (i.e., depth)  $\lambda_e = X_0 \cdot \ln 2$  over which electrons and positrons lose half their energy to Bremsstrahlung. Here the radiation length (depth)  $X_0 \approx 37 \text{ g/cm}^2$  corresponds to an e-fold decrease in energy due to Bremsstrahlung, but also to a  $7/9$  probability of pair production from photons [60]. The translation of the latter<sup>6</sup> to an average depth for pair production to take place  $\langle X \rangle_{\text{pair}}$ , shows that the splitting length neatly captures both processes;  $\lambda_e / \langle X \rangle_{\text{pair}} = \ln 2 \cdot \ln(9/2) \approx 1.04$ . Assuming the radiated energy from Bremsstrahlung after a splitting length to be carried away by a single photon, and a democratic pair production in which both electron and positron receive half the energy of the photon, the Heitler model combines electrons, positrons and photons into a single EM particle that splits into two after each of these splitting lengths [81, 84].

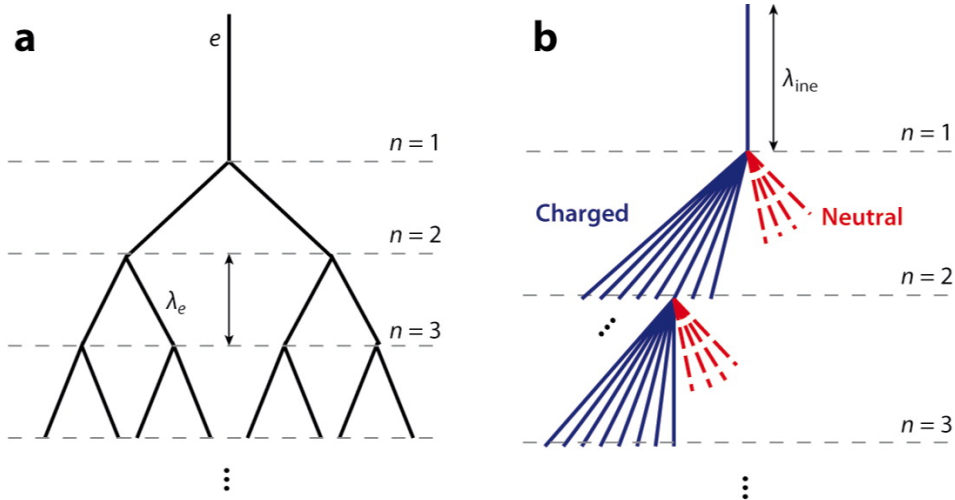


**Figure 2.4:** Schematic visualization of electromagnetic (a, left) and hadronic (b, right) air showers in the Heitler [82, 83] and Heitler-Matthews [84] models, respectively. Figure from [75], reproduced with permission.

Repeating this process, the primary particle with energy  $E_0$ <sup>7</sup> has split into  $N = 2^n$  particles

<sup>6</sup>This follows from defining a differential probability of pair production;  
 $\langle X \rangle_{\text{pair}} = \int_0^\infty X \frac{dP_{\text{pair}}}{dX} dX = \int_0^\infty X \frac{-\ln(1-7/9)}{X_0} (1-7/9)^{X/X_0} dX = X_0 / \ln(9/2)$ .

<sup>7</sup>When discussing air showers here and in Chapters 8 and 9 we will use the subscript 0 to denote the energy of the CR primary initiating the shower, and leave  $E$  without subscript available for secondaries in the shower.

after propagating  $n$  splitting lengths, each with an energy  $E_0/N$ . The resulting air shower is visualized in the left panel of Fig. 2.4. Once the energies of the secondary particles fall below a critical energy  $E_c^{\text{e.m.}} \approx 85$  MeV [81, 84] – where ionization losses start to dominate – the number of particles stops growing, giving rise to the shower maximum:

$$N_{\text{max}} = \frac{E_0}{E_c^{\text{e.m.}}}, \quad X_{\text{max}} = \lambda_e \cdot n_c = X_0 \cdot \ln \left( \frac{E_0}{E_c^{\text{e.m.}}} \right), \quad (2.5)$$

where the critical generation  $n_c$  followed from equating  $N_{\text{max}}$  to the number of particles at generation  $n$ , and the factor  $\ln 2$  dropped out by substituting in the radiation length  $X_0$ .

Despite the simplifications, the energy dependence of the shower maximum –  $N_{\text{max}} \propto E_0$  and  $X_{\text{max}} \propto \ln(E_0)$  – are reproduced<sup>8</sup> by experiments and detailed Monte Carlo simulations [84]. This shows that an analytic treatment of EASs can lead to a deeper understanding of these complex phenomena.

### 2.3.2 Heitler-Matthews Model: Hadronic Showers

The EM model of air showers was extended to include a hadronic component, now known as the Heitler-Matthews model [84]. Instead of considering a single type of EM particle, the shower consists of charged and neutral pions, with the latter promptly decaying into two photons inducing EM cascades, as illustrated in the right panel of Fig. 2.4. The charged pions keep interacting with air, producing lower-energetic charged and neutral pions at a 2:1 ratio, until their decay length becomes shorter than their interaction length and subsequently decay into muons that propagate relatively unaffected to the ground.

While this model explicitly deals with pions only, it can be generalized to capture the more abstract energy flow between the three shower components. Instead of fixing the ratio of EM to hadronic energy per interaction – as originally done by Matthews [84] – one can leave it variable [81] to be determined by detailed Monte Carlo simulations. This could then implicitly take into account that the hadronic component consists of more types of particles than only charged pions.

The energy remaining in the hadronic component after  $n$  interactions (hereafter called *generations*) is then simply  $E_{\text{had},n} = E_0 \cdot r^n$ , with  $r$  defined as the fraction of energy remaining in the hadronic component after a single generation. Thus for pure pionic showers ( $r = 2/3$ ) over 90% of the energy is transferred to the EM component within 6 generations [75], highlighting its dominant contribution to  $X_{\text{max}}$ .

To follow the particle numbers it is necessary to define a (total) multiplicity  $n_{\text{mult}}$  of an interaction, and how the energy is distributed among the secondaries. In the Heitler-Matthews model the multiplicity is assumed constant and the energy evenly distributed. While the multiplicity is expected to have only a small energy dependence ( $n_{\text{mult}} \propto E^{1/5}$  for  $pp$  collisions [84]) and thus seems a fair assumption, an equal division of energy contradicts the known leading particle effects of hadronic interactions in air showers [81].

Nevertheless, under these assumptions the Heitler-Matthews model enables a calculation of the number of muons on the ground. Since the energy is evenly distributed over all particles,  $r$  not only corresponds to the fraction of energy remaining in the hadronic component, but also to the fraction of the multiplicity producing hadronic particles. Therefore, the number of hadronic

<sup>8</sup>Due to the lack of intrinsic fluctuations in this model, these quantities can be assumed to correspond to the averages in simulations and experiment.

particles after  $n$  generations is simply  $N_{\text{had},n} = (rn_{\text{mult}})^n$ . A division of the aforementioned hadronic energy gives  $E_{\text{had},n}/N_{\text{had},n} = E_0/(n_{\text{mult}})^n$ , the energy of each hadronic particle. These decay to muons once their energies fall below the critical energy  $E_c$  – corresponding to the energy at which the decay length becomes shorter than the interaction length, analogous to  $E_c^{\text{e.m.}}$  defined in the previous section. For pure pionic air showers this is typically  $E_c^\pi \approx 20$  GeV [84], but for generalized hadronic showers we keep it variable and drop the superscript<sup>9</sup>.

The generation at which the energy of the hadronic particles reach the critical energy is known as the critical generation  $n_c$ :

$$n_c = \log(E_0/E_c)/\log(n_{\text{mult}}). \quad (2.6)$$

From their decay, the number of hadronic particles at this generation equals the number of muons  $N_\mu$  propagating to the ground

$$N_\mu = N_{\text{had},n_c} = (rn_{\text{mult}})^{n_c} = \left(\frac{E_0}{E_c}\right)^\beta, \quad (2.7)$$

where

$$\beta \equiv \log(rn_{\text{mult}})/\log(n_{\text{mult}}) \quad (2.8)$$

quantifies the energy dependence.

Since this derivation relied on the unphysical assumption of evenly distributed energy among secondaries, Matthews [84] further extended the model to include inelasticities of hadronic interactions. He assumed a leading hadronic particle to carry away a fraction of the primary energy, and the remainder to be divided between the two components according to the  $r$ -parameter. This implicitly increases the fraction of energy kept in the hadronic component, and thereby enhances the muon number<sup>10</sup>.

Alternatively, one could fix the energy fraction remaining in the hadronic component to  $r$ , and take the energy of the leading hadronic particle directly from that component. Now the only difference with respect to the standard Heitler-Matthews model is an uneven distribution of energy among hadronic secondaries, with the leading particle requiring more generations to reach the critical energy. This allows for more energy to be lost to the EM component, which turns out not to be compensated for by the fewer generations of the remaining particles. Accordingly, the muon number in such a scenario would be suppressed. This effect would be weaker if one furthermore relaxes the assumption of the leading particles to always be hadronic, as, e.g., considered in [85].

It is therefore not trivial how a consistent inelasticity-treatment influences the muon number. However, from the inelasticity-extension of Matthews, he found that these considerations do not significantly change the general shape of Eq. 2.7, but only affects the index  $\beta$  of the power-law (Eq. 2.8). Leading particle effects can thus likely be absorbed into the parameters  $r$  and/or  $n_{\text{mult}}$ , with their effective values fixed by comparisons with detailed Monte Carlo simulations [84]. Typical values obtained for  $\beta$  are then in the range 0.88-0.92 [45, 86].

---

<sup>9</sup>Our  $E_c$  thus corresponds to an effective value for the entire hadronic component, whereas in principle each type of hadron has its own critical energy. However, not all hadrons (predominantly) decay to muons, making such a division non-trivial.

<sup>10</sup>Technically, the energy-dependence parameter  $\beta$  (Eq 2.8) is enhanced, indicating a steeper increase of the muon number with energy.

For the computation of the shower maximum it suffices to only consider the EM component, whose energy budget  $E_{e.m.}$  implies [81]:

$$N_{\max} \approx N_{\max,e} = \frac{E_{e.m.}}{E_c^{e.m.}} = \frac{E_0}{E_c^{e.m.}} - N_\mu \frac{E_c}{E_c^{e.m.}}, \quad (2.9)$$

inheriting a weak dependence on the muon number. However, this assumes that all EM particles reach the critical energy at the same depth, but from the right panel of Fig. 2.4 it is clear that the EM subshowers are initiated at different depths and therefore do not all contribute to  $N_{\max}$ .

This also complicates the computation of  $X_{\max}$ . One could consider only the subshower from the first interaction since it feeds the most energy into the EM component, and showers initiated by subsequent generations reach their maximum size in shallower depths. Then with  $\lambda_{\text{ine}}$  the interaction length of the first (inelastic) interaction, and  $n_{\text{mult}}$  the total multiplicity, the application of Eq. 2.5 results in [45, 75]:

$$X_{\max} = \lambda_{\text{ine}} + X_0 \ln \left( \frac{E_0}{2 n_{\text{mult}} E_c^{e.m.}} \right), \quad (2.10)$$

where the factor 2 reflects the fact that neutral pions produce two photons in their decay. This again assumed an even distribution of energy among secondaries. A leading particle would carry the shower maximum deeper into the atmosphere [45, 81], and the same effect can be expected from taking into account the EM subshowers of later generations. These considerations are beyond the analytic Heitler-Matthews model.

Finally, applying the superposition principle to Eqs. 2.7 and 2.10 explicitly show their mass and energy dependencies as discussed in Sec. 2.3:

$$N_\mu \propto A^{1-\beta} E_0^\beta, \quad X_{\max} \sim c + D \ln(E_0/A), \quad (2.11)$$

with  $A$  the atomic mass of the primary CR, and  $c$  and  $D$  the appropriate<sup>11</sup> constants [45].

---

<sup>11</sup>Here  $D \equiv dX_{\max}/d \ln E_0$  is the elongation rate and includes the energy dependence of  $\lambda_{\text{ine}}$ . The constant term of  $\lambda_{\text{ine}}$  is absorbed into  $c$  along with the multiplicity and critical energy.



# 3 | The Pierre Auger Observatory

The Pierre Auger Observatory<sup>1</sup> is the world’s largest observatory for the detection of UHECRs, in terms of both surface area and exposure [77]. Located on the Pampa Amarilla plain at the foot of the Andes mountains, in the Mendoza province of western Argentina, it observes the southern sky with an area of approximately 3000 km<sup>2</sup> (see Fig. 3.1) – comparable to that of the country Luxembourg. The observatory has been taking data since 2004, and was ultimately completed in 2008 [77], resulting in an exposure<sup>2</sup> exceeding 60,000 km<sup>2</sup> sr yr [69]. This enabled the Pierre Auger Observatory to make invaluable contributions to our understanding of UHECRs, with in particular the extension of the all-particle spectrum to above 10<sup>20</sup> eV, measurements of the composition at these energies and the discovery of a large-scale dipole anisotropy above 8 · 10<sup>18</sup> eV [87]. A continuation of this scientific endeavor is ensured by the ongoing upgrade, dubbed AugerPrime [88, 89], extending the lifetime of the observatory to beyond 2030 [90].

Named after the discoverer of EASs, the Pierre Auger Observatory is built to analyze these phenomena by simultaneous measurements from a variety of detectors. Since data from the observatory – also referred to as ‘Auger data’ – constitute the main experimental reference for the work in this thesis, it is worthwhile to describe in some detail the various detector components in Sec. 3.1, and highlight the main scientific results in Sec. 3.2.

## 3.1 Detectors

Originally, the Pierre Auger Observatory was built as a hybrid observatory, consisting of a surface array of 1600 water Cherenkov detectors (WCDs) and four sites with each 6 fluorescence telescopes to provide measurements of respectively the lateral (i.e., footprint) and longitudinal profile of EASs [90]. The WCDs are placed in a triangular grid with 1.5 km spacing, and are collectively known as the surface detector (SD). From the border of this array, the sites with fluorescence telescopes overlook the SD and collectively make up the fluorescence detector (FD). This setup is visualized in the right panel of Fig. 3.1.

An EAS that is simultaneously detected by both the SD and the FD is known as a hybrid event. Such events provide valuable information for the energy-calibration of the SD – which produces a much larger data set – and allow for more precise determinations of the arrival direction [77]. The basic principle of a hybrid detection is visualized in Fig. 3.2, with example longitudinal and lateral profiles in the right panels.

---

<sup>1</sup>For the interested reader, see also the official website: <https://www.auger.org>.

<sup>2</sup>For showers arriving at zenith angles  $\theta \leq 60^\circ$ . The exposure exceeds 90,000 km<sup>2</sup> sr yr when extending this to  $\theta \leq 80^\circ$  [87].

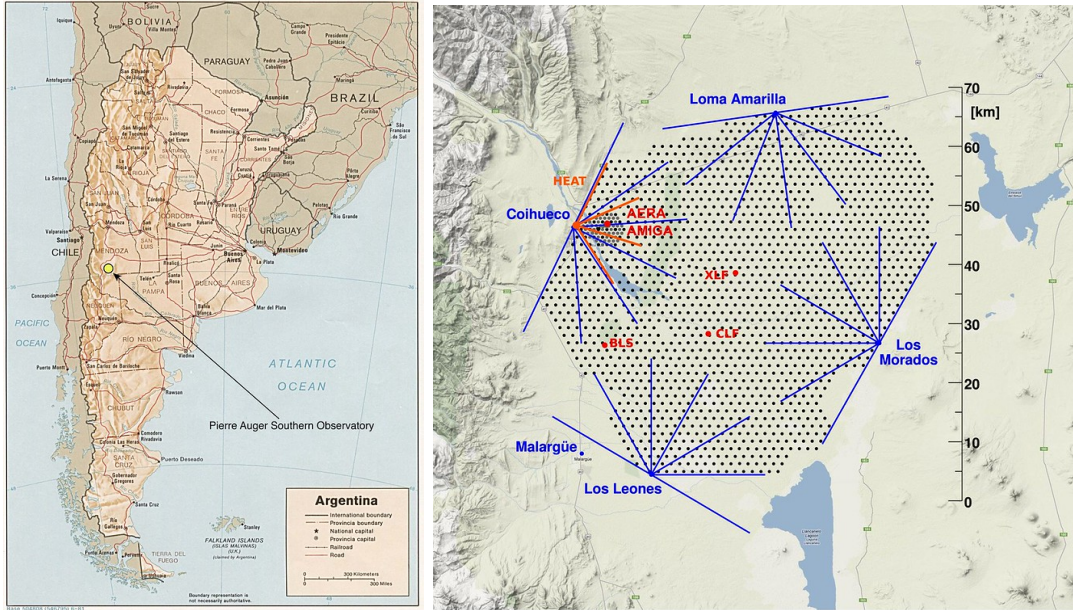


**Figure 3.1:** *Left:* Map of Argentina with the location of the Pierre Auger Observatory – near the town Malargüe in the Province of Mendoza – indicated by the yellow circle and corresponding arrow. *Right:* Map of the observatory itself with each black dot representing a WCD of the SD, and the blue lines representing the field of views of the telescopes making up the FD. Further indicated are HEAT, AERA, AMIGA, BLS, XLF and CLF, see text. Figures from [91], reproduced with permission.

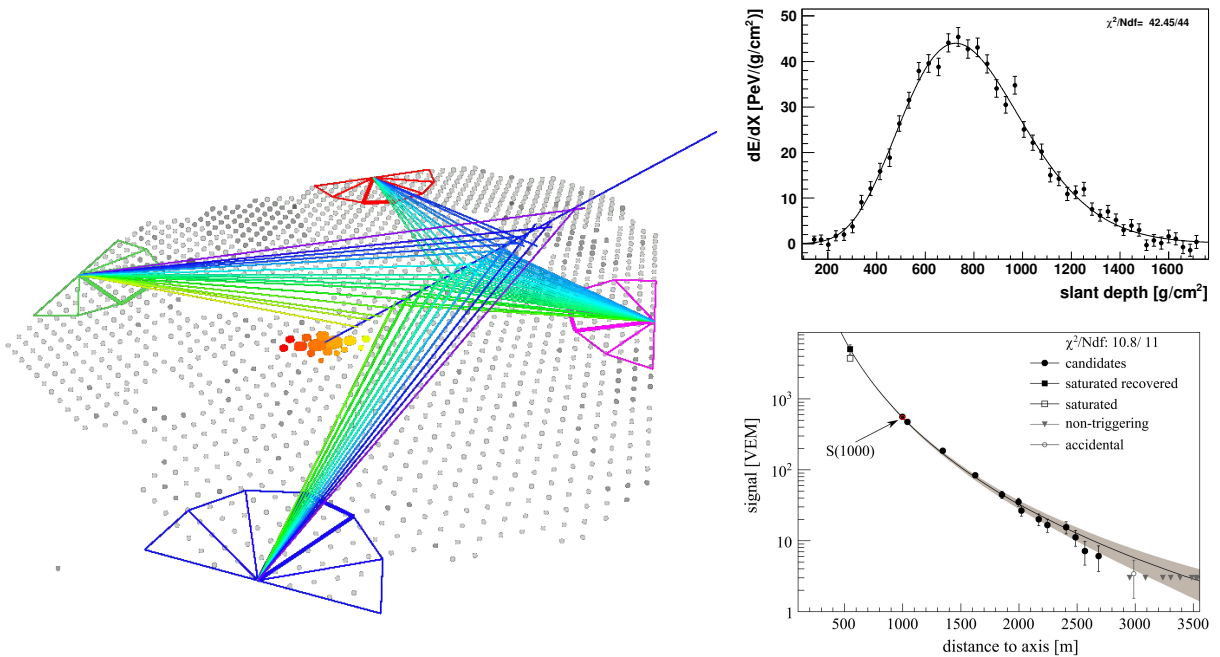


**Figure 3.2:** Hybrid measurement of an EAS at the Pierre Auger Observatory (left). The FD and SD provide measurements of the longitudinal (top right) and lateral (bottom right) profile, respectively. The panels do not correspond to the same event. Figures from [91] (left; author made the background white, provided under the same license), [92] (top right), and [77] (bottom right), reproduced with permission.

Throughout the years, further detectors were developed and added to the observatory to extend the sensitive energy range to lower values, and to enable a better reconstruction of EASs by obtaining additional independent measurements. In the following we will briefly describe the SD and FD, as well as point out the newer detectors and ongoing improvements.

### 3.1.1 Surface Detector

The WCDs of the SD consist of sealed cylindrical tanks with a 3.6 m diameter and 1.2 m height, filled with 12,000 litres of ultra-purified water [77]. Upon the traversal of charged relativistic particles – such as electrons, positrons and muons – through the tank, their velocities could exceed the speed of light in water and thereby produce Cherenkov radiation. This radiation produces signals in the three downward-facing photomultiplier tubes (PMTs) mounted at the top of the inside of the tank [90], see Fig. 3.3. Measured in units of the Cherenkov light produced by a muon traversing the tank vertically through the middle (vertical equivalent muon; VEM), a set of local triggers need to be overcome for the WCD to be considered activated. Further triggers associated with the neighboring WCDs then determine the detection of a coherent signal, and whether it can be attributed to an EAS [90].

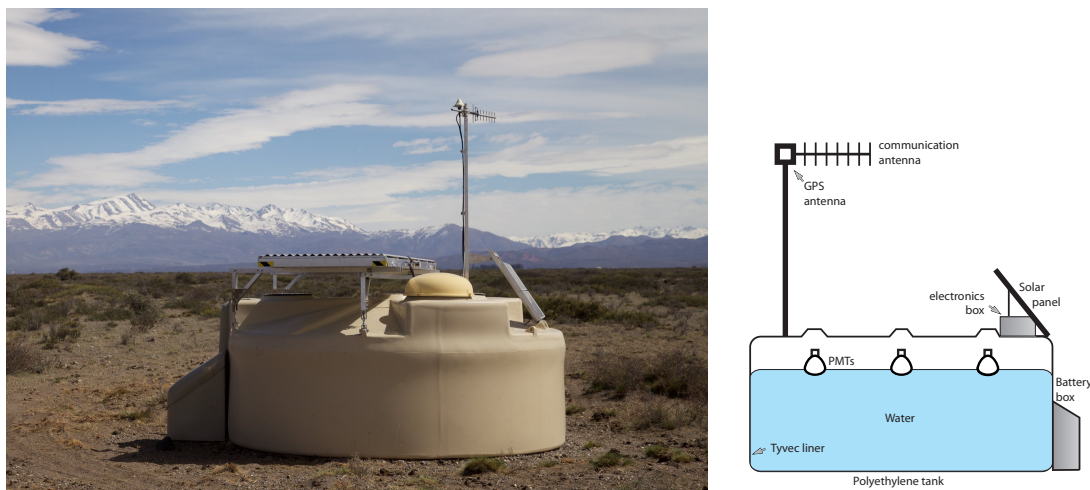


**Figure 3.3:** Photograph and schematic of a WCD of the SD. The tank is filled with ultra-purified water, inducing Cherenkov radiation from relativistic particles that is observed by the three PMTs. The WCD on the photo is already upgraded to include an SSD (the horizontally mounted panel), see Sec. 3.1.3. Photo and schematic from [91] and [53], respectively. Reproduced with permission.

For the required processing and communication of the signals, each WCD contains an electronic system powered by a solar panel, a radio antenna and a GPS receiver [90]. The obtained timing information enables the reconstruction of the location where the shower core intersects the SD array, along with the associated arrival direction. With the timing precision of 10 ns, the Pierre Auger Observatory has an angular resolution on the sky better than  $1^\circ$  [90]. With the location of the shower core, the distance can be computed from each WCD to this axis, resulting in a lateral profile as shown in the bottom-right panel of Fig. 3.2 [77]. The interpolated signal at 1000 m from the core,  $S(1000)$ , quantifies the size of the shower and thereby constitutes an important energy estimator. By first correcting for the zenith-angle-dependent attenuation – with

the so-called Constant Intensity Cut method – the energy follows from a power-law dependence on the shower size, based on a calibration with hybrid events [69, 80].

The energy-range the SD is sensitive to is determined by the sparsity of the array and its area. At the high-energy end of the spectrum (at a few  $10^{20}$  eV [87]) the flux becomes too low to obtain sufficient statistics with a  $3000 \text{ km}^2$  array. This is rather costly to enhance. On the contrary, at the low-energy end of the spectrum (around  $2.5 \cdot 10^{18}$  eV [90]) the footprints of EASs become too small to be sufficiently sampled by an array with 1.5 km spacing. Therefore, the sensitivity of the SD was extended to lower energies (around  $10^{17}$  eV [93]) by placing a relatively low number of additional WCDs to construct a smaller 750-m-array (SD-750) [90]. This array is colloquially known as the ‘infill array’ and is located near the Coihueco FD site, see Fig. 3.1. Note that due to the larger flux, the resulting area is adequate to obtain sufficient statistics. An even denser 433-m-array (SD-433) was recently installed, further enhancing the sensitivity down by half an order of magnitude [90].

### 3.1.2 Fluorescence Detector

The telescope building of each of the four FD sites is situated on a small elevation with respect to the SD. This allows for an obstacle-free view over the array. The buildings are subdivided into six bays, each containing one fluorescence telescope. See, e.g., the photograph of the Los Morados FD site in Fig. 3.4. In this setup, each telescope has a field of view of  $30^\circ \times 30^\circ$  in azimuth by elevation [92], as can be further understood from Figs. 3.1 and 3.2.

The passage of an air shower through the atmosphere induces the excitation of nitrogen molecules, which subsequently radiate away this excess energy in the near ultra-violet wavelength band. This fluorescence light from sufficiently energetic and nearby air showers developing within the field of view can be observed at the FD sites. The light then passes through a UV filter, and is concentrated by a segmented 13 m<sup>2</sup> mirror onto a camera consisting of  $22 \times 20 = 440$  PMTs [92], see the schematic in Fig. 3.4.

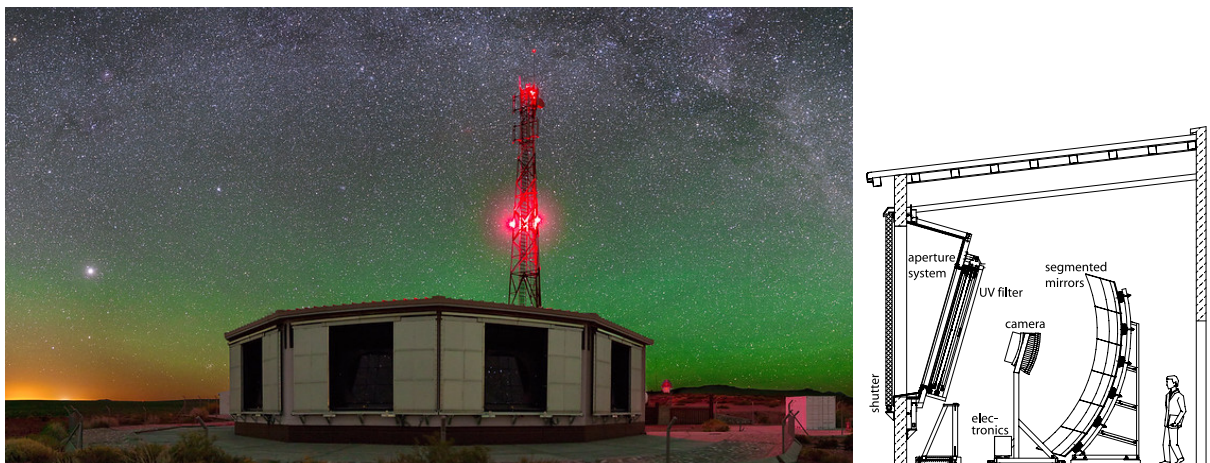


**Figure 3.4:** *Left:* Photograph of the Los Morados FD site with open shutters. Four out of six telescope bays are visible, along with the communications tower. *Right:* a schematic cross-section of one of these bays. Fluorescence light comes in from the left, passes through the UV filter, and is concentrated by the segmented mirrors onto the camera. Photo and schematic from [91] and [92], respectively. Reproduced with permission.

Through this excitation process, the air shower deposits around 90% of its energy in the atmosphere and thereby enables a calorimetric measurement of the energy of the primary CR [92]. The associated longitudinal profile of differential energy-deposit – see, e.g., the top-right panel of Fig. 3.2 – is reconstructed from the fluorescence yield based on information from an extensive atmospheric monitoring program [77, 90]. This program includes the operation of the central (CLF) and extreme (XLF) laser facilities as well as the balloon launching station (BLS), which are indicated in Fig. 3.1.

The obtained longitudinal profile is fitted with a Gaisser-Hillas function [77, 94]:

$$f_{\text{GH}}(X) = \left( \frac{dE}{dX} \right)_{\text{max}} \left( \frac{X - X_0}{X_{\text{max}} - X_0} \right)^{(X_{\text{max}} - X_0)/\lambda} \exp \left( \frac{X_{\text{max}} - X}{\lambda} \right), \quad (3.1)$$

providing direct access to the shower maximum  $X_{\text{max}}$ , and the integral of this function gives the aforementioned calorimetric energy measurement. The latter needs to be corrected for the invisible energy; approximately 10 – 15% of the primary energy is carried into the ground by neutrinos and high energy muons [95].

Unfortunately, these direct measurements can only be made on clear, moonless nights due to the faint nature of the emitted fluorescence light. This results in an FD duty cycle of around 15%, constituting a significant reduction in statistics compared to the 100% duty cycle of the SD [77]. This further emphasizes the importance of hybrid events, which enable a data-driven interpretation of the larger SD data set.

Air showers induced by CRs with energies below  $\sim 10^{18}$  eV produce insufficient fluorescence light to be detected by the FD [96]. However, relativistic particles in these showers produce air-Cherenkov radiation which can be detected with much the same technique, only that these lower-energetic showers develop higher up in the atmosphere [90]. For this reason, three additional fluorescence telescopes were installed with a hydraulic tilting system to shift the field of view upward by  $29^\circ$  [77]. These are known as the High Elevation Auger Telescopes (HEAT), and are located near the Coihueco FD site, see Fig. 3.1. Here, together with SD-750 and SD-433, they could potentially provide hybrid measurements at lower energies. With HEAT-data only the CR energy-spectrum was measured down to  $10^{16.5}$  eV [96].

### 3.1.3 Other Detectors and AugerPrime

In addition to the SD and the FD along with their extensions (SD-750, SD-433, and HEAT), there are several more detectors (being) installed as part of the AugerPrime upgrade [88, 89].

The main component of this upgrade is the placement of a  $(3.8 \times 1.3)$  m<sup>2</sup> surface scintillator detector (SSD) on top of each WCD [89], as visible in the photograph of Fig. 3.3. In contrast to the WCD, these flat detectors have identical responses to passing muons and EM particles. These two shower components can thus be distinguished by combining information from the WCDs and the SSDs [90]. One would then no longer need to rely on attenuation arguments of the EM component. This is particularly important in light of the muon deficit (see Chapter 5).

A further contribution to improving our understanding of the muonic component will come from the Underground Muon Detector (UMD), which consist of three 10 m<sup>2</sup> scintillator detectors – similar to the SSD [90] – buried 2.3 m underground next to each of the WCDs of the SD-750 [97]. Together, these form the Auger Muons and Infill for the Ground Array (AMIGA), indicated in Fig. 3.1. Corresponding to a 540 g/cm<sup>2</sup> depth, the overburden of the ground absorbs most of

the EM component and will enable the direct detection of muons with energies exceeding 1 GeV [90]. In fact, the prototype of the UMD already provided first measurements [98] of the muonic component from air showers with energies between  $2 \cdot 10^{17}$  eV and  $2 \cdot 10^{18}$  eV, which confirm the existence of the muon deficit.

The charged-particle front of EASs induces characteristic radio waves, which could provide another independent detection method for these showers. A prototype array of radio antennas – the Auger Engineering Radio Array (AERA) [99], see Fig. 3.1 – showed promising results for this technique, which is found to be particularly suitable for the detection of very inclined air showers due to the enlarged radio footprint [100]. Consequently, each of the WCDs in the large 1500-m-array will be equipped with a radio antenna [90, 101].

Finally, the AugerPrime upgrade includes more tweaks to the existing detectors, with in particular a fourth PMT for the WCDs, enhanced electronics and an extended duty cycle of the FD [90].

## 3.2 Scientific Results

The science case of the Pierre Auger Observatory is very broad. The main objective of studying UHECRs through their energy spectrum, nuclear composition, and arrival directions is complemented by **1)** an extension to energies below  $10^{18}$  eV, **2)** multi-messenger studies [102] through the air showers produced by photons [103] and neutrinos<sup>3</sup> [107], **3)** constraints on the hypothetical violation of Lorentz invariance [108], **4)** measurements of hadronic interaction properties at the highest energies [76, 109], and **5)** observations of geophysical phenomena such as ELVES [110]. In this section we will limit ourselves to the spectrum, composition and arrival directions of CRs, whereas the remainder of the thesis will be concerned with the relationship between the composition interpretation of Auger data and hadronic interactions in air showers.

### 3.2.1 Energy Spectrum

The all-particle energy-spectrum of CRs measured by the Pierre Auger Observatory is shown in Fig. 3.5. This follows from a variety of energy-reconstruction methods (left panel), which were touched upon in the previous section: the integrated energy-deposit measured by the FD – after correcting for the invisible energy – enable hybrid events (blue) to provide the calibration of the shower-sizes measured by the SD (black and red) and the SD-750 (gray) [111]. Air-Cherenkov emission enables a similar FD measurement of lower-energetic showers with HEAT and the Coihueco FD site (green) [96].

The combination of these spectra (right panel) show four statistically significant features. In addition to precision measurements of the second knee (at  $10^{17}$  eV), ankle (at  $5 \cdot 10^{18}$  eV), and suppression (at  $5 \cdot 10^{19}$  eV) discussed in Sec. 2.2, the Pierre Auger Collaboration recently discovered [69] a steepening around  $10^{19}$  eV. This feature does not possess a significant (celestial) declination dependence and is therefore unlikely a result of a local proton-emitting source that by its proximity contributes significantly to the observed spectrum [63]. Instead, the features above the ankle could reflect subsequently larger masses dominating the spectrum with increasing energy, with the one around  $10^{19}$  eV corresponding to the transition from helium to the carbon-nitrogen-oxygen group. These two components could arise from sources accelerating a mixture of

---

<sup>3</sup>Also as a follow-up for blazar [104] and gravitational wave [105, 106] events.

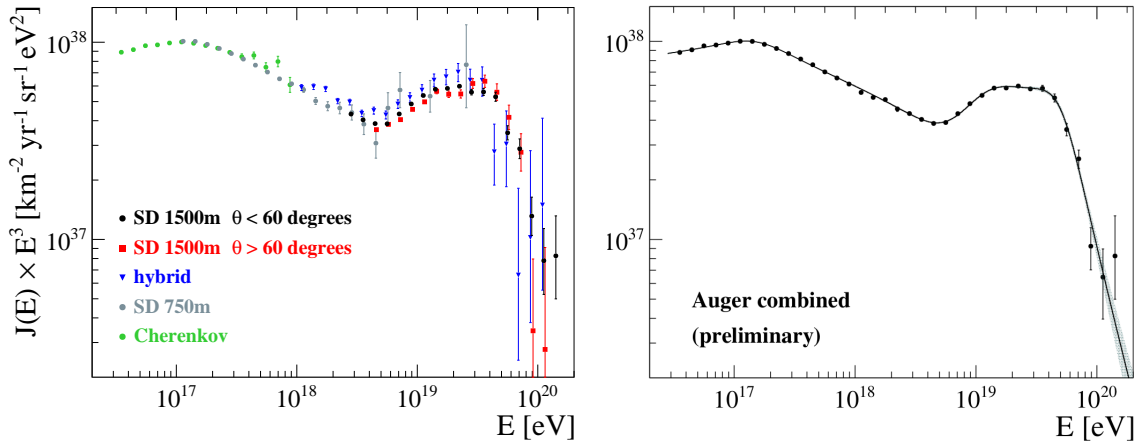


**Figure 3.5:** The all-particle CR energy-spectrum as measured at the Pierre Auger Observatory with the various techniques (left) and their combined result (right). Figures from [87], reproduced with permission.

nuclei to a rigidity-dependent maximum energy, but also from the photodisintegration of heavy nuclei at the source or on their propagation to Earth [63].

### 3.2.2 Mass Composition

As discussed in Sec. 2.3, the main indicator for the mass composition is the shower maximum  $X_{\max}$ . This is directly measured with the FD (see Sec. 3.1.2), but a complete shower reconstruction necessitates a simultaneous detection with the SD [112]. Based on 47,863 hybrid events, Fig. 3.6 shows the first two statistical moments of the energy-dependent  $X_{\max}$ -distributions.

The subsequent derivation of the CR mass composition follows from comparisons to Monte Carlo simulations of EASs. The results of these simulations depend on the used hadronic interaction models, which will be introduced in Chapter 4. In particular, the choice of the *high-energy* hadronic interaction model has a notable effect on the  $X_{\max}$ -prediction, corresponding to the various lines in Fig. 3.6. The proximity of the data to these proton (red) or iron (blue) lines indicate how light or heavy the composition is, respectively.

Independent of the specific model,  $\langle X_{\max} \rangle$ -data indicates the composition to get lighter until a minimum at around  $2 \cdot 10^{18}$  eV, and getting heavier again at the highest energies [113]. A similar behavior follows from  $\sigma(X_{\max})$ -data, but the asymmetry around the aforementioned minimum indicates a mixed composition at lower energies – resulting in larger fluctuations – and a pure composition towards the higher energies.

A precise interpretation of this data can be made after a conversion to the statistical moments of  $\ln A$  – i.e., the natural logarithm of the atomic mass – under the assumption of a particular high-energy hadronic interaction model [3]. Then it becomes clear that at the highest energies the average composition inferred with QGSJETII-04 is too light to accommodate the observed small  $\sigma(X_{\max})$ , corresponding to a tension between  $\langle X_{\max} \rangle$  and  $\sigma(X_{\max})$  [113]. The other models allow for a consistent interpretation over the entire energy range.

Nevertheless, the indications for heavier compositions with increasing energy agrees with the astrophysical picture associated to the energy spectrum. In fact, a combined fit of the energy spectrum and the mass composition inferred from  $X_{\max}$  above the ankle provides direct support

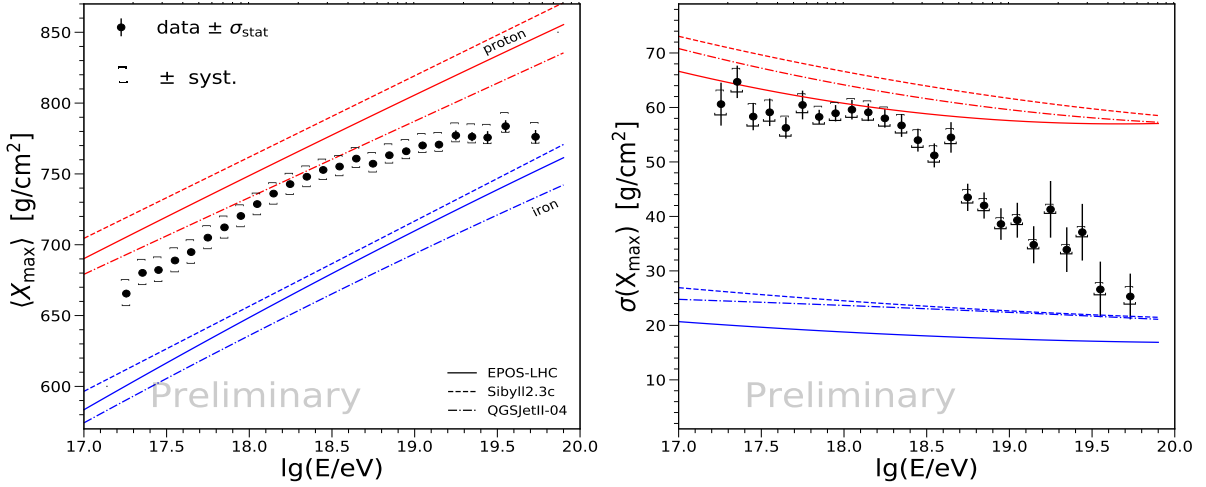


**Figure 3.6:** Energy dependence of the average (left) and fluctuations (right) of the shower maximum  $X_{\max}$  as inferred from hybrid events detected at the Pierre Auger Observatory. A comparison with Monte Carlo simulations (lines) – based on the high-energy hadronic interaction models (line-types) – reveals the CR mass composition relative to a pure proton (red) or iron (blue) composition. Figures from [113], reproduced with permission.

for sources with hard injection spectra of heavy nuclei and a relatively low rigidity-dependent maximum energy [114].

As mentioned in Sec. 2.3, the CR mass can be independently inferred from EAS-information other than direct observations of  $X_{\max}$ . For example, the correlation in hybrid events between  $X_{\max}$ , from the FD, and the size of the ground signal, from the SD, is a measure of the spread of  $\ln A$ . The Pierre Auger Collaboration found a negative correlation around the ankle, providing evidence for a heavy ( $A > 4$ ) and mixed composition [115].

Further mass inferences were performed using the time profiles of signals in the WCDs [116], and an inclination-dependent rise-time asymmetry of opposite regions of the SD [117]. Also the mass-sensitive depth at which most of the muons are produced – the muon production depth  $X_{\max}^{\mu}$  – was reconstructed from SD-data [118]. Each of these methods suffer to varying degrees from model-inconsistencies related to the muon deficit (see Chapter 5) and thereby lose explanatory power regarding the mass composition. Only through a calibration with hybrid events was the time-profile analysis able to extend  $X_{\max}$  measurements to higher energies, revealing that the rise to heavier compositions seems to stop around  $5 \cdot 10^{19}$  eV [116].

More muon-related measurements will be discussed in Chapter 5.

### 3.2.3 Arrival Directions

The study of CR arrival directions provides additional and potentially more direct information regarding their origin. At low energies, this idea of CR astronomy is challenged as magnetic deflections induce a random, diffusive propagation. Consequently, a potential correlation of the CR arrival directions with their sources is washed out, giving rise to a nearly isotropic sky [72, 119]. Only towards higher energies may one hope to retrieve such correlations due to smaller magnetic deflections and limits on source distances from interaction with the CMB and EBL (the

GZK-horizon) [60, 66], as mentioned in Sec. 2.2. Nevertheless, statistical analyses of large CR data sets – as obtained at the Pierre Auger Observatory – are able to probe potential anisotropies, and correlations with known objects.

Indeed, with over 30,000 events covering 85% of the sky, the Pierre Auger Collaboration discovered a 6% dipole anisotropy in the arrival directions of CRs with energies exceeding  $8 \cdot 10^{18}$  eV [73], as visualized in the upper panel of Fig. 3.7. With the dipole pointing  $125^\circ$  away from the galactic center – towards  $(\alpha, \delta) = (-24^\circ, 100^\circ)$ <sup>4</sup> – this observation gives a strong indication that CRs at these energies are of extragalactic origin. Extensions to these results found the dipole amplitude increasing with CR energy [120], and setting upper limits on the dipole amplitude at lower energies [121], as shown in the lower panel of Fig. 3.7.

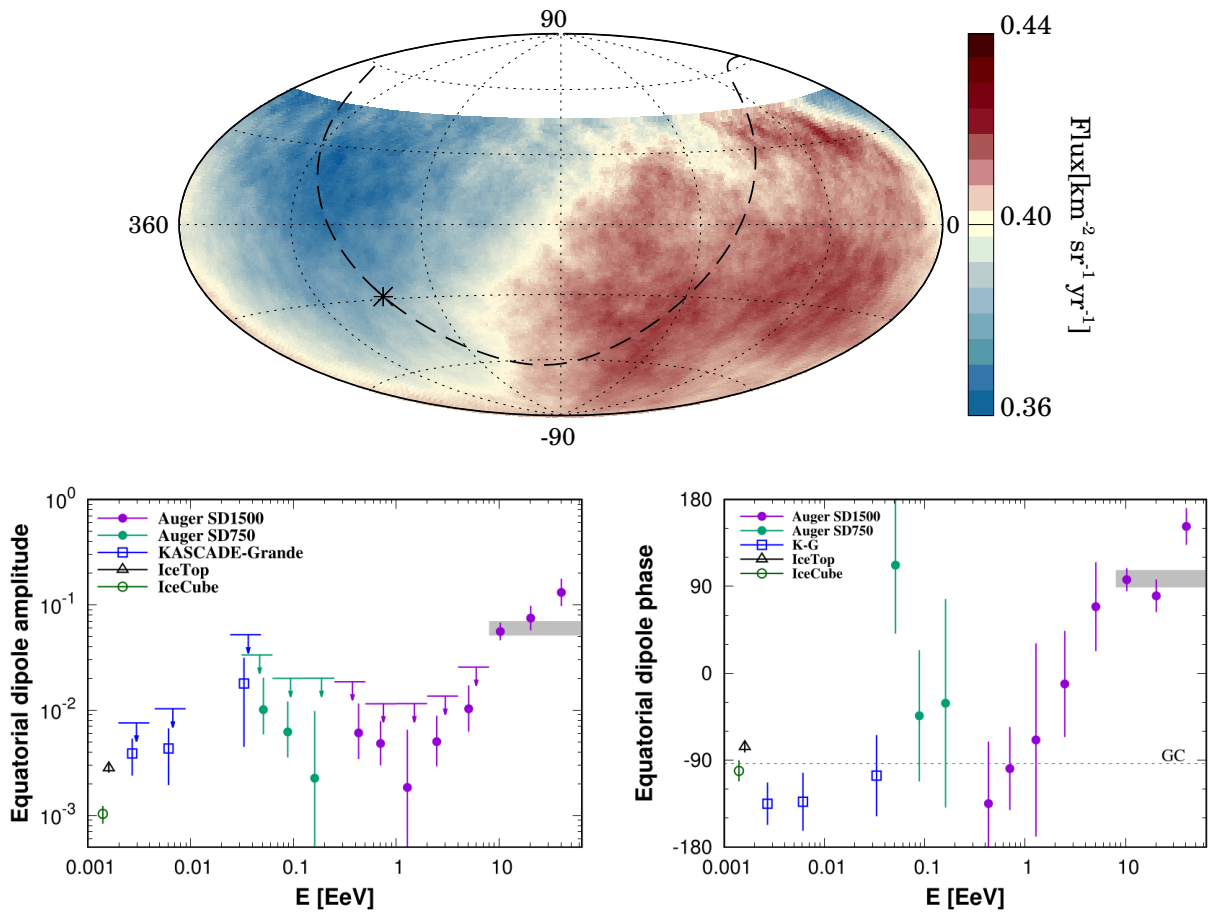


**Figure 3.7:** *Top:* Dipole anisotropy of CR arrival directions above 8 EeV as measured at the Pierre Auger Observatory, in equatorial coordinates. The gap at the north pole is due to the location of the Observatory, and the galactic plane (center) is indicated by the dashed line (star). Figure from [122], reproduced with permission. *Bottom:* Measurements (error bars) of the dipole amplitude (left) and phase (right) at various energies from the experiments indicated in the legend. Insignificant measurements of the dipole amplitude are complemented by 99% C.L. upper limits (horizontal lines with downward arrows). Figure from [121], © AAS. Reproduced with permission.

<sup>4</sup>These are equatorial coordinates, with  $\alpha$  the right ascension, and  $\delta$  the declination.

Various effects may contribute to a dipole anisotropy from extragalactic CRs [73]. Their arrival directions may be susceptible to the Compton-Getting effect [123]; a consequence of the peculiar motion of the Earth [60]. It could also be a direct reflection of an anisotropic distribution of the extragalactic sources themselves, which can in particular be expected at the highest energies again due to the GZK-horizon combined with the local inhomogeneous matter distribution [72]. A third contribution could arise from dominant sources whose CRs are strongly effected by turbulent extragalactic magnetic fields [72].

While the extension to lower energies are not yet statistically significant, it is interesting to note that the dipole direction seems to shift towards the galactic center at these lower energies, see the bottom right panel of Fig. 3.7. This could indicate that below 1 EeV the anisotropy may be of predominantly galactic origin [121], arising, e.g., from the escape of galactic CRs from the galaxy [72].

On smaller angular scales – i.e., at higher multipoles – the Pierre Auger Observatory did not observe significant deviations from isotropy above 4 EeV [124]. Further studies looking for an excess flux in localized regions of the sky and for potential correlations between the arrival directions themselves – varying both the minimum energy of CRs in the data set and the angular size or separation (depending on the study) – are also compatible with an isotropic sky [125].

Finally, the Pierre Auger Collaboration looked for correlations of CR arrival directions with celestial structures; the galactic plane and center, and the supergalactic plane [125], and known astrophysical objects; flux-limited galaxies, AGNs, and SBGs [74, 125]. While none of these studies found a statistically significant correlation, it is interesting to note that compared to isotropy there are  $4.5\sigma$  and  $3.9\sigma$  indications for SBGs and the AGN Centaurus A, respectively [126].

# 4 | Hadronic Interaction Models and Shower Simulations

The interpretation of Auger data – in particular in terms of the CR mass composition – relies on the accurate modelling of EASs. To this end, dedicated software packages were developed to simulate all relevant physical processes, of which hadronic interactions play a prominent role. Details of these interactions are captured in the so-called hadronic interaction models. Due to their application to UHECR-induced EASs, these models require an extrapolation to a region of phase-space inaccessible to collider experiments, with an associated large theoretical uncertainty [1, 75, 127]. In fact, the origin of the muon deficit (see Chapter 5) is likely to be found in the inaccuracy of these models.

Hadronic interactions and their modelling for EASs will be described in Sec. 4.1. Then a description of the various shower-simulation software packages follows in Sec. 4.2, all of which were extensively used for this thesis.

## 4.1 Hadronic Interactions

The term hadronic interactions refers to interactions between hadrons – which is the collective name for baryons ( $p$ ,  $n$ ,  $\Lambda$ , ...) and mesons ( $\pi$ ,  $K$ ,  $\rho$ , ...) – through the strong force. This is the strongest known force and is responsible for confining quarks into their hadronic bound states and, residually, the binding of nucleons (protons and neutrons) into nuclei [128]. The theory of the strong force is well-established as that of quantum chromodynamics (QCD), regulating the interactions between quarks and gluons based on color charges [129]. In contrast to the similar theory of quantum electrodynamics (QED) – describing EM interactions between charged particles mediated by photons – the mediating particles of QCD (i.e., gluons) carry the associated (i.e., color) charge [128, 129]. This has profound consequences for the behavior of strong interactions at various energy scales.

The corresponding gluon-gluon self-interactions give rise to a running coupling constant  $\alpha_S(q^2)$  that decreases with increasing scale of the transferred momentum  $|q^2|$  [129], with  $q$  the four-momentum of the exchanged gluon. Consequently, in the limit of very-high momentum transfers<sup>1</sup> the QCD coupling strength vanishes, allowing the treatment of quarks as free particles; a property that is known as asymptotic freedom. In the opposite limit of small momentum transfer, the large coupling strength leads to the confinement of quarks and gluons within

---

<sup>1</sup>Note that by Heisenberg’s uncertainty principle a high momentum transfer corresponds to probing small distance scales, providing an intuitive justification for why the substructure of hadrons (i.e., quarks and gluons) can be probed in such interactions.

hadrons. This running of the coupling constant divides QCD-calculations into two regimes. Processes with large momentum transfers (so-called hard processes) have sufficiently small coupling strengths –  $\alpha_S \sim 0.1$  for  $|q| > 100$  GeV [129] – such that interactions between individual partons (i.e., the quarks and gluons inside the hadrons) can be computed with perturbation theory. This technique breaks down for processes with small momentum transfers (so-called soft processes) due to the large coupling strength, and one subsequently relies on phenomenological modelling.

Which of these processes are most relevant depends on the experiment and its science goals. For instance, hadron-collider experiments such as those at the LHC mainly probe the nature of QCD through hard processes, computed perturbatively. These can be isolated by only considering the rare interactions that produced jets of secondaries above some minimum transverse momentum  $p_T$  [75, 130] (i.e., the momentum component perpendicular to the beam), which is a proxy for the momentum transfer  $|q|$  between the partons [128]. The associated soft processes before and after the hard parton scattering are factorized out into previously measured parton distribution and fragmentation functions, whose  $|q|^2$ -evolution is determined by the QCD-derived Dokshitzer-Gribov-Lipatov-Altarelli-Parisi (DGLAP [131]) equations [132]. Further phenomenological models capture the subsequent hadronization and decays of unstable particles for the formation of jets.

For EAS experiments these hard interactions are considered too rare to significantly contribute to the evolution of air showers. Instead, one relies on the accurate modelling of the most frequently and energetically produced secondaries, which disappear down the beam pipe in collider experiments. These secondaries have high (pseudo)rapidity<sup>2</sup> ( $\eta$ )  $y$ , and, in case of low  $p_T$ , require a thorough treatment of the relevant soft processes. To this end, dedicated high-energy hadronic interaction models are developed and tuned to collider-data to provide a theoretically justified extrapolation to the center of mass energies and kinematic regimes relevant for EASs.

#### 4.1.1 High-Energy Hadronic Interaction Models

Common to the various state-of-the-art high-energy hadronic interaction models – QGSJETII-04, EPOS-LHC, and SIBYLL-2.3D – is the application of Gribov-Regge Field Theory (GRFT [133]) [1, 75]. This theory introduces a quasi-particle known as the Pomeron, which corresponds to multi-gluon ladder diagrams, to simultaneously describe hard and soft processes [75, 130]. In this way, hard interactions can be retrieved by appropriately cutting Pomerons [130].

Complementary to base-GRFT, necessary considerations include that towards higher energies, multiple partons of the same hadron can interact independently, and that the growth of the partonic density eventually saturates the number of independent partons [75]. Also diffractive collisions are relevant for air showers, in which there is an exchange of color while the projectile and/or target disintegrates, or the transferred momentum produces particles [1]. Further relevant is the treatment of nuclear effects, since CRs can be heavier than proton and the shower develops based on collisions with air nuclei such as nitrogen and oxygen. The final production of secondaries is often based on string fragmentation, in which the parton kinetic energy is converted into the ‘string’ color-field connecting them, which then somehow hadronizes [1, 75]. The models differ in how they handle these effects, as described in the following.

---

<sup>2</sup>The rapidity  $y = 1/2 \ln((E + p_z)/(E - p_z))$  quantifies the contribution of the jet momentum along the beam direction  $p_z$  to the total jet energy  $E$ . Differences in rapidity are invariant under Lorentz boosts along this direction, which is particularly useful due to the unknown boost of the interacting partons w.r.t. the laboratory frame. For a negligible jet mass the rapidity reduces to the pseudorapidity  $\eta \equiv -\ln(\tan \theta/2)$  [129].

### QGSJETII-04

QGSJETII-04 [134] was originally based on the Quark-Gluon Strings model [75]. It is an upgrade of the previous version QGSJETII-03 [135], and now better accommodates LHC data at  $\sqrt{s} = 7$  TeV [127]. The main difference with the other models is the implementation of an enhanced Pomeron scheme to take into account nonlinear saturation effects [130, 75]. This leaves few free parameters, giving this model a high predictive power.

For the generalization to nuclear collisions the GRFT approach is extended to allow simultaneous Pomeron exchanges between different nucleons [134]. The fragmentation of strings is based on a generalized Field-Feynman model [134, 136], tuned to proton-proton data [1]. Diffractive collisions in which the transferred momentum is small are treated in the Good-Walker [137] formalism [1, 130].

### EPOS-LHC

EPOS-LHC [138] contains a microscopic treatment of the Pomeron coupling to individual partons, going beyond that on the broader hadron scale, such that an algorithm can be implemented for the consistent energy sharing between partons [75, 130]. With an updated flow parametrization, this model follows from EPOS 1.99 [139] and is in very good agreement with LHC data up to  $\sqrt{s} = 7$  TeV [138]. In fact, the EPOS models are also applied to heavy ion collisions, making them the most widely tested EAS-relevant models [75]. The correspondingly required flexibility is obtained through various parametrizations [75], with in particular nonlinear effects taken into account with a parametrized Pomeron amplitude [1].

The string fragmentation procedure follows the area law [140], tuned to electron-positron data, but unique to this model is that further collective effects are considered [1]. This enables a core-corona treatment [138], as will be described in Sec. 5.2. Diffractive collisions in EPOS-LHC are handled with special diffractive Pomerons [1].

### SIBYLL-2.3C/D

SIBYLL is based on the dual parton model [141], involving the description of so-called minijets [142]. The upgrade from version 2.1 [143] to 2.3 [144] concerned various improvements and new fits to accommodate LHC data, including the application of the Good-Walker formalism of diffraction also to interactions with nuclei and the implementation of potential excitations of hadron remnants [145]. Subsequent adjustments available in SIBYLL-2.3C [146, 147] and SIBYLL-2.3D [142] respectively correct for an undesired violation of Feynman scaling in the fragmentation region, and an unintended enhancement of the charged to neutral pion ratio.

From SIBYLL-2.1 onwards, parton saturation effects are taken into account by making the minimum  $p_T$  – denoting the transition from soft to hard processes – energy-dependent [143, 147]. The hadronization follows from an application of the Lund string fragmentation algorithm [148], as tuned to proton-proton data [1]. Interactions with a nuclear target are described with Glauber theory [149]. Based on the assumption that the nuclear profile can be decomposed into that of independent nucleons, this theory provides a quantum-mechanical description of the geometry of an interaction with appropriate integrals over the nucleon positions and the impact parameter [150]. The negligible binding energy of a projectile nucleus allows the use of

the simpler semi-superposition theorem [79], which does provide an accurate description of the projectile fragmentation in air showers [142].

### 4.1.2 Low-Energy Hadronic Interaction Models

At sufficiently low center-of-mass energies resonance and annihilation processes become important [151, 152]. These are not adequately treated in the aforementioned high-energy hadronic interaction models, and thus, for the simulation of EASs, it is necessary to further adopt a low-energy hadronic interaction model [1, 75]. This transition is typically fixed at a projectile energy of 80 GeV per nucleon, corresponding to  $\sqrt{s} \approx 12$  GeV. Such low energies are particularly relevant for the final stages of the shower, which also happens to contain most of the interactions and accordingly produce most of the muons [153, 154, 155]. Simultaneously, these energies (and the relevant rapidity regions) are accessible to man-made fixed-target experiments. From the frequently used low-energy models GHEISHA [156], FLUKA [157], and URQMD, only the latter two provide a satisfying agreement to fixed-target data obtained so far [158, 159, 160]. We opted for the last one, which is described below.

#### URQMD

URQMD<sup>3</sup> [161, 162] was originally developed for the modelling of heavy ion collisions. It therefore considers the collision of nuclei with laboratory energies per nucleon ranging from less than 100 MeV to more than 200 GeV [161], corresponding to what was relevant for the experiments planned and running at the time of the model's conception in 1998 [161]. This lends itself well as a low-energy hadronic interaction model for EAS simulations [163], and version 1.3 was subsequently implemented into CORSIKA (see Sec. 4.2.1).

The model applies relativistic transport theory to propagate collections of hadrons and compute their interactions – including resonances and annihilations – based on the relevant cross-sections. These are obtained from phenomenological fits to cross-section measurements or extrapolations by applying theoretical concepts such as the additive quark model [164] or detailed balance [161, 162]. At collision energies above  $\sqrt{s} \approx 2$  GeV per nucleon, the partonic substructure of hadrons is incorporated with a string-excitation and -fragmentation scheme. Further QCD effects of colour transparency and opacity are also taken into account [161, 162].

## 4.2 Air Shower Simulation Software

A variety of software packages were developed related to the simulation of EASs. This includes full 3D Monte Carlo simulations in CORSIKA and AIRES [165]; and faster 1D solutions to cascade equations in CONEX, MCEQ [166], and SENECA [167]. For this thesis we used the former of each group, and additionally studied individual hadronic interactions through CRMC. The used codes are described below.

---

<sup>3</sup>URQMD is an acronym for Ultra-relativistic Quantum Molecular Dynamics.

### 4.2.1 CORSIKA

CORSIKA<sup>4</sup> [151] was first developed as the detector simulation software for the KASCADE experiment [168]. The addition of many features and updated hadronic interaction models led it to the most complete software for air shower simulations [1].

The basic principle is the geometric computation of the interaction coordinates, based on the flight direction of the particle as well as the atmospheric profile and the relevant cross-section. For unstable particles, the decay length determines whether the next interaction point is actually reached. The propagation of charged particles between two interaction points is further affected by the energy loss due to ionization, and by the deflection due to multiple scattering and the Earth's magnetic field. At the interaction points secondary particles are produced as dictated by external hadronic interaction models (see Sec. 4.1). Produced high-energy muons feed the EM component also through Bremsstrahlung and pair production, whose Monte Carlo simulation is based on [169]. The propagation of EM particles can be delegated to the external EGS4 model [170], or computed analytically with Nishimura-Kamata-Greisen theory [171, 172]. The EAS is then made up from an appropriate repetition of interaction points and the various propagation processes until the kinetic energy of the tracked particles fall below some type-dependent cut-off [151]. Since each process contains a random component, CORSIKA implements the Monte Carlo technique to sample realistic and representative air showers

The program is steered with input files, in which it is necessary to specify the CR energy, mass, and arrival direction. Also environmental parameters need to be specified such as the atmospheric profile, Earth's magnetic field, the height of the observation level and the minimum energy of the particles that need to be tracked. This framework is complemented by a range of options to suit particular science cases. For example, the COREAS and CHERENKOV options respectively compute the radio and Cherenkov emission from the air shower; with the NEUTRINO option the produced neutrinos are explicitly tracked; and the STACKIN option allows one to produce the first interaction externally. With regard to the computing time and the disk space it is further useful to enable the THINNING option, which under certain conditions disregards some of the secondary particles while giving the remaining ones an appropriate weight; the CONEX option which delegates a part of the shower to CONEX to be computed in 1D by solving cascade equations (see Sec. 4.2.2); and the AUGERHIT option in case of the Auger experiment, which saves only particles that hit the Auger WCDs [151].

To keep CORSIKA equipped for the challenges and demands of modern shower physics experiments, a new version – dubbed CORSIKA 8 [173] – is being build from the ground up. This immense effort is necessary due to inherent limitations in the design of the current CORSIKA, which originate from historic technological constraints and unforeseen applications. For instance, the propagation medium is fixed to a particular density-parametrization of air; both the medium-type (including transitions) should be made flexible and more properties (temperature, humidity, etc.) specifiable. Additionally, processes initiated by the main cascade should be able to couple back to it and influence its further development. In general, a more modular, object-oriented design is expected to make CORSIKA 8 a worthy successor of the present version, and it could also become the most complete and comprehensive shower software available [173].

---

<sup>4</sup>CORSIKA is an acronym for COsmic Ray Simulations for KAScade.

### 4.2.2 CONEX

CONEX [174] is a program in which cascade equations are solved numerically. With respect to the full 3D treatment in CORSIKA, this enables a faster simulation of the longitudinal profile – both in terms of the number of particles and the energy deposit. To still capture the random nature of EASs, CONEX relies on a hybrid approach where the initial stages of the shower are simulated with a 3D Monte Carlo, and then below some energy threshold fed into cascade equations. These equations describe the evolution with depth  $X$  of the energy spectra  $h_a(E, X)$  of the various hadronic<sup>5</sup> particle species  $a$  [174, 175]:

$$\frac{\partial h_a}{\partial X} = -\frac{h_a}{\rho_{\text{air}}} \left[ \frac{1}{\lambda_a} + \frac{m_a}{E\tau_a c} \right] + \frac{\partial(\beta_a^{\text{ion}} h_a)}{\partial E} + \sum_b \int_E^{E_{\text{max}}} \frac{h_b}{\rho_{\text{air}}} \left[ \frac{I_{b \rightarrow a}}{\lambda_b} + \frac{D_{b \rightarrow a} m_b}{E' \tau_b c} \right] dE' + S_a^{\text{had}}, \quad (4.1)$$

where we suppressed the depth and energy dependencies of the individual parameters.

Without going into much detail, this equation can be readily understood. The first term with the square brackets denotes the loss of particles of species  $a$  due to interactions and decays, quantified by inverse factors of the respective depth scales. Here the mean free path  $\lambda_a = m_{\text{air}}/(\rho_{\text{air}}\sigma_a)$  follows from the air density  $\rho_{\text{air}}(X)$  and mass  $m_{\text{air}}$  as well as the interaction cross-section with air  $\sigma_a(E)$ . The decay length is determined by the time-dilated life-time  $\gamma\tau_a = E_a/m_a\tau_a$ , with the particle travelling at the speed of light  $c$ . The next term captures the energy-loss due to ionization, with  $\beta_a^{\text{ion}}(E) = -dE_a/dX$  the ionization rate. Then the sum and integral cover all other particles of species  $b$  with energy  $E < E' < E_{\text{max}}$  that can produce particles of species  $a$  with energy  $E$ , either through interactions  $I_{b \rightarrow a}(E', E)$  or decays  $D_{b \rightarrow a}(E', E)$ . This couples the cascade equations of the various species within the hadronic component. The last term is known as the source term and feeds these hadronic cascade equations from the initial Monte Carlo, and from the EM component through photonuclear interactions and muon pair production. The evolution of the EM component is described through a similar set of equations, but then with  $b$  running only over the other EM particles and the source term coupling them to the hadronic component [174].

Solving these coupled equations involves the discretization of both depth and energy, where for each step in depth first all hadronic and then all EM species evolve. Eventually this program returns the energy spectrum for each species as a function of depth, which suffices for the 1D study of the longitudinal profile of EASs. To further retrieve information on the lateral profile, CONEX has been implemented into CORSIKA [176], where in the final stages of the air shower the obtained spectra are propagated to the ground in CORSIKA with the 3D Monte Carlo technique. The corresponding trade-off between precision and computation time is then parametrized through a set of energy thresholds.

### 4.2.3 CRMC

CRMC<sup>6</sup> [177] provides a useful interface to the various hadronic interaction models, including those described in Sec. 4.1. It therefore does not simulate air showers directly, but can be used

<sup>5</sup> $a$  also denotes muons, which are thus sort of included in the hadronic component.

<sup>6</sup>CRMC is an acronym for Cosmic Ray Monte Carlo.

to analyze individual interactions with arbitrary energy and with any particle types that are defined in the models themselves. This is facilitated by the use of the HepMC [\[178\]](#) format to store the event information. An additionally useful feature is that the decay of specified particle species can be disabled, and then treated externally.



# 5 | The Muon Deficit and the Fireball Model

The muon deficit (or puzzle, problem, excess, etc.) refers to an open problem in the interpretation of EAS-data from a variety of CR-experiments [75, 6, 1]. More precisely, the muonic component as inferred from ground-reaching particles indicates a significantly heavier CR mass composition than the EM component does. As the reconstruction of the muonic component relies on the accurate modelling of the complete air shower – and in its extension on all hadronic interactions – this is typically assumed to correspond to a deficit of muons in the simulations. Various models were proposed to resolve this inconsistency, one of which is the so-called fireball model. The investigation of the potential of this model is the main topic of this thesis, for which we will set the stage in this chapter.

First, the experimental evidence for the muon deficit is reviewed in Sec. 5.1. Then, in Sec. 5.2 follows a general discussion on how the muon deficit can be resolved, putting particular emphasis on the fireball and the related core-corona model. Finally, Sec. 5.3 provides a description of how the fireball is phenomenologically modelled for this thesis.

## 5.1 Experimental Evidence for the Muon Deficit

The Pierre Auger Collaboration performed several analyses directly related to the muonic component. These studies are complicated by the need to separate the EM and muonic signals registered by the WCDs. One effective method is to consider only inclined showers (i.e., showers with a large zenith angle, typically  $\theta \geq 60^\circ$ ), in which most of the EM component is absorbed by the atmosphere and the remaining signal can be largely attributed to the hadronic cascade [179].

The subsequent reconstruction of the distribution of muon production depths – as briefly mentioned in Sec. 3.2.2 – follows from measuring a time delay in the WCD signal due to muons being produced close to the shower axis and only afterwards bending off towards the WCD. Later signals then correspond to muons produced deeper into the atmosphere. The maximum of this distribution  $X_{\max}^\mu$  is correlated with that of the EM component  $X_{\max}$  due to a common first interaction, but it further depends on the evolution of the hadronic cascade down to intermediate energies. This makes  $\langle X_{\max}^\mu \rangle$  an independent mass indicator, which was found to favor a heavier mass composition than  $\langle X_{\max} \rangle$  does [118].

A further investigation of the density profile at ground provided direct evidence for the associated muon deficit [180]. The muon number in inclined air showers ( $62^\circ < \theta < 82^\circ$ ,  $\langle \theta \rangle = 67^\circ$ ) was reconstructed by fitting the sampled WCD-signal to a reference profile multiplied by a

normalization factor [181]. The assumed universality in terms of energy and mass dependence of the shape of this profile – corresponding to a simulation of a  $10^{19}$  eV proton shower with QGSJETII-03 – was shown [182, 183] to hold for showers with  $\theta > 60^\circ$  and  $E > 10^{18}$  eV. Correcting the normalization factor for the introduced model bias gave the rescaled muon number  $R_\mu$ . This enables a direct comparison of the data with Monte Carlo predictions, where for, e.g.,  $\theta = 67^\circ$  the value  $R_\mu = 1$  corresponds to  $1.455 \cdot 10^7$  muons with energy above 0.3 GeV arriving at 1425 m above sea level. The measured  $R_\mu$  values were found to exceed iron predictions, and a simultaneous comparison with model predictions of  $\langle X_{\max} \rangle$ - and  $\langle \ln R_\mu \rangle$ -data at  $10^{19}$  eV showed a muon deficit in simulations between 30% and 80% [180].

The significance of this deficit was limited by the inability to distinguish it from a systematic shift in the absolute energy scale [5, 109]. Exploiting the zenith-angle dependence of the hadronic and EM contributions to the  $S(1000)$  signal, a subsequent analysis disentangled these components in an event by event ‘top-down’ reconstruction [184]. The longitudinal profiles of a set of hybrid events with  $0^\circ < \theta < 60^\circ$  were first reproduced by repeated simulations, from which then the  $S(1000)$  components could be retrieved. Introducing rescaling factors in the fitting of the  $S(1000)$  signals showed that the energy scale should not be altered whereas the hadronic (and thus muonic) component at the ground in simulations of  $E \approx 10^{19}$  eV showers need to be enhanced by a factor 1.3 – 1.6, depending on the hadronic interaction model [109].

The same picture is confirmed also at lower energies with the prototype of the UMD [98]. As mentioned in Sec. 3.1.3, the underground location of this detector enabled the separation of the muonic component, and the co-located SD-750 provided the required energy measurement. Comparing the reconstructed muon density again along with  $\langle X_{\max} \rangle$ -data to simulations shows a muon deficit of 40% to 50% at  $E = 10^{17.5}$  and  $E = 10^{18}$  eV [98].

The recently obtained sufficient statistics also enabled the computation of shower-to-shower fluctuations of  $R_\mu$  [5], which interestingly does indicate a composition compatible with the one inferred from  $X_{\max}$ -data.

For this thesis we consider the muon deficit as obtained in the study of inclined air showers, updated with data shown at the International Cosmic Ray Conference (ICRC) in 2019 [87]. A compilation of the relevant data on  $X_{\max}$  and  $R_\mu$  is shown in Fig. 5.1, alongside with model predictions for proton, nitrogen and iron CRs as colored bands. The boundaries of these bands correspond to the extremes of the predictions using the models QGSJETII-04, EPOS-LHC, and SIBYLL-2.3C, and thereby the bands indicate the theoretical uncertainty. With both moments of both observables uniquely dependent on the CR mass composition, they can be viewed as independent mass indicators. Then the muon deficit follows from inferring the composition from  $\langle R_\mu \rangle$  and comparing it to any of the others, most notably with that from  $\langle X_{\max} \rangle$ . Likewise, a resolution needs to only enhance the model predictions of  $\langle R_\mu \rangle$ , while leaving  $\sigma(R_\mu)/\langle R_\mu \rangle$  and both moments of  $X_{\max}$  unaffected.

A more explicit depiction of the size of the muon deficit is shown in Fig. 5.2, comparing the model predictions with the simultaneous measurement of  $\langle \ln R_\mu \rangle$  and  $\langle X_{\max} \rangle$  at  $E = 10^{19}$  eV and  $\theta = 67^\circ$ . The reason for using the natural logarithm instead of  $R_\mu$  itself is that in the Heitler-Matthews model both  $\langle \ln R_\mu \rangle$  and  $\langle X_{\max} \rangle$  scale linearly with  $\langle \ln A \rangle$  (see Eq. 2.11), causing straight lines in this figure for the model predictions [185, 186]. The data point is clearly in tension with the models, independent of the chosen composition. Only SIBYLL-2.3C appears to be able to agree with this data within the systematic uncertainties [186]. It should be noticed, however, that the tension could be significant when also considering other energies or

when regarding the slope of the energy evolution. This can be investigated by, e.g., combining measurements from multiple experiments.

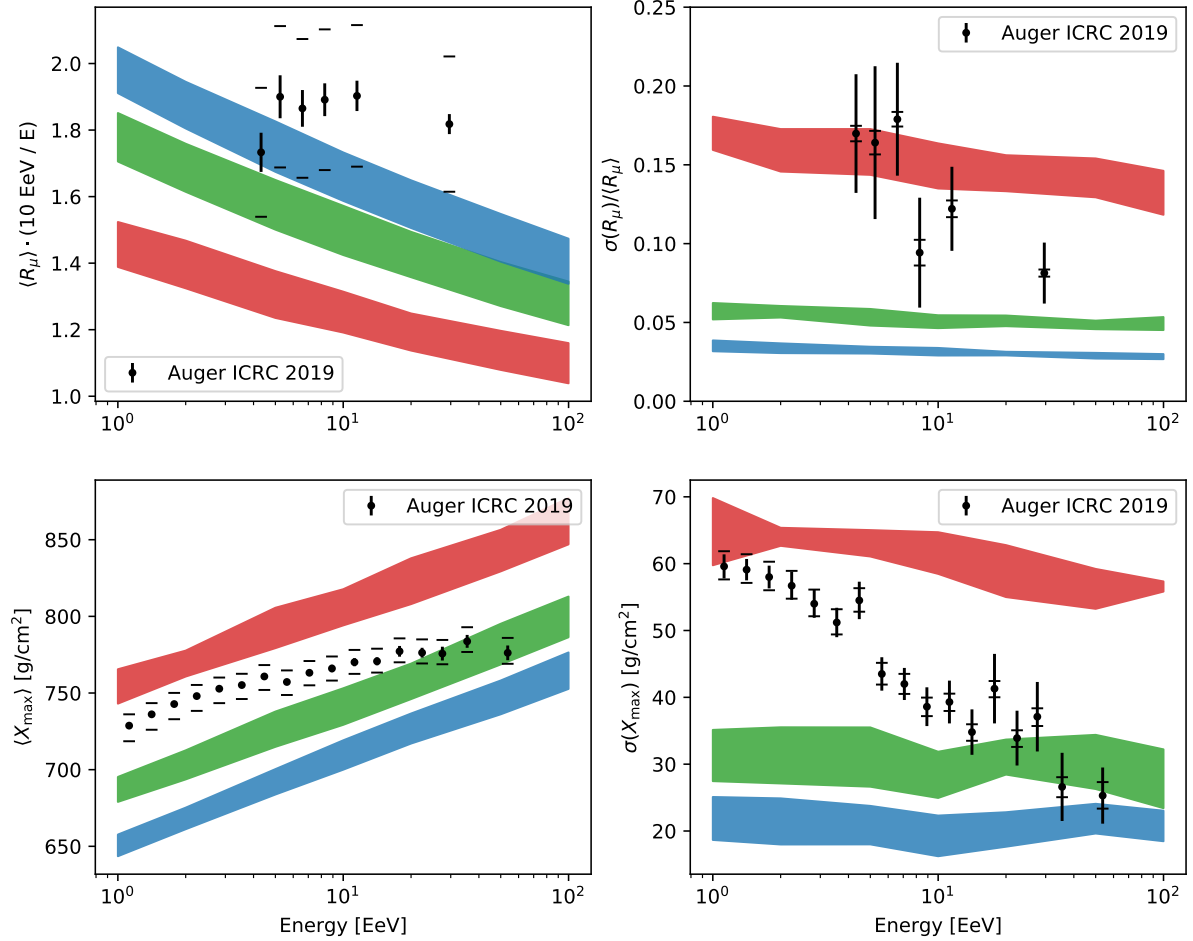


**Figure 5.1:** Energy evolution of the first two moments of the  $R_\mu$  (top) and  $X_{\max}$  (bottom) distributions as measured at the Pierre Auger Observatory and reported at the ICRC in 2019 [87], with statistical (bars) and systematic (brackets) uncertainties. The bands show the predictions from Monte Carlo simulations of EASs for various primary nuclei: proton (red), nitrogen (green), and iron (blue). The boundaries of the bands correspond to the extremes of predictions using the three high-energy hadronic interaction models QGSJETII-04, EPOS-LHC, and SIBYLL-2.3C. Thereby, the width of the bands provide an indication of the theoretical uncertainty.

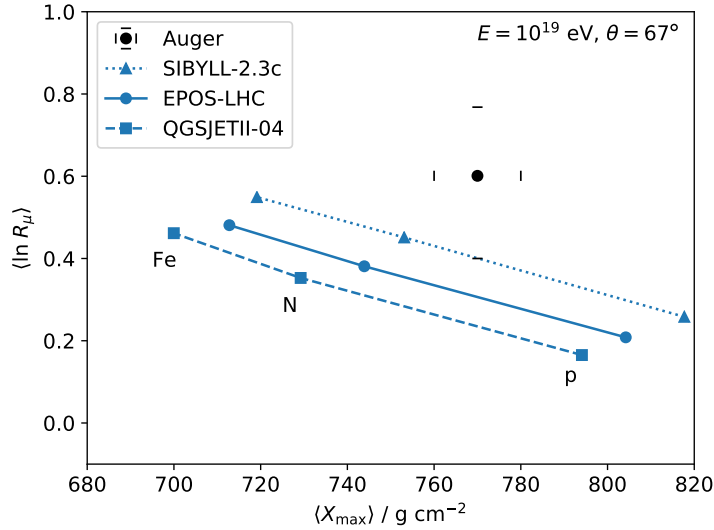


**Figure 5.2:** Average muon content  $\langle \ln R_\mu \rangle$  and shower maximum  $\langle X_{\max} \rangle$  for  $E = 10^{19}$  eV,  $\theta = 67^\circ$  EASs as measured at the Pierre Auger Observatory (black dot with systematic uncertainty) [180], along with the corresponding predictions from the high-energy hadronic interaction models SIBYLL-2.3c, EPOS-LHC and QGSJETII-04 for iron (Fe), nitrogen (N) and proton (p) CR primary nuclei.

### 5.1.1 Combining Measurements from Multiple Experiments

First indications of a muon deficit can be traced back to HiRes/MIA collaboration, finding [187] inconsistencies for air showers between  $10^{17}$  and  $10^{18}$  eV [188]. In the following years more experiments confirmed this finding, while others found no significant excess. Combining and comparing the various measurements in a meta-analysis requires the use of common hadronic interaction models and defining a common energy scale. The use of common models involves a reinterpretation of old experimental results with the post-LHC hadronic interaction models discussed in Sec. 4.1. A common energy scale is obtained by matching the observed energy spectra in a cross-calibration procedure. These tasks were picked up by the inter-experimental Working group on Hadronic Interaction and Shower Physics (WHISP) [6, 189, 190].

The comparison of the various muon-size observables  $x$  (e.g.,  $N_\mu$ ) is facilitated by introducing the  $z$ -scale [6, 98, 191], defined as

$$z = \frac{\langle \ln x \rangle - \langle \ln x \rangle_{\text{p}}}{\langle \ln x \rangle_{\text{Fe}} - \langle \ln x \rangle_{\text{p}}}, \quad (5.1)$$

where the subscripts p (proton) and Fe (iron) indicate the model prediction for the respective CR primary mass, while no subscript corresponds to the observed data. The main advantage of this variable is that particular (energy-)dependencies and biases of the muon content are removed, and thus simply represents the proximity to pure proton ( $z = 0$ ) and iron ( $z = 1$ ) simulations [6]. This provides a framework for a collective assessment of the muon deficit as long as the different muonic observables  $x$  from the various experiments reflect the same physical processes.

It furthermore relies on a common mass dependence of  $z$ , which follows from  $x$  assumed to scale with some power of  $A$  as in the Heitler-Matthews model (see Eq. 2.11). From this point of view the  $z$ -scale is nothing more than a rescaled mass interpretation. In fact, applying the

Heitler-Matthews mass dependence to Eq. 5.1 gives  $z_{\text{mass}} = \langle \ln A \rangle / \ln 56$ , which can be used to put the mass interpretation of the longitudinal development of the EM component (e.g., with  $X_{\text{max}}$ ) in the same framework. Its subsequent subtraction from the muonic  $z$ -values is a measure of the muon deficit:  $\Delta z = z - z_{\text{mass}}$ .

The energy dependence of the observed muon deficit  $\Delta z$  for QGSJETII-04 and EPOS-LHC is shown in Fig. 5.3, which is based on data from the Pierre Auger Observatory (inclined showers analysis [180] in red and UMD analysis [98] in green), the IceCube Neutrino Observatory [192], the Yakutsk EAS Array (see Ref. in [6]), NEVOD-DECOR [193], SUGAR [194], and AGASA [195]. The reference mass interpretation  $z_{\text{mass}}$  from the EM component is based on the Global Spline Fit (GSF) model [61], corresponding to the colored lines of Fig. 2.2. This is in good agreement with the expectation from  $X_{\text{max}}$  measurements, indicated by the gray band.

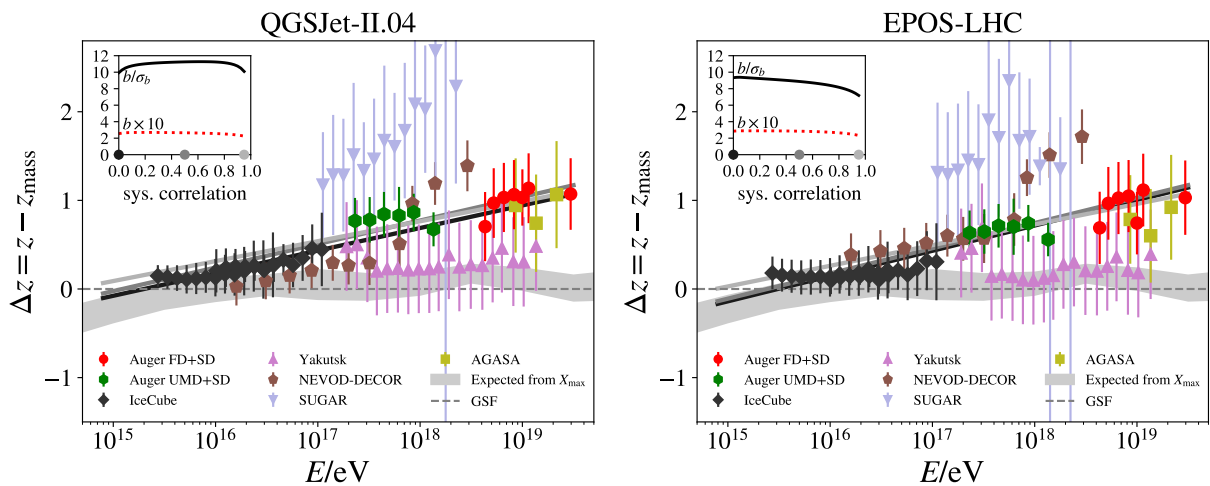


**Figure 5.3:** Energy dependence of the muon deficit  $\Delta z$  for QGSJETII-04 (left) and EPOS-LHC (right) from a meta-analysis of multiple experiments, see text. The error bars include both systematic and statistical uncertainties. The inset shows the slope and its significance of a logarithmic fit through the data points. Figures from [190], reproduced with permission.

The combined muon deficit is quantified by fitting the logarithmic parametrization  $\Delta z = a + b \log_{10}(E/10 \text{ PeV})$  and assessing the significance of a non-zero slope  $b$ . The results are shown in the inset plots as a function of the assumed systematic correlation between the data points of the individual experiments. Note also that the offset seems to start already around  $10^{16}$  eV [6, 190]. With the significance of a non-zero slope always exceeding  $8\sigma$  [6], the muon deficit can be regarded to arise from a real physical effect that is insufficiently captured in the hadronic interaction models.

## 5.2 Resolving the Muon Deficit

In general there are two approaches to resolve this established mismatch between theory and experiment. One way is to come up with a theoretically-motivated concrete model and test its impact on air showers. This is also the general method employed for the development of the high-energy hadronic interaction models. A different option is to apply a more phenomenological approach by parametrizing hadronic interaction properties and subsequently inferring which

adjustments are necessary to reproduce the observations. The latter could be particularly useful for guiding the model-building and providing indications of poorly-understood physics that could be explored at future collider experiments.

A first step of the phenomenological approach [81] involved changing the cross-section, multiplicity, elasticity, or  $\pi^0$ -fraction of individual interactions by a factor  $f(E)$  that increases (or decreases) logarithmically with the projectile energy  $E$  above  $E = 10^{15}$  eV. The resulting effects on the average and fluctuations of  $N_\mu$  and  $X_{\max}$  are shown in Fig. 5.4 for  $10^{19.5}$  eV proton showers simulated in CONEX with SIBYLL-2.1 [1]. Despite the specific hadronic interaction model, these effects can be interpreted as general shower features. Note that whereas the  $x$ -axis represents the adjustment factor evaluated at the LHC energy ( $\sqrt{s_{\text{LHC}}} = 13$  TeV  $\Leftrightarrow E_{\text{LHC}} = 8.45 \cdot 10^{16}$  eV), the adjustment is applied – in varying magnitude – at all projectile energies exceeding  $10^{15}$  eV.

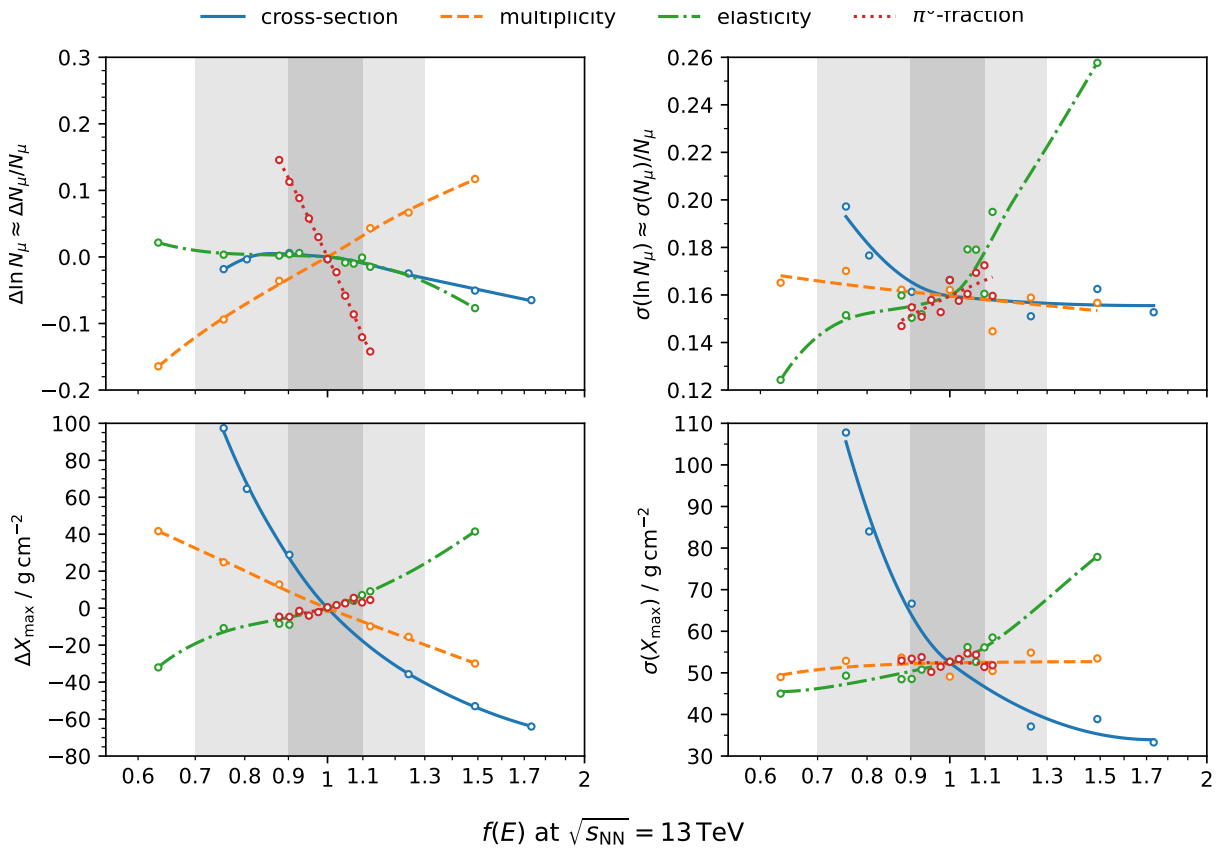


**Figure 5.4:** Impact on air shower observables of ad-hoc adjustments to hadronic interaction properties with an energy-dependent factor  $f(E)$ , as studied in [81] and refitted in [1]. On the  $x$ -axis  $f(E)$  is evaluated at a nucleon-nucleon center of mass energy of 13 TeV. With respect to the observables in Fig. 5.1 here the top-left panel depicts the percentual change of the average muon number (note that  $R_\mu \propto N_\mu$ ), and the bottom-left panel the absolute change in the depth of the shower maximum. Figure from [1], reproduced with permission.

This figure contains very rich information on the connection between the microscopic scale of hadronic interactions and the macroscopic scale of air shower observables. For instance, the (total) cross-section – quantifying the likelihood of an interaction – mainly affects  $X_{\max}$  by altering

the depth of the first interaction and the subsequent rate of air shower development. Enhancements to the elasticity – defined as the fraction of energy carried away by the most energetic secondary – appears to effectively skip interactions and thereby slow the shower development, while also significantly impacting the relative muon fluctuations. In addition to these undesirable effects, both of these properties seem to play a negligible role for the average muon number.

In contrast, both the multiplicity – i.e., the total number of secondaries in a collision – and the  $\pi^0$ -fraction – i.e., the fraction of produced pions that are neutral, typically 1/3 due to isospin symmetry – have a strong impact on the average muon number. This comes from their influence on the fraction of energy lost to the EM component throughout the shower, with the multiplicity determining the number of generations to reach the critical energy and thus the number of times energy can be lost, and the  $\pi^0$ -fraction quantifying the fraction that is lost at each generation through the decay  $\pi^0 \rightarrow \gamma\gamma$ . Simultaneously, the multiplicity has the undesired effect of modifying  $\langle X_{\max} \rangle$  by speeding up or slowing down the shower development. Only the  $\pi^0$ -fraction provides an opportunity to increase the average muon number while having a negligible effect on the other observables. Consequently, there is a general consensus that the muon deficit can be resolved by appropriately decreasing the  $\pi^0$ -fraction, or, in its extension, increasing the hadronic energy fraction  $r$ <sup>1</sup>. This can be readily understood from the Heitler-Matthews model (see Eqs. 2.7–2.8), where increasing  $r$  keeps more energy in the hadronic component, increases  $\beta$ , and produces more muons.

It is interesting to note that keeping more energy in the hadronic component also reduces the energy deposited into the atmosphere by the EM component. An associated underestimation of the primary CR energy – based on the integrated longitudinal profile measured by the FD – has already been taken into account by considering the observed muon numbers [95].

Of course, a satisfying resolution requires a more explicit model explaining this decreasing  $\pi^0$ -fraction / increasing hadronic energy fraction on a microscopic level. This couples back to the first approach of coming up with theoretically-motivated models. Such models can be divided into two categories: those that revert to rather exotic scenarios, proposed to occur in the first (few) interaction(s) and thereby evading collider constraints, and those that incorporate so far neglected (soft) processes in the hadronic interaction models, which could manifest itself over a broad range of energies.

The boundary between new exotic physics and overlooked standard-model physics is not always clear, but a phenomenological distinction can be made in terms of where in the shower the necessary adjustments are made. The corresponding extremes are a large O(30-60)% adjustment (based on the ‘top-down’ analysis [109], see Sec. 5.1) in only the first interaction, or equal adjustments in all generations that accumulate throughout the shower and thus can be rather small. To illustrate this accumulative effect, consider 6 generations each with a 7% enhancement of the hadronic energy fraction. The resulting muon number then increases by a factor  $1.07^6 = 1.5$ , which is sufficient to resolve the muon deficit.

An example of recent improvements to the hadronic interaction models is the enhancement of baryon-pair and leading  $\rho^0$  production [142]. Supported by data from O(100) GeV fixed-target and multi-TeV collider experiments, both changes leave less energy available for pion (and thus  $\pi^0$ ) production and consequently significantly enhance the muon number. As is evident from the previous section, this did not suffice for resolving the muon deficit, but it does imply that

---

<sup>1</sup>Remember from Sec. 2.3.2 that the hadronic energy fraction  $r$  is defined as the fraction of the projectile energy that remains in the hadronic component after an interaction.

much can be won by further testing and developing the current generation of hadronic interaction models [142, 196].

As listed in the introduction, there are various rather exotic proposals to suppress the neutral pion production. In the string percolation model [7] color strings between the beam and target could overlap and fuse. This increases the string tension and thereby reduces the mass suppression of producing heavier quarks. Another proposal [8] considers the restoration of chiral symmetry in the central region of an interaction. This creates an effective barrier for light mesons to escape the region and thus are not produced until the symmetry is broken again. Further proposals include the production of a fireball state [9], the presence of a core-corona effect [10], and a more conventional type of quark-gluon plasma [11, 12, 13]. Interestingly, also the violation of Lorentz invariance at the highest energy has been proposed [197] to extend the lifetime of neutral pions making them interact rather than decay more frequently in the early stages of the shower.

A detailed description of each proposal is beyond the scope of this thesis, and thus in the following we restrict ourselves to a comprehensive description of the fireball and core-corona models.

The strange fireball is a state of deconfined quark matter hypothesized to form when the energy density in a nuclear collision exceeds  $1 \text{ GeV}/\text{fm}^3$ , which could be attained in the first few interactions of UHECR-induced EASs [9]. After creation, the fireball is a plasma of up and down quarks and gluons in chemical equilibrium, but with a high baryochemical potential. In the subsequent explosive expansion the high baryochemical potential suppresses the fragmentation of gluons into light (up and down) quark-antiquark pairs, and thus they predominantly fragment into pairs of strange quarks and antiquarks. The hadronization process then gives rise to a significantly enhanced production of strange baryons and mesons with respect to a standard model collision, which is associated with an indirect suppression of (neutral) pion production [9].

Similar effects arise in the core-corona model, but then a plasma state of quarks and gluons is only formed in the densest, most central region of the interaction known as the core [198]. Its subsequent statistical hadronization also induces an enhanced production of strange and other massive particles [11], with the associated  $\pi^0$ -suppression, and thus plays the role of a fireball. The remainder of the event is known as the corona and hadronizes through string fragmentation as is conventional in the hadronic interaction models [10]. Such a hybrid state is notably different from the fireball model due to its implied continuous transition from a pure corona to a pure core type of event. The core-corona model was implemented into EPOS and an initial study [10] showed that it has the potential to resolve the muon deficit.

It is interesting to note that a state of quark-gluon plasma seems to be a real phenomenon [199]. In particular, the proposed strangeness-enhancements have been observed by the ALICE collaboration at mid rapidities [14]. They observe a specific correlation between the production of strange particles and the charged-particle multiplicity in a variety of events, independent of the system-size (from proton-proton to proton-lead and lead-lead) and nucleon-nucleon center of mass energy (2-13 TeV)<sup>2</sup>, which is not adequately described by the current hadronic interaction models [12]. This independence seems to imply the production of a universal final state [14], e.g. a quark-gluon plasma, and the fact that also small systems (proton-proton) are affected paves a way for its copious production in EASs [10]. Nevertheless, further experiments are required to validate that this enhancement also appears in the for EAS relevant forward phase-space [1].

---

<sup>2</sup>Of course, larger systems at higher energies are more likely to produce events with a large multiplicity.

### 5.3 A Phenomenological Fireball Model

In the remainder of this thesis we study the impact of producing fireballs in UHECR-induced EASs, and its resolving potential for the muon deficit. For this it is necessary to adopt an explicit description of the strange fireball model in terms of the produced secondary particles and its initiation conditions. Due to the lack of a detailed theoretical model we take the following phenomenological approach.

The mimicking of a fireball state is achieved through the procedure described in Ref. [200], which consists of two stages. First, the nuclear secondaries from a Standard Model (SM) interaction collide *in situ* with air particles, effectively increasing the multiplicity with respect to the SM. This process stops when certain conditions are met. Then in the list of secondaries all pions and kaons are exchanged conserving charge, total energy and the direction of momentum, effectively enhancing the strangeness of the entire interaction. Note that the effective increase in multiplicity allows the following strangeness-enhancement to have a larger effect.

The first stage of repeatedly colliding secondary nuclei reflects the production of a plasma from the entire nuclear projectile. The subsequent hadronization of this plasma is then assumed to be represented<sup>3</sup> by the disintegrated nuclear fragments from these repeated *in situ* collisions. With individual nucleons technically also being nuclei (of hydrogen), we include them (and other baryons) in this procedure. This requires an additional condition to stop the repeated collisions, for which we define a minimum fraction  $f_{\text{stop}} \equiv E_{\text{stop}}/E_{\text{proj}}$  of the projectile energy  $E_{\text{proj}}$  that needs to be carried away by a secondary nucleus or baryon for it to be eligible for a further collision. Physically, this could be interpreted as setting a lower limit on the multiplicity  $n_{\text{mult}}$  of a fireball interaction. In fact, if all secondaries were nuclei, it would imply that the process is only stopped if

$$E_{\text{pp}} = E_{\text{proj}}/n_{\text{mult}} \leq f_{\text{stop}} \cdot E_{\text{proj}} \implies n_{\text{mult}} \geq 1/f_{\text{stop}} , \quad (5.2)$$

with  $E_{\text{pp}}$  the energy per particle, and an equality in the case that the energy is equally divided over all particles (as, e.g., in the Heitler-Matthews model). This parameter therefore indirectly (and non-trivially) enhances the multiplicity of fireball interactions w.r.t. the SM case.

Note that  $f_{\text{stop}} = 1$  corresponds to no bound at all and therefore does not alter the multiplicity. With this setting one actually skips the stage of repeated collisions and the fireball does not contain a plasma. Technically, one may not consider this a fireball, but we will stick to this term even for that setting. The predictive power of the fireball model then solely comes down to the second stage of exchanging pion and kaon secondaries. Whether this corresponds to the strangeness enhancement associated with a true fireball is beyond the scope of this thesis.

With the procedure in place that mimics a fireball interaction, we need to specify the conditions for it to be initiated. From the proposal [9] we know that the energy density of a collision needs to exceed  $1 \text{ GeV}/\text{fm}^3$ . For a direct implementation in the modelling of air showers it is convenient to convert this condition into one on the energy of the projectile. Since – for a fixed projectile energy – head-on collisions attain a higher energy density than peripheral collisions, this conversion needs to take into account the impact parameter. Treating the impact parameter as being probabilistic in nature, a fixed energy density threshold becomes a threshold based on

---

<sup>3</sup>Note that a true fireball would emit isotropically in its rest frame, which is boosted with respect to the rest frame of the atmosphere. It is not trivial how this compares to our assumed representation.

an (projectile) energy-dependent probability. The net effect is that a fireball interaction becomes gradually more likely at higher energies.

The exact form of this energy-dependent probabilistic threshold depends on the distribution of impact parameters among all collisions, the influence of the impact parameter onto the attained energy density, and our value of the energy-density threshold for fireball creation. To encompass our ignorance on the former two topics, we parametrize the energy-dependent probability as

$$p_n(E) = \begin{cases} 0 & \text{if } E < E_{\min}, \\ \left( \frac{\log(E/E_{\min})}{\log(E_{\max}/E_{\min})} \right)^n & \text{if } E_{\min} < E < E_{\max}, \\ 1 & \text{if } E > E_{\max}, \end{cases} \quad (5.3)$$

with  $E_{\min}$  and  $E_{\max}$  the minimum and maximum energy of the growing probability, respectively, and  $n$  some power specifying the rate of growth<sup>4</sup>. This parametrization arose from wanting a linearly increasing probability on a logarithmic energy-scale, which is the case for  $n = 1$ . Then for any  $n > 1$ , we have  $d^2p_n/d\log(E)^2 > 0$ . This implies that the increase in probability of initiating a fireball interaction speeds up (convex behaviour) with increasing energy. For  $0 < n < 1$ , giving  $d^2p_n/d\log(E)^2 < 0$ , this increase slows down (concave behaviour). Whether a convex or a concave behaviour is more physical is not trivial, as well as the question whether the probability should eventually reach 1 at all. Nevertheless, this parametrization is expected to have sufficient freedom to test the general behaviour of fireball interactions in EASs.

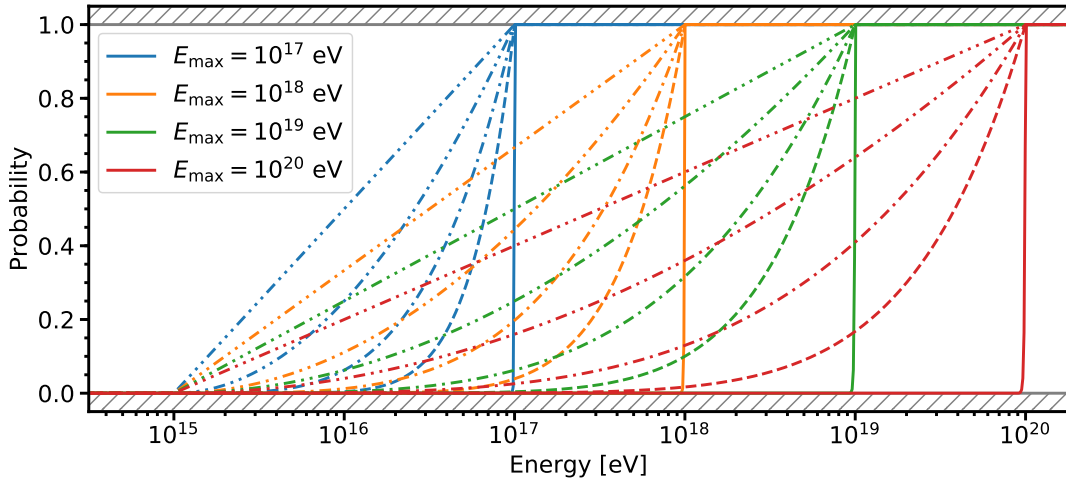


**Figure 5.5:** Various realizations of the parametrized (Eq. 5.3) probability of initiating a fireball as a function of the projectile energy. The minimum energy  $E_{\min} = 10^{15}$  eV is fixed whereas the maximum energy  $E_{\max}$  is set to  $10^{17}$  eV (blue),  $10^{18}$  eV (orange),  $10^{19}$  eV (green), and  $10^{20}$  eV (red). The  $n$ -parameter is set to 1 (triple-dot dashed), 2 (double-dot dashed), 4 (dot dashed), 8 (dashed), and 1000 (solid).

A visualization of this parametrization is shown in Fig. 5.5. The set of chosen parameters corresponds to the sampling used in Chapters 6 and 7.

<sup>4</sup>Note that the  $n$ -parameter could also be expressed in terms of, e.g.,  $E_{50} = E_{\min}(E_{\max}/E_{\min})^{\sqrt[0.5]{n}}$ , the energy where half of the interactions create fireballs.

Interestingly, both limiting cases of  $n$  reduce the probability function to a threshold at a single energy:

$$\lim_{n \rightarrow \infty} p_n(E) = H(E - E_{\max}) \quad \text{and} \quad \lim_{n \rightarrow 0^+} p_n(E) = H(E - E_{\min}), \quad (5.4)$$

with  $H(x)$  the Heaviside step function. This implies that by relaxing  $n$  from these limits one can study the effect of an energy-density threshold rather than a single energy threshold. Another advantage to such limiting behaviour is that it allows one to gradually implement the fireball mechanism. This can be done by selecting an  $E_{\max}$  above and an  $E_{\min}$  below the highest energies reached by cosmic rays. Consequently, the fireball mechanism can be implemented by slowly decreasing  $n$  from ‘infinity’ to smaller values.



# 6 | Compatibility between $R_\mu$ and $X_{\max}$ in the Fireball Model

As an initial study we implement the fireball model into CONEX simulations and quantify the size of the muon deficit. A subsequent variation of the fireball parameters could provide insight into the resolving potential of this model, with in particular clarifications of whether this effect is sufficient and does not introduce new tensions. To this end we first outline in Sec. 6.1 a general procedure to quantify the size of the muon deficit. The results from the fireball-implemented air shower simulations are then shown and discussed in Sec. 6.2.

## 6.1 Quantifying the Size of the Muon Deficit

Since the muon deficit reflects an inconsistency of the mass interpretation of various observables, it is convenient to define a common framework in which these observables can be compared. For this we generalize the  $z$ -scale of Sec. 5.1.1 (Eq. 5.1) by using *any* observable  $x$  instead of only the logarithm of the muon content observable. Accordingly, a *different*  $z$ -scale parameter is obtained:

$$z_x = \frac{x - x_p}{x_{\text{Fe}} - x_p}, \quad (6.1)$$

with no subscript referring to the data, and the subscripts p and Fe referring to model predictions for proton and iron showers, respectively.

This generalized  $z$ -scale makes sense for any observable that provides a unique measure of the mass composition. Since the standard deviations of both the  $X_{\max}$  and  $R_\mu$  distributions are independent mass probes, also these observables can be used to compute  $z_x$  values. At the same time, the subscript  $x$  stresses the fact that you cannot directly compare these generalized  $z_x$  values from different observables to each other: one first needs to align their mass dependencies through the following calibration procedure.

### 6.1.1 Calibration of $z_x$

The essence of the calibration is to convert  $z_x$ -values – computed from data on different observables – to a new common variable such that they all have the same mass dependence. For this new variable, it is convenient to use  $z_{\text{mass}} \equiv \langle \ln A \rangle / \ln 56$ . We thus need to find the values of  $\langle \ln A \rangle$  that, within the physical model, reproduce the  $z_x$  computed from data (i.e., infer the mass composition). Note that if the observable already scales linearly with  $\langle \ln A \rangle$  such a

calibration procedure will be redundant. This would be the case for  $\langle \ln R_\mu \rangle$  and  $\langle X_{\max} \rangle$  in the Heitler-Matthews model (see Sec. 2.3.2). However, these scaling relations may not be valid when implementing new physics such as the fireball model. This underlines the necessity for us to perform some kind of calibration.

The same simulations that obtain model predictions for  $x_{\text{Fe}}$  and  $x_{\text{p}}$  can provide the complete mass dependence of  $x$  within the model, under the assumption of a pure composition in data. A mixed composition introduces a potential degeneracy in terms of the  $\langle \ln A \rangle$ -inference, but – as studied in Appendix A.1 – its effect seems to be negligible for the current analysis. We thus need to simply simulate  $x$  for intermediate masses (i.e., between proton and iron), use these to compute simulated  $z_x$ -values replacing  $x$  from data in Eq. 6.1 with simulations at various masses, and interpolate its mass dependence. A simultaneous interpolation in energy is necessary to obtain the model predictions at the same energy as the data, both for the computation of  $z_x$  from data and for inferring its mass dependence. These interpolations give rise to a function  $z_x^{\text{model}} = g(\ln A, E)$  capturing the model prediction of  $z_x$ . The remainder of the mass interpretation follows from numerically solving the equation  $g(\ln A, E_{\text{data}}) = z_x$ , with  $z_x$  computed from data. Then for the assumed pure composition we have  $z_{\text{mass}} = \langle \ln A \rangle / \ln 56 = \ln A / \ln 56$ , completing the calibration.

For the sampling of the particular model predictions (described in Sec. 6.2) we simulate 1000 showers for each combination of CR energies  $E_{\text{CR}} \in \{1, 2, 5, 10, 20, 50, 100\}$  EeV and nuclei  $\in \{\text{p, He, N, Si, Fe}\}$ .

It is important to consider what happens to  $z_x$ -values that correspond to a mass outside of the sampled proton-iron range. In such a scenario, one usually refers to the model as incompatible with the data, as in the case of the muon deficit. However, for the current study we would like to know *how* incompatible the model is, such that we know whether a new physical model provides a step in the right direction. To do so, we linearly extrapolate the  $\langle \ln A \rangle$  dependence of  $g$  beyond the proton-iron limits.

### 6.1.2 Test Statistic $\Delta$

With the procedure of calibration in place, the data from different observables can now be compared directly. Since the muon deficit mainly manifests itself through the difference between the composition interpretation from  $\langle X_{\max} \rangle$ - and  $\langle \ln R_\mu \rangle$ -data, we will first focus on these observables. The data comes from the Pierre Auger Observatory as presented at the ICRC 2019, which is shown in Fig. 5.1. Both their raw computed  $z_x$ -values and the corresponding calibration for the three hadronic interaction models in the Standard Model (i.e., without an implemented fireball) are shown in Fig. 6.1.

The tension between these observables can be quantified by considering their difference in terms of their combined uncertainty. To this end we define a test statistic  $\Delta$  as

$$\Delta = \frac{1}{n} \sum_{i=1}^n \left( \frac{z_{\text{mass}}^{\langle \ln R_\mu \rangle}(E_i) - z_{\text{mass}}^{\langle X_{\max} \rangle}(E_i)}{\delta z_{\text{mass}}^{\langle \ln R_\mu \rangle}(E_i)} \right)^2, \quad (6.2)$$

where  $i$  runs over the data points of  $\langle \ln R_\mu \rangle$ . The notation  $z_{\text{mass}}^x(E_i)$  represents the value of  $z_{\text{mass}}$  corresponding to observable  $x$  evaluated at energy  $E_i$ . Similarly for  $\delta z_{\text{mass}}^x(E_i)$ , which represents the uncertainty on  $z_{\text{mass}}$  corresponding to observable  $x$  evaluated at energy  $E_i$ .

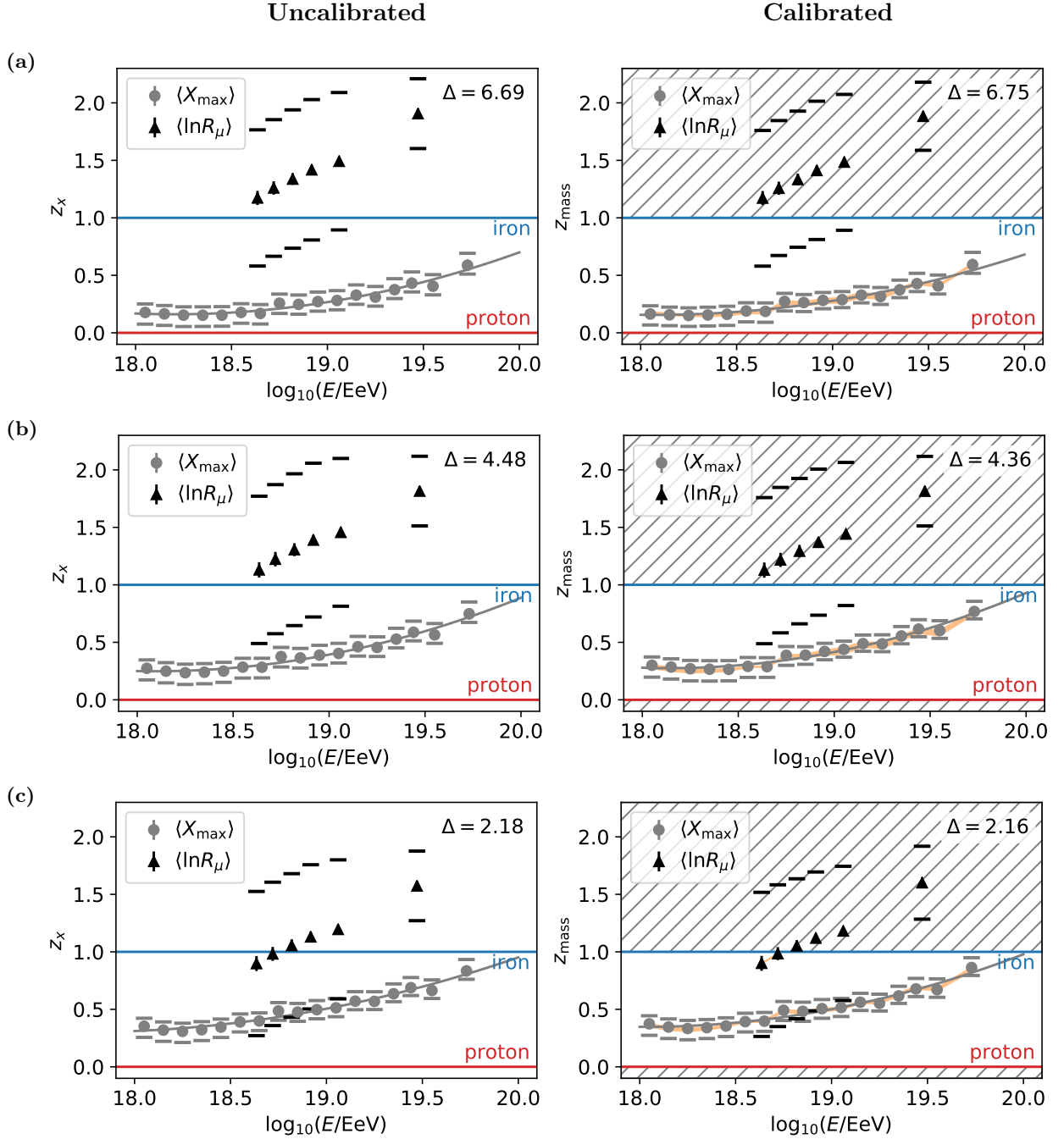


**Figure 6.1:** Uncalibrated (left) and calibrated (right)  $z$ -parameters from  $\langle X_{\max} \rangle$  (gray circles) and  $\langle \ln R_\mu \rangle$  (black triangles) in the **Standard Model scenario** for the three hadronic interaction models: **a)** QGSJETII-04 (top), **b)** EPOS-LHC (middle), **c)** SIBYLL-2.3C (bottom). Both statistical (vertical bars) and systematic (brackets) uncertainties are indicated. Also shown are the quadratic fit of  $\langle X_{\max} \rangle$  (gray line) used for the computation of the test statistic  $\Delta$  (inset top right), as well as reference values of  $z$  in the pure proton (red line) and pure iron (blue line) cases. In the calibrated plots, values in the hatched region are obtained through linear extrapolation and the orange band represents the effect of a mixed composition.

Since we choose  $i$  to run over the data points of  $\langle \ln R_\mu \rangle$ , we need to evaluate  $z_{\text{mass}}^{\langle X_{\max} \rangle}(E_i)$  at different energies than their data points. To do so, we fit a polynomial of  $2^{\text{nd}}$  degree to the  $z_{\text{mass}}$ -values corresponding to  $\langle X_{\max} \rangle$ , which can then be evaluated at the energies of the data points of  $\langle \ln R_\mu \rangle$ . At the same time we neglect any uncertainty on  $z_{\text{mass}}^{\langle X_{\max} \rangle}$ , which can be justified by them being relatively small. This allows us to focus on the error on  $z_{\text{mass}}^{\langle \ln R_\mu \rangle}$ . We compute this  $\delta z_{\text{mass}}^{\langle \ln R_\mu \rangle}$  as the quadratic sum of the corresponding statistical and systematic uncertainties. Uncertainties on  $z_x$  follow from standard error propagation from uncertainties on the data  $x$ , while not assigning uncertainties to the model predictions  $x_{\text{Fe}}$  and  $x_{\text{p}}$ .

The test statistic  $\Delta$  can be interpreted as the squared difference between  $\langle \ln A \rangle$  inferred from the muon content and  $\langle \ln A \rangle$  inferred from the longitudinal development of the shower in terms of the uncertainty on the  $\langle \ln A \rangle$  inferred from muons, averaged over the energy bins for which we have this muon data. Thus, higher values of  $\Delta$  imply the presence of a larger muon deficit, whereas smaller values imply that the muon deficit is less significant.

From Fig. 6.1 it can be clearly seen that the muon deficit is most prominent for the hadronic interaction model QGSJETII-04, with  $\Delta = 6.75$ . EPOS-LHC follows with  $\Delta = 4.36$  and SIBYLL-2.3C seems to be almost consistent within systematic uncertainties with  $\Delta = 2.16$ .

Note that the effect of the calibration is minimal in Fig. 6.1 because the simulations show a near linear dependence of these observables on  $\langle \ln A \rangle$ , in accordance with the Heitler-Matthews model.

## 6.2 Fireball Simulations and the Effect on the Muon Deficit

To study the effect of the fireball model on the muon deficit we implement its phenomenological description of Sec. 5.3 into the subroutines of the CONEX module of CORSIKA. This constitutes a change to the interface of the shower modelling of CONEX with the hadronic interaction models. Depending on the fireball probability parametrized in Eq. 5.3, a high-level procedure is activated that triggers repeated *in situ* collisions regulated by the parameter  $f_{\text{stop}}$  and a subsequent swapping of pions and kaons. Since the probability already contains three parameters ( $E_{\text{min}}$ ,  $E_{\text{max}}$ , and  $n$ ) we fix in this analysis  $f_{\text{stop}} = 0.01$  under the supposition that it only affects the size of the fireball. Furthermore we also fix  $E_{\text{min}} = 10^{15}$  eV. While maybe not expecting fireballs to be produced down to this energy, the corresponding probability could be made negligible by increasing  $n$ . The following phase-space exploration is done by sampling  $n \in \{1, 2, 4, 8, 1000\}$ , where  $n = 1000$  mimics a step function, and  $E_{\text{max}} \in \{10^{17}, 10^{18}, 10^{19}, 10^{20}\}$  eV. These sampled energy-dependent fireball-initiating probabilities are visualized in Fig. 5.5. Advantageous to this sampling is that with  $E_{\text{max}} = 10^{20}$  eV and  $n = 1000$ , one (almost) has the Standard Model case, since fireballs are only initiated above energies attainable by most showers (with  $E < 10^{20}$  eV).

For each of these fireball scenarios, we simulated a total of  $7 \times 5 \times 3 \times 1000 = 105,000$  EASs. The factors 7 and 5 represent the aforementioned energy and mass sampling for quantifying the muon deficit, respectively, and the 1000 showers are expected to provide sufficient statistics for the computation of the statistical moments. The factor 3 reflects the remaining freedom of choosing the high-energy hadronic interaction model: QGSJETII-04, EPOS-LHC, and SIBYLL-2.3C. We use URQMD as the low-energy hadronic interaction model. For the sake of reasonable simulation times, we use the CONEX-option of applying cascade equations throughout the entire shower. This method can be justified by the fact that we are only interested in the longitudinal development (number of muons at the ground and depth where the number of particles peak),

which is known to be accurately calculated with cascade equations. On top of this, we use a thinning factor of  $10^{-6}$  to further reduce CPU time. Finally, all showers were simulated with a zenith angle of  $\theta = 67^\circ$  to allow a direct comparison to available muon data of the Pierre Auger Observatory [180].

Contours of the resulting  $\Delta$ -values, as computed from Eq. 6.2, are shown in Fig. 6.2. Towards the top-right of each plot ( $E_{\max} = 10^{20}$  eV,  $n = 10^3$ ), one approaches the corresponding standard model scenario. For each of the three interaction models, this is also the region with the highest tension, implying that the implementation of the fireball model generally reduces the tension between  $\langle \ln R_\mu \rangle$  and  $\langle X_{\max} \rangle$ . Regarding the plots in Fig. 6.1, this translates to a faster decrease of  $z_{\text{mass}}$ -values related to  $\langle \ln R_\mu \rangle$  than those related to  $\langle X_{\max} \rangle$ . In turn, this can be interpreted as the increase in muon number, following the implementation of a fireball scenario, to be more significant than the corresponding speed-up of the longitudinal development.

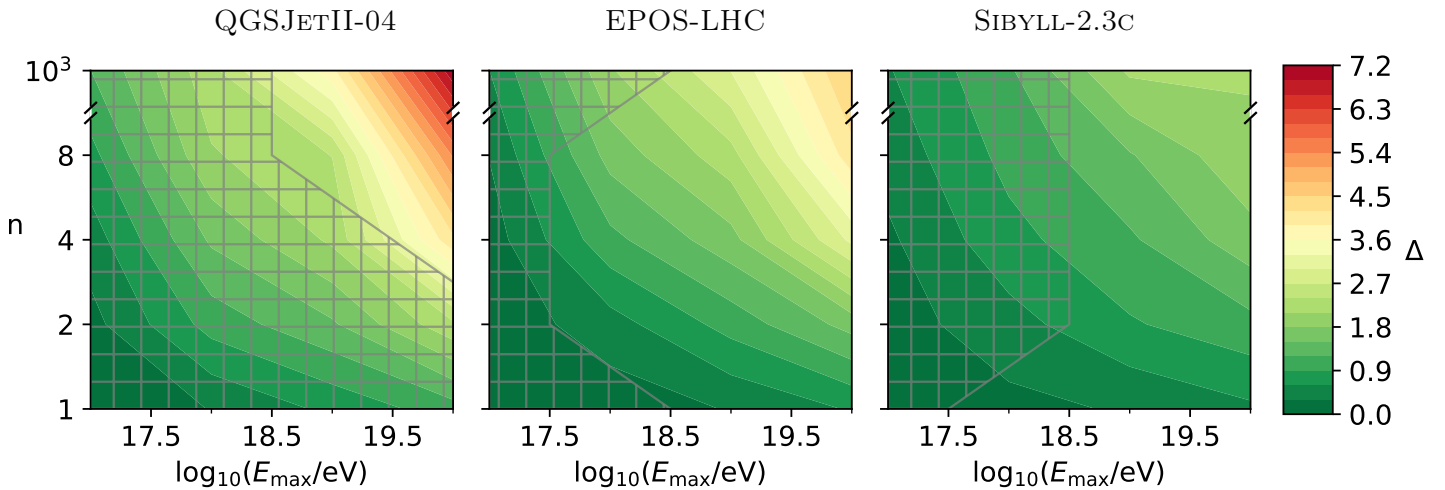


**Figure 6.2:** Contours of the tension  $\Delta$  between the observed muon content  $\langle \ln R_\mu \rangle$  and longitudinal development  $\langle X_{\max} \rangle$  as interpreted in various fireball scenarios. The scenarios are varied through the parameters  $E_{\max}$  and  $n$  of the fireball-initiation threshold (Eq. 5.3). The panels correspond to the high-energy hadronic interaction models QGSJETII-04 (left), EPOS-LHC (middle) and SIBYLL-2.3C (right). The checkered region indicates fireball scenarios for which some of the  $z_{\text{mass}}$  interpretation of  $\langle X_{\max} \rangle$  becomes negative and is thus excluded.

In fact, for some parameters  $\Delta$  even falls below 1, implying the average tension to be within one standard deviation. However, one needs to be careful interpreting these plots since the composition in a fireball scenario should remain plausible. For example, the checkered region in Fig. 6.2 indicates where some values of the  $z_{\text{mass}}$  inferred from  $\langle X_{\max} \rangle$  fall below zero. This would imply a composition lighter than proton, and thus most likely exclude such a fireball scenario. Similarly, it could happen that values of  $z_{\text{mass}}$  inferred from  $\langle \ln R_\mu \rangle$  become negative. To get a better impression of the detailed fireball behavior, the  $z_{\text{mass}}$ -plots corresponding to each corner of the panels in Fig. 6.2 are given in Appendix B.1.

Using the checkered region to exclude unphysical scenarios, one can get to tensions as low as  $\Delta = 2.41$  for QGSJETII-04,  $\Delta = 0.32$  for EPOS-LHC, and  $\Delta = 0.21$  for SIBYLL-2.3C. These values should be regarded as rather optimistic since possible negative values of  $z_{\text{mass}}$

corresponding to  $\langle \ln R_\mu \rangle$  have not been taken into account. On top of this, the fireball interactions have not yet been subjected to LHC constraints, which could restrict the allowed phase-space of the fireball-initiation threshold.

In addition to the average muon content, the fireball model likely affects fluctuations of the muon number. To verify this behavior and its impact, a similar test statistic  $\Delta_\sigma$  has been defined to capture the tension between the relative muon fluctuations  $\sigma(R_\mu)/\langle R_\mu \rangle$  and  $\langle X_{\max} \rangle$ . Its definition is as in Eq. 6.2, with the role of  $\langle \ln R_\mu \rangle$  replaced by  $\sigma(R_\mu)/\langle R_\mu \rangle$ . The subsequently obtained contours are shown in Fig. 6.3.

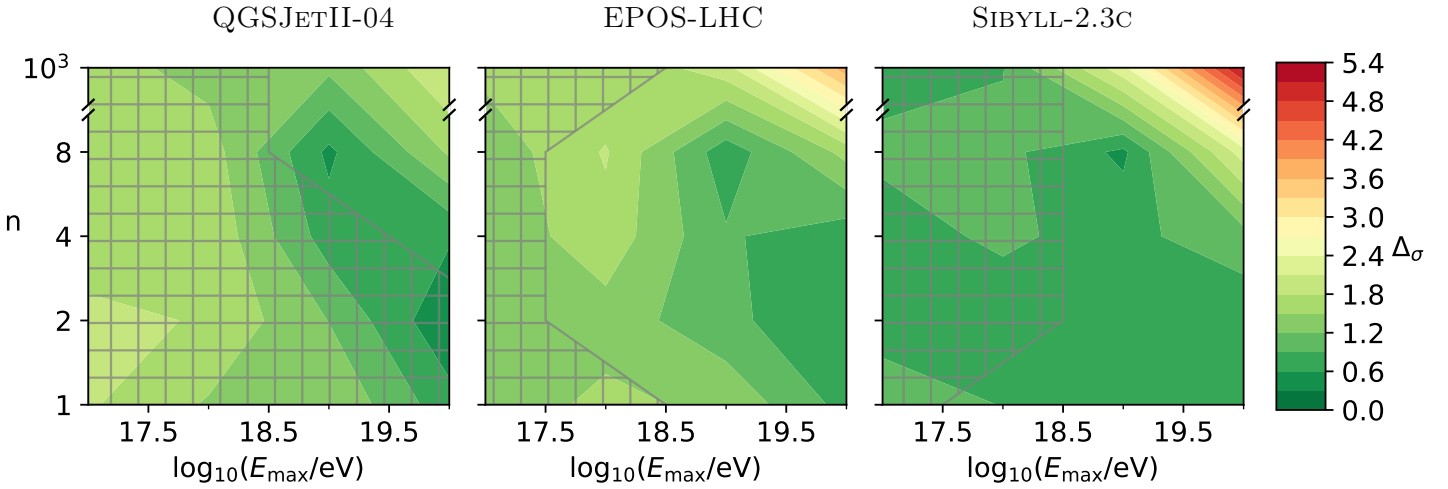


**Figure 6.3:** Same as Fig. 6.2, but then for the tension  $\Delta_\sigma$  between the observed relative muon fluctuations  $\sigma(R_\mu)/\langle R_\mu \rangle$  and longitudinal development  $\langle X_{\max} \rangle$  as interpreted in various fireball scenarios.

Regarding only the region that is not checked, one finds most tension to be in the top right, again implying that the implementation of a fireball scenario leads to a reduction in tension. However, this time it is important to note that in the Standard Model case data on muon fluctuations already suggested lower masses than data on  $\langle X_{\max} \rangle$  (see Fig. 5.1). Consequently, better agreement is reached when lowering the  $\langle X_{\max} \rangle$  mass interpretation. Nevertheless, also here it is important to be wary of potential negative  $z_{\text{mass}}$ -values, both due to and before the implementation of a fireball scenario. A better understanding can be obtained from  $z_{\text{mass}}$ -plots corresponding to the corners of Fig. 6.3, which can be found in Appendix B.2.

While any fireball scenario seems to shift things into the right direction, no complete agreement appears to be possible within the varied phase-space. Therefore, the need of a stronger effect remains necessary, potentially by also varying  $f_{\text{stop}}$ . Nevertheless, this study suggests that the phenomenological fireball model has sufficient predictive power to induce nontrivial effects in air showers, which could in turn be used to put constraints on the fireball model itself.

# 7 | Impact of the Fireball Model on Individual Observables

Whereas the previous analysis gave insight in the general compatibility of various settings of the fireball model with observations from the Pierre Auger Observatory, it fails to distinguish the two ways to obtain better agreements. Ideally, better agreement is obtained by making predictions that are closer to the data. However, better agreement can also be obtained by making the data interpretation less precise. From the figures in Appendix B.1 it can be seen that while the values of  $z_{\text{mass}}$  are getting closer to each other when implementing the fireball model, most of the reduction in  $\Delta$  seems to come from a significant increase of the systematic uncertainty on the muon-inferred  $z_{\text{mass}}$ . The latter behaviour can be traced back to the error propagation through Eq. 6.1: no errors are assigned to the theory predictions of  $x_{\text{p}}$  and  $x_{\text{Fe}}$ , therefore the error on  $z_x$  is simply  $\delta z_x = \delta x / (x_{\text{Fe}} - x_{\text{p}})$ , with  $\delta x$  the error on the data. From this it is evident that the uncertainties on  $z_{\text{mass}}$  increase when the difference between iron and proton predictions gets smaller, or equivalently: when the observables get less sensitive to the CR mass. This is a general feature of any composition-independent model, including the fireball model, that intends to increase the muon number.

Another flaw of the previous analysis is the heavy dependence on the extrapolation to likely unphysical masses, outside of the proton-iron mass range. Combining this with the fact that no complete agreement with the data was found, it is worth analyzing the impact of the fireball model on the observables in a more systematic framework. This could help identifying the shortcomings of the fireball model, and see whether such shortcomings are inherent features or could potentially be corrected for with a detailed QCD description. At the same time it is an interesting question whether the previously-fixed  $f_{\text{stop}}$ -parameter could open up a parameter space allowing for a resolution of the muon deficit.

Altogether, this section provides a systematic analysis of the impact of the fireball model on the individual observables, and extends the phase-space to include variations of  $f_{\text{stop}}$ . The general method for this study is described in Sec. 7.1 and its application follows in Sec. 7.2.

## 7.1 Step-wise Constraining the Fireball Model

*A priori*, any model could potentially resolve the muon deficit. Only once a model is compared to the data, one could say something about the compatibility. Such a comparison could be done in multiple steps, where one gradually introduces additional data requirements of the model and see when the agreement breaks down. This systematic approach will be used throughout this analysis.

The first step requires the model to produce moments of observables that encompass the data, at a fixed energy. To verify whether this requirement is met, it suffices to calculate the extreme values the moments could attain by allowing variations in the composition, at a fixed energy and within the model. Subsequently, the data should lie between these extremes. The extremes of the average observables  $\langle X_{\max} \rangle$  and  $\langle R_{\mu} \rangle$  correspond to pure compositions of proton and iron nuclei. The extremes of the (relative) fluctuations  $\sigma(X_{\max})$  and  $\sigma(R_{\mu})/\langle R_{\mu} \rangle$  are less trivial to compute as they could correspond to mixed compositions. Their computation is nevertheless possible and is described in Appendix A.2.

The second step requires the mass interpretation of both moments of both observables to be consistent. In principle, one could try to infer a single composition from each of the moments and compare the results. However, the composition that could reproduce the observable is likely degenerate. Therefore, it is more convenient to keep the composition implicit and instead map the moments to each other through the model interpretation. Due to the degeneracy of the composition such a mapping would provide a range of other moments that are compatible. A subsequent comparison of each moment with the mapped range of moments checks a potential consistency. In practice, only the mappings from an average to its fluctuations and the other average are feasible. Therefore, this procedure consists of two stages: 1) whether  $\langle X_{\max} \rangle$  is simultaneously consistent with  $\sigma(X_{\max})$  and  $\langle R_{\mu} \rangle$ , and 2) whether  $\langle R_{\mu} \rangle$  is simultaneously consistent with  $\sigma(R_{\mu})/\langle R_{\mu} \rangle$  and  $\langle X_{\max} \rangle$ . This still covers both moments of the two observables and therefore provides a complete consistency check. We would like to stress that these mappings originate purely from adequately combining the observable distributions of the individual nuclei making up the composition. More detail on how these mappings are obtained can be found in Appendix A.3.

The third step requires the first two phases to simultaneously hold for multiple energies. For this analysis, the first two phases will first be checked for an energy of 10 EeV. This could be repeated for energies of 5 and 20 EeV, but that is beyond the scope of the current study. At these energies there is sufficient muon data, see, e.g., Fig. 5.1.

A fourth and final step could focus on the energy dependence of the moments. Since data at different energies are subject to the same physical world, they are not completely unrelated. In fact, the energy evolution of the observables are a combination of the energy evolution of the composition and the energy evolution of the EAS particle physics. In principle, neither of which is random; both should have physical models underneath. Therefore, more information could be extracted when focusing on, e.g., the slope of the muon deficit, as was used to quantify its significance (see Sec. 5.1.1). Such a constraint on the fireball model is also beyond the scope of this analysis.

## 7.2 Results and Discussion

To impose each of the aforementioned constraints, one first needs to obtain the model predictions through adequate EAS simulations. The set of simulations performed for this analysis is very similar to the one used in the previous analysis, see Sec. 6.2. The sampling of the fireball-initiation threshold through  $E_{\min} = 10^{15}$  eV,  $E_{\max} \in \{10^{17}, 10^{18}, 10^{19}, 10^{20}\}$  eV and  $n \in \{1, 2, 4, 8, 1000\}$  is kept the same. An important difference with respect to previous simulations is that  $f_{\text{stop}}$  is no longer fixed to 0.01, but sampled from  $\{1, 0.1, 0.01, 0.001\}$  instead. To compensate for the increase in the number of required simulations, we fixed the energy of the primary CR to 10 EeV.

A further difference is that the atmospheric parameters has been revised. Instead of fixing the atmosphere to a yearly average, we used monthly specific settings from within CORSIKA. For each winter month (southern hemisphere; April-September) we simulate 105 showers and for each summer month (October-March) we simulate 70 showers, giving a total of 1050 showers per setting. This way there is a 3:2 ratio of showers from winter to summer months, which reflects the fact that at the Pierre Auger Observatory there is more hybrid observation time during the winter months [77]. This change had, however, little impact on the observables of interest.

Finally, for this analysis both CORSIKA and CONEX were updated, from versions 7.70 and 6.4 to versions 7.74 and 7.5, respectively. This also includes the updated hadronic interaction model SIBYLL-2.3D.

### 7.2.1 Range of Predictions

The impact of a fireball on the prediction of observables from proton and iron showers are shown in Figs. 7.1 ( $f_{\text{stop}} = 1$ ), 7.2 ( $f_{\text{stop}} = 0.1$ ), 7.3 ( $f_{\text{stop}} = 0.01$ ), and 7.4 ( $f_{\text{stop}} = 0.001$ ). Also shown in the case of  $\sigma(R_\mu)/\langle R_\mu \rangle$  and  $\sigma(X_{\text{max}})$  are maximal values of the observables when allowing mixed compositions, indicating the range of observables the model can predict. The computation of these extremes is described in Appendix A.2. In each of these figures, 20 fireball-initiation settings are shown in combination with the three hadronic interaction models. The energy of the primary CR as well as  $f_{\text{stop}}$  are fixed for each figure, as indicated in the top left. The  $x$ -axis on top specifies the 4 settings of the  $E_{\text{max}}$ -parameter, with the light-shaded background color-coded according to Fig. 5.5. The  $x$ -axis on the bottom specifies the 5 settings of the  $n$ -parameter, repeating for each  $E_{\text{max}}$ -value. As before, we retrieve the Standard Model scenario by setting  $E_{\text{max}} = 10^{20}$  eV and  $n = 10^3$ , i.e., all the way on the left of each plot. A subsequent evaluation of the impact of a particular fireball model follows from its comparison to the left-most points. The  $y$ -axes indicate the observables and their fluctuations as in Fig. 5.1. The black horizontal lines are measurements from the Pierre Auger Observatory, with the bands indicating systematic (light-gray) and statistical (dark-gray) uncertainties. Imposing the first constraint, one thus needs the model predictions to encompass these horizontal lines, for both moments of both observables.

Starting with the case of  $f_{\text{stop}} = 1$  in Fig. 7.1, we see that the implementation of any fireball scenario only affects the muon number and their fluctuations; both  $\langle X_{\text{max}} \rangle$  and  $\sigma(X_{\text{max}})$  remain unaffected. Such behavior is expected in the  $f_{\text{stop}} = 1$  case since the stage of repeated collisions is skipped, removing the artificial development of the shower. Thus, a fireball here simply corresponds to swapping pions and kaons of the secondaries of a SM interaction, which affects the muon number. The muon number increases strongly with both threshold parameters and causes the data to fall within the prediction range for any  $E_{\text{max}}$  with  $n = 1$ , and even for all  $n$  with  $E_{\text{max}} = 10^{17}$  eV. If one includes the systematic error on the data, already a modest fireball threshold is sufficient to have the muon number fall within the range of predictions. Note that for some threshold settings the difference between proton and iron predictions get significantly smaller, underlining the fact that a fireball model makes the muon number less sensitive to the composition. The largest predictions of  $\sigma(R_\mu)/\langle R_\mu \rangle$  decrease to  $\sim 0.1$ , which would likely enforce a proton-dominated composition interpretation. Nevertheless, the range of predictions on muon fluctuations remain compatible with the data. Therefore, only with the aforementioned threshold settings that sufficiently increase the muon number one could

potentially find a consistent composition.

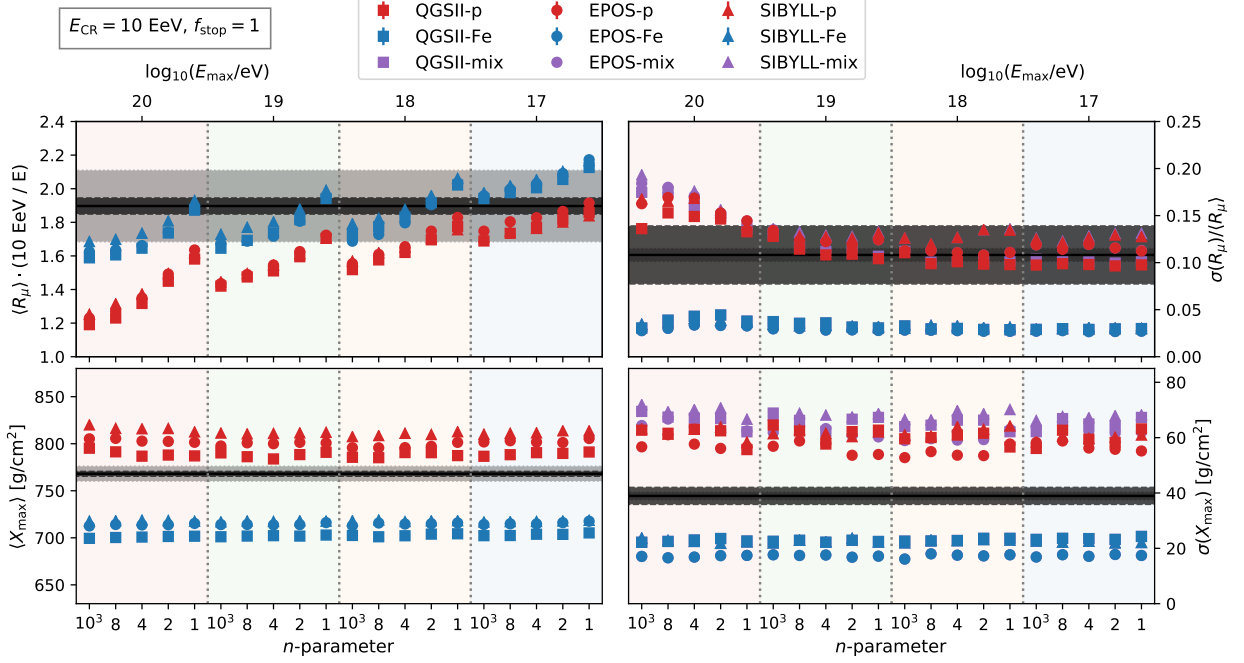


**Figure 7.1:** Impact of various settings of the fireball model with  $f_{\text{stop}} = 1$  on the ranges of  $\langle R_\mu \rangle$  (top-left),  $\sigma(R_\mu)/\langle R_\mu \rangle$  (top-right),  $\langle X_{\text{max}} \rangle$  (bottom-left) and  $\sigma(X_{\text{max}})$  (bottom-right) from 10 EeV cosmic-ray extensive air showers. Varied on the  $x$ -axis are the fireball-initiation threshold parameters  $E_{\text{max}}$  (top axis, background color-coding corresponding to Fig. 5.5) and  $n$  (bottom axis), while  $E_{\text{min}} = 10^{15}$  eV is fixed. The settings on the far left,  $E_{\text{max}} = 10^{20}$  eV and  $n = 10^3$ , correspond to the Standard Model scenario (i.e., no fireball). For each scenario, the high-energy hadronic interaction models QGSJETII-04 (squares), EPOS-LHC (circles), and SIBYLL-2.3D (triangles) are used in combination with a pure proton (red) and iron (blue) composition. Mixed compositions that maximize the fluctuations are indicated in purple. Data from the Pierre Auger Observatory from ICRC 2019 [201] are shown by black horizontal lines, with systematic (light gray) and statistical (dark gray) errors as bands.

Decreasing to  $f_{\text{stop}} = 0.1$  introduces the stage of repeated collisions and thus affects the shower development, as can be seen from the moments of  $X_{\text{max}}$  in Fig. 7.2. Similarly to the previous discussion of  $\sigma(R_\mu)/\langle R_\mu \rangle$ , now  $\langle X_{\text{max}} \rangle$  seems to enforce a proton-dominated composition inference. At the same time,  $\sigma(X_{\text{max}})$  decreases a bit, but not sufficient to draw the same conclusions. This decrease of  $f_{\text{stop}}$  seems to have little effect on the muon number and its fluctuations.

A further decrease to  $f_{\text{stop}} = 0.01$  extends the aforementioned behavior. In particular, one can clearly see a splitting of proton and mixed composition predictions of  $\sigma(X_{\text{max}})$ . This implies that while proton fluctuations seem to go down, there is also a more pronounced separation of the  $X_{\text{max}}$  distributions expected from proton and iron induced EASs. Therefore, mixed compositions could result in even larger fluctuations. At the same time, the *range* of  $\sigma(X_{\text{max}})$  predictions increases only slightly, and could thus still accommodate the data. Another feature seen for the case  $f_{\text{stop}} = 0.01$  is that implementing the fireball model seems to have a much larger effect on the proton predictions of the average muon number than on the corresponding iron predictions. This

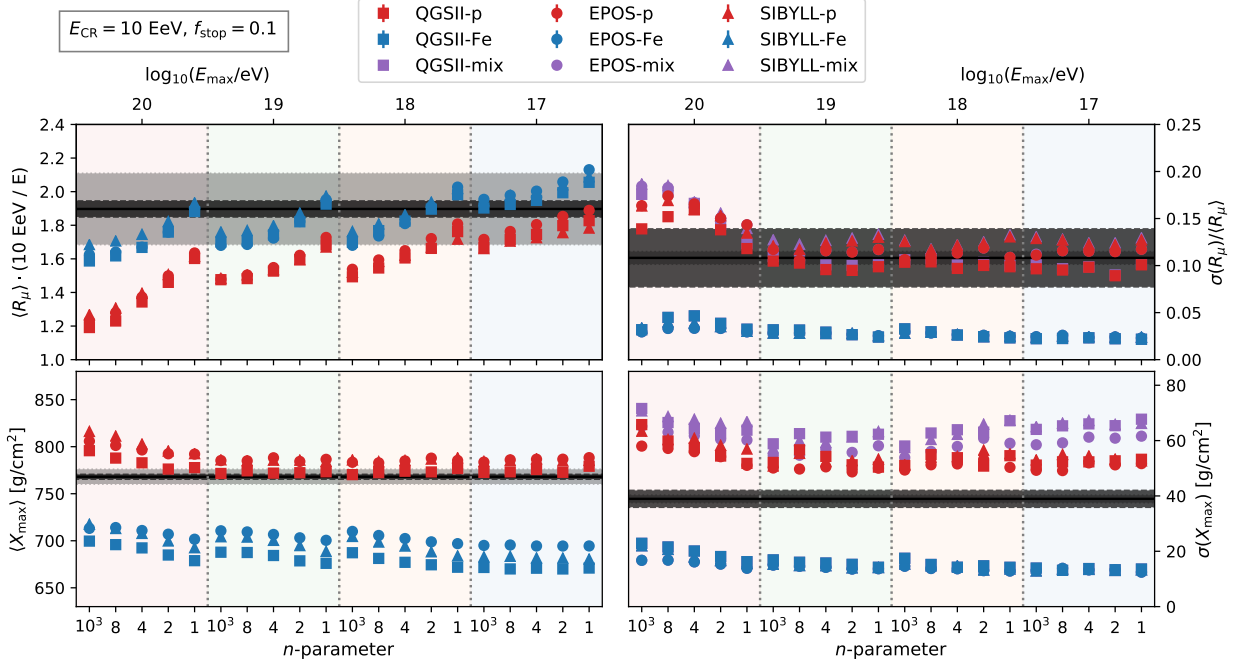


Figure 7.2: Same as Fig. 7.1, but then for  $f_{\text{stop}} = 0.1$ .

shows a clear decrease in sensitivity of the average muon observable to the mass composition.

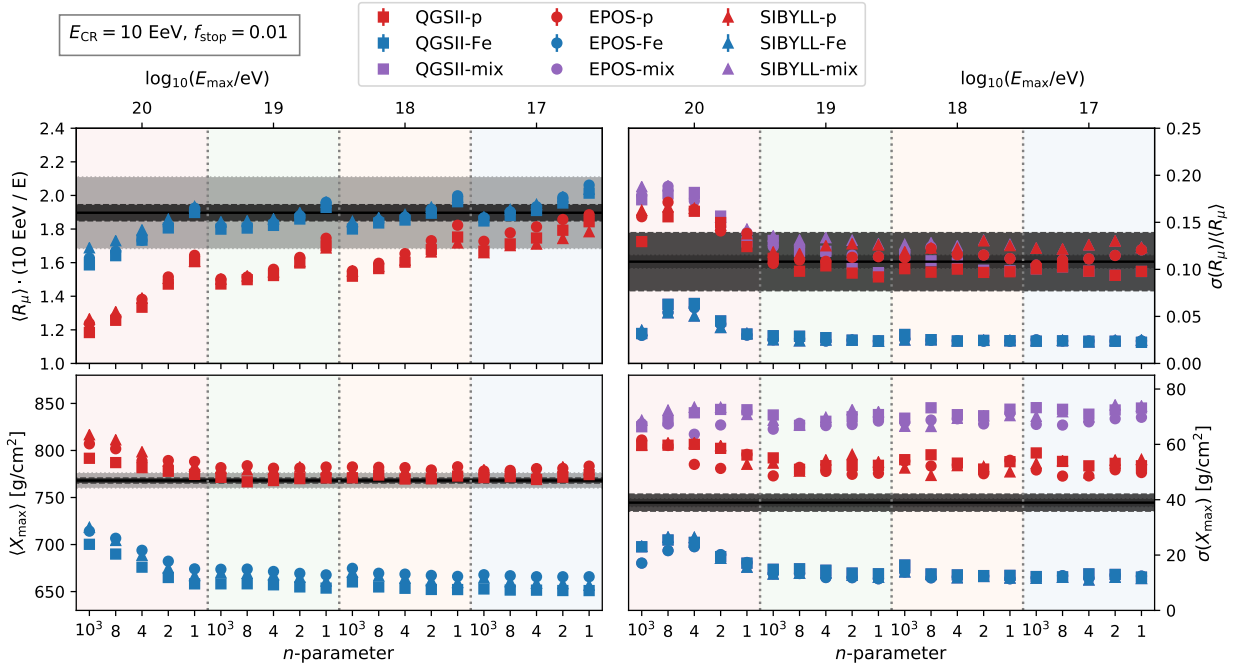


Figure 7.3: Same as Fig. 7.1, but then for  $f_{\text{stop}} = 0.01$ .

Finally, the case of  $f_{\text{stop}} = 0.001$  shows little difference to the previous case, probably indicating a sub-dominance of lower-energetic nuclei to the observables of interest. Only the splitting of proton and mixed composition predictions of  $\sigma(X_{\text{max}})$  is more pronounced.

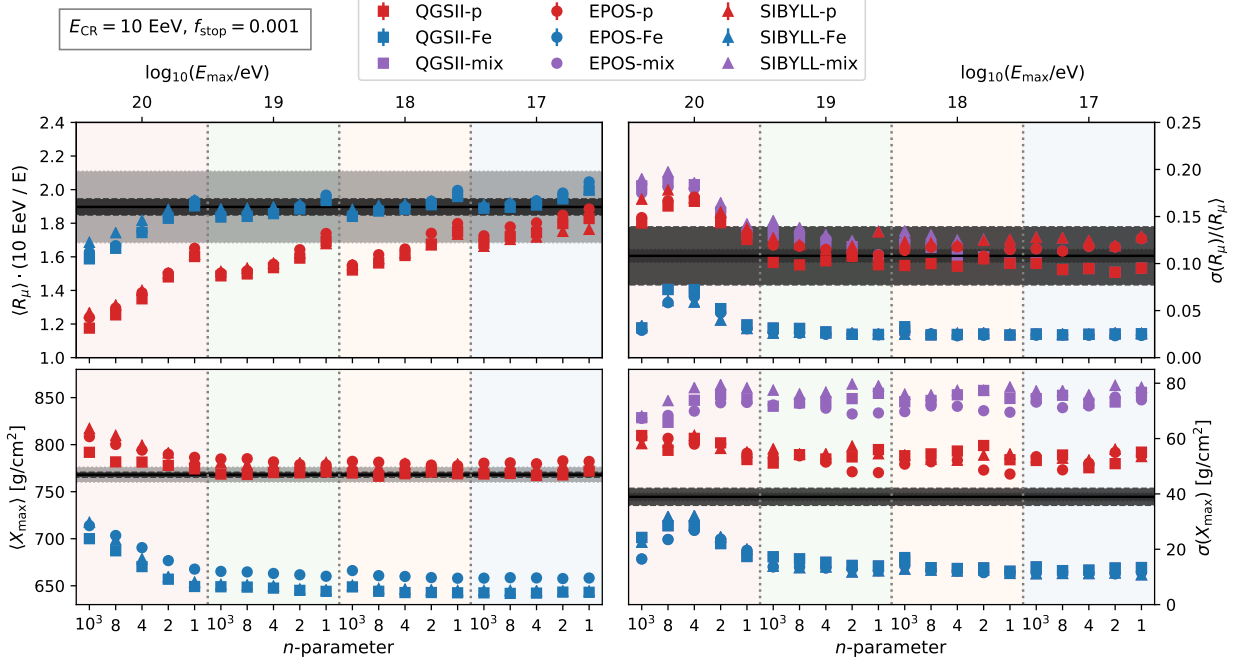


Figure 7.4: Same as Fig. 7.1, but then for  $f_{\text{stop}} = 0.001$ .

## 7.2.2 Cross-Interpretation in terms of Composition

Following the procedure from Appendix A.3 data on  $\langle R_\mu \rangle$  and  $\langle X_{\text{max}} \rangle$  can be mapped to the other moments through the model predictions, and in this way provide a cross-interpretation in terms of the mass composition. Such mappings are shown in Figs. 7.5 ( $f_{\text{stop}} = 1$ ), 7.6 ( $f_{\text{stop}} = 0.1$ ), 7.7 ( $f_{\text{stop}} = 0.01$ ), and 7.8 ( $f_{\text{stop}} = 0.001$ ) for the different cases of  $f_{\text{stop}}$ . Here the green data points show which values of  $\langle R_\mu \rangle \cdot (10 \text{ EeV} / E)$  and  $\sigma(X_{\text{max}})$  correspond to the observed  $\langle X_{\text{max}} \rangle$ -data when assuming a particular model. The corresponding error bars take into account a possible degeneracy due to the composition. For example, in Fig. 7.5 the green data with error bars in the bottom-right plot show the range of  $\sigma(X_{\text{max}})$  values that correspond to the  $\langle X_{\text{max}} \rangle$ -data value of the black horizontal line in the plot on the bottom-left. Likewise, the orange data points provide a mapping from  $\langle R_\mu \rangle \cdot (10 \text{ EeV} / E)$  to  $\langle X_{\text{max}} \rangle$  and  $\sigma(R_\mu) / \langle R_\mu \rangle$ . Note that in the orange case not for every fireball scenario a point could be calculated. This is due to the observed  $\langle R_\mu \rangle$  data line lying outside of the proton-iron range, thus making a composition inference impossible. However, such an inference could be possible when including the uncertainty on the data. The corresponding mappings of the uncertainties are indicated by the vertical light-gray bands. These bands are open if the uncertainties on the data stretches beyond the proton-iron range, and closed (i.e., ends with a gray bracket) if the end of the uncertainty falls within this range.

Starting again with the case of  $f_{\text{stop}} = 1$  in Fig. 7.5, we find that many fireball-initiation

threshold settings could provide a complete agreement within the total uncertainty on the data. However, looking at the actual data points, only the cases of ( $E_{\max} = 10^{18}$  eV,  $n = 1$ ) and ( $E_{\max} = 10^{17}$  eV,  $n = 4$ ) with both EPOS-LHC and SIBYLL-2.3D as well as ( $E_{\max} = 10^{17}$  eV,  $n = 2$ ) with QGSJETII-04 show a perfect agreement between  $\langle X_{\max} \rangle$  and  $\langle R_{\mu} \rangle$ . Additionally, these points seem also to be compatible with the relative fluctuations on the muon number, while fluctuations on  $X_{\max}$  seem to always allow a mixture that reproduces the observed average. This agreement shows the strength of the fireball model, but one should realize that the muon deficit is observed over a range of energies and not just at 10 EeV. On top of this, the compatibility of these fireball-initiation thresholds with other measurements should be verified.

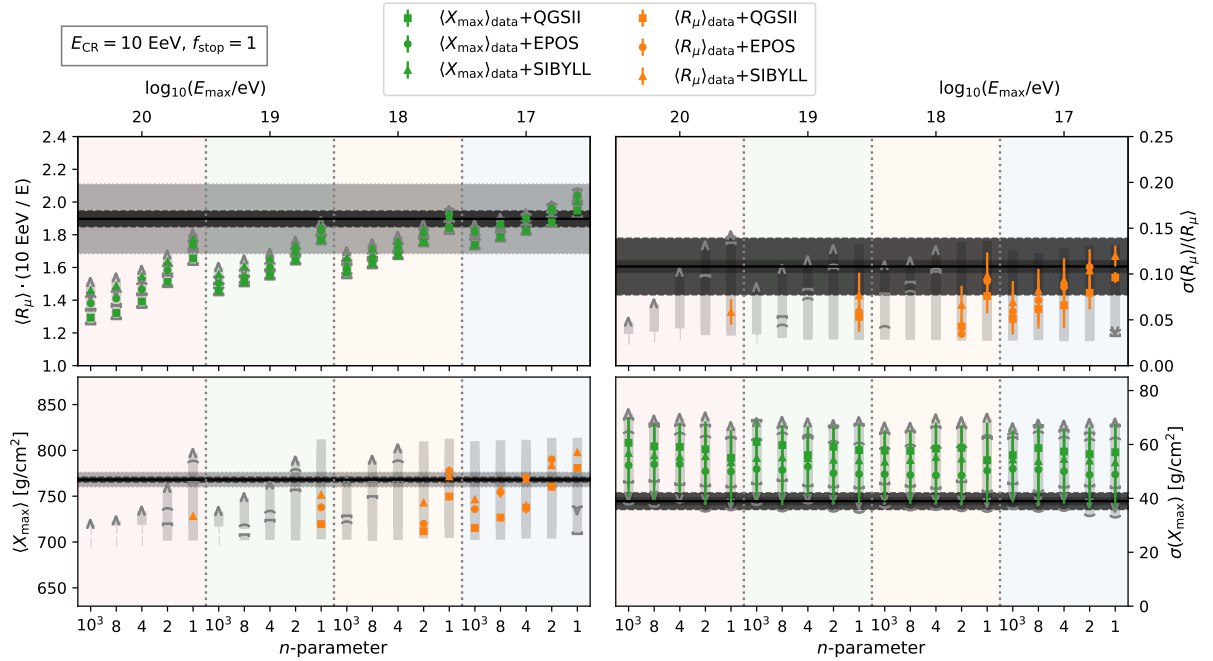


**Figure 7.5:** Impact of various settings of the fireball model with  $f_{\text{stop}} = 1$  on the compatibility of data on  $\langle X_{\max} \rangle$  (green) or  $\langle R_{\mu} \rangle$  (orange) with data on  $\langle R_{\mu} \rangle$  (top-left),  $\sigma(R_{\mu})/\langle R_{\mu} \rangle$  (top-right),  $\langle X_{\max} \rangle$  (bottom-left) and  $\sigma(X_{\max})$  (bottom-right) from 10 EeV cosmic-ray extensive air showers. Varied on the  $x$ -axis are the fireball-initiation threshold parameters  $E_{\max}$  (top axis, background color-coding corresponding to Fig. 5.5) and  $n$  (bottom axis), while  $E_{\min} = 10^{15}$  eV is fixed. The settings on the far left,  $E_{\max} = 10^{20}$  eV and  $n = 10^3$ , correspond to the Standard Model scenario (i.e., no fireball). For each scenario, the used high-energy hadronic interaction models are QGSJETII-04 (squares), EPOS-LHC (circles), and SIBYLL-2.3D (triangles). The error bars indicate the allowed variation due to composition mixtures. Effects of uncertainties on the data are indicated by the vertical light-gray bands with dark-gray bracketing ends. Open ends indicate uncertainties to extend beyond the proton-iron range. Data from the Pierre Auger Observatory from ICRC 2019 [201] are shown by black horizontal lines, with systematic (light gray) and statistical (dark gray) errors as bands.

The previously found perfect agreement is lost when decreasing  $f_{\text{stop}}$  to 0.1 in Fig. 7.6. In fact, one finds that it is no longer possible to simultaneously reconcile  $\sigma(X_{\max})$ -data with  $\langle X_{\max} \rangle$ -data and solve the muon deficit. A further decrease to  $f_{\text{stop}} = 0.01$  in Fig. 7.7 only worsens this behavior, making  $\langle X_{\max} \rangle$ -data infer lighter compositions than data on their fluctuations do. Lastly, for the case  $f_{\text{stop}} = 0.001$  as shown in Fig. 7.8, also no agreement can be found between

the average and fluctuations on  $X_{\max}$ , despite sufficiently increasing the muon number for a larger range of fireball-threshold settings.

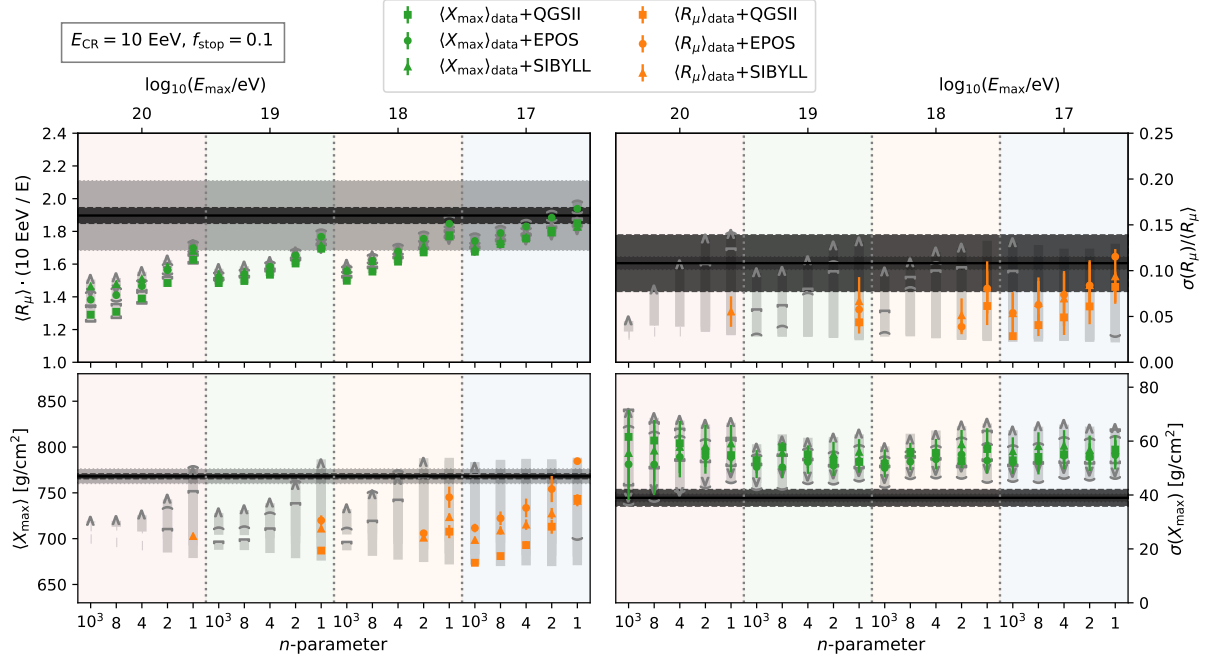


Figure 7.6: Same as Fig. 7.5, but then for  $f_{\text{stop}} = 0.1$ .

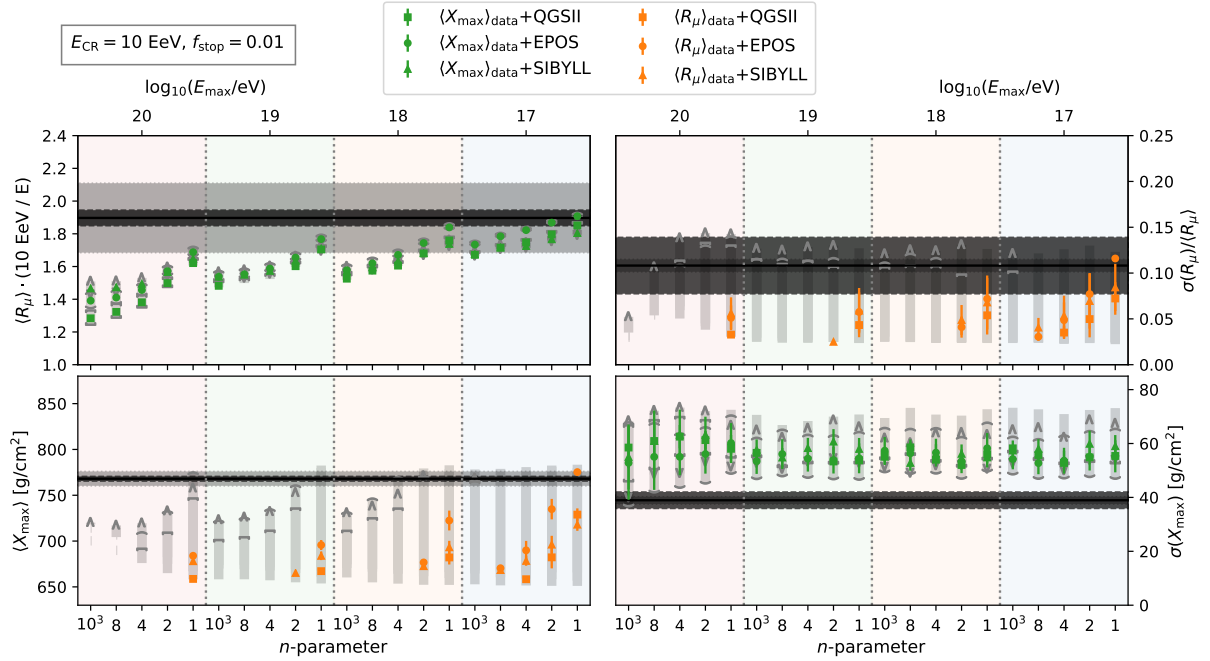
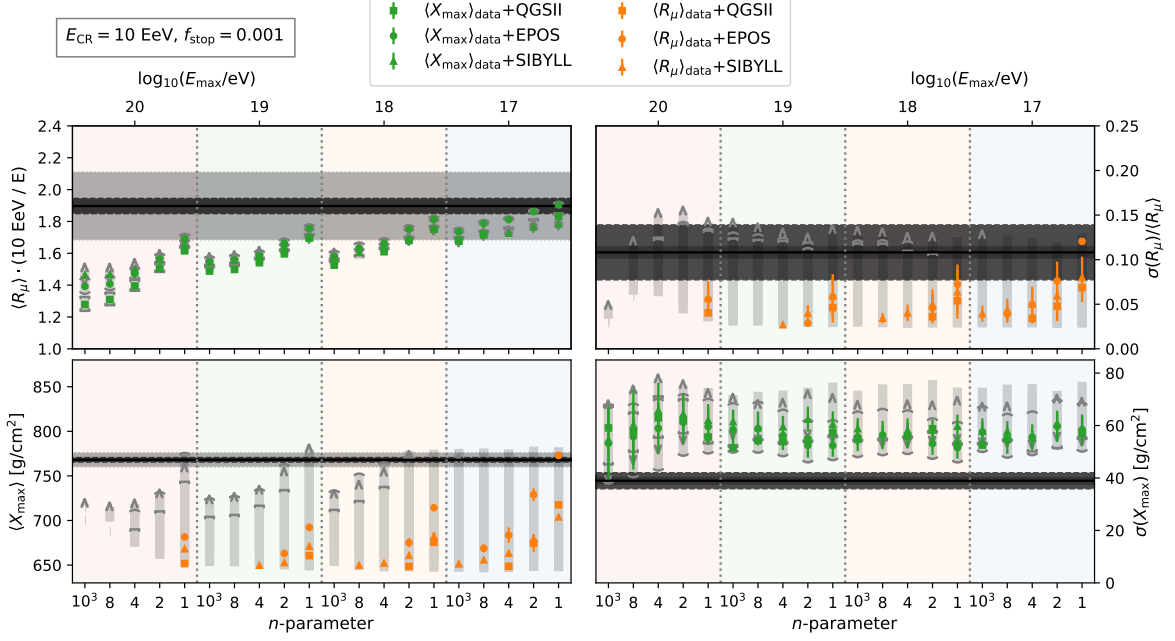


Figure 7.7: Same as Fig. 7.5, but then for  $f_{\text{stop}} = 0.01$ .



**Figure 7.8:** Same as Fig. 7.5, but then for  $f_{\text{stop}} = 0.001$ .

In general, the introduction of the stage of repeated *in situ* collisions seems to be counter-productive for obtaining a complete consistency between the observables. Such a conclusion could be drawn based on the following two observations. First, breaking up particles further through repeated collisions barely increases the muon number, therefore implying that the dominant contribution comes from swapping the highest-energetic pions for kaons. This intuitively makes sense as it corresponds to suppressing the largest energy loss to the EM component. Second, the decrease in  $\langle X_{\text{max}} \rangle$  predictions, originating from the artificial acceleration of the shower development, appears to require compositions too light to be compatible with  $\sigma(X_{\text{max}})$ -data.

These observations do not exclude a light variant of the fireball model where one turns off the stage of repeated collisions by setting  $f_{\text{stop}} = 1$ . In fact, we found the fireball model to enable a consistent composition interpretation for the specific set of parameters summarized in Table 7.1. Therefore, in the remainder of this thesis we will only consider the fireball model without the formation of a plasma and only a strangeness enhancement. In essence, the resolution comes from the flexibility of the energy-dependent fireball-initiation threshold. It remains to be seen whether this also works for showers from 5 and 20 EeV CRs.

**Table 7.1:** Settings of the fireball model allowing for a consistent composition interpretation of data from the Pierre Auger Observatory on both moments of  $X_{\text{max}}$  and  $R_{\mu}$  at 10 EeV.

	$\log_{10}(E_{\text{min}}/\text{eV})$	$\log_{10}(E_{\text{max}}/\text{eV})$	$n$	$f_{\text{stop}}$
QGSJETII-04	15	17	2	1.0
EPOS-LHC	15	18	1	1.0
	15	17	4	1.0
SIBYLL-2.3D	15	18	1	1.0
	15	17	4	1.0



# 8 | Extending the Heitler-Matthews Model of the Muon Number

Instead of repeating the previous analysis at different energies, it may be worthwhile to analytically investigate the effect of the fireball model on the muon number. This may provide a deeper insight into the physics of air showers and constitute an independent confirmation of the results from Monte Carlo simulations. We will take an approach inspired by the Heitler-Matthews model, and the framework developed in this chapter will be used in Chapter 9. Following the implementation of the general effect of the fireball model in Sec. 8.1, we continue extending the Heitler-Matthews model by introducing an energy-dependent multiplicity in Sec. 8.2.

## 8.1 Muon Number in a Fireball-Extended Heitler Model

Exchanging pions for kaons and vice-versa – as suggested for the implementation of a phenomenological fireball model in Sec. 5.3 – affects the fraction of the energy that remains in the hadronic component. In the Heitler-Matthews model, this fraction  $r$  is taken to be a constant throughout the shower, which together with the multiplicity  $n_{\text{mult}}$  determines the exponent  $\beta$  (see Sec. 2.3.2). One way of implementing the fireball model<sup>1</sup> into this Heitler-Matthews framework is to allow some interactions in the shower to have a different  $r$ -value. To this end we define  $r_{\text{fb}}$  as the fraction of energy remaining in the hadronic component after a fireball interaction, in contrast to the analogous definition of  $r_{\text{SM}}$  for a Standard Model interaction.

This hybrid  $r$ -value approach to change the flow of energy in a shower can be implemented into an air shower by defining an effective  $r$ -value,

$$r_{\text{eff}}(E) \equiv [1 - p(E)] r_{\text{SM}} + p(E) r_{\text{fb}}, \quad (8.1)$$

which depends on the energy  $E$  of the projectile in the interaction, and  $p(E)$  is given by Eq. 5.3. Splitting a single interaction into a Standard Model (corona) and a ‘fireball’ (core) component is an important feature of the core-corona model (see Sec. 5.2). While the fireball model itself does not predict such a splitting, in the limit of many showers  $p(E)$  could be interpreted as the statistical fraction of many interactions rather than the physical fraction of a single interaction, justifying the above definition with  $p(E)$  from Eq. 5.3. In fact, for the statistical moments of the muon number such a limit of many showers is essential. In some sense, we therefore follow the probabilistic nature of a shower rather than one of its realizations.

---

<sup>1</sup>Note that we no longer consider the formation of a plasma, as was excluded in Sec. 7.2.2.

In the Heitler-Matthews model,  $\log r$  can be interpreted as the infinitesimal change in the logarithm of the fraction of particles in the hadronic component with generation  $k$ <sup>2</sup>:  $\log r = d \log(N_{\text{had}}/N_{\text{tot}})/dk$ .<sup>3</sup> Generalizing this idea that  $r$  captures this generational rate of energy remaining in the hadronic component, one can integrate  $\log r$  over all generations to obtain the logarithm of the fraction of particles that is left in the hadronic component at the end of the shower. A subsequent exponentiation and a multiplication by the total number of particles,  $N_{\text{tot}} = E_0/E_c$ , gives the muon number as:

$$N_\mu = \left(\frac{E_0}{E_c}\right) \exp \left[ \int_0^{k_c} \log r \, dk \right], \quad (8.2)$$

where the potential  $k$ -dependence of  $r$  has been kept implicit. For a constant  $r$ -value as in the Standard Model case ( $r = r_{\text{SM}}$ ), we retrieve the Heitler-Matthews model. For an energy- (and thus generation-) dependent  $r$ -value as in Eq. 8.1, the integral captures the change in  $r$ -value as fireball interactions become less likely at later generations.

We assume – in accordance with the Heitler-Matthews model – that in each interaction the energy of the projectile is equally divided over its secondaries. Consequently, the generation  $k$  is directly related to the energy of the particles at this generation. Substituting in Eq. 8.1 and making a change of variables to the energy of the particles at generation  $k$  gives

$$N_\mu = \left(\frac{E_0}{E_c}\right) \exp \left[ - \int_{\log E_c}^{\log E_0} \log \{r_{\text{SM}} + p(E)(r_{\text{fb}} - r_{\text{SM}})\} \frac{dk}{d \log E} \, d \log E \right], \quad (8.3)$$

where  $dk/d \log E$  is completely determined by the energy-evolution of the multiplicity. In the Heitler-Matthews model the multiplicity is assumed to be constant, giving  $dk/d \log E = -1/\log(n_{\text{mult}})$ .<sup>4</sup> This assumption may be too crude for our purposes, but for now we will stick to a constant multiplicity.

With  $p(E)$  given by Eq. 5.3 and a constant multiplicity, the integral in Eq. 8.3 can be solved analytically in terms of the hypergeometric function, as shown in Appendix D.1.

### 8.1.1 The Effect of Discrete Interactions

So far, we glossed over the fact that  $r$  is *not* defined as the infinitesimal change with generations, but rather as a constant factor for a single generation. Therefore,  $\log r$  in the integral of Eq. 8.2 becomes a step-function, plateauing for each generation. Not taking this into account would underestimate the effect of the fireball: since the height of the plateau is determined by the interaction, and thus the beginning of the generation, the fireball seeps down to lower energies.

A visualization of this effect is shown in the left plot of Fig. 8.1. The solid black line visualizes (the logarithm of) Eq. 8.1 for a particular set of fireball parameters:  $n = 2$ ,  $E_{\text{min}} = 10^{15}$  and  $E_{\text{max}} = 10^{17}$  eV. Choosing a constant multiplicity of 10, a single generation corresponds to one order of magnitude in energy. The subsequent evolution of  $r(E)$  in showers from  $10^{19}$  eV and

<sup>2</sup>To avoid confusion with the fireball parameter  $n$ , here we use  $k$  ( $k_c$ ) to denote the (critical) generation (cf. Sec. 2.3.2).

<sup>3</sup>Recall that at generation  $k$  the number of particles in the hadronic component is given by  $N_{\text{had}} = (rn_{\text{mult}})^k$ , and the total number of particles is given by  $N_{\text{tot}} = n_{\text{mult}}^k$ . See Appendix C for a complete list of symbols used in this Chapter.

<sup>4</sup>Note that analogous to Eq. 2.6, one has  $k = \log(E_0/E)/\log(n_{\text{mult}})$  when shower particles have energy  $E \geq E_c$ .

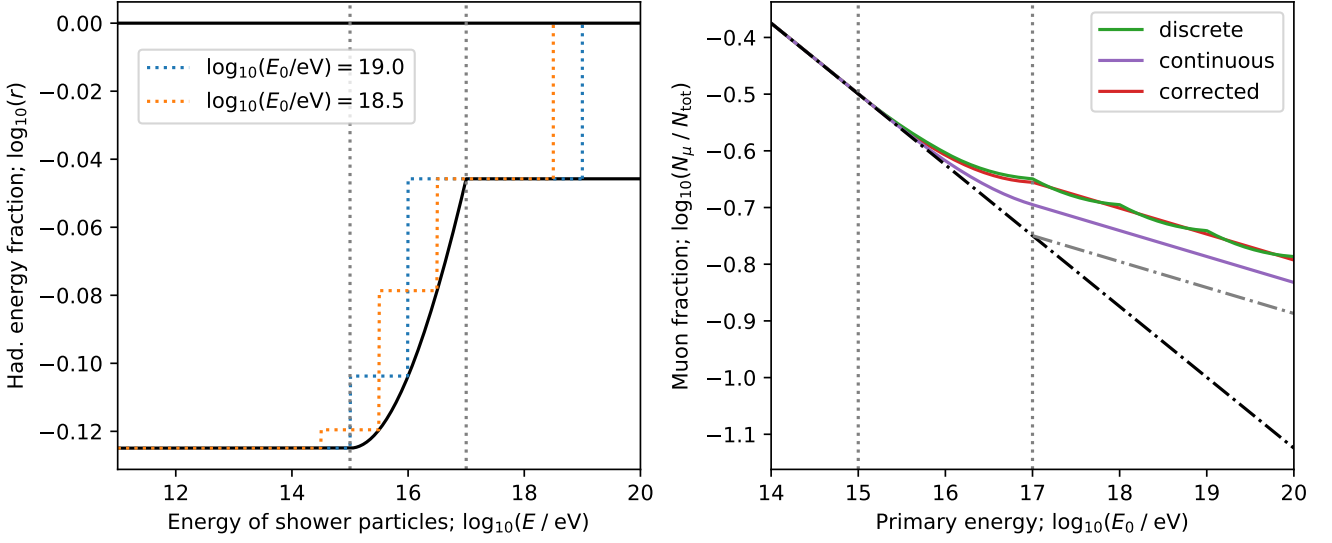


**Figure 8.1:** Visualization of the effect of discrete interactions on the hybrid-r approach for implementing a fireball model. Fireball settings are fixed to  $n = 2$ ,  $E_{\min} = 10^{15}$  eV, and  $E_{\max} = 10^{17}$  eV. The latter two are represented by the left and right vertical gray dotted lines, respectively. The multiplicity is fixed to 10. *Left:* the energy evolution of the hadronic energy fraction  $r$  in the fireball model for a continuous energy loss (black solid), and two showers ( $10^{19}$  eV, blue dotted;  $10^{18.5}$  eV, orange dotted) with discrete interactions. *Right:* muon fraction  $N_{\mu}/N_{\text{tot}}$  as a function of the primary energy  $E_0$  without (purple) and with (green and red) discrete interactions. The red curve arises from a discreteness correction  $\Delta_{\text{disc}}$  to the purple curve. Also shown with dash-dotted lines are the Standard Model case (black) and a pure fireball above  $E_{\max}$  (gray) without discreteness correction.

$10^{18.5}$  eV CRs are indicated by the blue and orange dotted lines, respectively. Note in particular the aforementioned step-function behavior. The integral of Eq. 8.2 should correspond to the area that is enclosed by such a step-function, and the vertical lines at the primary energy and the critical energy  $\sim 10^{11}$  eV. This area is negative and has a smaller absolute value than the one bound by the continuous black line, and thus corresponds to a larger muon number.

By increasing the primary energy of the CR, the step-functions shift in a way reminiscent of an escalator. The exact area bound by the escalator region alone ( $10^{14} - 10^{17}$  eV in the left plot of Fig. 8.1) oscillates as the primary energy increases, with a period of 1 generation. This translates itself to the rather unphysical behavior of the green curve in the right plot of Fig. 8.1. This oscillatory effect gets more extreme for a step-function threshold (e.g.,  $n \rightarrow \infty$  in Eq. 5.3) or a large multiplicity, and can be attributed to relying too much on the assumption of an equal division of energy of the secondaries. Such oscillatory behavior would likely be smoothed out when the secondaries of the first interaction vary in energy, each inducing independent subshowers. Therefore, a more physical approximation would be to correct the integral of the continuous black curve in the left plot – leading to a muon number prediction shown by the purple curve in the right plot – by some constant factor above  $E_{\max}$  (right vertical gray dotted line). A reasonable average behavior is given by half a generation of extra fireballs, corresponding to a shift of  $\frac{1}{2} \log(r_{\text{fb}}/r_{\text{SM}})$ . To generalize this correction factor to energies below  $E_{\max}$ , a simple

multiplication by  $p(E = E_0)$  suffices:

$$\Delta_{\text{disc}} \equiv \frac{1}{2} \log(r_{\text{fb}}/r_{\text{SM}}) p(E_0). \quad (8.4)$$

Adding this to the continuous (purple) curve in the right plot of Fig. 8.1 results into the corrected version (red curve).

### 8.1.2 Resulting Muon Number

Substituting the integration results of Appendix D.1 in Eq. 8.3 and applying the correction of Eq. 8.4, we get for the muon number  $N_\mu$  as function of primary energy  $E_0$

$$N_\mu = \left(\frac{E_0}{E_c}\right)^\beta \times \begin{cases} 1, & \text{if } E_0 \leq E_{\min}, \\ \left(\frac{E_0}{E_{\min}}\right)^{\delta(E_0)}, & \text{if } E_{\min} \leq E_0 \leq E_{\max}, \\ \left(\frac{E_{\max}}{E_{\min}}\right)^{\delta(E_{\max})} \left(\frac{E_0}{E_{\max}}\right)^\gamma, & \text{if } E_0 \geq E_{\max}, \end{cases} \quad (8.5)$$

where the exponents are given by

$$\beta \equiv \frac{\log(r_{\text{SM}} n_{\text{mult}})}{\log(n_{\text{mult}})}, \quad (8.6)$$

$$\gamma \equiv \frac{\log(r_{\text{fb}}/r_{\text{SM}})}{\log(n_{\text{mult}})}, \quad (8.7)$$

$$\begin{aligned} \delta(E) \equiv & \frac{1}{\log(n_{\text{mult}})} \left[ \log \{r_{\text{SM}} + p(E)(r_{\text{fb}} - r_{\text{SM}})\} - \log r_{\text{SM}} \right. \\ & \left. + \frac{n}{n+1} \left(1 - \frac{r_{\text{fb}}}{r_{\text{SM}}}\right) p(E) {}_2F_1 \left(1, 1 + \frac{1}{n}; 2 + \frac{1}{n}; \left(1 - \frac{r_{\text{fb}}}{r_{\text{SM}}}\right) p(E)\right) \right] \\ & + \frac{1}{2} \frac{\log(r_{\text{fb}}/r_{\text{SM}})}{\log(E_{\max}/E_{\min})} p(E)^{\frac{n-1}{n}}, \end{aligned} \quad (8.8)$$

with  $p(E)$  the probability of initiating a fireball given in Eq. 5.3, and  ${}_2F_1(a, b; c; x)$  the hypergeometric function. Note that the last term in  $\delta(E)$  originates from the correction  $\Delta_{\text{disc}}$  given by Eq. 8.4.

The muon number thus has the energy dependence of the Heitler-Matthews model for CRs below the minimum energy  $E_{\min}$ , with exponent  $\beta$ . Then there is a transition region where the exponent itself  $\beta + \delta(E)$  increases with energy. For CRs above the maximum energy  $E_{\max}$  the exponent becomes constant again at  $\beta + \gamma$ . The remaining parameter  $n$  determines how fast the exponent is increased towards its eventual constant value, which also affects the normalization of the muon number above  $E_{\max}$ . See Fig. 8.2 for a visualization of Eq. 8.5 for various values of  $n$ . The rather jumpy behavior around  $E_{\max}$  is – due to the discreteness of interactions – a direct reflection of the energy-dependent fireball-initiation probability. Interestingly, the definition of  $\gamma$  explicitly shows that if the fireball keeps more energy in the hadronic component  $r_{\text{fb}} > r_{\text{SM}}$ , the muon number is larger w.r.t. the SM case due to  $\gamma > 0$ .

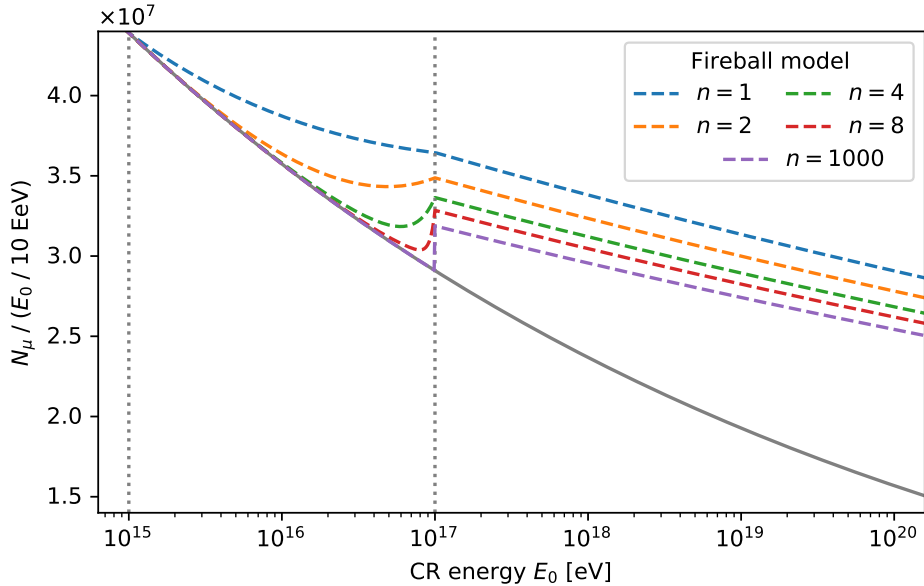


**Figure 8.2:** Muon number  $N_\mu$  in the Fireball-extended Heitler-Matthews model as a function of CR energy  $E_0$ . The Standard Model case (gray solid line) has a constant power-law with exponent  $\beta$  as in Eq. 2.7. In contrast, the fireball case (dashed lines) transitions between  $E_{\min} = 10^{15}$  eV and  $E_{\max} = 10^{17}$  eV (vertical grey dotted lines) to a larger power-law exponent  $\beta + \gamma$  as in Eq. 8.5. Various values for the fireball parameter  $n$  are shown: 1 (blue), 2 (orange), 4 (green), 8 (red), and 1000 (purple). The underlying parameters were estimated as  $n_{\text{mult}} = 25$ ,  $r_{\text{SM}} = 0.75$ ,  $r_{\text{fb}} = 0.9$ , and  $E_c = 10^{11}$  eV.

## 8.2 Introducing an Energy-Dependent Multiplicity

One of the vital assumptions for the derivations of Eqs. 2.7 and 8.5 in the previous sections is that the multiplicity is constant throughout the shower. In reality, as we will also see in Sec. 9.1.2, this is clearly not the case, and in fact is randomly taken from an energy-dependent distribution of multiplicities. To take these complications into account, we develop in this section a formalism for dealing with an energy-dependent multiplicity, extending on the previous results.

Under our assumption of an equal division of energy over the secondaries, the energy per particle of each following generation is given by

$$E_{k+1} = E_k / n_{\text{mult}}(E_k). \quad (8.9)$$

Expressing the energy level  $E_k$  of generation  $k$  in terms of the primary energy  $E_0$  would involve recursive use of this equation. However, only for integer values of  $k$  does one reach  $E_0$  exactly, for other values one would need to use an appropriate interpolation. After this interpolation, one can obtain  $dk/d \log E_k$ , where we usually suppress the subscript. A subsequent calculation of the muon number follows from Eq. 8.3 and potentially the correction of Eq. 8.4. For the interpolation itself it is necessary to have an explicit expression for the energy-dependent multiplicity. In the following we consider a power-law dependence in Sec. 8.2.1 and a generalization to arbitrary curves in Sec. 8.2.2.

### 8.2.1 Power-law Dependence

We adopt the following parametrization of a power-law energy-dependent multiplicity:

$$n_{\text{mult}}(E) = n_{\text{scale}} \left( \frac{E}{E_{\text{scale}}} \right)^b, \quad (8.10)$$

with parameters  $n_{\text{scale}}$ ,  $E_{\text{scale}}$ , and  $b$ <sup>5</sup>. Applying the recursion relation, we find

$$\log E_k = (1 - b)^k \log E_0 + \left[ 1 - (1 - b)^k \right] \left( \log E_{\text{scale}} - \frac{1}{b} \log n_{\text{scale}} \right), \quad (8.11)$$

which can be implicitly interpolated by allowing  $k$  to take non-integer values. Note that this is only valid for  $b < 1$ . For  $b \geq 1$  the multiplicity reaches 1 within one generation, stopping the shower evolution before the recursion relation can be used. Inverting Eq. 8.11 gives

$$k(E, E_0) = \frac{1}{\log(1 - b)} \log \left[ \frac{\log \left( n_{\text{scale}}^{1/b} E / E_{\text{scale}} \right)}{\log \left( n_{\text{scale}}^{1/b} E_0 / E_{\text{scale}} \right)} \right], \quad (8.12)$$

where the subscript  $k$  has been suppressed. Correspondingly, we find

$$\frac{dk}{d \log E} = \frac{1}{\log(1 - b)} \frac{1}{\log \left( n_{\text{scale}}^{1/b} E / E_{\text{scale}} \right)}, \quad (8.13)$$

which can be used in the integral of Eq. 8.3.

#### Standard Model

Recall that in the Standard Model  $r = r_{\text{SM}}$  is constant throughout the shower. This renders the integrals of Eqs. 8.2 and 8.3 irrelevant/trivial, and we can simply evaluate Eq. 2.7 with an updated  $k_c$ . The generation at which the critical energy is reached follows from Eq. 8.12 at  $k(E_c, E_0) \equiv k_c(E_0)$ . Consequently, we find for the muon number in the Standard Model:

$$N_\mu = \left( \frac{E_0}{E_c} \right) \left[ \frac{\log \left( n_{\text{scale}}^{1/b} E_c / E_{\text{scale}} \right)}{\log \left( n_{\text{scale}}^{1/b} E_0 / E_{\text{scale}} \right)} \right]^{\frac{\log r_{\text{SM}}}{\log(1-b)}}. \quad (8.14)$$

Note that the second factor represents the fraction of the total number of particles that remains in the hadronic component till  $E = E_c$  and thus produces muons.

#### Fireball Model

Combining the power-law energy-dependent multiplicity with our previous fireball extension to the Heitler-Matthews model in Sec. 8.1 does require the evaluation of the integral in Eq. 8.3. The difference w.r.t. the derivation in Sec. 8.1 is that  $dk/d \log E$  (given by Eq. 8.13) is no longer

---

<sup>5</sup>The degeneracy between  $n_{\text{scale}}$  and  $E_{\text{scale}}$  allows for a convenient interpretation and explicitly enforces appropriate units. If preferred, either parameter could be set to 1.

independent of the energy and thus cannot be taken out of the integral. To obtain the muon number we need to evaluate

$$N_\mu = \left(\frac{E_0}{E_c}\right) \exp \left[ \frac{-1}{\log(1-b)} \int_{\log E_c}^{\log E_0} \frac{\log \{r_{\text{SM}} + p(E)(r_{\text{fb}} - r_{\text{SM}})\}}{\log \left(n_{\text{scale}}^{1/b} E/E_{\text{scale}}\right)} d \log E + \Delta_{\text{disc}} \right], \quad (8.15)$$

with  $p(E)$  again given by Eq. 5.3, and  $\Delta_{\text{disc}}$  from Eq. 8.4 taking into account discrete interactions. Unfortunately, the integral cannot be solved analytically. Instead, one can approximate this integral very accurately by replacing the arithmetic average of  $r$  by a geometric average. This approach is outlined in Appendix D.2. Consequently, the muon number in the fireball model is given by:

$$N_\mu = \left(\frac{E_0}{E_c}\right) \left[\frac{x_c}{x_0}\right]^{c_1} \times \begin{cases} 1, & \text{if } E_0 \leq E_{\text{min}}, \\ \left(\frac{E_0}{E_{\text{min}}}\right)^{\delta'(E_0)}, & \text{if } E_{\text{min}} \leq E_0 \leq E_{\text{max}}, \\ \left(\frac{E_{\text{max}}}{E_{\text{min}}}\right)^{\delta'(E_{\text{max}})} \left[\frac{x_{\text{max}}}{x_0}\right]^{c_2}, & \text{if } E_0 \geq E_{\text{max}}, \end{cases} \quad (8.16)$$

where we defined

$$c_1 \equiv \frac{\log r_{\text{SM}}}{\log(1-b)}, \quad (8.17)$$

$$c_2 \equiv \frac{\log(r_{\text{fb}}/r_{\text{SM}})}{\log(1-b)}, \quad (8.18)$$

$$x_i \equiv \log \left(n_{\text{scale}}^{1/b} E_i/E_{\text{scale}}\right), \quad i \in \{c, 0, \text{min}, \text{max}\}, \quad (8.19)$$

$$\delta'(E) \equiv -\frac{p(E)}{n+1} \frac{c_2}{x_{\text{min}}} {}_2F_1 \left(1, 1+n; 2+n; \frac{-\log(E/E_{\text{min}})}{x_{\text{min}}}\right) + \frac{1}{2} \frac{\log(r_{\text{fb}}/r_{\text{SM}})}{\log(E_{\text{max}}/E_{\text{min}})} p(E)^{\frac{n-1}{n}}, \quad (8.20)$$

for compactness and readability.

## 8.2.2 Generalized Dependence

For a more complicated energy dependence of the multiplicity, the application of the recursion relation (Eq. 8.9) might not allow for an analytic interpolation of  $k$ . Instead, a general energy-dependent multiplicity  $n(E)$  can be approximated by piece-wise power-law multiplicities. The muon number – or rather the number of hadronic particles – for such power-law multiplicities were derived in the previous section and depend on the primary as well as the critical energy. These power-law multiplicities can be attached by multiplying the hadronic particle numbers with an appropriate choice of the primary and critical energies. Attaching  $m$  power-laws we find the muon number to be given by

$$N_\mu = \prod_{i=0}^{m-1} N_{\text{had}}(E_i, E_{i+1}) = \prod_{i=0}^{m-1} \left(\frac{E_i}{E_{i+1}}\right) \exp \left[ - \int_{\log E_{i+1}}^{\log E_i} \log r \left(\frac{dk}{d \log E}\right)_i d \log E \right] \quad (8.21)$$

where the number of hadronic particles produced within a given generation  $N_{\text{had}}$  follows from Eq. 8.3. The subscript  $i$  of  $dk/d\log E$  emphasizes the piece-wise power-law behavior, and  $dk/d\log E$  is given by Eq. 8.13 with parameters  $b_i$ ,  $n_{\text{scale},i}$ , and  $E_{\text{scale},i}$ . These parameters need to be well-chosen such that the power-laws are connected and approach  $n(E)$ . Choosing  $E_{\text{scale},i} = E_{i+1}$ , we thus need  $n_{\text{scale},i} = n(E_{i+1}) \equiv n_{i+1}$  and  $b_i = \log(n_i/n_{i+1})/\log(E_i/E_{i+1})$ .

Furthermore, due to the boundary conditions of  $E_0$  being the primary energy and  $E_m = E_c$  the critical energy, we can evaluate the product and obtain

$$N_\mu = \left(\frac{E_0}{E_c}\right) \exp \left[ - \int_{\log E_c}^{\log E_0} \log r \left( \frac{dk}{d\log E} \right)_{i,m} d\log E \right], \quad (8.22)$$

where the sum of integrals was combined into a single integral by adding a second subscript  $m$  such that

$$\left( \frac{dk}{d\log E} \right)_{i,m} \equiv \left( \frac{dk}{d\log E} \right)_i = \frac{1}{\log(1-b_i)} \frac{1}{\log \left( n_{i+1}^{1/b_i} E / E_{i+1} \right)}, \quad \text{if } E_{i+1} \leq E \leq E_i, \quad (8.23)$$

where  $i \in \{1, \dots, m-1\}$ . In the limit of  $m \rightarrow \infty$  the second log term loses its explicit energy dependence since the range of  $E$  gets smaller and thus also closer to  $E_{i+1}$ . At the same time,  $b_i$  converges to the derivative  $d\log n/d\log E$  directly from its definition:

$$\begin{aligned} \lim_{m \rightarrow \infty} b_i &= \lim_{m \rightarrow \infty} \frac{\log(n_i/n_{i+1})}{\log(E_i/E_{i+1})} = \lim_{\Delta \log E \rightarrow 0} \frac{\log n(\exp[\log E_i]) - \log n(\exp[\log E_i - \Delta \log E])}{\Delta \log E} \\ &= \frac{d\log n(E)}{d\log E} \end{aligned} \quad (8.24)$$

where the change of limit comes from  $\Delta \log E \equiv \log E_i - \log E_{i+1}$  going to zero as we keep dividing the energy range into more and thus smaller pieces.

In its full glory, the muon number for an arbitrary energy-dependent multiplicity is thus given by

$$N_\mu = \left(\frac{E_0}{E_c}\right) \exp \left[ - \int_{\log E_c}^{\log E_0} \frac{\log r}{\log \left( 1 - \frac{d\log n(E)}{d\log E} \right)} \frac{d\log n(E)}{d\log E} \frac{1}{\log n(E)} d\log E \right], \quad (8.25)$$

which only works as long as the multiplicity does not increase too fast with energy (i.e., as long as  $d\log(n(E))/d\log E < 1$ ), as was also required in the power-law case.

Analytic solutions to this integral are likely to be restricted to a small set of energy-dependent multiplicity parametrizations, as for example the constant and the power-law ones described before. Nevertheless, the generality of this equation can be useful to better approximate more complicated energy dependencies numerically.

# 9 | Parameter Inference and Auger Data Interpretation

For the application of the framework developed in Chapter 8 to the muon deficit in Auger data it is necessary to obtain (effective) values of the free parameters. Some of these parameters are related to those from individual interactions, which can be inferred from hadronic interaction models. Such parameters are studied with CRMC in Sec. 9.1. Then, in Sec. 9.2 we investigate the subsequent propagation of interaction-level parameters to shower-level muonic observables through the Heitler-Matthews framework. Finally, the obtained analytic treatment enables a complete interpretation of Auger data in terms of the requirements of the fireball production probability, as shown in Sec. 9.3.

## 9.1 Particle Interaction Parameters from CRMC

The interaction-level parameters that the muon numbers of the previous chapter depend on are the hadronic energy fraction  $r$  and the multiplicity  $n_{\text{mult}}$ . Since these parameters vary from interaction to interaction they induce distributions – even for a fixed projectile, target and center of mass energy of the collision. In this section we explore these distributions as predicted by the current hadronic interaction models.

To this end we used CRMC to perform sets of Monte Carlo simulations, each involving  $10^4$  collisions. We consider the hadronic interaction models QGSJETII-04, EPOS-LHC, and SIBYLL-2.3C. For the particles initiating the collisions we choose a set of energetic projectiles  $\{\pi^+, p\}$  and stationary targets  $\{p, {}^{14}\text{N}\}$  representative of the hadronic particle content of extensive air showers. We vary the energy of these projectiles from  $10^2$  GeV to  $10^{11}$  GeV.

### 9.1.1 Hadronic Energy Fraction

The hadronic energy fraction  $r$  is defined as the fraction of energy that remains in the hadronic component after an interaction. The distinction between the fireball  $r_{\text{fb}}$  and the Standard Model  $r_{\text{SM}}$  case comes from the selection of particles that are counted towards the hadronic and EM components. In the Standard Model we count the set  $\{e^\pm, \gamma, \pi^0\}$  towards the EM component, leaving the rest of the particles in the hadronic component. For the fireball model we swap pions for kaons and therefore count  $K_{L/S}^0$  towards the EM component, while neutral pions are counted towards the hadronic component. Since neutral pions carry more energy than neutral kaons, this should lead to  $r_{\text{fb}} > r_{\text{SM}}$  and thus to an increase in the muon number w.r.t. the Standard Model.

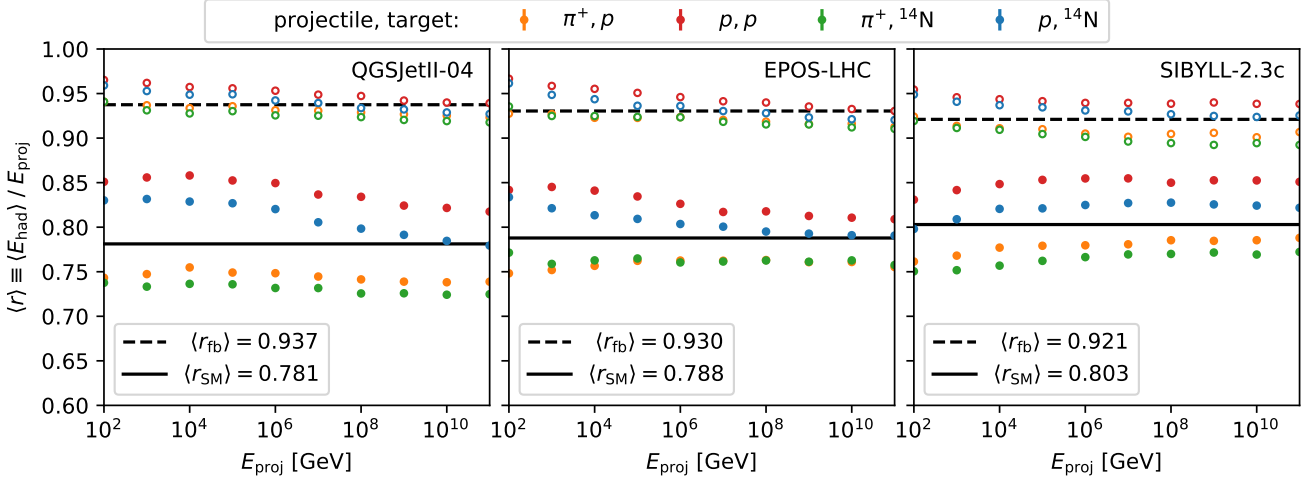


**Figure 9.1:** Averages of the hadronic energy fraction  $r \equiv E_{\text{had}}/E_{\text{proj}}$  as a function of projectile energy in the standard (closed circles) and fireball (open circles) model, with the three hadronic interaction models QGSJETII-04 (left), EPOS-LHC (middle), and SIBYLL-2.3C (right). The projectile-target combinations are indicated in the top legend and each average is obtained from  $10^4$  Monte Carlo collisions in CRMC. Further averaging over the different collision types and projectile energies with equal weights give the black horizontal lines, of which the values are summarized in the inset legends and Table 9.1.

The averages of the resulting  $r_{\text{SM}}$  and  $r_{\text{fb}}$  distributions from  $10^4$  collisions per setting are shown in Fig. 9.1. For each projectile-target combination, these averages seem to be roughly constant with energy<sup>1</sup>. Therefore, by simply averaging over the projectile-target combinations and energies, we obtain rough estimates for  $\langle r_{\text{SM}} \rangle$  and  $\langle r_{\text{fb}} \rangle$  that are valid throughout the entire shower, as summarized in the legends and in Table 9.1. These imply that fireball interactions keep approximately 10-15% more energy in the hadronic component.

**Table 9.1:** Fraction of energy in hadronic secondaries from Standard Model  $r_{\text{SM}}$  and fireball  $r_{\text{fb}}$  collisions, averaged over the  $\{\pi^+, p\} \times \{p, ^{14}\text{N}\}$  projectile-target combinations and  $10^2 - 10^{11}$  GeV projectile energies, based on  $10^4$  CRMC Monte Carlo collisions per setting.

	QGSJETII-04	EPOS-LHC	SIBYLL-2.3C
$\langle r_{\text{SM}} \rangle$	0.781	0.788	0.803
$\langle r_{\text{fb}} \rangle$	0.937	0.930	0.921

Variations around these average hadronic energy fractions could induce fluctuations in the muon number and potentially also affect the average of the muon number. In fact, there are significant variations of  $r_{\text{SM}}$  and  $r_{\text{fb}}$  on the interaction level, see, e.g., the left plot of Fig. 9.2 for their distributions from a  $10^{19}$  eV projectile. However, it should be noted that these fluctuations get averaged on the shower level due to the many interactions it contains. This effect is illustrated in the right plot of Fig. 9.2.

The effective  $r$ -value throughout a shower of  $n$  generations is a geometric mean of the values

<sup>1</sup>The small energy dependence does contain interesting hadronic physics, with the decrease in QGSJETII-04 and EPOS-LHC due to a rising inelasticity, and the opposite in SIBYLL-2.3C due to its forward scaling. The lower values from pion projectiles can be attributed to producing more pionic (and thus  $\pi^0$ ) secondaries.

from each generation:  $r_{\text{sh}} = (\prod_{i=1}^n r_i)^{1/n}$ , where  $r_i$  is the averaged hadronic energy fraction at generation  $i$ . This  $r_i$  is averaged by the number of particles in that generation, each taking a random value from a distribution like the one in the left plot of Fig. 9.2. Consequently, the fluctuations of  $r_i$  are suppressed by a factor of  $1/\sqrt{N_i}$ , with  $N_i$  the number of particles at that generation. Therefore, the geometric averaging suppresses fluctuations from the first interaction, and  $r_{\text{eff}}$  tends towards  $\langle r_{\text{SM}} \rangle$  or  $\langle r_{\text{fb}} \rangle$  from Table 9.1 as the number of generations increases.

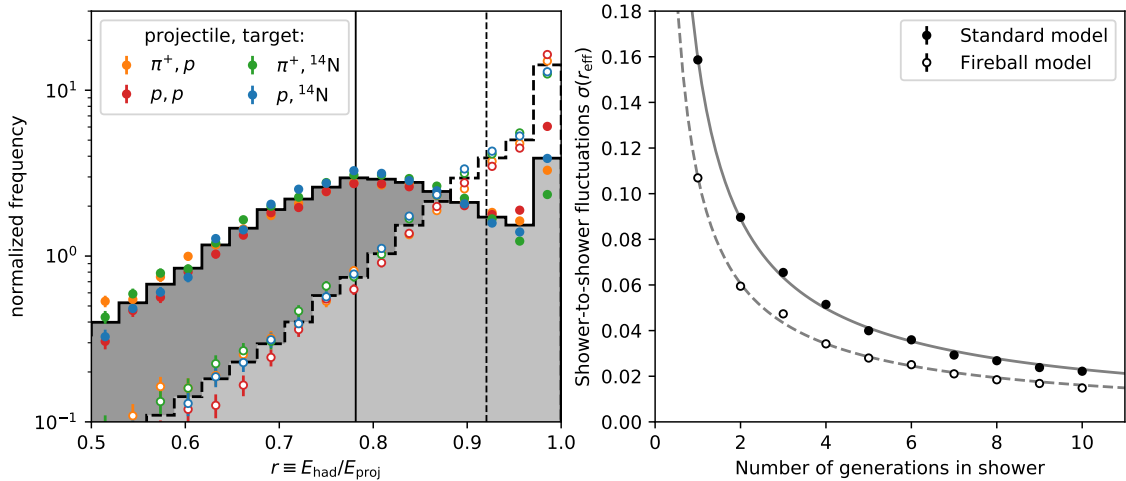


**Figure 9.2:** *Left:* distribution of the hadronic energy fraction  $r \equiv E_{\text{had}}/E_{\text{proj}}$  for  $10^{19}$  eV projectiles in the Standard Model (closed circles) and fireball model (open circles) using EPOS-LHC. The projectile-target combinations are indicated in the legend and their averages are indicated by the gray (solid line, Standard Model) and white (dashed line, fireball model) filled histograms, with the overlapping area light-gray. Vertical lines indicate the average of these histograms. *Right:* shower-to-shower fluctuations of the effective  $r$ -value as a function of the number of generations that the shower has, in the Standard Model (closed circles, solid line) and fireball model (open circles, dashed line). The error bars are computed with a simple Monte Carlo simulation based on the distributions of  $r$ -values from individual collisions.

The shower-to-shower fluctuations of  $r_{\text{eff}}$  in the right plot of Fig. 9.2 was obtained with a simplified Monte Carlo simulation. The exact influence of these fluctuations on the muon number (both average and fluctuations) is rather complicated and will be investigated in Sec. 9.2.

### 9.1.2 Multiplicity

The multiplicity  $n_{\text{mult}}$  is defined as the total number of secondary particles – both EM and hadronic, and of all energies – that are produced in an interaction. For fixed parameters of an interaction, the multiplicity can vary and therefore forms a distribution. For example, Fig. 9.3 shows multiplicity distributions from collisions of  $10^{19}$  eV charged pion and proton projectiles with stationary proton and nitrogen targets, for the three hadronic interaction models QGSJETII-04, EPOS-LHC, and SIBYLL-2.3C.

By eye, the multiplicity distributions can be roughly approximated by lognormal probability density functions (pdfs) with the same average and (sample) variance<sup>2</sup>. Such a rough approx-

<sup>2</sup>The actual distributions originate from the geometry of the collision, with central collisions giving rise to larger multiplicities.

imation can be justified by restricting our interest to an averaged behavior from the different projectile-target combinations. This holds similarly well at other energies and can therefore provide a useful tool to parametrize and interpolate the probabilities in both projectile energy and multiplicity.

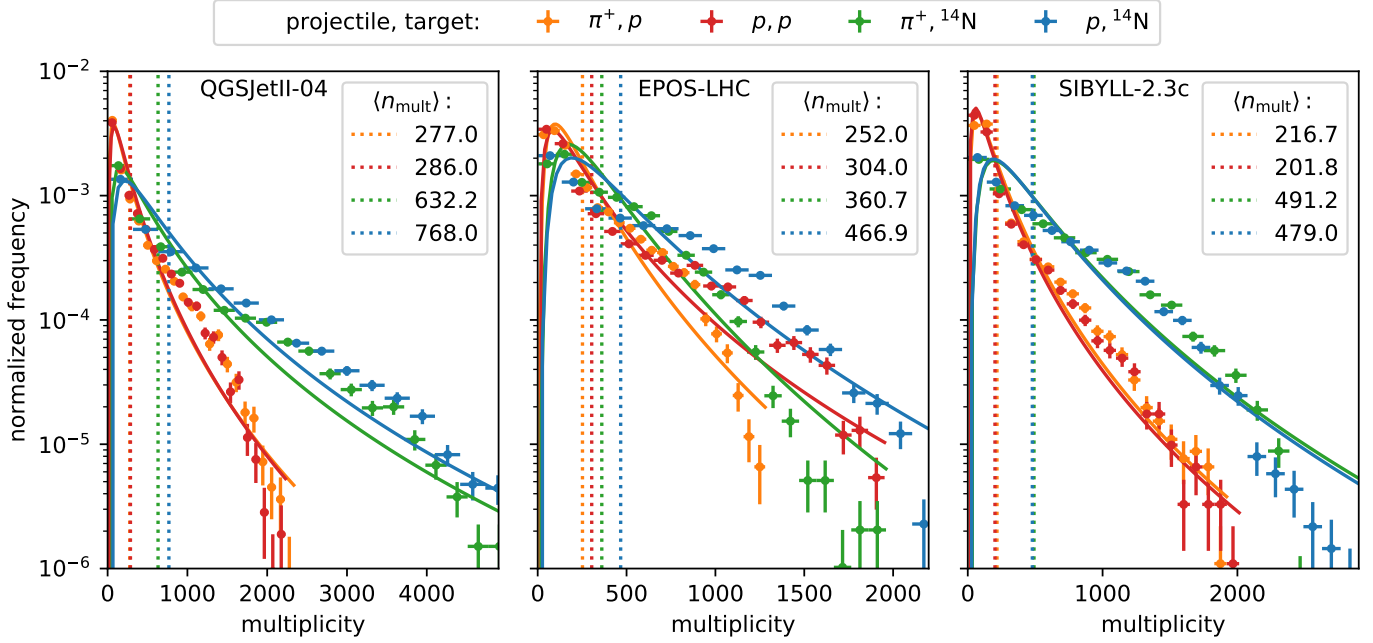


**Figure 9.3:** Multiplicity distributions from CRMC of  $10^{19}$  eV projectiles colliding with stationary targets, for the three hadronic interaction models QGSJETII-04 (left), EPOS-LHC (middle), and SIBYLL-2.3c (right). The projectile-target combinations are indicated in the legend and the Monte Carlo data set consists of  $10^4$  collisions per setting. Also shown are average multiplicities  $\langle n_{\text{mult}} \rangle$  (vertical dotted lines, legends), and lognormal probability density functions (solid lines) with average and (sample) variance equal to that of the simulated data.

The lognormal distribution is usually parametrized in terms of the mean  $\mu$  and standard deviation  $s$  of the associated normal distribution

$$\text{Lognormal}(x; \mu, s) = \frac{1}{xs\sqrt{2\pi}} \exp\left(-\frac{[\log(x) - \mu]^2}{2s^2}\right) \quad (9.1)$$

The first two moments of the lognormal distribution are then given by  $\langle x \rangle = \exp(\mu + s^2/2)$  and  $\sigma^2(x) = [\exp(s^2) - 1] \exp(2\mu + s^2)$ , respectively. Inverting these equations we find

$$s^2 = \log\left(\frac{\sigma^2(x)}{\langle x \rangle^2} + 1\right), \quad \mu = \log\left(\frac{\langle x \rangle^2}{\sqrt{\sigma^2(x) + \langle x \rangle^2}}\right). \quad (9.2)$$

It should be noted that the multiplicity cannot physically fall below one. Therefore, the multiplicity is distributed as  $\text{Lognormal}(n_{\text{mult}} - 1; \mu, s)$ , with  $\mu$  and  $s$  given by Eq. 9.2 where  $x = n_{\text{mult}} - 1$ .

**Table 9.2:** Fit parameters of power law fits to the energy dependence of the average and standard deviation of the multiplicity for the hadronic interaction models QGSJETII-04, EPOS-LHC, and SIBYLL-2.3C. The fitted points are the average of the four projectile-target combinations, i.e., the black dots of Fig. 9.4. The parameters  $a$  and  $b$  correspond to a power law of the form  $a(E/\text{GeV})^b$ .

parameter: $a(E/\text{GeV})^b$	QGSJETII-04		EPOS-LHC		SIBYLL-2.3C	
	$a$	$b$	$a$	$b$	$a$	$b$
$\langle n_{\text{mult}} \rangle$	5.69	0.193	7.70	0.166	6.74	0.173
$\sigma(n_{\text{mult}})$	2.80	0.233	2.93	0.205	2.92	0.211

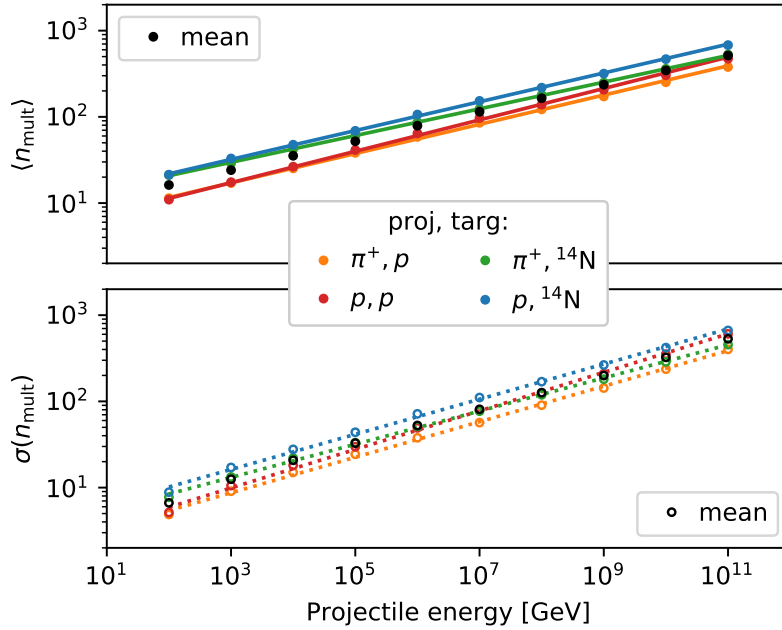


**Figure 9.4:** Energy dependence of the average multiplicities  $\langle n_{\text{mult}} \rangle$  (top) and their standard deviations  $\sigma(n_{\text{mult}})$  (bottom) from collisions of the projectile-target combinations given in the legend. The points are obtained with  $10^4$  CRMC simulations per setting using the EPOS-LHC hadronic interaction model. The additional black points are the arithmetic mean of the projectile-target combinations at that energy.

The energy dependence of the average and standard deviation of the multiplicity distributions are both well-described by power laws, see, e.g., Fig 9.4 for the case of EPOS-LHC. To approximate an average behavior of the collisions of different particle types, we simply take arithmetic means of the moments. The fit parameters from fits to the resulting power laws (through the black points) for each of the hadronic interaction models are summarized in Table 9.2. Combining these power laws with our previous observation of lognormally distributed multiplicities, we can interpolate the multiplicity distributions to intermediate projectile energies. This gives

$$\text{pdf}(n_{\text{mult}}; E_{\text{proj}}) = \frac{1}{n_{\text{mult}} - 1} \frac{1}{\sqrt{2\pi \log(y^2)}} \exp\left(-\frac{1}{2 \log(y^2)} \left[\log\left(\frac{n_{\text{mult}} - 1}{\langle n_{\text{mult}} \rangle - 1} y\right)\right]^2\right), \quad (9.3)$$

where we defined  $y^2 \equiv \sigma^2(n_{\text{mult}})/(\langle n_{\text{mult}} \rangle - 1)^2 + 1$  for convenience, and kept the energy dependence of  $\sigma(n_{\text{mult}})$  and  $\langle n_{\text{mult}} \rangle$  implicit.

### 9.1.3 Correlations

At this point it is important to investigate potential correlations between the hadronic energy fraction and the multiplicity. This becomes a crucial check if one intends to treat these parameters independently. To give an impression of their interdependence, Fig. 9.5 shows the two-dimensional distributions for the Standard Model (top) and fireball cases (bottom) for  $10^{19}$  eV projectiles within each of the hadronic interaction models. In line with the averaging over projectile-target combinations of the previous sections, these plots contain data from each of the projectile-target combinations:  $\{\pi^+, p\} \times \{p, {}^{14}\text{N}\}$ , with in total thus  $4 \cdot 10^4$  events. To guide the eyes, the red points show the average in each horizontal or vertical bin.

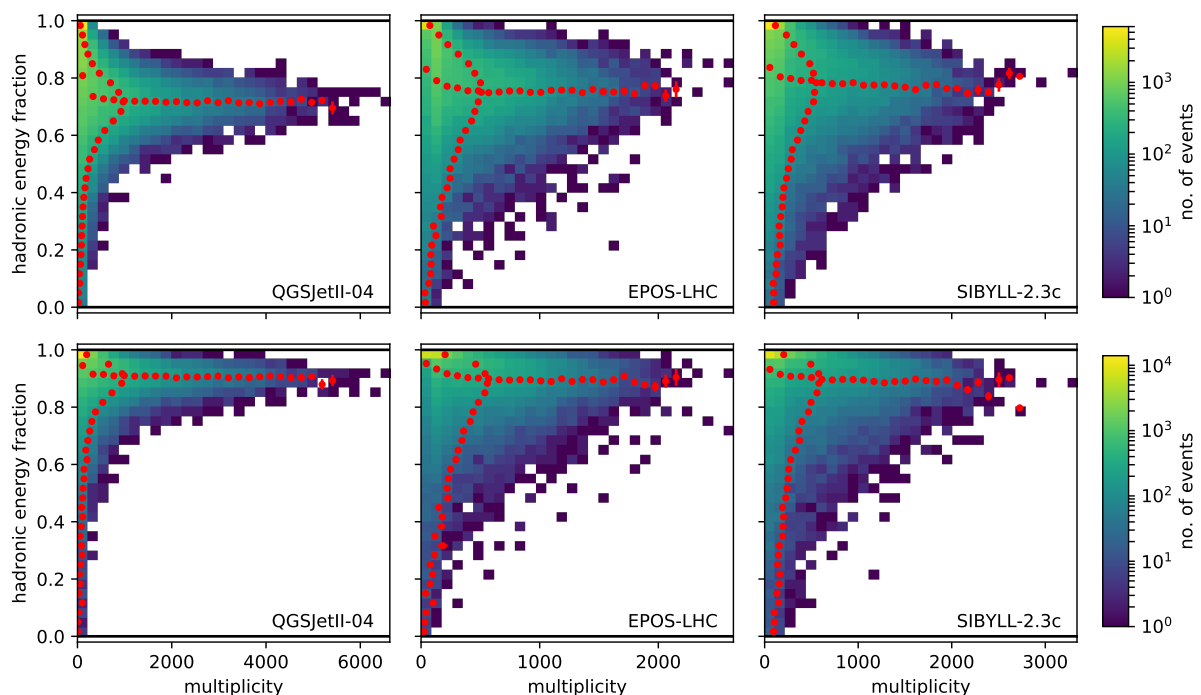


**Figure 9.5:** Two-dimensional distribution of events based on their multiplicity and hadronic energy fraction in the Standard Model (top) and fireball (bottom) scenarios, using the hadronic interaction models QGSJETII-04 (left), EPOS-LHC (middle), and SIBYLL-2.3c (right). The red points show bin-wise averages of the multiplicity (vertical line) and hadronic energy fraction (horizontal line). The events were simulated with CRMC with  $10^4$  events per plot.

Note that the shape itself (without color) does not necessarily indicate a correlation. In particular, if the horizontal line of vertical averages (i.e., the average hadronic energy fraction in each multiplicity bin) was exactly flat, there would likely be no correlation. However, when looking at the color distribution, there is a clear peak in the top left – at low multiplicity and high hadronic energy fraction. This also translates to the bin-wise average hadronic energy fraction increasing at low multiplicities, i.e., the horizontal red points bend upwards on the left.

The source of this peak at low multiplicities and high energy fractions is non-trivial and originates from details of the hadronic interaction models. A reasonable hypothesis is that a significant fraction of these events can be attributed to target diffraction dissociation, similar to

the pile-up at  $\alpha_1 = 1$  in Fig. 2 of [202]. In these events the high-energetic projectile remains intact while only losing a very small fraction of its energy to breaking up (dissociating) the atmospheric nucleus (target) [203]. Consequently, most of the energy is trivially kept in the hadronic component, while only inducing small multiplicities.

Note that this origin would also imply a large elasticity. Such events may therefore not be very relevant for the muon number: with a large elasticity the hadronic component does not evolve further due to not dividing much energy over the secondaries.

For a simple chi-squared test of independence between the hadronic energy fraction and the multiplicity we bin these variables and use the test statistic  $\chi^2 = \sum_{i,j} (O_{i,j} - E_{i,j})^2 / E_{i,j}$ . Here the sum runs over all bins and the observed frequency of events in a bin  $O_{i,j}$  is expected to be close to the expected frequency  $E_{i,j} = N p_i p_j$  in the case of independence between the two variables. The probabilities  $p_i = \sum_j O_{i,j} / N$  and  $p_j = \sum_i O_{i,j} / N$  are obtained from the data set itself by ignoring one of the variables, and  $N$  denotes the total number of events ( $10^4$  in our case). Using 20 bins for each variable gives  $(20 - 1)^2 = 361$  degrees of freedom. Taking a size of 0.05, the independence hypothesis can already be rejected at  $\chi^2 > 406.3$ . We find  $\chi^2$  to always be a factor few greater than 1000 and therefore, for all models and energies, the dependence between the hadronic energy fraction and multiplicity is statistically very significant.

Note that the statistical significance is not a measure for the strength of the correlation. To get an impression of how strong the two are correlated, we compute Pearson's correlation coefficient

$$\rho_{r,n_{\text{mult}}} = \frac{\langle (r - \langle r \rangle)(n_{\text{mult}} - \langle n_{\text{mult}} \rangle) \rangle}{\sigma(r)\sigma(n_{\text{mult}})}, \quad (9.4)$$

which ranges from +1 to -1, and 0 implies no linear correlation. The resulting values as a function of energy, for each of the models and projectile-target combinations are shown in Fig. 9.6.

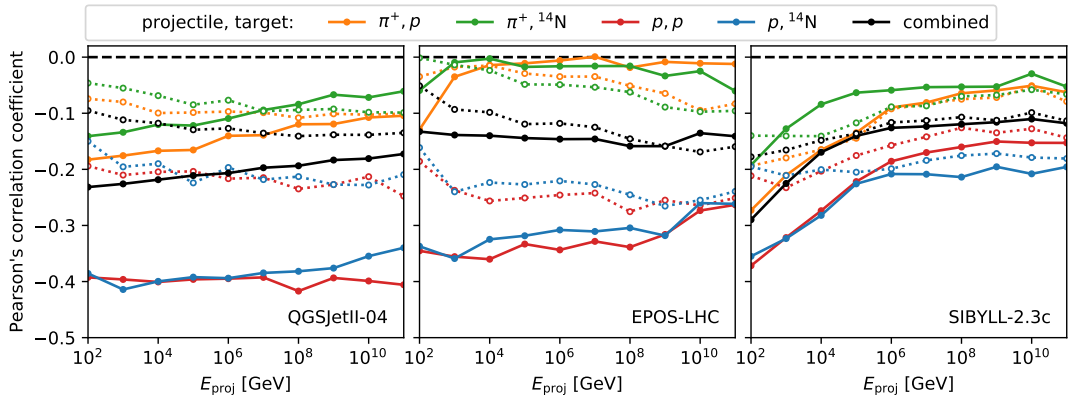


**Figure 9.6:** Pearson's correlation coefficient (Eq. 9.4) for the linear correlation between the hadronic energy fraction and the multiplicity. The correlation is computed as a function of the projectile energy for each of the three hadronic interaction models: QGSJETII-04 (left), EPOS-LHC (middle), and SIBYLL-2.3c (right). The various lines represent the projectile-target combinations (colors, see legend), and the fireball (dotted lines, open circles) versus Standard Model (solid line, closed circles) scenarios. The black lines represent the correlation coefficient when including each of the projectile-target combinations in equal ratios.

While the detailed dependence of the correlation coefficient can be attributed to the underlying hadronic interaction models, some general observations can be made. First, notice that the coefficient is always negative, implying that larger hadronic energy fractions are correlated with lower multiplicities. This is in line with the previous observation of a peak in the top left of Fig. 9.5. Second, interactions from pion projectiles have smaller (absolute) correlations than those from proton projectiles. Third, also the fireball model exhibit fewer correlations than the Standard Model, which can be traced back to the bulk of fireball interactions having larger hadronic energy fractions and are therefore closer to this aforementioned peak. Fourth, the correlations seem to decrease with energy. This is especially evident for SIBYLL-2.3C. Fifth, the combined correlations are roughly between  $-0.1$  and  $-0.2$ . Whether correlations of this size need to be taken into account is not trivial and will therefore be determined through *a posteriori* cross-checks of the muon number with EAS simulations.

## 9.2 Propagating Intrinsic Fluctuations to the Muon Number

The propagation of the distributions obtained in the previous section to the muon number is not trivial. In particular, if one intends to use Eqs. 8.5 or 8.16, a careful distinction must be made between the hadronic energy fraction and the multiplicity at the interaction level on the one hand and these at the shower level on the other hand. For example, as also touched upon in Sec. 9.1.1, the many interactions within a shower suppresses variations of  $r$  at later generations. Taking this into account turns out to be possible for the average and fluctuations of the muon number, as will be outlined in this section.

### 9.2.1 Average Muon Number $\langle N_\mu \rangle$

In a generational picture of air showers where all particles have the same energy, and thus are in sync, the muon number is given by

$$N_\mu = (n_{\text{mult,sh}} r_{\text{sh}})^{k_c} = N_{\text{tot}} (r_{\text{sh}})^{k_c}, \quad (9.5)$$

analogous to Eq 2.7, where the subscripts ‘sh’ remind us that these are effective constants throughout the shower. Here  $n_{\text{mult,sh}}$  is the effective constant multiplicity such that in  $k_c$  generations one obtains the total number of particles  $N_{\text{tot}} = E_0/E_c$ . Associated is an  $r_{\text{sh}}$ , the effective constant energy fraction kept in the hadronic component per generation, such that in  $k_c$  generations the muon number is obtained. The critical number of generations  $k_c$  itself can be determined through knowledge on the energy-evolution of the generational multiplicity:

- For a constant multiplicity  $n_{\text{mult}}$ ,  $k_c$  is given by Eq. 2.6 and we simply have  $n_{\text{mult,sh}} = n_{\text{mult}}$ .
- For a power-law multiplicity,  $k_c$  is given by Eq. 8.12 with  $E = E_c$ .
- For an even more complicated multiplicity,  $k_c$  can be computed from the integral of Eq. 8.25 when taking out  $\log r$ .

Note that these multiplicities are effective multiplicities for an entire generation.

In real air showers the multiplicity can vary from interaction to interaction, which would – even under the assumption of an equal division of projectile energy over its secondaries – introduce different energy levels within a shower. Since this contradicts the generational picture

of air showers, we require the multiplicity to be the same for an entire generation. To still incorporate the effect of many particles, each individually interacting and inducing a unique multiplicity, we take the average of those multiplicities to represent the multiplicity of that generation. This effectively corresponds to an artificial redistribution of energy from particles produced in low multiplicity interactions to particles produced in high multiplicity interactions such that the sub-showers remain in sync.

From Eq. 9.5 it follows that the muon number can be obtained from appropriately multiplying energy losses to the EM component. Taking this idea further, the muon number is proportional to a product of hadronic energy fractions per generation  $i$  until the critical generation  $k_c$ :

$$N_\mu = N_{\text{tot}} \prod_{i=1}^{k_c} r_i . \quad (9.6)$$

Here each  $r_i$  represents the fraction of energy that remains in the hadronic component after each generation, which in turn is an average of the hadronic energy fractions from the individual interactions in that generation. If we were to assume that the multiplicity and hadronic energy fraction of an interaction are independent parameters, then we can first average over variations in the hadronic energy fraction (denoted by  $\langle \cdot \rangle_r$ ) and then over variations in the multiplicity (denoted by  $\langle \cdot \rangle_n$ ) of individual interactions. Consequently, the average muon number would be given by

$$\langle N_\mu \rangle = N_{\text{tot}} \langle \prod_{i=1}^{k_c} r_i \rangle = N_{\text{tot}} \langle \langle \prod_{i=1}^{k_c} r_i \rangle_r \rangle_n = N_{\text{tot}} \langle \prod_{i=1}^{k_c} \langle r_i \rangle_r \rangle_n . \quad (9.7)$$

In the first step we were able to pull  $N_{\text{tot}} = E_0/E_c$  out of the averaging because this is constrained by the primary and critical energy. In the second step we assumed independence between the hadronic energy fraction and the multiplicity of an interaction. In the third step we assumed that the effective hadronic energy fraction of a generation is independent of that of the other generations. This last assumption is in line with the idea of having independent sub-showers.

From the relative energy-independence of the average hadronic energy fraction shown in Fig. 9.1, and the clear power-law energy dependence of the average multiplicity shown in Fig. 9.4, it could be expected that these parameters are independent. However, as shown in Sec. 9.1.3, there is a statistically significant dependence. An impression of the size of this dependence is shown through the linear correlation coefficient in Fig. 9.6. Since the origin of this dependence might be due to quasi-elastic collisions – which do not significantly contribute to the development of the shower – it is not trivial how much the average muon number would be affected. Therefore, we will stick with the assumption of independence for simplicity, and subsequently verify our results with Monte Carlo simulations of air showers.

Turning our attention back to Eq. 9.7, we need to average over variations in the effective hadronic energy fraction  $r_i$  of a generation  $i$ , quantified by the energy  $E$  of the particles in that generation. At this generation, there are a total of  $E_0/E$  interactions, of which a fraction  $p(E)$  are fireball interactions and the remainder are Standard Model interactions. The hadronic energy fraction from each of these interactions are drawn from their respective distributions, e.g., as shown in the left plot of Fig. 9.2 for  $E = 10^{19}$  eV. The effective hadronic energy fraction  $r_i$  is then simply the average of the drawn hadronic energy fractions. A subsequent averaging over

many realizations (i.e., showers) converges  $\langle r_i \rangle_r$  to a linear combination of the averages of the fireball and Standard Model distributions:

$$\langle r_i \rangle_r = [1 - p(E)]\langle r_{\text{SM}} \rangle + p(E)\langle r_{\text{fb}} \rangle . \quad (9.8)$$

In principle, the fireball and Standard Model distributions of the hadronic energy fraction can vary as a function of energy, but for simplicity we neglect this effect. Therefore, the complete energy dependence of  $\langle r_i \rangle_r$  comes from the fireball-initiation probability  $p(E)$  given in Eq. 5.3.

Notice in particular the similarity to  $r_{\text{eff}}$  of Eq. 8.1. Therefore, the subsequent appropriate multiplication of these hadronic energy fractions to obtain the muon number follows the same procedure as outlined in Secs. 8.1 and 8.2. Thus, the average muon number when only averaging over variations in the hadronic energy fraction is given by Eqs. 8.5 or 8.16 with the hadronic energy fractions substituted by their respective averages,  $r_{\text{SM}} = \langle r_{\text{SM}} \rangle$  and  $r_{\text{fb}} = \langle r_{\text{fb}} \rangle$ , with the values summarized in Table 9.1.

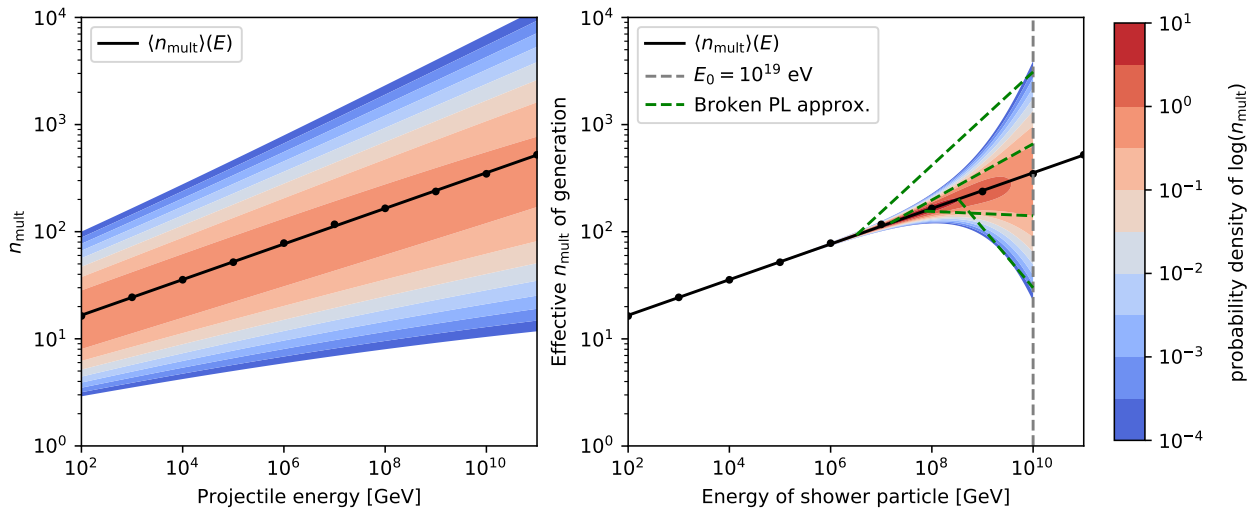


**Figure 9.7:** Interaction- (left) and shower-level (right,  $E_0 = 10^{19}$  eV) multiplicity distributions as a function of energy for EPOS-LHC. Both distributions are given by Eq. 9.3, but the multiplicity fluctuations at the shower-level are suppressed by the square root of the number of particles  $\sqrt{N} = \sqrt{E_0/E}$ . The black line represents the power-law of the average multiplicity, with the black points from CRMC simulations, see Fig 9.4. The broken power-laws (green dashed lines) indicate our approximation of splitting off the first interaction.

Now we still need to average over variations in the multiplicity of the individual interactions. To do so, we can make use of our interpolated energy-dependent multiplicity distribution given by Eq. 9.3. This distribution is visualized in the left plot of Fig. 9.7. For each projectile energy the probability density of the lognormal distribution is shown along the vertical axis. Since the computation of the muon number relies on the multiplicities of the generations rather than of the individual interactions, we need to average these random multiplicities over the number of particles in each generation. The corresponding distribution of the effective multiplicity of a generation as a function of the energy of the particles in that generation  $E$  follows from dividing the standard deviation by the square root of the number of particles in that generation  $\sqrt{N} = \sqrt{E_0/E}$ , where the latter follows from an equal division of energy over the secondaries.

The right plot of Fig 9.7 shows this energy-dependent effective multiplicity distribution for air showers induced by a  $E_0 = 10^{19}$  eV CR.

To average over these variations in the multiplicity, we could in principle use the muon number for a generalized energy-dependent multiplicity (Eq. 8.25) and subsequently find an appropriate weighing based on our lognormal distributions. This is, however, rather complicated; both in the exact meaning of such a multiplicity evolution and in the evaluation of two-dimensional integrals (i.e., over the shower evolution and over effective multiplicities) at each CR energy. Instead, an easier method would be to approximate the multiplicity variations only to manifest itself in the first interaction, as indicated by the broken power laws (green dashed lines) in Fig. 9.7. Since the most likely multiplicities are around  $O(10^2)$ , the second generation will already have sufficient particles to average out fluctuations of the multiplicity.

We can therefore split out the first interaction in the calculation of the muon number,

$$N'_\mu(E_0) = r_1 n_1 \cdot N_\mu(E_0/n_1), \quad (9.9)$$

and average over the multiplicity of the first interaction  $n_1$ ,

$$\langle N_\mu \rangle = r_1 \int n_1 \cdot N_\mu(E_0/n_1) \text{pdf}(n_1; E_0) dn_1. \quad (9.10)$$

Here  $r_1 = [1 - p(E_0)]\langle r_{\text{SM}} \rangle + p(E_0)\langle r_{\text{fb}} \rangle$  is the effective hadronic energy fraction of the first interaction,  $\text{pdf}(n_1; E_0)$  is the lognormal multiplicity distribution of the first interaction (Eq. 9.3), and  $N_\mu$  is the muon number computed with a power-law multiplicity function (Eq. 8.16).

The resulting average muon number as a function of primary energy is shown in Fig. 9.8 (dot-dashed lines) for the EPOS-LHC hadronic interaction model. Further shown are the muon numbers corresponding to the black power-law of Fig. 9.7 (dashed lines), and results from fireball-implemented CONEX simulations with proton primaries (error bars). In these simulations, the interface of CONEX to the hadronic interaction models are adjusted in such a way that with the fireball probability (Eq. 5.3) the output of the hadronic interaction model is processed through a swapping-procedure where pions are exchanged for kaons and vice versa, see Sec. 5.3.

The multiplicity averaging of Eq. 9.10 seems to increase the muon number around  $E_{\text{max}}$  for  $n \geq 4$ , while creating a dip at higher energies for all  $n$ . Both features find their origin in the discretization effect discussed in Sec. 8.1.1. This effect takes into account that real air showers have discrete interactions, implying that the fireball-enhanced effective  $r$ -value remains at a constant level (and therefore a higher level w.r.t. a continuous treatment) until the end of a generation.

The general behavior of this effect can be best understood with a step-function fireball threshold as is well-approximated by the case of  $n = 1000$ . At  $E_0 = E_{\text{max}}$  the entire first generation suddenly produces fireballs, with an associated abrupt increase in the muon number. Further increasing the primary energy does not introduce another generation of fireballs and therefore simply follows the Standard Model power-law energy dependence, giving rise to the Z-shaped curve. Only after an entire generation do we again see an increase from the fireball effect due to secondaries inducing fireballs. This time, the abruptness is smoothed out by a distribution of multiplicities and thus secondary energies, causing the smooth dip feature. Only beyond this dip feature does the energy dependence of the muon number converge to the fireball power-law. As we reduce  $n$ , fireballs were already present at lower energies and thus in later generations, damping the aforementioned effect.

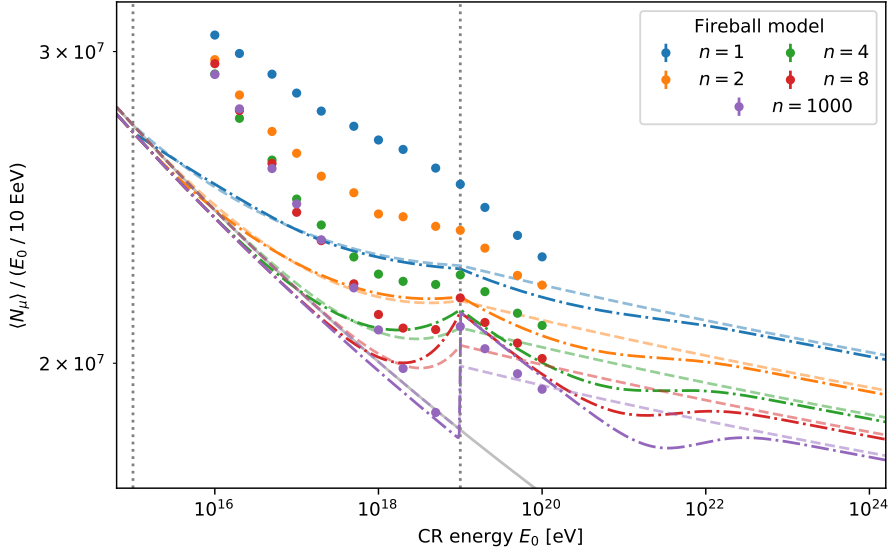


**Figure 9.8:** The average muon number  $\langle N_\mu \rangle$  as a function of the cosmic-ray energy  $E_0$  from an average over the multiplicity (dot-dashed lines; Eq. 9.10), using the average multiplicity parameters (light dashed lines; Eq. 8.16), and from fireball-implemented CONEX simulations (error bars), for various values of  $n$ . Also shown is the Heitler-Matthews or Standard Model limit using the average multiplicity parameters (gray line). The minimum and maximum energy were set to  $E_{\min} = 10^{15}$  eV and  $E_{\max} = 10^{19}$  eV, respectively (vertical dotted lines). The hadronic interaction model EPOS-LHC was used for both the CONEX simulations (2100 showers per point) and the parameters obtained from CRMC (see Sec. 9.1). The critical energy  $E_c$  is set to 220 GeV.

As concluded in Sec. 8.1.1, such an effect seems to be rather unphysical as it relies too much on the equal division of energy among the secondaries. A comparison with CONEX simulations at  $E_{\max}$  supports this conclusion: the indistinguishability of scenarios with  $n \geq 4$  is not reproduced. This indistinguishability would be expected from a discrete first interaction in combination with an equal division of energy among the secondaries, because with typical multiplicities around  $O(10^2 - 10^3)$  the first interaction would skip the fireball evolution up to  $E_{\max}$ . Instead, interactions in real air showers are known to exhibit highly elastic behavior, causing the leading particles of the first few interactions to traverse the energy-levels that distinguish the various values of  $n$ .

A genuine effect of our averaging over the multiplicity seems to be a constant offset to lower muon numbers. This bias seems to be of a systematic nature as it introduces the same offset for each  $n$ , and could therefore be compensated for by a global normalization through the critical energy  $E_c$ . Furthermore, this effect is rather small and should be safe to ignore for our purposes. We will thus ignore the effect of multiplicity fluctuations on the average muon number, and thereby promote Eq. 8.16 to the average muon number.

Comparing this average muon number to the CONEX simulations shows a clear disagreement. Note that the normalization can be tuned with the critical energy  $E_c$ , which in Fig. 9.8 is set to 220 GeV. Despite the disagreement, some general behavior is reproduced by Eq. 8.16 (light dashed lines): a smaller  $n$  gives rise to larger muon numbers, the average muon number per energy falls with energy, and there is a discontinuity at  $E_{\max}$ .

The use of our CRMC-inferred parameters thus clearly does not reproduce the CONEX sim-

ulations. In particular, the spacing of the dashed lines between the various  $n$  values is too small - which is determined by the multiplicity. But more importantly, the slopes of the power-laws below and above  $E_{\max}$  are too shallow - which are determined by  $\langle r_{\text{SM}} \rangle$  and  $\langle r_{\text{fb}} \rangle$ , respectively, given the previously constrained multiplicity<sup>3</sup>. Perhaps we overestimated the effective hadronic energy fraction - in both the fireball and Standard Model cases - due to our rather strict definition of the EM component, or more likely due to the inability of the Heitler-Matthews model to incorporate leading-particle effects (see also the discussion in Sec. 2.3.2). Instead of going back to our CRMC simulations and *a posteriori* tune the EM definition to match the CONEX simulations while hoping the role of the elasticity to be subdominant, it may be interesting to see what (if any) parameters can reproduce the CONEX simulations.

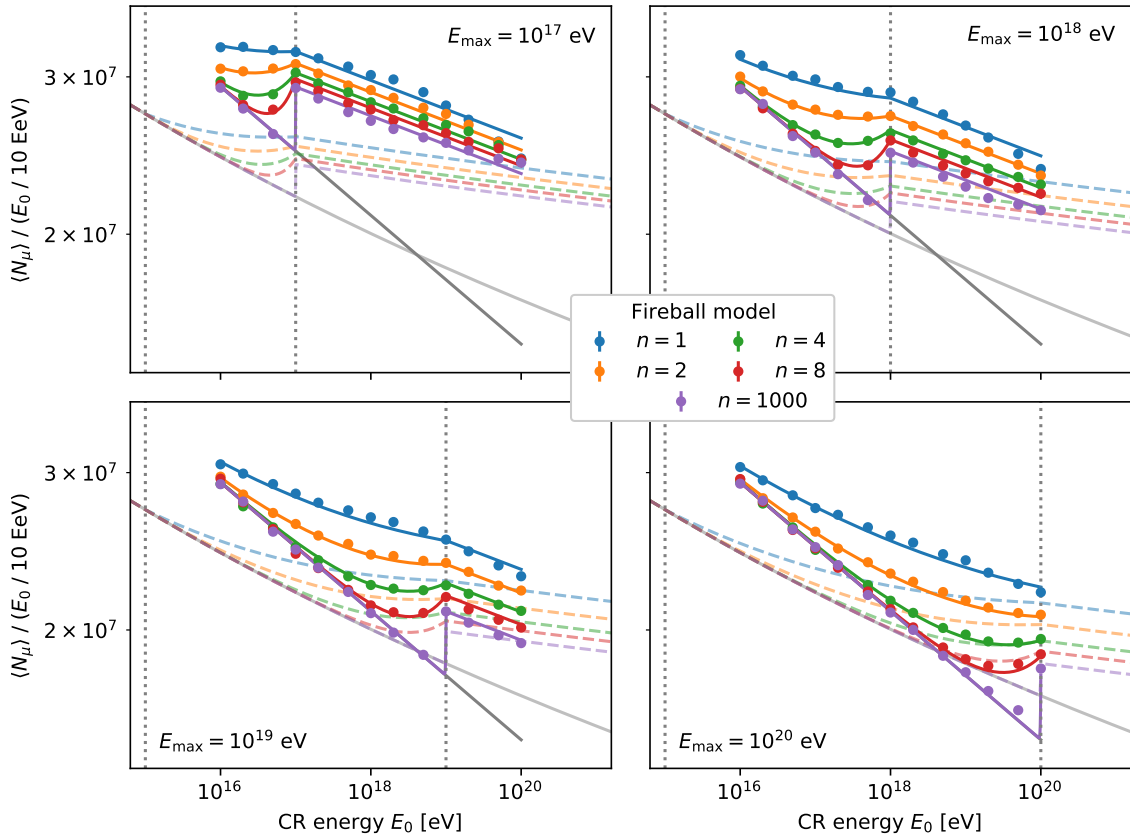


**Figure 9.9:** Simultaneous fit of Eq. 8.16 (solid lines) to fireball-extended CONEX simulations (error bars), for various values of  $n$  (colors) and  $E_{\max}$ :  $10^{17}$  eV (top left),  $10^{18}$  eV (top right),  $10^{19}$  eV (bottom left),  $10^{20}$  eV (bottom right). The parameter  $E_{\min}$  is fixed to  $10^{15}$  eV. The CONEX simulations (2100 showers per point) correspond to proton primaries and used the EPOS-LHC hadronic interaction model. The global fit parameters are summarized in Table 9.3. For reference, also the Standard Model case is shown (gray line), and the evaluation of Eq. 8.16 with the average parameters obtained from CRMC (light dashed lines, same as in Fig. 9.8).

<sup>3</sup>The ratio of (one minus) the slopes is in fact independent of the multiplicity and still disagrees;  $(1 - \beta_{\max}) / (1 - \beta_{\min}) = \log r_{\text{fb}} / \log r_{\text{SM}}$ , with  $\beta = d \log N_{\mu} / d \log E_0$  applied to Eq. 8.5 or 8.16 and evaluated below  $E_{\min}$  and above  $E_{\max}$  as indicated by the subscripts.

To this end, we fitted Eq. 8.16 to the CONEX points, with the following 5 fit parameters:  $r_{\text{SM}}$ ,  $r_{\text{fb}}$ ,  $n_{\text{scale}}$  (setting  $E_{\text{scale}} = 1$  GeV),  $b$ , and  $E_c$ . The results are shown in Fig. 9.9 for EPOS-LHC and in Appendix E.1 for QGSJETII-04 and SIBYLL-2.3D. These fits were performed simultaneously for the different  $E_{\text{max}} \in \{10^{17}, 10^{18}, 10^{19}, 10^{20}\}$  eV and  $n \in \{1, 2, 4, 8, 1000\}$  values while fixing  $E_{\text{min}} = 10^{15}$  eV, such that we have one set of fit parameters for all curves in Fig. 9.9. The fit parameters are summarized in Table 9.3.

**Table 9.3:** Fit parameters of Eq. 8.16 to fireball-extended CONEX simulations for the three hadronic interaction models. The fits are simultaneous to simulations with various values of  $E_{\text{max}} \in \{10^{17}, 10^{18}, 10^{19}, 10^{20}\}$  eV and  $n \in \{1, 2, 4, 8, 1000\}$ , see, e.g., Fig. 9.9.

	$r_{\text{SM}}$	$r_{\text{fb}}$	$n_{\text{scale}}$	$b$	$E_c$ [GeV]
QGSJETII-04	0.5094	0.7201	968.1	$8.682 \cdot 10^{-2}$	136.0
EPOS-LHC	0.5496	0.7644	3819	$2.580 \cdot 10^{-3}$	153.5
SIBYLL-2.3D	0.5648	0.7359	3233	$3.915 \cdot 10^{-5}$	151.1

By eye, the fit seems to work very well, with only CONEX points sufficiently above  $E_{\text{max}}$  showing some deviation from the fit. This is most prominent for  $E_{\text{max}} = 10^{17}$  eV (top left), where the CONEX points for the various  $n$ -values seem to converge at  $10^{20}$  eV. This could imply that the average muon number will be independent of the precise introduction of fireballs at low energies. At this point, however, it is not clear whether this is a physical effect or an artifact from the simulation method.

The fits work similarly well with the same sets of parameters when comparing to CONEX simulations for  $E_{\text{min}} = 10^{14}$  and  $10^{16}$  eV, indicating that an interpolation works for each of the three fireball parameters  $E_{\text{min}}$ ,  $E_{\text{max}}$ , and  $n$ .

While using the CRMC-derived parameters did not work out, the fit shows that a physically motivated interpolation can be made and that proper scaling relations were derived. This could prove useful in a further analysis involving Auger data.

## 9.2.2 Relative Fluctuations of the Muon Number $\sigma(N_\mu)/\langle N_\mu \rangle$

The presence of fireball interactions would also affect the relative fluctuations of the muon number. In the generational picture of air showers – where each generation is independent of the next – a similar argument as for Eq. 9.7 can be made for fluctuations:

$$\text{var}(N_\mu) = \text{var} \left( N_{\text{tot}} \prod_{i=1}^{k_c} r_i \right) = N_{\text{tot}}^2 \prod_{i=1}^{k_c} [\sigma^2(r_i) + \langle r_i \rangle^2] - N_{\text{tot}}^2 \prod_{i=1}^{k_c} \langle r_i \rangle^2, \quad (9.11)$$

where  $\sigma^2(r_i)$  and  $\langle r_i \rangle$  are the variance and average of the hadronic energy fraction of generation  $i$ , respectively. The second step purely follows from the independence of generations, given a fixed number of generations  $k_c$ . To be able to treat it as a fixed number of generations, we furthermore implicitly assumed independence between the hadronic energy fraction and the multiplicity, such that one can first take into account fluctuations from the hadronic energy fraction. At the moment we ignore the subsequent effect of fluctuations from the multiplicity.

Taking the square root and dividing by the average muon number as given by Eq. 9.7 we get

the relative fluctuations of the muon number as

$$\frac{\sigma(N_\mu)}{\langle N_\mu \rangle} = \sqrt{\prod_{i=1}^{k_c} \left[ \left( \frac{\sigma(r_i)}{\langle r_i \rangle} \right)^2 + 1 \right]} - 1. \quad (9.12)$$

If one now sticks to the assumption of an equal division of energy over the secondaries, the hadronic energy fraction fluctuations  $\sigma(r_i)$  at generation  $i$  is suppressed by the square root of the number of particles at that generation  $\sqrt{N_i} = \sqrt{E_0/E_i}$ . This explicitly shows that the first few interactions dominate the fluctuations in the muon number.

Motivated by the simulations performed for Sec. 9.1.1 it seems reasonable to approximate the distribution of hadronic energy fractions of individual interactions to be independent of the projectile energy, for both the fireball and the Standard Model case. Then the only energy dependence originates from the probability  $p(E)$  of producing a fireball. This implies an effective hadronic energy fraction as in Eq. 8.1 for individual interactions induced by a projectile with energy  $E$ . Consequently, from the properties of the variance and average we have

$$\frac{\sigma^2(r_{\text{eff}})}{\langle r_{\text{eff}} \rangle^2} = \frac{(1-p)\sigma^2(r_{\text{SM}}) + p\sigma^2(r_{\text{fb}}) + p(1-p)[\langle r_{\text{fb}} \rangle - \langle r_{\text{SM}} \rangle]^2}{[(1-p)\langle r_{\text{SM}} \rangle + p\langle r_{\text{fb}} \rangle]^2}, \quad (9.13)$$

where we suppressed the  $E$  in  $p \equiv p(E)$  for readability.

Plugging this back into Eq. 9.12 and using the energy-dependent fireball probability of Eq. 5.3, we obtain an analytic model for the relative muon fluctuations. At low energies these fluctuations are approximately constant at a plateau corresponding to SM interactions, and at high energies – where the first few interactions produce only fireballs – a second (lower) plateau is reached. Since the later interactions only provide consecutively smaller corrections, one can – as a first approximation – only take into account the first interaction, see the blue line in Fig. 9.10. From a comparison with EPOS-LHC CONEX simulations this seems a good approximation for  $n = 1$ , but the associated step for  $n = 1000$  is too abrupt. Including later generations provides an overall increase to the relative fluctuations and introduces additional step features for  $n = 1000$ , see the green line in Fig. 9.10. The size of this correction is determined by the suppression from the assumed (effective) multiplicity, taken to be  $n_{\text{mult}} = 5$  for this visualization. The additional step features have the potential of reproducing the observed energy dependence above  $E_{\text{max}} = 10^{18}$  eV, but the abrupt nature of these steps – which is a consequence of the discrete product – seems rather unphysical.

Instead, one can attempt to make the generations continuous, as done for the average muon number in Sec. 8.1. Physically, this could take into account the inelasticity of interactions in real air showers by letting particles directly below the primary energy contribute to the observable. Taking the logarithm of the product in Eq. 9.12 and promoting the obtained sum to an integral gives:

$$\frac{\sigma(N_\mu)}{\langle N_\mu \rangle} = \sqrt{\exp \left[ \int_0^{k_c} \log \left( 1 + \left( \frac{\sigma(r_{\text{eff}})}{\langle r_{\text{eff}} \rangle} \right)^2 \frac{E}{E_0} \right) dk + \Delta_{\text{corr}} \right]} - 1. \quad (9.14)$$

Here we expressed the moments of the generational hadronic energy fractions  $r_i$  in terms of those of the effective ones for the individual collisions  $r_{\text{eff}}$  by including the particle suppression

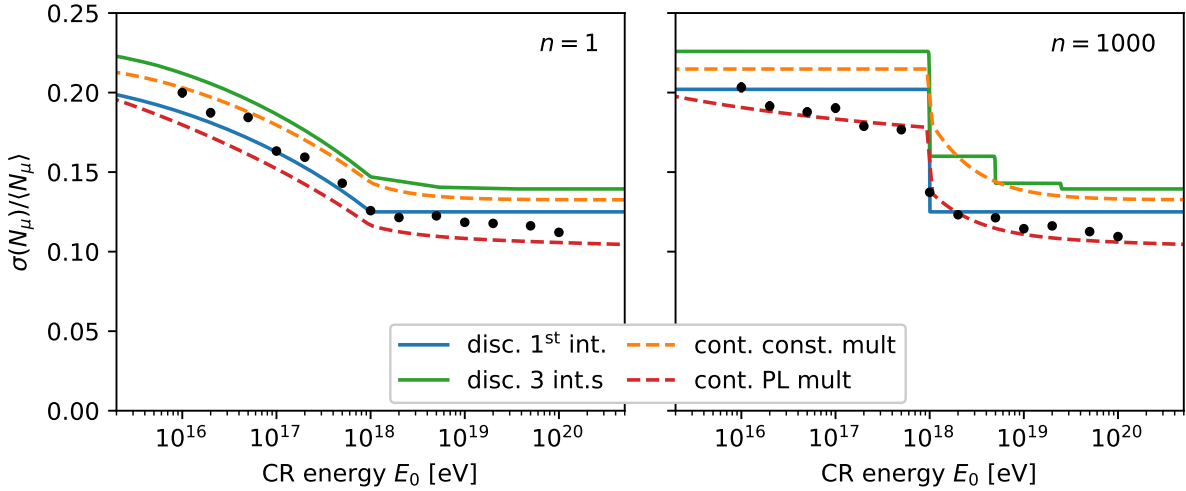


**Figure 9.10:** Comparison between EPOS-LHC CONEX simulations (black points) and various analytical models (legend; see text) for the relative fluctuations of the muon number. Both plots correspond to a fireball scenario with  $E_{\min} = 10^{15}$  eV and  $E_{\max} = 10^{18}$  eV, but they differ in  $n$ : 1 (left) and 1000 (right). Parameters used for the model lines are:  $\langle r_{\text{SM}} \rangle = 0.7$ ;  $\langle r_{\text{fb}} \rangle = 0.8$ ;  $\sigma^2(r_{\text{SM}}) = 0.02$ ;  $\sigma^2(r_{\text{fb}}) = 0.01$ ;  $n_{\text{mult}} = 5$ ;  $b = 0.2$ ;  $n_{\text{scale}} = 0.5$ ;  $E_{\text{scale}} = 10^9$  eV.

term  $1/N = E/E_0$ . Furthermore, we defined a correction factor  $\Delta_{\text{corr}}$  to take into account the difference between the sum and the integral, which is necessary given the discrete nature of interactions. The value that this factor takes is not trivial, but inspired by the discussion of Sec. 8.1.1 we take it as half a generation and thus as half the integrand evaluated at the first interaction

$$\Delta_{\text{corr}} = \frac{1}{2} \cdot \log \left[ 1 + \left( \frac{\sigma(r_{\text{eff}})}{\langle r_{\text{eff}} \rangle} \right)^2 \right], \quad (9.15)$$

where the ratio of moments given by Eq. 9.13 is evaluated at  $E = E_0$ .

To solve the integral we need to perform a change of variables such that we can integrate over the energy of the shower particles, as was also done in Secs. 8.1 and 8.2. The Jacobian depends on the multiplicity, with  $dk/d \log E = -1/\log(n_{\text{mult}})$  for a constant multiplicity and Eq. 8.13 for a power-law multiplicity. Evaluating these integrals numerically, we obtain the relative fluctuations shown by the dashed lines in Fig. 9.10. In both cases, a smooth energy dependence above  $E_{\max} = 10^{18}$  eV is obtained. Interestingly, for the power-law case (PL; red-dashed) with  $n = 1000$ , also below  $E_{\max} = 10^{18}$  eV an energy dependence is introduced. The latter seems to accurately reproduce the behavior of the simulations.

Sticking to the power-law multiplicity case and leaving the parameters  $\{\langle r_{\text{SM}} \rangle, \langle r_{\text{fb}} \rangle, \sigma(r_{\text{SM}}), \sigma(r_{\text{fb}}), b, n_{\text{scale}}\}$  free to vary, we fitted this model to the relative fluctuations from EPOS-LHC CONEX simulations for the region of phase-space where  $E_{\min} = 10^{15}$  eV,  $E_{\max} \in \{10^{17}, 10^{18}, 10^{19}, 10^{20}\}$  eV, and  $n \in \{1, 2, 4, 8, 1000\}$ . The results are shown in Fig. 9.11.

At this point it is worth noting that the general behavior of the fireball model is to decrease the relative muon fluctuations. This is not per se a trivial result, but can be understood within our analytic model. From Eq. 9.12 we see that the relative muon fluctuations is a direct reflection

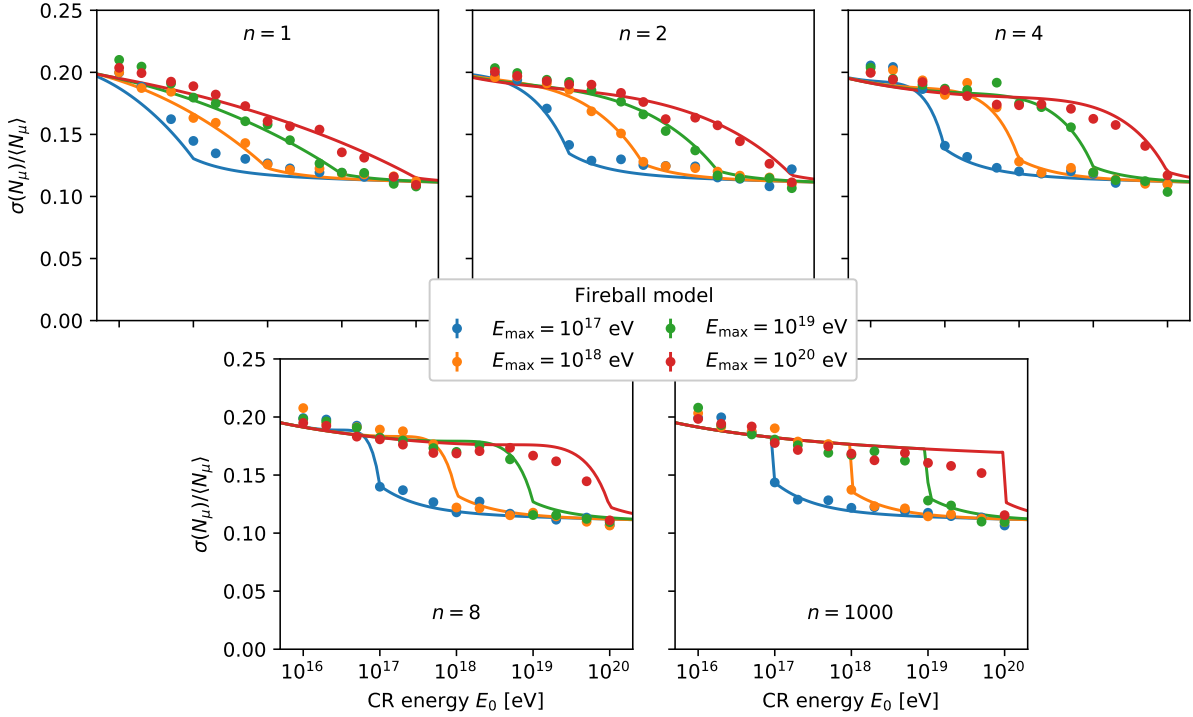


**Figure 9.11:** Simultaneous fit of Eq. 9.14 with a power-law multiplicity (solid lines) to fireball-extended EPOS-LHC CONEX simulations (error bars), for  $E_{\text{min}} = 10^{15}$  eV, and various values of  $E_{\text{max}}$  (colors) and  $n$ : 1 (top left), 2 (top center), 4 (top right), 8 (bottom left), 1000 (bottom right). The fit parameters are:  $\langle r_{\text{SM}} \rangle = 0.7458$ ,  $\langle r_{\text{fb}} \rangle = 0.9294$ ,  $\sigma^2(r_{\text{SM}}) = 0.02506$ ,  $\sigma^2(r_{\text{fb}}) = 0.01698$ ,  $b = 0.3413$ ,  $n_{\text{scale}} = 0.07897$ , with  $E_{\text{scale}} = 1$  GeV.

of the relative fluctuations of the hadronic energy fraction of the first interaction  $\sigma(r_1)/\langle r_1 \rangle$ , with later generation being suppressed. Then a decrease can be expected since the fireball model enhances  $\langle r_1 \rangle$ , while not necessarily enhancing  $\sigma(r_1)$ . In fact, one might even expect a suppression of  $\sigma(r_1)$  since  $r$  is bounded from above by unity and  $\langle r_1 \rangle$  already exceeds 0.5 in the Standard Model.

While the overall behavior of the fit in Fig. 9.11 seems to reproduce the simulations, it consistently underestimates the fluctuations at low energies. This could indicate that the energy dependence for the pure Standard Model case (e.g., below  $E_{\text{max}}$  for  $n = 1000$ ) does not completely arise from the introduction of the power-law multiplicity. Instead, it seems necessary to introduce a (logarithmic) energy dependence of the fluctuations and/or average of the hadronic energy fractions  $r_{\text{SM}}$  and  $r_{\text{fb}}$ . Looking at Fig. 9.1, this is not unheard of, but will strongly depend on the hadronic interaction model.

Extending our fit by parametrizing the variances in Eq. 9.13 with a logarithmic energy dependence – i.e.,  $\sigma^2 = \alpha - \beta \log_{10}(E/\text{GeV})$  – the agreement with CONEX simulations improves significantly, as shown in Fig. 9.12. For later reference we also included data from Auger. The other hadronic interaction models QGSJETII-04 and SIBYLL-2.3D allow for a similarly good fit for different sets of parameters, see Appendix E.1. The three sets of parameters are summarized in Table 9.4. While these parameters were fitted for a fixed  $E_{\text{min}} = 10^{15}$  eV, the agreement with

CONEX simulations for  $E_{\min} = 10^{14}$  eV and  $10^{16}$  eV is still very good, indicating that the fit constitutes an interpolation for each of the fireball parameters  $E_{\min}$ ,  $E_{\max}$ , and  $n$ .

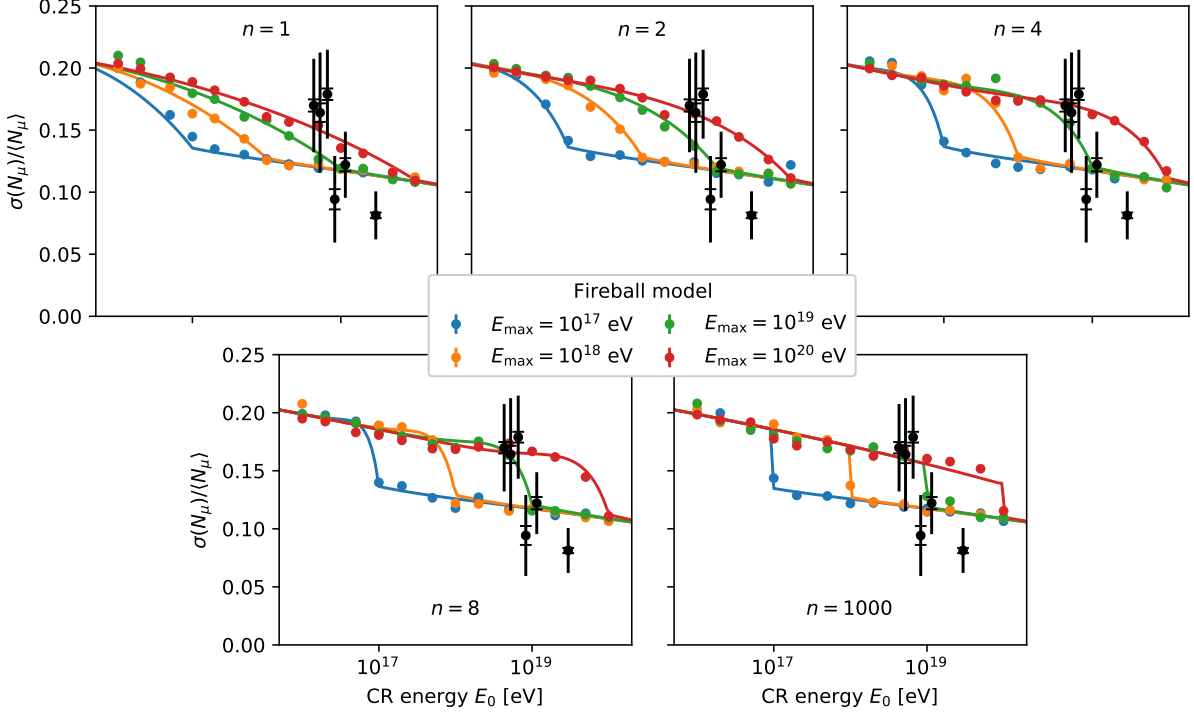


**Figure 9.12:** Same as Fig. 9.11, but the variances of the hadronic energy fractions in the Standard Model  $\sigma^2(r_{\text{SM}})$  and fireball model  $\sigma^2(r_{\text{fb}})$  were parametrized with a logarithmic energy dependence:  $\sigma^2 = \alpha - \beta \log_{10}(E/\text{GeV})$ . This propagates to the relative muon number through consecutively Eqs. 9.13 and 9.14. For later reference also Auger data is shown (black error bars). The fit parameters are summarized in Table 9.4.

**Table 9.4:** Fit parameters for an accurate description – i.e., agreeing with CONEX simulations – of the relative muon fluctuations using Eqs. 9.13, 9.14, and 9.15. Note that these are not completely consistent with the parameters of Table 9.3. This could have many causes due to the various simplifications w.r.t. real air showers. Maybe by including the two further energy dependencies of  $\langle r_{\text{SM}} \rangle$  and  $\langle r_{\text{fb}} \rangle$  – in both the model for  $\sigma(N_{\mu})/\langle N_{\mu} \rangle$  and in that for  $\langle N_{\mu} \rangle$  – a better consistency of the common parameters could be obtained. The variances of the hadronic energy fractions are parametrized as  $\sigma^2 = \alpha - \beta \log_{10}(E/\text{GeV})$ .

	$\langle r_{\text{SM}} \rangle$	$\langle r_{\text{fb}} \rangle$	$\sigma^2(r_{\text{SM}})$		$\sigma^2(r_{\text{fb}})$		$b$	$n_{\text{scale}}$
			$\alpha$	$\beta$	$\alpha$	$\beta$		
QGSJetII-04	0.6691	0.8404	0.09998	0.001962	0.07428	0.001398	0.001836	51.29
EPOS-LHC	0.5035	0.6433	0.06214	0.001142	0.04279	0.0007186	0.1897	2722
Sibyll-2.3d	0.5314	0.6584	0.06633	0.001171	0.05268	0.0008971	0.1772	2429

### 9.3 Interpretation of Auger Data

So far we only considered proton-induced EASs. For the interpretation of Auger data it is necessary to implement a mass dependence, such that one can take into account the composition that is folded within the data. Furthermore, if one assumes the currently derived composition from  $X_{\max}$ -data to be correct, the fireball model is not allowed to significantly affect the predictions for  $X_{\max}$ . These two remaining obstacles will be discussed in Sec. 9.3.1 – with in particular a confirmation of the latter from numerical simulations – before a proper interpretation of Auger data can be made in Sec. 9.3.2.

#### 9.3.1 Mass Dependence and Effect on $X_{\max}$

In the Heitler-Matthews model the mass dependence of the (average) muon number is obtained by invoking the superposition principle, which states that a CR with  $A$  nucleons produces  $A$  times the number of muons as a proton CR  $A$  times lower in energy:

$$N_{\mu}(E_0, A) = A \cdot N_{\mu}(E_0/A, 1) . \quad (9.16)$$

As mentioned in Sec. 2.3, this principle only holds on average due to a nontrivial alignment of cross sections and the number of wounded nucleons. The production of a plasma in a real fireball likely breaks this alignment, but whether that is also the case when only swapping pions and kaons is not trivial.

The mass dependence of fireball showers initiated by 10 EeV CRs is shown in Fig. 9.13. The error bars represent EPOS-LHC CONEX simulations, while the solid lines follow from the application of the superposition principle to Eq. 8.16 with the EPOS-LHC parameters of Table 9.3.

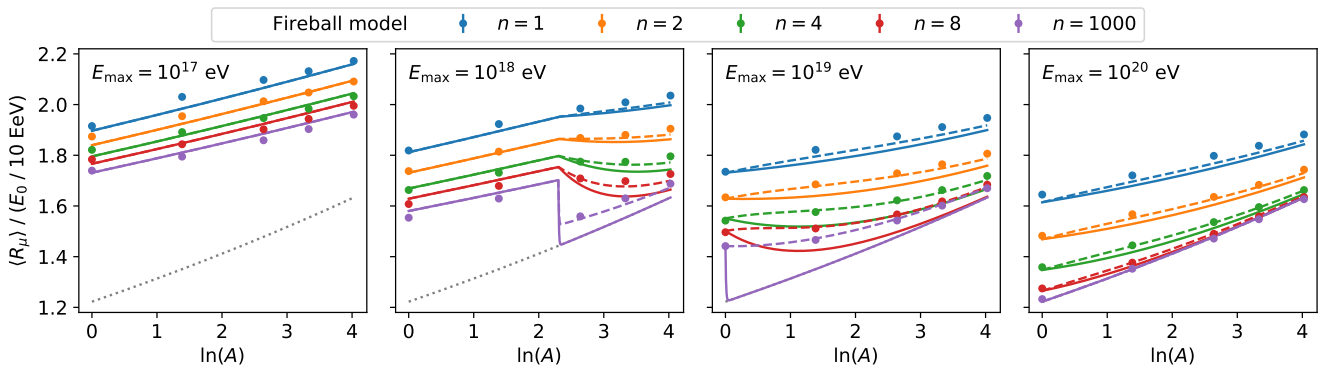


**Figure 9.13:** CR mass dependence  $A$  of the average muon number  $\langle R_{\mu} \rangle$  of 10 EeV CR air showers for various fireball settings:  $E_{\min} = 10^{15}$  eV,  $E_{\max}$  (plots), and  $n$  (colours). The error bars correspond to EPOS-LHC CONEX simulations. Using Eq. 8.16 – with the parameters of Table 9.3 – for proton primaries, the solid lines follow from an application of the superposition principle (Eq. 9.16) and the dashed lines from a corrected version of the superposition principle (Eq. 9.17).

The purple line ( $n = 1000$ ) in the rightmost plot ( $E_{\max} = 10^{20}$  eV) – for these fireball parameters a 10 EeV CR shower contains no fireballs – shows that the superposition principle is accurate in the Standard Model case. The other solid lines in the same plot as well as

all lines in the leftmost plot also show a reasonable agreement with the CONEX simulations. Only the central two plots exhibit some significant deviation from a simple application of the superposition principle, with in particular the sharp drop of the solid purple line for  $E_{\max} = 10^{19}$  eV not reproduced by the CONEX simulations.

The sharp drop is expected from the superposition principle since  $E_0/A$  falls below  $E_{\max} = 10^{19}$  eV for any  $A$  exceeding one and therefore abruptly stops producing fireballs for nuclei larger than proton. However, for the current implementation of the fireball model in CONEX simulations we assume that the total energy of the CR nucleus rather than that of the individual nucleons is decisive for activating a fireball.<sup>4</sup> Therefore, the simulations also produce fireballs in the first interaction for CRs heavier than proton. In such a first interaction, a fraction  $s$  of the CR nucleons remains intact after scattering off the atmospheric nucleus (so-called spectator nucleons), while the remainder  $1 - s$  undergo an inelastic scattering and – due to the fireball – has its fraction of pions and kaons swapped. The unscathed scattered nucleons can be expected to comply with the superposition principle, but the inelastically scattered nucleons obtain an additional fireball-enhancement of the muon number.

The size of this fireball-enhancement depends on the difference between the fireball probability of the complete nucleus  $p(E_0)$  and that of the individual nucleons  $p(E_0/A)$ , i.e., enhancing the fireball probability by  $\Delta p \equiv p(E_0) - p(E_0/A)$ . Associated with this probability is then a factor  $(r_{\text{fb}}/r_{\text{SM}})^{\Delta p/2}$  for the muon number<sup>5</sup>, where the square root originates from the necessity to take into account the elasticity of the first interaction by only affecting half a generation. This is similar to what has been done in Sec. 8.1.1 to take into account discrete interactions. In fact, this correction factor mathematically corresponds to revising  $\Delta_{\text{disc}}$  (Eq. 8.4) to be taken at the energy of the nucleus rather than the nucleons.

The fraction  $s$  of spectator nucleons grows with the size of the CR nucleus. A detailed calculation would involve the Glauber model, but we found a good agreement with EPOS-LHC CONEX simulations when taking  $s = 1 - 1/\sqrt{A}$ , i.e., the number of wounded nucleons scaling as  $\sqrt{A}$ .

Putting everything together we obtain a correction factor to the superposition principle, giving:

$$N_{\mu}(E_0, A) = A \cdot N_{\mu}(E_0/A, 1) \left[ 1 - 1/\sqrt{A} + 1/\sqrt{A} \cdot (r_{\text{fb}}/r_{\text{SM}})^{\Delta p/2} \right] \quad (9.17)$$

The effect of this correction factor is shown by the dashed lines in Fig. 9.13, which resolves the aforementioned disagreements in the central two plots. While the same factor also significantly improves the agreement for the other hadronic interaction models QGSJETII-04 and SIBYLL-2.3D, as shown in Appendix E.2, the enhancement for  $E_{\max} = 10^{18}$  eV seems insufficient. Taking this into account is beyond the scope of this study and the question remains whether the fireball treatment of the CONEX simulations themselves is more physical than a simple application of the (extended) superposition principle. Therefore we stick to this mass dependence extension to Eq. 8.16 to predict the average muon number for a given set of fireball parameters.

The mass dependence of the relative fluctuations of the muon number is rather complicated even in the Standard Model case [204], and we therefore do not attempt to extend this formalism

<sup>4</sup>Whether this assumption holds depends on the details of the fireball model.

<sup>5</sup>Technically the appropriate factor would be of the form  $\exp[\log(r_{\text{SM}} + p(E_0)(r_{\text{fb}} - r_{\text{SM}}))/2 - \log(r_{\text{SM}} + p(E_0/A)(r_{\text{fb}} - r_{\text{SM}}))/2]$ , but due to the range of  $p(E)$  this can be well approximated by geometric averaging as shown in App. D.2, Fig. D.2.1.

for the fireball model.

Regarding the effect of the fireball model on  $X_{\max}$ , Fig. 9.14 shows it to be negligible for both moments  $\langle X_{\max} \rangle$  and  $\sigma(X_{\max})$  and each of the hadronic interaction models. Differences between the various fireball settings translate to at most a few grams difference in the moments, but these could also be caused by a finite set of Monte Carlo simulations and the presence of outliers. In particular, the  $\sigma(X_{\max})$  of iron-induced showers for EPOS-LHC shows some variations among the fireball models, but not sufficient to significantly change the average over all fireball settings. Therefore it seems safe to conclude that  $X_{\max}$  can be modeled with Standard Model simulations and thereby determine the mass composition that the muon number needs to adhere to.

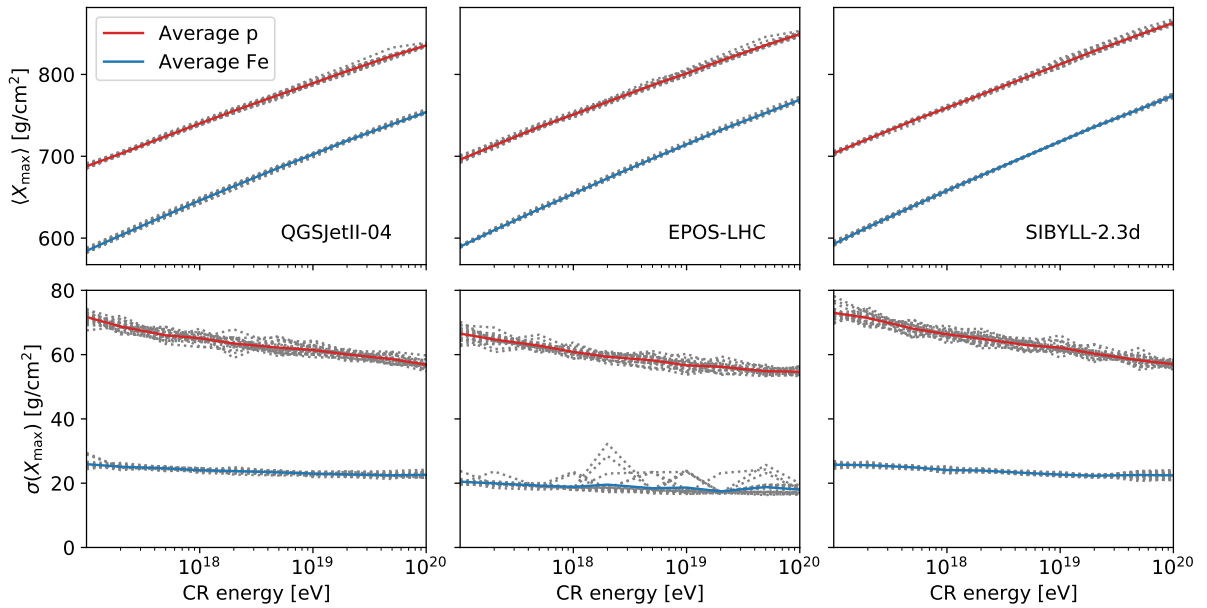


**Figure 9.14:** The effect of the fireball model on the moments of  $X_{\max}$ ;  $\langle X_{\max} \rangle$  (top row) and  $\sigma(X_{\max})$  (bottom row), for the three hadronic interaction models QGSJETII-04 (left), EPOS-LHC (middle), SIBYLL-2.3D (right) based on CONEX simulations. The individual fireball settings ( $E_{\min} = 10^{15}$  eV;  $E_{\max} \in \{10^{17}, 10^{18}, 10^{19}, 10^{20}\}$  eV;  $n \in \{1, 2, 4, 8, 1000\}$ ) are indicated by the gray dotted lines, and the average of all correspond to the red (proton) and blue (iron) solid lines.

### 9.3.2 Constraints on the Fireball Model

The obtained analytic model for  $\langle R_{\mu} \rangle(E_0, A; E_{\min}, E_{\max}, n)$ , can be used to look for fireball parameters that provide a consistent interpretation of Auger data on  $\langle X_{\max} \rangle$  and  $\langle R_{\mu} \rangle$  in terms of the CR mass composition. Since  $\langle X_{\max} \rangle$  is unaffected by the fireball model, its mass composition can be inferred with the Standard Model. Subsequently, this puts a requirement on the amount the model predictions for  $\langle R_{\mu} \rangle$  needs to change, and thus constrains the fireball parameters.

The composition interpretation of  $\langle X_{\max} \rangle$ -data is shown in the left plot of Fig. 9.15 for EPOS-LHC <sup>6</sup>. Here, for each of the masses, the energy dependence of the  $\langle X_{\max} \rangle$  model pre-

<sup>6</sup>Equivalent Figs. for the hadronic interaction models QGSJETII-04 and SIBYLL-2.3D are shown in Appendix E.3

diction is very well approximated by a power law. This allows for a direct interpolation to the energies corresponding to the Auger data points. The analogous interpolation of  $\langle R_\mu \rangle$  to these energies follows from our analytic model, as shown in the right plots of Fig. 9.15. Then requiring  $\langle X_{\max} \rangle_{\text{data}} = \sum_i f_i \langle X_{\max} \rangle_i$  we can obtain a corresponding  $\langle R_\mu \rangle_{\langle X_{\max} \rangle_{\text{data}}} = \sum_i f_i \langle R_\mu \rangle_i$  by implicitly solving for the composition fractions  $f_i$  with  $i \in \{p, \text{He}, \text{N}, \text{Si}, \text{Fe}\}$ .

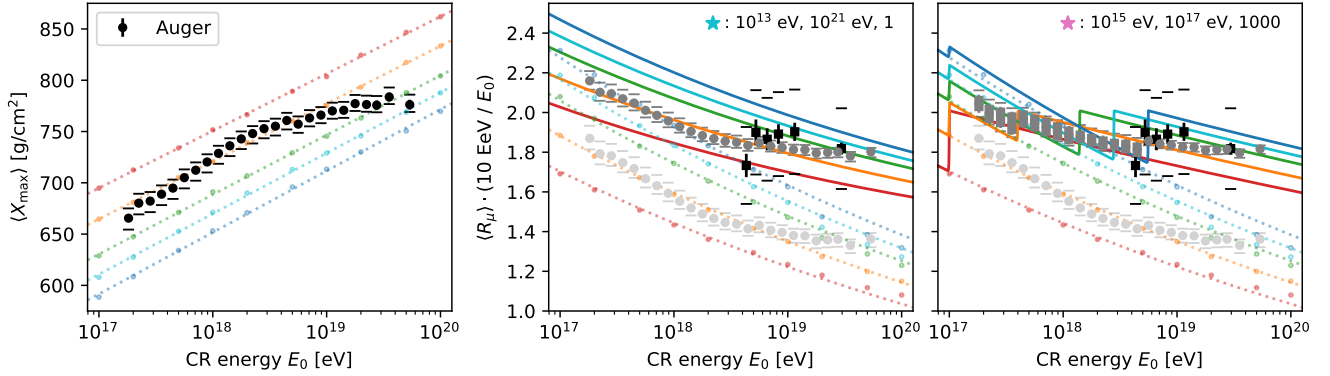


**Figure 9.15:** Indications of the UHECR composition from Auger data on  $\langle X_{\max} \rangle$  (left) and  $\langle R_\mu \rangle$  (center and right) for EPOS-LHC. The fireball model (solid lines) has no effect on  $\langle X_{\max} \rangle$ , data on which (black error bars) can thus be interpreted within the Standard Model (dotted lines). In the two right plots a direct comparison with  $\langle R_\mu \rangle$ -data (black error bars) follows from mapping  $\langle X_{\max} \rangle$ -data to  $\langle R_\mu \rangle$  within the Standard Model (light gray error bars) and two fireball scenarios (dark gray error bars):  $E_{\min} = 10^{13}$  eV,  $E_{\max} = 10^{21}$  eV and  $n = 1$  (center), and  $E_{\min} = 10^{15}$  eV,  $E_{\max} = 10^{17}$  eV and  $n = 1000$  (right). The line colors correspond to various nuclei: proton (red), helium (orange), nitrogen (green), silicon (cyan), and iron (blue).

Due to the degeneracy of these sums with regard to the precise composition a *range* of  $\langle R_\mu \rangle_{\langle X_{\max} \rangle_{\text{data}}}$  values can be obtained, corresponding to various mixed compositions. The linearity of the sums assures that the extremes of this range is composed of at most two fractions, which significantly simplifies its calculation. The resulting interpretation of  $\langle X_{\max} \rangle$ -data in terms of  $\langle R_\mu \rangle$  are indicated by the (light) gray data points in the right two plots of Fig. 9.15, corresponding to particular settings of the fireball (standard) model. Notice in particular the *range-behavior*<sup>7</sup> for the fireball in the rightmost plot.

A direct comparison with the average muon data  $\langle R_\mu \rangle$  quantifies the degree of consistency between these independent mass observables. Various settings of the fireball model provide a perfect agreement, where one can distinguish between two extremes: either the fireball effect kicks in at low energies  $E_{\text{CR}} \sim O(10^{13}$  eV) which gradually increases the muon number throughout the entire shower (middle panel of Fig. 9.15), or the fireball effect is abruptly activated at  $E_{\text{CR}} = 10^{17}$  eV and occurs only in the first few interactions (right panel of Fig. 9.15). Both scenarios accurately reproduce Auger muon data above  $E_{\text{CR}} \gtrsim 4 \cdot 10^{18}$  eV of highly inclined EAS events.

Note that in the abrupt threshold scenario the model predictions for the individual masses jump at specific energies: at  $E_0 = E_{\max}$  where the fireball is activated for protons and larger nuclei can partly undergo the fireball effect (see Eq. 9.17), and at  $E_0 = A \cdot E_{\max}$  where the

<sup>7</sup>i.e., that a range of  $\langle R_\mu \rangle$ -values correspond to the same  $\langle X_{\max} \rangle$ -value due to degeneracies in the composition.

individual nucleons have sufficient energies to produce fireballs.

To quantify the agreement provided by particular fireball settings we define the chi-squared statistic

$$\chi^2(E_{\min}, E_{\max}, n) \equiv \sum_{i=1}^6 \left( \frac{\langle R_{\mu} \rangle_{\langle X_{\max} \rangle_{\text{data}}}(E_i; E_{\min}, E_{\max}, n) - \langle R_{\mu} \rangle_{\text{data},i}}{\delta \langle R_{\mu} \rangle_{\text{data},i}} \right)^2, \quad (9.18)$$

where the sum is over the six muon data points and the interpolation of  $\langle R_{\mu} \rangle_{\langle X_{\max} \rangle_{\text{data}}}(E_i; E_{\min}, E_{\max}, n)$  to the corresponding energies follows from a linear interpolation in  $\log E$ . The uncertainty on  $\langle X_{\max} \rangle$ -data is neglected and that on the muon data is taken to be the quadratic sum of the systematic and statistical uncertainties:

$$\delta \langle R_{\mu} \rangle_{\text{data},i} = \sqrt{\delta \langle R_{\mu} \rangle_{\text{syst},i}^2 + \delta \langle R_{\mu} \rangle_{\text{stat},i}^2}. \quad (9.19)$$

Dividing  $\langle R_{\mu} \rangle$  by the CR primary energy  $E_0$  as seen in Fig. 9.15 would be cancelled out by the uncertainties in the computation of  $\chi^2$  through Eq. 9.18, and is therefore unnecessary.

For the exploration of the fireball parameter space we fix  $n \in \{1, 2, 4, 8, 1000\}$  and vary  $10^{12} \leq E_{\min}/\text{eV} \leq 10^{18}$  and  $10^{16} \leq E_{\max}/\text{eV} \leq 10^{22}$ . Contour plots of the resulting  $\chi^2$  for EPOS-LHC are shown in Fig. 9.16, with the stars corresponding to the settings of Fig. 9.15. The equivalent plots for QGSJETII-04 and SIBYLL-2.3D are left to Appendix E.3 since the conclusions are the same.

At every  $n$  we find a line of  $(E_{\min}, E_{\max})$ -combinations that minimize the chi-squared to approximately  $\chi_{\min}^2 \approx 0.4$ , indicating a very good agreement. Increasing  $n$  beyond 1 – i.e., a faster than logarithmic increase with energy of the probability to initiate a fireball – forces the minimum  $\chi^2$  to correspond to lower  $E_{\max}$  values, with at  $n = 1000$  the minimum  $\chi^2$  fixed to  $E_{\max} = 10^{17}$  eV, independent of  $E_{\min}$ . This is a direct consequence of the requirement to reproduce the elevated plateau of muon numbers seen in Auger data (see Fig. 9.15) and thus to deviate from the Standard Model at sufficiently low energies.

From Fig. 9.16 it becomes apparent that the average muon data only provides a single constraint on the fireball parameters. A further constraint comes from the relative fluctuations of the muon number, for which we developed a theoretical model in Sec. 9.2.2. Here we in particular noticed that the introduction of a fireball decreases the relative fluctuations. This could potentially give rise to problems with the current consistency between  $\sigma(R_{\mu})/\langle R_{\mu} \rangle$ - and  $\langle X_{\max} \rangle$ -data [5], and thus shift the muon problem to its fluctuations.

While in Sec. 9.2.2 we were able to obtain  $\sigma(N_{\mu})/\langle N_{\mu} \rangle$ -predictions for proton primaries, an extension to heavier nuclei is not trivial and beyond the scope of this study. To still incorporate the constraints provided by data on the relative muon fluctuations we require the proton predictions to not fall more than one sigma below Auger data. This can be interpreted as a rather strict requirement since we know from  $\langle X_{\max} \rangle$ -data that the composition is in fact heavier than proton at these energies, and thus would correspondingly imply even lower fluctuations.

From Fig. 9.12 we see that our requirement on the fluctuations translates to a lower limit on  $E_{\max}$ . Using the theoretical model (Eqs. 9.13, 9.14, and 9.15 and Table 9.4) to interpolate the proton fluctuation predictions, we obtain these lower limits on  $E_{\max}$  for each data point and as a function of  $E_{\min}$  and  $n$ . The bounds are indicated by lines in Fig. 9.16, where the number of dots  $j = i - 1$  between the dashes identifies the  $i^{\text{th}}$  Auger data point on the relative fluctuation

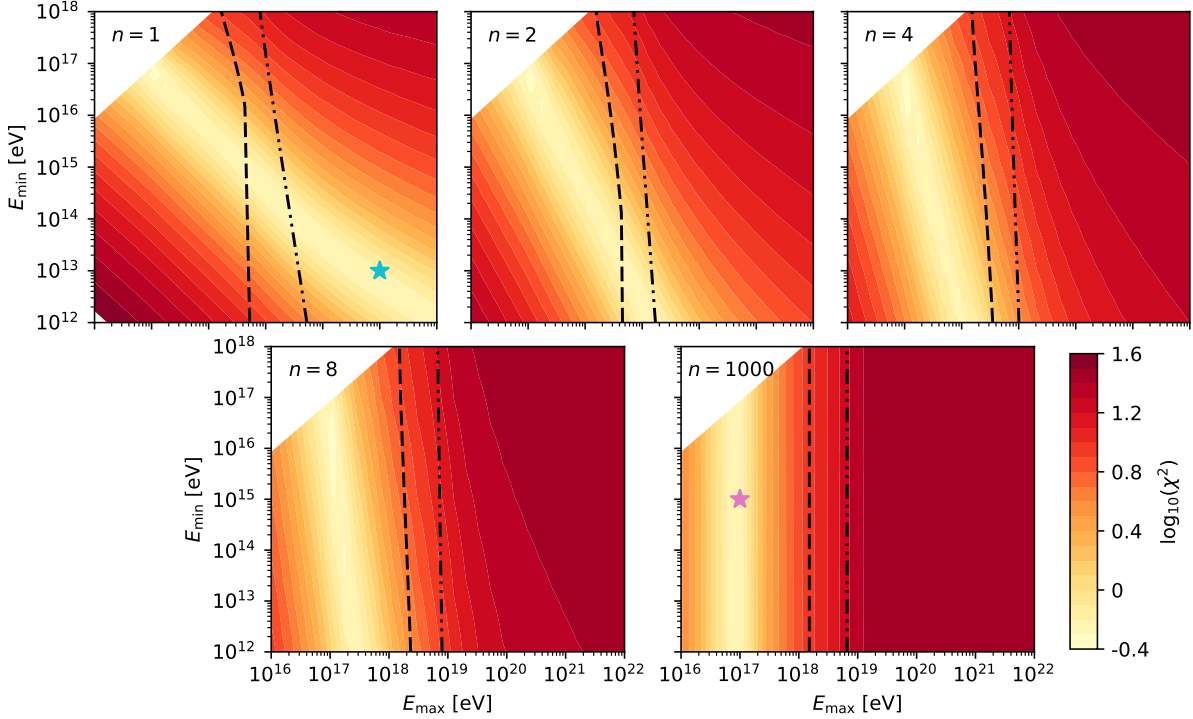


**Figure 9.16:** Fireball parameter-space exploration of the compatibility of the composition interpretation of Auger data on  $\langle X_{\max} \rangle$  and  $\langle R_{\mu} \rangle$  as quantified by the test statistic  $\chi^2$  (Eq. 9.18) for EPOS-LHC. A lower  $\chi^2$  implies a better compatibility. The inset stars correspond to the central (cyan) and right (purple) plots in Fig. 9.15. The black lines are lower limits on  $E_{\max}$  required by data on the muon fluctuations.

in Fig. 9.12. Fireball settings to the left of these lines can be assumed to be excluded by Auger data on the relative muon fluctuations.

Interestingly, this excludes a large fraction of the fireball phase-space that resolves the tension between  $\langle X_{\max} \rangle$  and  $\langle R_{\mu} \rangle$ . In particular, rather abrupt changes in the hadronic energy fraction (e.g.,  $n = 1000$ , purple star) are excluded, but not a gradual introduction of the fireball effect (e.g.,  $n = 1$ , cyan star). This is in line with the conclusions drawn in [5] that the muon enhancement cannot originate solely from the first (few) interactions and needs to accumulate throughout the shower. Note that this inversely requires an effect to start at low energies in order to accumulate a sufficient deviation from the Standard Model.

Taking the data on muon fluctuations to exclude any values of  $n$  other than unity, we explicitly solve for the  $(E_{\min}, E_{\max})$ -combinations<sup>8</sup> that minimize  $\chi^2$  and thus resolve the muon deficit. The resulting optimal fireball parameters for each of the hadronic interaction models are shown in the left plot of Fig. 9.17. The range of  $E_{\max}$  is purposefully chosen to start at  $10^{18}$  eV to mostly comply with the fluctuation constraints, with settings up to  $E_{\max} = 10^{20}$  eV still being

<sup>8</sup>Note that for some of the combinations  $E_{\min}$  falls below  $E_c$ . This violates the assumption made in Appendix D.2 for the derivation of Eq. 8.16. To make sure that the fireball enhancement stops at the end of the shower, we need the additional factor  $(E_c/E_{\min})^\omega$ , with  $\omega = p(E_c)/(n+1) {}_2F_1(1, 1+n; 2+n; -\log(E_c/E_{\min})/x_{\min})$ .

debatable. Differences between the EPOS-LHC and SIBYLL-2.3D hadronic interaction models seem to be negligible, while QGSJETII-04 consistently requires a larger fireball effect at lower energies. The latter is to compensate for the lower muon numbers predicted by the QGSJETII-04 hadronic interaction model.

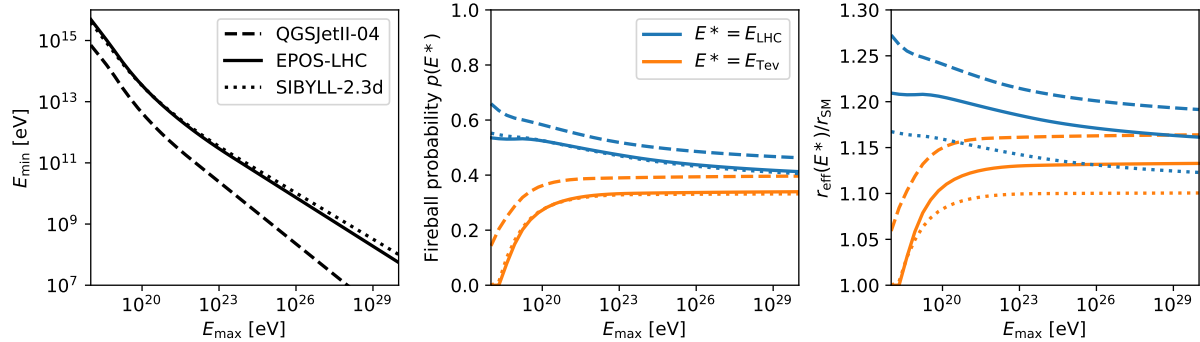


**Figure 9.17:** *Left:* Fireball settings resolving the muon deficit without violating constraints from the muon fluctuations (i.e.,  $E_{\max} \gtrsim 10^{19}$  eV). *Center and right:* Conversion of these fireball settings to the fireball-initiation probability (center, Eq. 5.3) and effective enhancement of the hadronic energy fraction (right, Eq. 8.1) at LHC (blue,  $E_{\text{LHC}} \approx 10^{17}$  eV) and Tevatron (orange,  $E_{\text{TeV}} \approx 10^{15}$  eV) energies.

An equally good resolution of the muon deficit is possible by continuously extending the range over which the fireball becomes more likely and thus making its introduction more gradual. This does not necessarily imply that deviations of the hadronic energy fraction from its Standard Model value can be made arbitrarily small since the number of generations in an EAS is limited by the multiplicity and the critical energy. Therefore it is worthwhile to convert these  $(E_{\min}, E_{\max})$ -combinations to explicit fireball probabilities (Eq. 5.3) at some relevant energies.

In the central plot of Fig. 9.17 we do so for LHC ( $\sqrt{s_{\text{LHC}}} = 13$  TeV  $\Leftrightarrow E_{\text{LHC}} = 8.45 \cdot 10^{16}$  eV) and Tevatron ( $\sqrt{s_{\text{TeV}}} = 2$  TeV  $\Leftrightarrow E_{\text{TeV}} = 2 \cdot 10^{15}$  eV) energies, where collider experiments might be able to put constraints. A further conversion (Eq. 8.1) to the corresponding effective increase in the hadronic energy fraction with respect to the Standard Model is shown in the right plot of Fig. 9.17. Both plots show a similar behavior, with only the latter conversion breaking the degeneracy between EPOS-LHC and SIBYLL-2.3D.

Only for the lowest allowed values of  $E_{\max}$  may fireball effects be invisible at the Tevatron. For all larger  $E_{\max}$  values – more compatible with the fluctuations – the effect is always visible: it first increases and subsequently flattens off to an  $O(10 - 15)\%$  increase in the hadronic energy fraction, depending on the hadronic interaction model. At LHC energies an even larger effect can be expected of  $O(15 - 20)\%$ . Interestingly, such large effects on the hadronic are expected for all  $E_{\max}$  values and thus for all viable resolutions of the muon deficit. For QGSJETII-04 the enhancement may even be up to 25% for the lowest allowed  $E_{\max}$  values.

It should be noted that these results follow directly from fits of our analytical model to CONEX EAS simulations. Therefore, it is plausible that some of the parameters attain rather extreme values by compensating for simplifications<sup>9</sup> w.r.t. real EASs. For example, the multiplicities listed in Table 9.3 are nearly constant at  $O(\text{few } 1000)$ , which implies that  $O(2 - 3)$  generations

<sup>9</sup>e.g., the inability to capture inelasticity, which likely also prevented the use of CRMC simulations directly; see the discussion around Fig. 9.8.

are already sufficient to reach the critical energy. This likely gives an artificial enhancement of the aforementioned required sizes of the fireball effect. To compensate for this, one can take, e.g., the third or fourth root of  $r_{\text{eff}}(E^*)/r_{\text{SM}}$  – such that the number of generations is increased by a factor 3 or 4. Consequently, more realistic resolutions of the muon deficit follow from enhancements of the hadronic energy fraction (w.r.t. its SM-value) that lie in the range  $O(3 - 8)\%$  at Tevatron and LHC energies.

### Discussion

These results show that Auger data indicates that we do not completely understand the for EASs relevant particle physics at energies accessible to the current generation of colliders. This motivates further accelerator experiments, in particular those that can probe an effective  $r$ -value.

We found here that the strangeness enhancement resulting from a swapping of pions and kaons – as applied for the mimicking of the fireball – is sufficient to resolve the muon deficit. Therefore, it would be particularly interesting to see if the strangeness signatures found by the ALICE experiment can also be observed at forward rapidities. One contribution to investigating this could come from the planned Forward Physics Facility [205] by providing (indirect) measurements of the pion to kaon ratio.

A more direct constraint on  $r$ , independent of the strangeness, comes from the LHCf measurements of the neutral pion yield [206, 207]. In particular, the integrated energy-weighted Feynman- $x$  ( $x_F$ ) distribution constitutes a proxy for the energy lost to the EM component,  $1 - r$ . The required  $O(3 - 8)\%$  increase of  $r$  translates into a sizable  $O(10 - 25)\%$  decrease of  $1 - r$  under the assumption of  $r \approx 3/4$ . Whereas it may be that such a difference would have already been apparent with the current LHCf measurements, the integral of this distribution seems to be dominated by secondaries with low  $x_F$ . Their detection is limited by the size of the detector, with no measurements for  $x_F < 0.25$ . Any estimation of  $1 - r$  would rely on an extrapolation. In light of our results, it would thus be important to quantify the associated theoretical uncertainty.

Note that simultaneously looking for strangeness enhancements and studying the neutral pion yield could mediate such inherent phase-space limitations of particle detectors.

In addition to, and potentially more important than, these phase-space considerations is the fact that air shower interactions are not directly represented by proton-proton collisions. Therefore, the required increase of the hadronic energy fraction may only manifest itself when studying collisions of the appropriate beams. Current proposals [208] for future runs of the LHC focus on oxygen beams as an intermediate-mass nucleus to represent interactions with air (see also the discussion in [1]). Ideally, one would go even further and also include charged pion beams to better understand their contribution to the hadronic cascade. Nevertheless, studies of the strangeness and neutral pion production with upcoming  $p - O$  and  $O - O$  runs at the LHC are sure to shed light on the muon deficit.

## 10 | Conclusion

Experimental observations of the number of muons in air showers that reach the ground revealed a corresponding deficit in simulations. A solution to the open problem of interpreting this muon deficit would enable a precise determination of the UHECR mass composition, and thereby have profound consequences for illuminating the origin of UHECRs. In this thesis we set out to explore the potential of the fireball model to appropriately alter current air shower predictions, with a particular focus on reproducing  $X_{\max}$ - and  $R_{\mu}$ -data from the Pierre Auger Observatory.

With the implementation of a phenomenological fireball model in existing EAS simulation software, our initial study (Chapter 6) showed that this model generally reduces the tension of the muon deficit, but the explored phase-space did not provide an immediate resolution. A subsequent systematic analysis (Chapter 7) of the effect of the fireball model on individual observables from 10 EeV showers revealed that the production of a plasma, as mimicked by repeated *in situ* collisions, has an undesirable effect on the longitudinal development. A pure strangeness enhancement, however, enables a consistent mass interpretation of Auger data for specific forms of the fireball-production probability. This result confirmed that the muon deficit can only be resolved with small adjustments over a wide range of energies whose effect on the air shower accumulates over multiple generations.

For a complete interpretation of Auger data, in terms of the required energy-dependent strangeness enhancements, we developed an analytic framework (Chapter 8) inspired by the Heitler-Matthews model for muons. This provided a deeper insight into the effect of varying the various fireball parameters on the resulting muon number and enabled more flexibility w.r.t. Monte Carlo simulations. While feeding the analytic framework directly with the relevant hadronic interaction model predictions using CRMC did not reproduce fireball-extended CONEX simulations – most likely due to the inability of the framework to incorporate inelasticity – it did provide a useful interpolation (Chapter 9). The subsequent application to Auger data found that a fireball that solely enhances the strangeness is capable of resolving the muon deficit. Simultaneous constraints from shower-to-shower fluctuations of the muon number requires the effect to occur already at lower energies. At Tevatron and LHC energies we estimated it more generally as a required  $O(3 - 8)\%$  increase of the average energy fraction going into hadronic particles. This result constitutes a direct interpretation of Auger data in terms of the hadronic energy flow, which could serve as a guidance for accelerator experiments. In particular, this motivates forward physics experiments during the proposed LHC run with oxygen beams.

More precise predictions for collider experiments could be obtained by extending the last analysis with the inclusion of data at lower energies from the Auger Underground Muon Detector [98]. In this regard, also including data from other CR experiments can be beneficial – as done in [6] – but this suffers from the difficulty of cross-calibrations and common energy scales. From

a more experimental side, a reduction of systematic and statistical uncertainties on respectively the average and the relative fluctuations of the muon number would be an enormous help.

Whereas our initial Ansatz of the production of a new plasma fireball state is disfavored by its large impact on  $X_{\max}$ , the associated strangeness enhancement constitutes a promising solution to the muon deficit. This is a concrete prediction of the remainder (i.e., without plasma formation) of the fireball model and is also motivated by ALICE measurements [14].

Alternative contributions to a resolution of the muon deficit may come from a generally improved understanding of the soft QCD regime. This is illustrated by past inclusions of leading  $\rho^0$  and baryon-pair production in high-energy hadronic interaction models [142, 196], and it is indicated by a recent study [209] finding inconsistencies at low energies between state-of-the-art hadronic interaction models.

Therefore, it would be interesting to also test the prediction of strangeness enhancements with air shower observations beyond the number of muons at ground. In particular, the larger critical energy of kaons compared to pions would likely give rise to a harder energy spectrum of the muons at ground and a shallower muon production depth. While such spectra have not yet been measured, a shallower muon production depth would in fact be advantageous given the current tension with data from the Pierre Auger Observatory. A detailed theoretical study of the influence of strangeness enhancements on these observables – maybe also by further extending the Heitler-Matthews model to include separate pionic and kaonic components – could outline further tests from the astroparticle side. By providing the corresponding measurements, the Pierre Auger Observatory is in an ideal position to aid in pinpointing the origin of the muon deficit.

This synergy between cosmic ray observatories and collider experiments connected through the theory of air showers and hadronic interactions promises concrete advances in our understanding of the fundamental nature of matter as well as the origin of cosmic rays.

# Acknowledgements

This thesis is the culmination of over 3 years of studies conducted at the II. Institut für Theoretische Physik of the University of Hamburg. Whereas only my name appears on the cover, a number of people have supported me on this journey. For this I would like to thank them here.

First and foremost, I would like to thank my professor and supervisor Günter Sigl for giving me the opportunity to pursue a PhD on the fascinating topic of cosmic rays. I very much appreciate the faith he put in me to independently bring the project to a (hopefully) successful completion. This also gave me the freedom to grow as an individual, which will definitely prove useful in my further career. Simultaneously, his comments and feedback at crucial junctions of this journey kept me on the right track and were invaluable for the final work. In this regard, also the comments provided by Maria V. Garzelli and Sergey Ostapchenko significantly improved the thesis. Going out of their way to help me, even in the busy periods at the end of the year, really deserves my gratitude.

It has been a real pleasure to be part of the international Pierre Auger Collaboration, adding an extra dimension to my stay in Hamburg. For this I again thank Günter Sigl. Unfortunately, I was unable to visit the observatory myself due to the pandemic, but I learned a lot from the various conferences and meetings, both off- and online. In this way, many people contributed to my understanding of the observatory and the associated physics. Some Auger members also contributed more directly to this work, for which I would like to thank them explicitly: Tanguy Pierog for his suggestion of and help with implementing a fireball into CONEX, and for his advice to use URQMD; Lorenzo Cazon, Felix Riehn, and Ruben Canceição for the email exchanges about diffraction and muon fluctuations; and Felix Riehn again for providing me with the Auger data used throughout this thesis.

The simulations were performed on the PHYSnet Compute Cloud of the University of Hamburg, which was made really accessible to me by Martin Stieben, whom I give my thanks. Other gratitude on the University's side is due to our secretary Elizabeth Duarte. Right from the start she made me feel welcome and has been very supportive with any administrative concerns. I also very much appreciate our pleasant collaboration for the creation and extension of DESY accounts.

The composition of our astroparticle group changed throughout the years, but all their members contributed to shaping my PhD experience. I will forever be grateful to Andrej for welcoming me both to the group and to the city of Hamburg. While he left before I began, the support continued over email. I also thank Peter and Pranjali for the interesting discussions whenever they were around, and an additional thanks goes to Peter for his corrections to the German abstract. My office was livened up when Koschi joined our group and I very much thank him, Lucas, Paulina, and Valerie for inviting me along for lunch and including me as your friend also

outside DESY. Unfortunately for me, their projects were only of short duration. I also thank Cannon for his short stay, and for the helpful book he left me. With the arrival of Oindrila, Marvin, and Alexandra it appeared a group was forming again, but circumstances soon sent us to work from home. The addition of Simone and Dennis completes our current group, which I am very fond of. It is a shame we did not get to see each other more. Nevertheless, I would like to thank you all for being there for me and for each other, and I hope we can keep our connection after I have left.

On a more personal level, I would like to thank Jakob, Erwin, and Aron, who have been great friends over these past years. Jakob has furthermore been a very pleasant flatmate, and during the pandemic also turned into somewhat of an office mate. With all our discussions, he may, in fact, be the one that helped me the most with this work. I hope I was also of some help to him. On top of that, he helped me stay sane during the pandemic. This credit also extends to Erwin, who keeps motivating me to do sports together, for which I am very grateful.

I end these acknowledgments by thanking my parents and my brothers, including *aanhang*. They have been an endless source of support, and they remind me that I have a home outside of Hamburg. While the pandemic made visits considerably more difficult, it also made me realize how much I appreciate having them and the time I spend with them. Concluding the PhD I hope the circumstances allow me to come home more often and allow them to (again) visit my current *Wahlheimat*. On a side note, I would also like to thank *de eenvoudige taalkundige* Marc for his brilliant comments and advice on the English in this thesis. Finally, my dearest Uta has been very supportive of me, kept me sane during the pandemic, and helped me correct the German abstract. I cannot put in words how much she means to me, but she already deserves all my gratitude and love for being my best friend, for brightening up my days, and for being my partner in life.

# References

- [1] Johannes Albrecht et al. “The Muon Puzzle in cosmic-ray induced air showers and its connection to the Large Hadron Collider”. In: *arXiv e-prints* (May 2021). arXiv: [2105.06148 \[astro-ph.HE\]](#).
- [2] S. Müller et al. “Impact of muon detection thresholds on the separability of primary cosmic rays”. In: *Astroparticle Physics* 97 (Jan. 2018), pp. 174–185. DOI: [10.1016/j.astropartphys.2017.11.005](#).
- [3] Pedro Abreu et al. “Interpretation of the Depths of Maximum of Extensive Air Showers Measured by the Pierre Auger Observatory”. In: *JCAP* 02 (2013), p. 026. DOI: [10.1088/1475-7516/2013/02/026](#). arXiv: [1301.6637 \[astro-ph.HE\]](#).
- [4] A. Aab et al. “Depth of maximum of air-shower profiles at the Pierre Auger Observatory. II. Composition implications”. In: *Phys. Rev. D* 90.12 (2014), p. 122006. DOI: [10.1103/PhysRevD.90.122006](#). arXiv: [1409.5083 \[astro-ph.HE\]](#).
- [5] A. Aab et al. “Measurement of the Fluctuations in the Number of Muons in Extensive Air Showers with the Pierre Auger Observatory”. In: *Phys. Rev. Lett.* 126 (15 Apr. 2021), p. 152002. DOI: [10.1103/PhysRevLett.126.152002](#). URL: <https://link.aps.org/doi/10.1103/PhysRevLett.126.152002>.
- [6] H. P. Dembinski et al. “Report on Tests and Measurements of Hadronic Interaction Properties with Air Showers”. In: *EPJ Web Conf.* 210 (2019), p. 02004. DOI: [10.1051/epjconf/201921002004](#). arXiv: [1902.08124 \[astro-ph.HE\]](#).
- [7] J. Alvarez-Muniz et al. “Muon production and string percolation effects in cosmic rays at the highest energies”. In: (Sept. 2012). arXiv: [1209.6474 \[hep-ph\]](#).
- [8] Glennys R. Farrar and Jeffrey D. Allen. “A new physical phenomenon in ultra-high energy collisions”. In: *EPJ Web Conf.* 53 (2013). Ed. by K. -H. Kampert et al., p. 07007. DOI: [10.1051/epjconf/20135307007](#). arXiv: [1307.2322 \[hep-ph\]](#).
- [9] Luis A. Anchordoqui, Haim Goldberg, and Thomas J. Weiler. “Strange fireball as an explanation of the muon excess in Auger data”. In: *Phys. Rev. D* 95.6 (2017), p. 063005. DOI: [10.1103/PhysRevD.95.063005](#). arXiv: [1612.07328 \[hep-ph\]](#).
- [10] Sebastian Baur et al. “Core-corona effect in hadron collisions and muon production in air showers”. In: (Feb. 2019). arXiv: [1902.09265 \[hep-ph\]](#).
- [11] Tanguy Pierog et al. “Collective Hadronization and Air Showers: Can LHC Data Solve the Muon Puzzle ?” In: *PoS ICRC2019* (2020), p. 387. DOI: [10.22323/1.358.0387](#).

- [12] Luis A. Anchordoqui et al. “Through the looking-glass with ALICE into the quark-gluon plasma: A new test for hadronic interaction models used in air shower simulations”. In: *Phys. Lett. B* 810 (2020), p. 135837. DOI: [10.1016/j.physletb.2020.135837](https://doi.org/10.1016/j.physletb.2020.135837). arXiv: [1907.09816](https://arxiv.org/abs/1907.09816) [hep-ph].
- [13] Tanguy Pierog et al. “When heavy ions meet cosmic rays: potential impact of QGP formation on the muon puzzle”. In: *PoS ICRC2021* (2021), p. 469. DOI: [10.22323/1.395.0469](https://doi.org/10.22323/1.395.0469).
- [14] Jaroslav Adam et al. “Enhanced production of multi-strange hadrons in high-multiplicity proton-proton collisions”. In: *Nature Phys.* 13 (2017), pp. 535–539. DOI: [10.1038/nphys4111](https://doi.org/10.1038/nphys4111). arXiv: [1606.07424](https://arxiv.org/abs/1606.07424) [nucl-ex].
- [15] Victor F. Hess. “Über Beobachtungen der durchdringenden Strahlung bei sieben Freiballonfahrten”. In: *Phys. Z.* 13 (1912), pp. 1084–1091.
- [16] M. Walter and A. W. Wolfendale. “Early history of cosmic particle physics”. In: *European Physical Journal H* 37.3 (Aug. 2012), pp. 323–358. DOI: [10.1140/epjh/e2012-30020-1](https://doi.org/10.1140/epjh/e2012-30020-1).
- [17] Henri Becquerel. “Sur les radiations invisibles émises par les corps phosphorescents”. In: *Comptes rendus* 122.1896 (1896), pp. 501–503.
- [18] Hans Geitel. “Über die Elektrizitätszerstreuung in abgeschlossenen Luftmengen”. In: *Phys. Z* 2 (1900), pp. 116–119.
- [19] E Elster. “Weitere versuche uber die elektrizitatszerstreuung in abgeschlossen luftmengen.” In: *Physik. Z.* 2 (1901), pp. 560–563.
- [20] Charles TR Wilson. “On the leakage of electricity through dust-free air”. In: *Proc. Cambridge Philos. Soc.* Vol. 11. 1900, p. 32.
- [21] Vitalii L Ginzburg. “Cosmic ray astrophysics (history and general review)”. In: *Physics-Uspokhi* 39.2 (Feb. 1996), pp. 155–168. DOI: [10.1070/pu1996v039n02abeh000132](https://doi.org/10.1070/pu1996v039n02abeh000132). URL: <https://doi.org/10.1070/pu1996v039n02abeh000132>.
- [22] Karl Kurz. “The radioactive materials of the earth and air as the origin of the invasive radiation in the atmosphere”. In: *Phys. Zeit* 10 (1909), pp. 834–845.
- [23] Alessandro De Angelis et al. “Domenico Pacini and the discovery of cosmic rays”. In: *32nd Intern. Cosmic Ray Conference, Beijing, 2011, proceedings, paper*. Vol. 1. 2011.
- [24] Theodor Wulf. “Beobachtungen über die Strahlung hoher Durchdringungsfähigkeit auf dem Eiffelturm”. In: *Physikalische Zeitschrift* 11 (1910), pp. 811–813.
- [25] Albert Gockel. “Luftelektrische beobachtungen bei einer ballonfahrt”. In: *Phys. Z* 11 (1910), pp. 280–282.
- [26] Albert Gockel. “Messungen der druchdringenden Strahlung bei Ballonfahren”. In: *Phys. Zeits.* 12 (1911), pp. 595–597.
- [27] Domenico Pacini. “Penetrating radiation on the sea”. In: *Le Radium* 8: 307-312 (1910). Translated and commented by M. De Maria and A. De Angelis; arXiv:1101.3015.
- [28] Domenico Pacini. “Penetrating radiation at the surface of and in water”. In: *Nuovo Cimento. 6:93-100* (1912). Translated and commented by A. De Angelis; arXiv:1002.1810.
- [29] Per Carlson. “Discovery of cosmic rays”. In: *AIP Conf. Proc.* 1516.1 (2013). Ed. by Jonathan F. Ormes. The right panel of Fig. 2.1 is reprinted from this article, with the permission of AIP Publishing, pp. 9–16. DOI: [10.1063/1.4792532](https://doi.org/10.1063/1.4792532).

- 
- [30] Werner Kollhörster. “Messungen der durchdringenden Strahlung im Freiballon in grosseren Höhen”. In: *Phys. Zeits.* 14 (1913), pp. 1153–1156.
- [31] Werner Kollhörster. “Messungen der durchdringenden Strahlungen bis in Höhen von 9300 m”. In: *Verh. deutsche phys. Gesellschaft* 16 (1914), pp. 719–721.
- [32] Arthur H Compton. “Recent developments in cosmic rays”. In: *Review of Scientific Instruments* 7.2 (1936), pp. 71–81.
- [33] Jacob Clay. “Penetrating Radiation”. In: *Proc. Acad. Sci. Amsterdam* 30 (1927), pp. 1115–1127; in: *Proc. Acad. Sci. Amsterdam* 31 (1928), p. 1091.
- [34] Walther Bothe and Werner Kollhörster. “Das wesen der höhenstrahlung”. In: *Zeitschrift für Physik* 56.11-12 (1929), pp. 751–777.
- [35] J Clay, PM Van Alphen, et al. “Results of the Dutch Cosmic Ray Expedition 1933: II. The magnetic latitude effect of cosmic rays a magnetic longitude effect”. In: *Physica* 1.7-12 (1934), pp. 829–838.
- [36] Arthur H. Compton. “Progress of Cosmic-Ray Survey”. In: *Phys. Rev.* 41 (5 Sept. 1932), pp. 681–682. DOI: [10.1103/PhysRev.41.681](https://doi.org/10.1103/PhysRev.41.681). URL: <https://link.aps.org/doi/10.1103/PhysRev.41.681>.
- [37] Arthur H. Compton. “A Geographic Study of Cosmic Rays”. In: *Phys. Rev.* 43 (6 Mar. 1933), pp. 387–403. DOI: [10.1103/PhysRev.43.387](https://doi.org/10.1103/PhysRev.43.387). URL: <https://link.aps.org/doi/10.1103/PhysRev.43.387>.
- [38] Luisa Bonolis. “Walther Bothe and Bruno Rossi: the birth and development of coincidence methods in cosmic-ray physics”. In: *Am. J. Phys.* 79 (2011), p. 1133. DOI: [10.1119/1.3619808](https://doi.org/10.1119/1.3619808). arXiv: [1106.1365 \[physics.hist-ph\]](https://arxiv.org/abs/1106.1365).
- [39] Bruno Rossi. “On the Magnetic Deflection of Cosmic Rays”. In: *Phys. Rev.* 36 (3 Aug. 1930), pp. 606–606. DOI: [10.1103/PhysRev.36.606](https://doi.org/10.1103/PhysRev.36.606). URL: <https://link.aps.org/doi/10.1103/PhysRev.36.606>.
- [40] Luis Alvarez and Arthur H. Compton. “A Positively Charged Component of Cosmic Rays”. In: *Phys. Rev.* 43 (10 May 1933), pp. 835–836. DOI: [10.1103/PhysRev.43.835](https://doi.org/10.1103/PhysRev.43.835). URL: <https://link.aps.org/doi/10.1103/PhysRev.43.835>.
- [41] Thomas H. Johnson. “The Azimuthal Asymmetry of the Cosmic Radiation”. In: *Phys. Rev.* 43 (10 May 1933), pp. 834–835. DOI: [10.1103/PhysRev.43.834](https://doi.org/10.1103/PhysRev.43.834). URL: <https://link.aps.org/doi/10.1103/PhysRev.43.834>.
- [42] Bruno Rossi. “Directional Measurements on the Cosmic Rays Near the Geomagnetic Equator”. In: *Phys. Rev.* 45 (3 Feb. 1934), pp. 212–214. DOI: [10.1103/PhysRev.45.212](https://doi.org/10.1103/PhysRev.45.212). URL: <https://link.aps.org/doi/10.1103/PhysRev.45.212>.
- [43] Marcel Schein, William P. Jesse, and E. O. Wollan. “The Nature of the Primary Cosmic Radiation and the Origin of the Mesotron”. In: *Phys. Rev.* 59 (7 Apr. 1941), pp. 615–615. DOI: [10.1103/PhysRev.59.615](https://doi.org/10.1103/PhysRev.59.615). URL: <https://link.aps.org/doi/10.1103/PhysRev.59.615>.

- [44] Phyllis Freier et al. “Evidence for Heavy Nuclei in the Primary Cosmic Radiation”. In: *Phys. Rev.* 74 (2 July 1948), pp. 213–217. DOI: [10.1103/PhysRev.74.213](https://doi.org/10.1103/PhysRev.74.213). URL: <https://link.aps.org/doi/10.1103/PhysRev.74.213>; H. L. Bradt and B. Peters. “Investigation of the Primary Cosmic Radiation with Nuclear Photographic Emulsions”. In: *Phys. Rev.* 74 (12 Dec. 1948), pp. 1828–1837. DOI: [10.1103/PhysRev.74.1828](https://doi.org/10.1103/PhysRev.74.1828). URL: <https://link.aps.org/doi/10.1103/PhysRev.74.1828>.
- [45] Karl-Heinz Kampert and Michael Unger. “Measurements of the cosmic ray composition with air shower experiments”. In: *Astroparticle Physics* 35.10 (2012), pp. 660–678. ISSN: 0927-6505. DOI: <https://doi.org/10.1016/j.astropartphys.2012.02.004>. URL: <http://www.sciencedirect.com/science/article/pii/S0927650512000382>.
- [46] Carl D Anderson. “The positive electron”. In: *Physical Review* 43.6 (1933), p. 491.
- [47] Carl D Anderson and Seth H Neddermeyer. “Cloud chamber observations of cosmic rays at 4300 meters elevation and near sea-level”. In: *Physical Review* 50.4 (1936), p. 263.
- [48] M. Kachelriess. “Lecture notes on high energy cosmic rays”. In: (Jan. 2008). arXiv: [0801.4376](https://arxiv.org/abs/0801.4376) [[astro-ph](https://arxiv.org/abs/0801.4376)].
- [49] Glennys R. Farrar. “Particle Physics at Ultrahigh Energies”. In: *18th International Symposium on Very High Energy Cosmic Ray Interactions*. Feb. 2019. arXiv: [1902.11271](https://arxiv.org/abs/1902.11271) [[hep-ph](https://arxiv.org/abs/1902.11271)].
- [50] Walther Bothe. “Zur Vereinfachung von Koinzidenzzählungen”. In: *Zeitschrift für Physik* 59.1 (1930), pp. 1–5.
- [51] Bruno Rossi. “Method of registering multiple simultaneous impulses of several Geiger’s counters”. In: *Nature* 125.3156 (1930), pp. 636–636.
- [52] Bruno Rossi. “Über die Eigenschaften der durchdringenden Korpuskularstrahlung im Meeresniveau”. In: *Zeitschrift für Physik* 82.3 (1933), pp. 151–178.
- [53] Karl-Heinz Kampert and Alan A. Watson. “Extensive air showers and ultra high-energy cosmic rays: a historical review”. In: *European Physical Journal H* 37.3 (Aug. 2012), pp. 359–412. DOI: [10.1140/epjh/e2012-30013-x](https://doi.org/10.1140/epjh/e2012-30013-x). arXiv: [1207.4827](https://arxiv.org/abs/1207.4827) [[physics.hist-ph](https://arxiv.org/abs/1207.4827)].
- [54] Kurt Schmeiser and W Bothe. “Die harten Ultrastrahlschauer”. In: *Annalen der Physik* 424.1-2 (1938), pp. 161–177.
- [55] W Kolhörster, I Matthes, and E Weber. “Gekoppelte Höhenstrahlen”. In: *Naturwissenschaften* 26.35 (1938), pp. 576–576.
- [56] Bruno Rossi. “Misura sulla distribuzione angolare di intensità della radiazione penetrante all’Asmara”. In: *Supplemento a la Ricerca Scientifica* 1 (1934), p. 579.
- [57] P Auger, R Maze, and AF Robley. “Extension et pouvoir pénétrant des grandes gerbes de rayons cosmiques”. In: *Comptes rendus* 208 (1939), pp. 339–349; Pierre Auger et al. “Extensive Cosmic-Ray Showers”. In: *Rev. Mod. Phys.* 11 (3-4 July 1939), pp. 288–291. DOI: [10.1103/RevModPhys.11.288](https://doi.org/10.1103/RevModPhys.11.288). URL: <https://link.aps.org/doi/10.1103/RevModPhys.11.288>.
- [58] M. Nagano and A. A. Watson. “Observations and implications of the ultrahigh-energy cosmic rays”. In: *Rev. Mod. Phys.* 72 (3 July 2000), pp. 689–732. DOI: [10.1103/RevModPhys.72.689](https://doi.org/10.1103/RevModPhys.72.689). URL: <https://link.aps.org/doi/10.1103/RevModPhys.72.689>.

- [59] Ilya G. Usoskin, Galina A. Bazilevskaya, and Gennady A. Kovaltsov. “Solar modulation parameter for cosmic rays since 1936 reconstructed from ground-based neutron monitors and ionization chambers”. In: *Journal of Geophysical Research: Space Physics* 116.A2 (2011). DOI: <https://doi.org/10.1029/2010JA016105>. URL: <https://agupubs.onlinelibrary.wiley.com/doi/abs/10.1029/2010JA016105>.
- [60] Luis A. Anchordoqui. “Ultra-High-Energy Cosmic Rays”. In: *Phys. Rept.* 801 (2019). Fig. 2.2 is reprinted from this article with permission from Elsevier, pp. 1–93. DOI: [10.1016/j.physrep.2019.01.002](https://doi.org/10.1016/j.physrep.2019.01.002). arXiv: [1807.09645](https://arxiv.org/abs/1807.09645) [astro-ph.HE].
- [61] Hans Peter Dembinski et al. “Data-driven model of the cosmic-ray flux and mass composition from 10 GeV to  $10^{11}$  GeV”. In: *PoS ICRC2017* (2018), p. 533. DOI: [10.22323/1.301.0533](https://doi.org/10.22323/1.301.0533). arXiv: [1711.11432](https://arxiv.org/abs/1711.11432) [astro-ph.HE].
- [62] F. Aharonian et al. “First ground based measurement of atmospheric Cherenkov light from cosmic rays”. In: *Phys. Rev. D* 75 (2007), p. 042004. DOI: [10.1103/PhysRevD.75.042004](https://doi.org/10.1103/PhysRevD.75.042004). arXiv: [astro-ph/0701766](https://arxiv.org/abs/astro-ph/0701766).
- [63] Alexander Aab et al. “Features of the Energy Spectrum of Cosmic Rays above  $2.5 \times 10^{18}$  eV Using the Pierre Auger Observatory”. In: *Phys. Rev. Lett.* 125.12 (2020), p. 121106. DOI: [10.1103/PhysRevLett.125.121106](https://doi.org/10.1103/PhysRevLett.125.121106). arXiv: [2008.06488](https://arxiv.org/abs/2008.06488) [astro-ph.HE].
- [64] P. O. Lagage and C. J. Cesarsky. “The maximum energy of cosmic rays accelerated by supernova shocks.” In: 125 (Sept. 1983), pp. 249–257.
- [65] Günter Sigl. “Astroparticle Physics: Theory and Phenomenology”. In: (2017). URL: <https://link.springer.com/book/10.2991/978-94-6239-243-4>.
- [66] Rafael Alves Batista et al. “Open Questions in Cosmic-Ray Research at Ultrahigh Energies”. In: *Front. Astron. Space Sci.* 6 (2019). Figure in Fig. 2.3 provided under the Creative Commons Attribution 4.0 International License (CC BY 4.0), p. 23. DOI: [10.3389/fspas.2019.00023](https://doi.org/10.3389/fspas.2019.00023). arXiv: [1903.06714](https://arxiv.org/abs/1903.06714) [astro-ph.HE].
- [67] Michael Unger, Glennys R. Farrar, and Luis A. Anchordoqui. “Origin of the ankle in the ultrahigh energy cosmic ray spectrum, and of the extragalactic protons below it”. In: 92.12, 123001 (Dec. 2015), p. 123001. DOI: [10.1103/PhysRevD.92.123001](https://doi.org/10.1103/PhysRevD.92.123001). arXiv: [1505.02153](https://arxiv.org/abs/1505.02153) [astro-ph.HE].
- [68] J. Abraham et al. “Observation of the suppression of the flux of cosmic rays above  $4 \times 10^{19}$  eV”. In: *Phys. Rev. Lett.* 101 (2008), p. 061101. DOI: [10.1103/PhysRevLett.101.061101](https://doi.org/10.1103/PhysRevLett.101.061101). arXiv: [0806.4302](https://arxiv.org/abs/0806.4302) [astro-ph].
- [69] Alexander Aab et al. “Measurement of the cosmic-ray energy spectrum above  $2.5 \times 10^{18}$  eV using the Pierre Auger Observatory”. In: *Phys. Rev. D* 102.6 (2020), p. 062005. DOI: [10.1103/PhysRevD.102.062005](https://doi.org/10.1103/PhysRevD.102.062005). arXiv: [2008.06486](https://arxiv.org/abs/2008.06486) [astro-ph.HE].
- [70] Kenneth Greisen. “End to the Cosmic-Ray Spectrum?” In: 16.17 (Apr. 1966), pp. 748–750. DOI: [10.1103/PhysRevLett.16.748](https://doi.org/10.1103/PhysRevLett.16.748).
- [71] G. T. Zatsepin and V. A. Kuzmin. “Upper limit of the spectrum of cosmic rays”. In: *JETP Lett.* 4 (1966), pp. 78–80.

- [72] S. Mollerach and E. Roulet. “Progress in high-energy cosmic ray physics”. In: *Progress in Particle and Nuclear Physics* 98 (2018), pp. 85–118. ISSN: 0146-6410. DOI: <https://doi.org/10.1016/j.pnpnp.2017.10.002>. URL: <https://www.sciencedirect.com/science/article/pii/S0146641017300881>.
- [73] Alexander Aab et al. “Observation of a Large-scale Anisotropy in the Arrival Directions of Cosmic Rays above  $8 \times 10^{18}$  eV”. In: *Science* 357.6537 (2017), pp. 1266–1270. DOI: [10.1126/science.aan4338](https://doi.org/10.1126/science.aan4338). arXiv: [1709.07321](https://arxiv.org/abs/1709.07321) [astro-ph.HE].
- [74] Alexander Aab et al. “An Indication of anisotropy in arrival directions of ultra-high-energy cosmic rays through comparison to the flux pattern of extragalactic gamma-ray sources”. In: *Astrophys. J. Lett.* 853.2 (2018), p. L29. DOI: [10.3847/2041-8213/aaa66d](https://doi.org/10.3847/2041-8213/aaa66d). arXiv: [1801.06160](https://arxiv.org/abs/1801.06160) [astro-ph.HE].
- [75] Ralph Engel, Dieter Heck, and Tanguy Pierog. “Extensive Air Showers and Hadronic Interactions at High Energy”. In: *Annual Review of Nuclear and Particle Science* 61.1 (2011), pp. 467–489. DOI: [10.1146/annurev.nucl.012809.104544](https://doi.org/10.1146/annurev.nucl.012809.104544). eprint: <https://doi.org/10.1146/annurev.nucl.012809.104544>. URL: <https://doi.org/10.1146/annurev.nucl.012809.104544>.
- [76] P. Abreu et al. “Measurement of the Proton-Air Cross Section at  $\sqrt{s}=57$  TeV with the Pierre Auger Observatory”. In: *Phys. Rev. Lett.* 109 (6 Aug. 2012), p. 062002. DOI: [10.1103/PhysRevLett.109.062002](https://doi.org/10.1103/PhysRevLett.109.062002). URL: <https://link.aps.org/doi/10.1103/PhysRevLett.109.062002>.
- [77] “The Pierre Auger Cosmic Ray Observatory”. In: *Nuclear Instruments and Methods in Physics Research Section A: Accelerators, Spectrometers, Detectors and Associated Equipment* 798 (2015), pp. 172–213. ISSN: 0168-9002. DOI: <https://doi.org/10.1016/j.nima.2015.06.058>. URL: <http://www.sciencedirect.com/science/article/pii/S0168900215008086>.
- [78] Todor Stanev. *High Energy Cosmic Rays*. 3rd ed. Springer, 2021. DOI: <https://doi.org/10.1007/978-3-030-71567-0>.
- [79] J. Engel et al. “Nucleus-nucleus collisions and interpretation of cosmic-ray cascades”. In: *Phys. Rev. D* 46 (11 Dec. 1992), pp. 5013–5025. DOI: [10.1103/PhysRevD.46.5013](https://doi.org/10.1103/PhysRevD.46.5013). URL: <https://link.aps.org/doi/10.1103/PhysRevD.46.5013>.
- [80] Alexander Aab et al. “Reconstruction of events recorded with the surface detector of the Pierre Auger Observatory”. In: *JINST* 15.10 (2020), P10021. DOI: [10.1088/1748-0221/15/10/P10021](https://doi.org/10.1088/1748-0221/15/10/P10021). arXiv: [2007.09035](https://arxiv.org/abs/2007.09035) [astro-ph.IM].
- [81] Ralf Ulrich, Ralph Engel, and Michael Unger. “Hadronic Multiparticle Production at Ultra-High Energies and Extensive Air Showers”. In: *Phys. Rev. D* 83 (2011), p. 054026. DOI: [10.1103/PhysRevD.83.054026](https://doi.org/10.1103/PhysRevD.83.054026). arXiv: [1010.4310](https://arxiv.org/abs/1010.4310) [hep-ph].
- [82] J. F. Carlson and J. R. Oppenheimer. “On Multiplicative Showers”. In: *Phys. Rev.* 51 (4 Feb. 1937), pp. 220–231. DOI: [10.1103/PhysRev.51.220](https://doi.org/10.1103/PhysRev.51.220). URL: <https://link.aps.org/doi/10.1103/PhysRev.51.220>.
- [83] W. Heitler. *The Quantum Theory of Radiation*. Oxford University Press, 1954.

- 
- [84] J. Matthews. “A Heitler model of extensive air showers”. In: *Astroparticle Physics* 22.5 (2005), pp. 387–397. ISSN: 0927-6505. DOI: <https://doi.org/10.1016/j.astropartphys.2004.09.003>. URL: <http://www.sciencedirect.com/science/article/pii/S0927650504001598>.
- [85] Stefan Grimm, Darko Veberic, and Ralph Engel. “Heitler-Matthews model with leading-particle effect”. In: *PoS ICRC2017* (2017), p. 299. DOI: [10.22323/1.301.0299](https://doi.org/10.22323/1.301.0299).
- [86] Jaime Alvarez-Muniz et al. “Hybrid simulations of extensive air showers”. In: *Phys. Rev. D* 66 (2002), p. 033011. DOI: [10.1103/PhysRevD.66.033011](https://doi.org/10.1103/PhysRevD.66.033011). arXiv: [astro-ph/0205302](https://arxiv.org/abs/astro-ph/0205302).
- [87] A. Castellina. “Highlights from the Pierre Auger Observatory and prospects for Auger-Prime”. In: *36th International Cosmic Ray Conference (ICRC2019)*. Vol. 36. International Cosmic Ray Conference. Figures in Fig. 3.5 provided under the Creative Commons Attribution-NonCommercial-NoDerivatives 4.0 International License (CC BY-NC-ND 4.0). July 2019, p. 4. arXiv: [1909.10791](https://arxiv.org/abs/1909.10791) [[astro-ph.HE](https://arxiv.org/abs/1909.10791)].
- [88] The Pierre Auger Collaboration et al. “The Pierre Auger Observatory Upgrade - Preliminary Design Report”. In: *arXiv e-prints*, arXiv:1604.03637 (Apr. 2016), arXiv:1604.03637. arXiv: [1604.03637](https://arxiv.org/abs/1604.03637) [[astro-ph.IM](https://arxiv.org/abs/1604.03637)].
- [89] Antonella Castellina and Pierre Auger Collaboration. “AugerPrime: the Pierre Auger Observatory Upgrade”. In: *European Physical Journal Web of Conferences*. Vol. 210. European Physical Journal Web of Conferences. Oct. 2019, p. 06002. DOI: [10.1051/epjconf/201921006002](https://doi.org/10.1051/epjconf/201921006002). arXiv: [1905.04472](https://arxiv.org/abs/1905.04472) [[astro-ph.HE](https://arxiv.org/abs/1905.04472)].
- [90] Pierre Auger collaboration et al. “The Pierre Auger Observatory and its Upgrade”. In: *Science Reviews-from the end of the world* 1.4 (2020), pp. 8–33. DOI: [10.52712/sciencereviews.v1i4.31](https://doi.org/10.52712/sciencereviews.v1i4.31).
- [91] Pierre Auger Collaboration. *Pierre Auger Observatory Media Gallery*. Licensed under the Creative Commons Attribution-ShareAlike 4.0 International License (CC BY-SA 4.0). URL: <https://www.flickr.com/photos/134252569@N07/albums>.
- [92] J. Abraham et al. “The fluorescence detector of the Pierre Auger Observatory”. In: *Nuclear Instruments and Methods in Physics Research Section A: Accelerators, Spectrometers, Detectors and Associated Equipment* 620.2 (2010), pp. 227–251. ISSN: 0168-9002. DOI: <https://doi.org/10.1016/j.nima.2010.04.023>. URL: <https://www.sciencedirect.com/science/article/pii/S0168900210008727>.
- [93] A. Coleman. “Measurement of the Cosmic Ray Flux near the Second Knee with the Pierre Auger Observatory”. In: *36th International Cosmic Ray Conference (ICRC2019)*. Vol. 36. International Cosmic Ray Conference. July 2019, p. 225.
- [94] T. K. Gaisser and A. M. Hillas. “Reliability of the Method of Constant Intensity Cuts for Reconstructing the Average Development of Vertical Showers”. In: *International Cosmic Ray Conference*. Vol. 8. International Cosmic Ray Conference. Jan. 1977, p. 353.
- [95] A. Aab et al. “Data-driven estimation of the invisible energy of cosmic ray showers with the Pierre Auger Observatory”. In: *Phys. Rev. D* 100 (8 Oct. 2019), p. 082003. DOI: [10.1103/PhysRevD.100.082003](https://doi.org/10.1103/PhysRevD.100.082003). URL: <https://link.aps.org/doi/10.1103/PhysRevD.100.082003>.

- [96] V. Novotny. “Measurement of the spectrum of cosmic rays above 10(16.5) eV with Cherenkov-dominated events at the Pierre Auger Observatory”. In: *36th International Cosmic Ray Conference (ICRC2019)*. Vol. 36. International Cosmic Ray Conference. July 2019, p. 374.
- [97] A. Aab et al. “Design and implementation of the AMIGA embedded system for data acquisition”. In: 16.07 (July 2021), T07008. DOI: [10.1088/1748-0221/16/07/t07008](https://doi.org/10.1088/1748-0221/16/07/t07008). URL: <https://doi.org/10.1088/1748-0221/16/07/t07008>.
- [98] A. Aab et al. “Direct measurement of the muonic content of extensive air showers between  $2 \times 10^{17}$  and  $2 \times 10^{18}$  eV at the Pierre Auger Observatory”. In: *Eur. Phys. J. C* 80.8 (2020), p. 751. DOI: [10.1140/epjc/s10052-020-8055-y](https://doi.org/10.1140/epjc/s10052-020-8055-y).
- [99] Johannes Schulz. “Status and Prospects of the Auger Engineering Radio Array”. In: *Proceedings of The 34th International Cosmic Ray Conference — PoS(ICRC2015)*. Vol. 236. 2016, p. 615. DOI: [10.22323/1.236.0615](https://doi.org/10.22323/1.236.0615).
- [100] Alexander Aab et al. “Observation of inclined EeV air showers with the radio detector of the Pierre Auger Observatory”. In: *JCAP* 10 (2018), p. 026. DOI: [10.1088/1475-7516/2018/10/026](https://doi.org/10.1088/1475-7516/2018/10/026). arXiv: [1806.05386](https://arxiv.org/abs/1806.05386) [[astro-ph.IM](https://arxiv.org/abs/1806.05386)].
- [101] Bjarni Pont. “A Large Radio Detector at the Pierre Auger Observatory - Measuring the Properties of Cosmic Rays up to the Highest Energies”. In: *Proceedings of 36th International Cosmic Ray Conference — PoS(ICRC2019)*. Vol. 358. 2019, p. 395. DOI: [10.22323/1.358.0395](https://doi.org/10.22323/1.358.0395).
- [102] Alexander Aab et al. “Multi-Messenger Physics with the Pierre Auger Observatory”. In: *Front. Astron. Space Sci.* 6 (2019), p. 24. DOI: [10.3389/fspas.2019.00024](https://doi.org/10.3389/fspas.2019.00024). arXiv: [1904.11918](https://arxiv.org/abs/1904.11918) [[astro-ph.HE](https://arxiv.org/abs/1904.11918)].
- [103] Alexander Aab et al. “Search for photons with energies above  $10^{18}$  eV using the hybrid detector of the Pierre Auger Observatory”. In: *JCAP* 04 (2017). [Erratum: *JCAP* 09, E02 (2020)], p. 009. DOI: [10.1088/1475-7516/2017/04/009](https://doi.org/10.1088/1475-7516/2017/04/009). arXiv: [1612.01517](https://arxiv.org/abs/1612.01517) [[astro-ph.HE](https://arxiv.org/abs/1612.01517)].
- [104] Alexander Aab et al. “A Search for Ultra-high-energy Neutrinos from TXS 0506+056 Using the Pierre Auger Observatory”. In: *Astrophys. J.* 902.2 (2020), p. 105. DOI: [10.3847/1538-4357/abb476](https://doi.org/10.3847/1538-4357/abb476). arXiv: [2010.10953](https://arxiv.org/abs/2010.10953) [[astro-ph.HE](https://arxiv.org/abs/2010.10953)].
- [105] Alexander Aab et al. “Ultrahigh-Energy Neutrino Follow-Up of Gravitational Wave Events GW150914 and GW151226 with the Pierre Auger Observatory”. In: *Phys. Rev. D* 94.12 (2016), p. 122007. DOI: [10.1103/PhysRevD.94.122007](https://doi.org/10.1103/PhysRevD.94.122007). arXiv: [1608.07378](https://arxiv.org/abs/1608.07378) [[astro-ph.HE](https://arxiv.org/abs/1608.07378)].
- [106] A. Albert et al. “Search for High-energy Neutrinos from Binary Neutron Star Merger GW170817 with ANTARES, IceCube, and the Pierre Auger Observatory”. In: *Astrophys. J. Lett.* 850.2 (2017), p. L35. DOI: [10.3847/2041-8213/aa9aed](https://doi.org/10.3847/2041-8213/aa9aed). arXiv: [1710.05839](https://arxiv.org/abs/1710.05839) [[astro-ph.HE](https://arxiv.org/abs/1710.05839)].
- [107] Alexander Aab et al. “Limits on point-like sources of ultra-high-energy neutrinos with the Pierre Auger Observatory”. In: *JCAP* 11 (2019), p. 004. DOI: [10.1088/1475-7516/2019/11/004](https://doi.org/10.1088/1475-7516/2019/11/004). arXiv: [1906.07419](https://arxiv.org/abs/1906.07419) [[astro-ph.HE](https://arxiv.org/abs/1906.07419)].
- [108] R. G. Lang. “Testing Lorentz Invariance Violation at the Pierre Auger Observatory”. In: *36th International Cosmic Ray Conference (ICRC2019)*. Vol. 36. International Cosmic Ray Conference. July 2019, p. 327.

- 
- [109] A. Aab et al. “Testing Hadronic Interactions at Ultrahigh Energies with Air Showers Measured by the Pierre Auger Observatory”. In: *Phys. Rev. Lett.* 117 (19 Oct. 2016), p. 192001. DOI: [10.1103/PhysRevLett.117.192001](https://doi.org/10.1103/PhysRevLett.117.192001). URL: <https://link.aps.org/doi/10.1103/PhysRevLett.117.192001>.
- [110] A. Aab et al. “A 3-Year Sample of Almost 1,600 Elves Recorded Above South America by the Pierre Auger Cosmic-Ray Observatory”. In: *Earth and Space Science* 7.4 (2020). e2019EA000582 10.1029/2019EA000582, e2019EA000582. DOI: <https://doi.org/10.1029/2019EA000582>. URL: <https://agupubs.onlinelibrary.wiley.com/doi/abs/10.1029/2019EA000582>.
- [111] Valerio Verzi. “Measurement of the energy spectrum of ultra-high energy cosmic rays using the Pierre Auger Observatory”. In: *Proceedings of 36th International Cosmic Ray Conference — PoS(ICRC2019)*. Vol. 358. 2019, p. 450. DOI: [10.22323/1.358.0450](https://doi.org/10.22323/1.358.0450).
- [112] A. Aab et al. “Depth of maximum of air-shower profiles at the Pierre Auger Observatory. I. Measurements at energies above  $10^{17.8}$  eV”. In: *Phys. Rev. D* 90 (12 Dec. 2014), p. 122005. DOI: [10.1103/PhysRevD.90.122005](https://doi.org/10.1103/PhysRevD.90.122005). URL: <https://link.aps.org/doi/10.1103/PhysRevD.90.122005>.
- [113] Alexey Yushkov. “Mass Composition of Cosmic Rays with Energies above  $10^{17.2}$  eV from the Hybrid Data of the Pierre Auger Observatory”. In: *Proceedings of 36th International Cosmic Ray Conference — PoS(ICRC2019)*. Vol. 358. Figures in Fig. 3.6 provided under the Creative Commons Attribution-NonCommercial-NoDerivatives 4.0 International License (CC BY-NC-ND 4.0). 2019, p. 482. DOI: [10.22323/1.358.0482](https://doi.org/10.22323/1.358.0482).
- [114] A. Aab et al. “Combined fit of spectrum and composition data as measured by the Pierre Auger Observatory”. In: 2017.04 (Apr. 2017), pp. 038–038. DOI: [10.1088/1475-7516/2017/04/038](https://doi.org/10.1088/1475-7516/2017/04/038). URL: <https://doi.org/10.1088/1475-7516/2017/04/038>.
- [115] A. Aab et al. “Evidence for a mixed mass composition at the ‘ankle’ in the cosmic-ray spectrum”. In: *Physics Letters B* 762 (2016), pp. 288–295. ISSN: 0370-2693. DOI: <https://doi.org/10.1016/j.physletb.2016.09.039>. URL: <https://www.sciencedirect.com/science/article/pii/S0370269316305433>.
- [116] Alexander Aab et al. “Inferences on mass composition and tests of hadronic interactions from 0.3 to 100 EeV using the water-Cherenkov detectors of the Pierre Auger Observatory”. In: *Phys. Rev. D* 96.12 (2017), p. 122003. DOI: [10.1103/PhysRevD.96.122003](https://doi.org/10.1103/PhysRevD.96.122003). arXiv: [1710.07249](https://arxiv.org/abs/1710.07249) [astro-ph.HE].
- [117] A. Aab et al. “Azimuthal asymmetry in the risetime of the surface detector signals of the Pierre Auger Observatory”. In: *Phys. Rev. D* 93 (7 Apr. 2016), p. 072006. DOI: [10.1103/PhysRevD.93.072006](https://doi.org/10.1103/PhysRevD.93.072006). URL: <https://link.aps.org/doi/10.1103/PhysRevD.93.072006>.
- [118] A. Aab et al. “Muons in air showers at the Pierre Auger Observatory: Measurement of atmospheric production depth”. In: *Phys. Rev. D* 90 (1 July 2014), p. 012012. DOI: [10.1103/PhysRevD.90.012012](https://doi.org/10.1103/PhysRevD.90.012012). URL: <https://link.aps.org/doi/10.1103/PhysRevD.90.012012>.
- [119] Markus Ahlers. “Deciphering the Dipole Anisotropy of Galactic Cosmic Rays”. In: *Phys. Rev. Lett.* 117 (15 Oct. 2016), p. 151103. DOI: [10.1103/PhysRevLett.117.151103](https://doi.org/10.1103/PhysRevLett.117.151103). URL: <https://link.aps.org/doi/10.1103/PhysRevLett.117.151103>.

- [120] A. Aab et al. “Large-scale Cosmic-Ray Anisotropies above 4 EeV Measured by the Pierre Auger Observatory”. In: 868.1, 4 (Nov. 2018), p. 4. DOI: [10.3847/1538-4357/aae689](https://doi.org/10.3847/1538-4357/aae689). arXiv: [1808.03579](https://arxiv.org/abs/1808.03579) [astro-ph.HE].
- [121] A. Aab et al. “Cosmic-Ray Anisotropies in Right Ascension Measured by the Pierre Auger Observatory”. In: *Astrophys. J.* 891.2 (Mar. 2020), p. 142. DOI: [10.3847/1538-4357/ab7236](https://doi.org/10.3847/1538-4357/ab7236). URL: <https://doi.org/10.3847/1538-4357/ab7236>.
- [122] Esteban Roulet. “Large-scale anisotropies above 0.03 EeV measured by the Pierre Auger Observatory”. In: *Proceedings of 36th International Cosmic Ray Conference — PoS(ICRC2019)*. Vol. 358. Top figure in Fig. 3.7 provided under the Creative Commons Attribution-NonCommercial-NoDerivatives 4.0 International License (CC BY-NC-ND 4.0). 2019, p. 408. DOI: [10.22323/1.358.0408](https://doi.org/10.22323/1.358.0408).
- [123] Arthur H. Compton and Ivan A. Getting. “An Apparent Effect of Galactic Rotation on the Intensity of Cosmic Rays”. In: *Phys. Rev.* 47 (11 June 1935), pp. 817–821. DOI: [10.1103/PhysRev.47.817](https://doi.org/10.1103/PhysRev.47.817). URL: <https://link.aps.org/doi/10.1103/PhysRev.47.817>.
- [124] A. Aab et al. “Multi-resolution anisotropy studies of ultrahigh-energy cosmic rays detected at the Pierre Auger Observatory”. In: 2017.06 (June 2017), pp. 026–026. DOI: [10.1088/1475-7516/2017/06/026](https://doi.org/10.1088/1475-7516/2017/06/026). URL: <https://doi.org/10.1088/1475-7516/2017/06/026>.
- [125] A. Aab et al. “Searches for Anisotropies in the Arrival Directions of the Highest Energy Cosmic Rays Detected by the Pierre Auger Observatory”. In: 804.1 (Apr. 2015), p. 15. DOI: [10.1088/0004-637x/804/1/15](https://doi.org/10.1088/0004-637x/804/1/15). URL: <https://doi.org/10.1088/0004-637x/804/1/15>.
- [126] Lorenzo Caccianiga. “Anisotropies of the Highest Energy Cosmic-ray Events Recorded by the Pierre Auger Observatory in 15 years of Operation”. In: *Proceedings of 36th International Cosmic Ray Conference — PoS(ICRC2019)*. Vol. 358. 2019, p. 206. DOI: [10.22323/1.358.0206](https://doi.org/10.22323/1.358.0206).
- [127] Tanguy Pierog. “Air Shower Simulation with a New Generation of post-LHC Hadronic Interaction Models in CORSIKA”. In: *Proceedings of 35th International Cosmic Ray Conference — PoS(ICRC2017)*. Vol. 301. 2017, p. 1100. DOI: [10.22323/1.301.1100](https://doi.org/10.22323/1.301.1100).
- [128] A Das and T Ferbel. *Introduction to Nuclear and Particle Physics*. 2nd. WORLD SCIENTIFIC, 2003. DOI: [10.1142/5460](https://doi.org/10.1142/5460). eprint: <https://www.worldscientific.com/doi/pdf/10.1142/5460>. URL: <https://www.worldscientific.com/doi/abs/10.1142/5460>.
- [129] Mark Thomson. *Modern Particle Physics*. Cambridge University Press, 2013. DOI: [10.1017/CB09781139525367](https://doi.org/10.1017/CB09781139525367).
- [130] David d’Enterria et al. “Constraints from the first LHC data on hadronic event generators for ultra-high energy cosmic-ray physics”. In: *Astroparticle Physics* 35.2 (2011), pp. 98–113. ISSN: 0927-6505. DOI: <https://doi.org/10.1016/j.astropartphys.2011.05.002>. URL: <https://www.sciencedirect.com/science/article/pii/S0927650511000867>.
- [131] V. N. Gribov and L. N. Lipatov. “Deep inelastic e p scattering in perturbation theory”. In: *Sov. J. Nucl. Phys.* 15 (1972), pp. 438–450; G. Altarelli and G. Parisi. “Asymptotic freedom in parton language”. In: *Nuclear Physics B* 126.2 (1977), pp. 298–318. ISSN: 0550-3213. DOI: [https://doi.org/10.1016/0550-3213\(77\)90384-4](https://doi.org/10.1016/0550-3213(77)90384-4). URL: <https://www.sciencedirect.com/science/article/pii/0550321377903844>; Yuri L Dokshitzer. In: *Sov. Phys. JETP* 46 (1977), p. 641.

- [132] T William Donnelly et al. *Foundations of nuclear and particle physics*. Cambridge University Press, 2017.
- [133] V. N. Gribov. “A Reggeon Diagram Technique”. In: *Soviet Journal of Experimental and Theoretical Physics* 26 (Feb. 1968), pp. 414–423.
- [134] S. Ostapchenko. “Monte Carlo treatment of hadronic interactions in enhanced Pomeron scheme: QGSJET-II model”. In: *Phys. Rev. D* 83 (1 Jan. 2011), p. 014018. DOI: [10.1103/PhysRevD.83.014018](https://doi.org/10.1103/PhysRevD.83.014018); S. Ostapchenko. “QGSJET-II: physics, recent improvements, and results for air showers”. In: *EPJ Web Conf.* 52 (2013). Ed. by U. Gensch and M. Walter, p. 02001. DOI: [10.1051/epjconf/20125202001](https://doi.org/10.1051/epjconf/20125202001).
- [135] S. Ostapchenko. “QGSJET-II: towards reliable description of very high energy hadronic interactions”. In: *Nuclear Physics B - Proceedings Supplements* 151.1 (2006), pp. 143–146. ISSN: 0920-5632. DOI: <https://doi.org/10.1016/j.nuclphysbps.2005.07.026>; S. Ostapchenko. “Nonlinear screening effects in high energy hadronic interactions”. In: *Phys. Rev. D* 74.1 (2006), p. 014026. DOI: [10.1103/PhysRevD.74.014026](https://doi.org/10.1103/PhysRevD.74.014026). arXiv: [hep-ph/0505259](https://arxiv.org/abs/hep-ph/0505259); Sergey Ostapchenko. “Status of QGSJET”. In: *AIP Conf. Proc.* 928.1 (2007). Ed. by S. Mani Tripathi and Richard E. Breedon, pp. 118–125. DOI: [10.1063/1.2775904](https://doi.org/10.1063/1.2775904). arXiv: [0706.3784](https://arxiv.org/abs/0706.3784) [[hep-ph](https://arxiv.org/abs/0706.3784)].
- [136] K. Werner. “Multiparticle production in p-p, p-Ar, and p-Xe collisions at 200 GeV by the multistring model venus”. In: *Phys. Rev. D* 39 (3 Feb. 1989), pp. 780–791. DOI: [10.1103/PhysRevD.39.780](https://doi.org/10.1103/PhysRevD.39.780). URL: <https://link.aps.org/doi/10.1103/PhysRevD.39.780>.
- [137] M. L. Good and W. D. Walker. “Diffraction Dissociation of Beam Particles”. In: *Phys. Rev.* 120 (5 Dec. 1960), pp. 1857–1860. DOI: [10.1103/PhysRev.120.1857](https://doi.org/10.1103/PhysRev.120.1857). URL: <https://link.aps.org/doi/10.1103/PhysRev.120.1857>.
- [138] T. Pierog et al. “EPOS LHC: Test of collective hadronization with data measured at the CERN Large Hadron Collider”. In: *Phys. Rev. C* 92 (3 Sept. 2015), p. 034906. DOI: [10.1103/PhysRevC.92.034906](https://doi.org/10.1103/PhysRevC.92.034906). URL: <https://link.aps.org/doi/10.1103/PhysRevC.92.034906>.
- [139] Klaus Werner, Fu-Ming Liu, and Tanguy Pierog. “Parton ladder splitting and the rapidity dependence of transverse momentum spectra in deuteron-gold collisions at the BNL Relativistic Heavy Ion Collider”. In: *Phys. Rev. C* 74 (4 Oct. 2006), p. 044902. DOI: [10.1103/PhysRevC.74.044902](https://doi.org/10.1103/PhysRevC.74.044902). URL: <https://link.aps.org/doi/10.1103/PhysRevC.74.044902>.
- [140] X. Artru and G. Mennessier. “String model and multiproduction”. In: *Nuclear Physics B* 70.1 (1974), pp. 93–115. ISSN: 0550-3213. DOI: [https://doi.org/10.1016/0550-3213\(74\)90360-5](https://doi.org/10.1016/0550-3213(74)90360-5). URL: <https://www.sciencedirect.com/science/article/pii/0550321374903605>.
- [141] A. Capella et al. “Dual parton model”. In: *Physics Reports* 236.4 (1994), pp. 225–329. ISSN: 0370-1573. DOI: [https://doi.org/10.1016/0370-1573\(94\)90064-7](https://doi.org/10.1016/0370-1573(94)90064-7). URL: <https://www.sciencedirect.com/science/article/pii/0370157394900647>.
- [142] Felix Riehn et al. “Hadronic interaction model sibyll 2.3d and extensive air showers”. In: *Phys. Rev. D* 102 (6 Sept. 2020), p. 063002. DOI: [10.1103/PhysRevD.102.063002](https://doi.org/10.1103/PhysRevD.102.063002). URL: <https://link.aps.org/doi/10.1103/PhysRevD.102.063002>.

- [143] Eun-Joo Ahn et al. “Cosmic ray interaction event generator SIBYLL 2.1”. In: *Phys. Rev. D* 80 (9 Nov. 2009), p. 094003. DOI: [10.1103/PhysRevD.80.094003](https://doi.org/10.1103/PhysRevD.80.094003). URL: <https://link.aps.org/doi/10.1103/PhysRevD.80.094003>.
- [144] Felix riehn et al. “A new version of the event generator Sibyll ”. In: *Proceedings of The 34th International Cosmic Ray Conference — PoS(ICRC2015)*. Vol. 236. 2016, p. 558. DOI: [10.22323/1.236.0558](https://doi.org/10.22323/1.236.0558).
- [145] Ralph Engel et al. “The hadronic interaction model Sibyll – past, present and future”. In: *EPJ Web Conf.* 145 (2017). Ed. by B. Pattison, p. 08001. DOI: [10.1051/epjconf/201614508001](https://doi.org/10.1051/epjconf/201614508001).
- [146] Felix Riehn et al. “The hadronic interaction model Sibyll 2.3c and Feynman scaling”. In: *Proceedings of 35th International Cosmic Ray Conference — PoS(ICRC2017)*. Vol. 301. 2017, p. 301. DOI: [10.22323/1.301.0301](https://doi.org/10.22323/1.301.0301).
- [147] Anatoli Fedynitch et al. “Hadronic interaction model sibyll 2.3c and inclusive lepton fluxes”. In: *Phys. Rev. D* 100 (10 Nov. 2019), p. 103018. DOI: [10.1103/PhysRevD.100.103018](https://doi.org/10.1103/PhysRevD.100.103018). URL: <https://link.aps.org/doi/10.1103/PhysRevD.100.103018>.
- [148] Hans-Uno Bengtsson and Torbjorn Sjostrand. “The Lund Monte Carlo for Hadronic Processes: Pythia Version 4.8”. In: *Comput. Phys. Commun.* 46 (1987), p. 43. DOI: [10.1016/0010-4655\(87\)90036-1](https://doi.org/10.1016/0010-4655(87)90036-1).
- [149] R.J. Glauber and G. Matthiae. “High-energy scattering of protons by nuclei”. In: *Nuclear Physics B* 21.2 (1970), pp. 135–157. ISSN: 0550-3213. DOI: [https://doi.org/10.1016/0550-3213\(70\)90511-0](https://doi.org/10.1016/0550-3213(70)90511-0). URL: <https://www.sciencedirect.com/science/article/pii/0550321370905110>; Michael L. Miller et al. “Glauber Modeling in High-Energy Nuclear Collisions”. In: *Annual Review of Nuclear and Particle Science* 57.1 (2007), pp. 205–243. DOI: [10.1146/annurev.nucl.57.090506.123020](https://doi.org/10.1146/annurev.nucl.57.090506.123020). URL: <https://doi.org/10.1146/annurev.nucl.57.090506.123020>.
- [150] Felix Riehn. “Hadronic multiparticle production with Sibyll”. 51.03.03; LK 01. PhD thesis. Karlsruher Institut für Technologie (KIT), 2015. DOI: [10.5445/IR/1000052699](https://doi.org/10.5445/IR/1000052699).
- [151] D. Heck et al. “CORSIKA: A Monte Carlo Code to Simulate Extensive Air Showers”. In: *Forschungszentrum Karlsruhe Report FZKA 6019* (1998). DOI: [10.5445/IR/270043064](https://doi.org/10.5445/IR/270043064). URL: <https://www.ikp.kit.edu/corsika/70.php>.
- [152] J. Knapp et al. “Extensive air shower simulations at the highest energies”. In: *Astropart. Phys.* 19 (2003), pp. 77–99. DOI: [10.1016/S0927-6505\(02\)00187-1](https://doi.org/10.1016/S0927-6505(02)00187-1). arXiv: [astro-ph/0206414](https://arxiv.org/abs/astro-ph/0206414).
- [153] Hans-Joachim Drescher and Glennys R. Farrar. “Dominant contributions to lateral distribution functions in ultrahigh-energy cosmic ray air showers”. In: *Astropart. Phys.* 19 (2003), pp. 235–244. DOI: [10.1016/S0927-6505\(02\)00203-7](https://doi.org/10.1016/S0927-6505(02)00203-7). arXiv: [hep-ph/0206112](https://arxiv.org/abs/hep-ph/0206112).
- [154] Christine Meurer et al. “Muon production in extensive air showers and its relation to hadronic interactions”. In: *Czech. J. Phys.* 56 (2006). Ed. by J. Ridky et al., A211. DOI: [10.1007/s10582-006-0156-9](https://doi.org/10.1007/s10582-006-0156-9). arXiv: [astro-ph/0512536](https://arxiv.org/abs/astro-ph/0512536).
- [155] I. C. Mariş et al. “Influence of low energy hadronic interactions on air-shower simulations”. In: *Nuclear Physics B Proceedings Supplements* 196 (Dec. 2009), pp. 86–89. DOI: [10.1016/j.nuclphysbps.2009.09.013](https://doi.org/10.1016/j.nuclphysbps.2009.09.013). arXiv: [0907.0409](https://arxiv.org/abs/0907.0409) [[astro-ph.CO](https://arxiv.org/abs/astro-ph)].

- 
- [156] HC Fesefeldt. “Technical Report PITHA 85-02, III Physikalisches Institut”. In: *RWTH Aachen Physikzentrum* 5100 (1985).
- [157] Alfredo Ferrari et al. “FLUKA: A multi-particle transport code (Program version 2005)”. In: (Oct. 2005). DOI: [10.2172/877507](https://doi.org/10.2172/877507); T. T. Böhlen et al. “The FLUKA Code: Developments and Challenges for High Energy and Medical Applications”. In: *Nuclear Data Sheets* 120 (June 2014), pp. 211–214. DOI: [10.1016/j.nds.2014.07.049](https://doi.org/10.1016/j.nds.2014.07.049).
- [158] Hans-Joachim Drescher et al. “Model dependence of lateral distribution functions of high energy cosmic ray air showers”. In: *Astropart. Phys.* 21 (2004), pp. 87–94. DOI: [10.1016/j.astropartphys.2003.10.007](https://doi.org/10.1016/j.astropartphys.2003.10.007). arXiv: [astro-ph/0307453](https://arxiv.org/abs/astro-ph/0307453).
- [159] Dieter Heck. “Low energy hadronic interaction models”. In: *Nucl. Phys. B Proc. Suppl.* 151 (2006). Ed. by P. K. F. Grieder, B. Pattison, and L. K. Resvanis, pp. 127–134. DOI: [10.1016/j.nuclphysbps.2005.07.024](https://doi.org/10.1016/j.nuclphysbps.2005.07.024). arXiv: [astro-ph/0410735](https://arxiv.org/abs/astro-ph/0410735).
- [160] Michael Unger. “Hadron production at fixed target energies and extensive air showers”. In: *Proceedings of 35th International Conference of High Energy Physics — PoS(ICHEP 2010)*. Vol. 120. 2011, p. 449. DOI: [10.22323/1.120.0449](https://doi.org/10.22323/1.120.0449).
- [161] S.A. Bass et al. “Microscopic models for ultrarelativistic heavy ion collisions”. In: *Progress in Particle and Nuclear Physics* 41 (1998), pp. 255–369. ISSN: 0146-6410. DOI: [https://doi.org/10.1016/S0146-6410\(98\)00058-1](https://doi.org/10.1016/S0146-6410(98)00058-1). URL: <https://www.sciencedirect.com/science/article/pii/S0146641098000581>.
- [162] M Bleicher et al. “Relativistic hadron-hadron collisions in the ultra-relativistic quantum molecular dynamics model”. In: 25.9 (Sept. 1999), pp. 1859–1896. DOI: [10.1088/0954-3899/25/9/308](https://doi.org/10.1088/0954-3899/25/9/308). URL: <https://doi.org/10.1088/0954-3899/25/9/308>.
- [163] Hannah Petersen et al. “UrQMD v2.3: Changes and Comparisons”. In: (May 2008). arXiv: [0805.0567](https://arxiv.org/abs/0805.0567) [[hep-ph](https://arxiv.org/abs/hep-ph)].
- [164] A. Bialas, W. Czyz, and L. Lesniak. “Additive quark model of multiparticle production and nucleus-nucleus collisions at high energies”. In: *Phys. Rev. D* 25 (9 May 1982), pp. 2328–2340. DOI: [10.1103/PhysRevD.25.2328](https://doi.org/10.1103/PhysRevD.25.2328). URL: <https://link.aps.org/doi/10.1103/PhysRevD.25.2328>.
- [165] S. J. Sciutto. “AIRES: A system for air shower simulations”. In: (Nov. 1999). DOI: [10.13140/RG.2.2.12566.40002](https://doi.org/10.13140/RG.2.2.12566.40002). arXiv: [astro-ph/9911331](https://arxiv.org/abs/astro-ph/9911331).
- [166] Fedynitch, Anatoli et al. “Calculation of conventional and prompt lepton fluxes at very high energy”. In: *EPJ Web of Conferences* 99 (2015), p. 08001. DOI: [10.1051/epjconf/20159908001](https://doi.org/10.1051/epjconf/20159908001). URL: <https://doi.org/10.1051/epjconf/20159908001>.
- [167] Hans-Joachim Drescher and Glennys R. Farrar. “Air shower simulations in a hybrid approach using cascade equations”. In: *Phys. Rev. D* 67 (2003), p. 116001. DOI: [10.1103/PhysRevD.67.116001](https://doi.org/10.1103/PhysRevD.67.116001). arXiv: [astro-ph/0212018](https://arxiv.org/abs/astro-ph/0212018).
- [168] T Antoni et al. “The Cosmic ray experiment KASCADE”. In: *Nucl. Instrum. Meth. A* 513 (2003), pp. 490–510. DOI: [10.1016/S0168-9002\(03\)02076-X](https://doi.org/10.1016/S0168-9002(03)02076-X).
- [169] W Lohmann, R Kopp, and R Voss. *Energy loss of muons in the energy range 1-10000 GeV*. CERN Yellow Report 85–03. 1985.

- [170] W. Ralph Nelson, H. Hirayama, and David W. O. Rogers. *The EGS4 Code System*. Tech. rep. Stanford Linear Accelerator Center, Menlo Park, CA (USA), Dec. 1985.
- [171] K Greisen. In: *Prog. Cosmic Ray Physics* Vol. III.1 (1956). Ed. by J.G. Wilson. Amsterdam, Netherlands.
- [172] Peter K.F. Grieder. *Extensive Air Showers: High Energy Phenomena and Astrophysical Aspects - A Tutorial, Reference Manual and Data Book*. Springer, Berlin, Heidelberg, 2010. DOI: [10.1007/978-3-540-76941-5](https://doi.org/10.1007/978-3-540-76941-5).
- [173] Ralph Engel et al. “Towards a Next Generation of CORSIKA: A Framework for the Simulation of Particle Cascades in Astroparticle Physics”. In: *Comput. Softw. Big Sci.* 3.1 (2019), p. 2. DOI: [10.1007/s41781-018-0013-0](https://doi.org/10.1007/s41781-018-0013-0). arXiv: [1808.08226](https://arxiv.org/abs/1808.08226) [[astro-ph.IM](#)]; Maximilian Reininghaus and Ralf Ulrich. “CORSIKA 8 – Towards a modern framework for the simulation of extensive air showers”. In: *EPJ Web Conf.* 210 (2019). Ed. by I. Lhenry-Yvon et al., p. 02011. DOI: [10.1051/epjconf/201921002011](https://doi.org/10.1051/epjconf/201921002011). arXiv: [1902.02822](https://arxiv.org/abs/1902.02822) [[astro-ph.IM](#)]; Antonio Augusto Alves et al. “CORSIKA 8 - A novel high-performance computing tool for particle cascade Monte Carlo simulations”. In: *EPJ Web Conf.* 251 (2021), p. 03038. DOI: [10.1051/epjconf/202125103038](https://doi.org/10.1051/epjconf/202125103038).
- [174] T. Pierog et al. “First results of fast one-dimensional hybrid simulation of EAS using CONEX”. In: *Nucl. Phys. B Proc. Suppl.* 151 (2006). Ed. by P. K. F. Grieder, B. Pattison, and L. K. Resvanis, pp. 159–162. DOI: [10.1016/j.nuclphysbps.2005.07.029](https://doi.org/10.1016/j.nuclphysbps.2005.07.029). arXiv: [astro-ph/0411260](https://arxiv.org/abs/astro-ph/0411260); Till Bergmann et al. “One-dimensional Hybrid Approach to Extensive Air Shower Simulation”. In: *Astropart. Phys.* 26 (2007), pp. 420–432. DOI: [10.1016/j.astropartphys.2006.08.005](https://doi.org/10.1016/j.astropartphys.2006.08.005). arXiv: [astro-ph/0606564](https://arxiv.org/abs/astro-ph/0606564).
- [175] G. Bossard et al. “Cosmic ray air shower characteristics in the framework of the parton based Gribov-Regge model NEXUS”. In: *Phys. Rev. D* 63 (2001), p. 054030. DOI: [10.1103/PhysRevD.63.054030](https://doi.org/10.1103/PhysRevD.63.054030). arXiv: [hep-ph/0009119](https://arxiv.org/abs/hep-ph/0009119).
- [176] T. Pierog, R. Engel, and D. Heck. “3D Air Shower Simulations Using CONEX in CORSIKA”. In: *Proc. 31st Int. Cosmic Ray Conf., Lodz (Poland), (2009) contr. 0425*. URL: <http://icrc2009.uni.lodz.pl/proc/pdf/icrc0425.pdf>; T. Pierog et al. “3D hybrid air shower simulation in CORSIKA”. In: *32nd Internat. Cosmic Ray Conf., Beijing, China, August 11-18, 2011. Vol. 2*. 51.53.01; LK 02. 2012, pp. 222–225. DOI: [10.7529/ICRC2011/V02/1170](https://doi.org/10.7529/ICRC2011/V02/1170). URL: <http://www.ihep.ac.cn/english/conference/icrc2011/paper/proc/v2.pdf>.
- [177] Ralf Ulrich, Tanguy Pierog, and Colin Baus. *Cosmic Ray Monte Carlo Package, CRMC*. Version 2.0.1. Aug. 2021. DOI: [10.5281/zenodo.5270381](https://doi.org/10.5281/zenodo.5270381). URL: <https://web.ikp.kit.edu/rulrich/crmc.html>.
- [178] Matt Dobbs and Jorgen Beck Hansen. “The HepMC C++ Monte Carlo event record for High Energy Physics”. In: *Comput. Phys. Commun.* 134 (2001), pp. 41–46. DOI: [10.1016/S0010-4655\(00\)00189-2](https://doi.org/10.1016/S0010-4655(00)00189-2).
- [179] I. Valino et al. “Characterisation of the electromagnetic component in ultra-high energy inclined air showers”. In: *Astropart. Phys.* 32 (2010), pp. 304–317. DOI: [10.1016/j.astropartphys.2009.09.008](https://doi.org/10.1016/j.astropartphys.2009.09.008). arXiv: [0910.2873](https://arxiv.org/abs/0910.2873) [[astro-ph.HE](#)].

- 
- [180] A. Aab et al. “Muons in air showers at the Pierre Auger Observatory: Mean number in highly inclined events”. In: *Phys. Rev. D* 91 (3 Feb. 2015), p. 032003. DOI: [10.1103/PhysRevD.91.032003](https://doi.org/10.1103/PhysRevD.91.032003). URL: <https://link.aps.org/doi/10.1103/PhysRevD.91.032003>.
- [181] Alexander Aab et al. “Reconstruction of Inclined Air Showers Detected with the Pierre Auger Observatory”. In: *JCAP* 08 (2014), p. 019. DOI: [10.1088/1475-7516/2014/08/019](https://doi.org/10.1088/1475-7516/2014/08/019). arXiv: [1407.3214](https://arxiv.org/abs/1407.3214) [[astro-ph.HE](#)].
- [182] M. Ave, R.A. Vázquez, and E. Zas. “Modeling horizontal air showers induced by cosmic rays”. In: *Astroparticle Physics* 14.2 (2000), pp. 91–107. ISSN: 0927-6505. DOI: [https://doi.org/10.1016/S0927-6505\(00\)00113-4](https://doi.org/10.1016/S0927-6505(00)00113-4). URL: <http://www.sciencedirect.com/science/article/pii/S0927650500001134>.
- [183] H.P. Dembinski et al. “A phenomenological model of the muon density profile on the ground of very inclined air showers”. In: *Astroparticle Physics* 34.2 (2010), pp. 128–138. ISSN: 0927-6505. DOI: <https://doi.org/10.1016/j.astropartphys.2010.06.006>. URL: <http://www.sciencedirect.com/science/article/pii/S0927650510001180>.
- [184] R. R. Prado. “Tests of hadronic interactions with measurements by Pierre Auger Observatory”. In: *EPJ Web Conf.* 208 (2019). Ed. by B. Pattison et al., p. 08003. DOI: [10.1051/epjconf/201920808003](https://doi.org/10.1051/epjconf/201920808003). arXiv: [1810.00586](https://arxiv.org/abs/1810.00586) [[astro-ph.HE](#)].
- [185] Sebastian Baur et al. “Core-corona effect in hadron collisions and muon production in air showers”. In: (2019). arXiv: [1902.09265](https://arxiv.org/abs/1902.09265) [[hep-ph](#)].
- [186] Felix Riehn. “Measurement of the fluctuations in the number of muons in inclined air showers with the Pierre Auger Observatory”. In: *The Pierre Auger Observatory: Contributions to the 36th International Cosmic Ray Conference (ICRC 2019)*. 2019, pp. 132–139. arXiv: [1909.09073](https://arxiv.org/abs/1909.09073) [[astro-ph.HE](#)].
- [187] T. Abu-Zayyad et al. “Evidence for Changing of Cosmic Ray Composition between  $10^{17}$ -eV and  $10^{18}$ -eV from Multicomponent Measurements”. In: *Phys. Rev. Lett.* 84 (2000), pp. 4276–4279. DOI: [10.1103/PhysRevLett.84.4276](https://doi.org/10.1103/PhysRevLett.84.4276). arXiv: [astro-ph/9911144](https://arxiv.org/abs/astro-ph/9911144).
- [188] Lorenzo Cazon. “Probing High-Energy Hadronic Interactions with Extensive Air Showers”. In: *Proceedings of 36th International Cosmic Ray Conference — PoS(ICRC2019)*. Vol. 358. 2019, p. 005. DOI: [10.22323/1.358.0005](https://doi.org/10.22323/1.358.0005).
- [189] Lorenzo Cazon. “Working Group Report on the Combined Analysis of Muon Density Measurements from Eight Air Shower Experiments”. In: *Proceedings of 36th International Cosmic Ray Conference — PoS(ICRC2019)*. Vol. 358. 2019, p. 214. DOI: [10.22323/1.358.0214](https://doi.org/10.22323/1.358.0214).
- [190] Dennis Soldin. “Update on the Combined Analysis of Muon Measurements from Nine Air Shower Experiments”. In: *Proceedings of 37th International Cosmic Ray Conference — PoS(ICRC2021)*. Vol. 395. Figures in Fig. 5.3 provided under the Creative Commons Attribution-NonCommercial-NoDerivatives 4.0 International License ([CC BY-NC-ND 4.0](https://creativecommons.org/licenses/by-nc-nd/4.0/)). 2021, p. 349. DOI: [10.22323/1.395.0349](https://doi.org/10.22323/1.395.0349).

- [191] Federico Sánchez. “The muon component of extensive air showers above  $10^{17.5}$  eV measured with the Pierre Auger Observatory”. In: *The Pierre Auger Observatory: Contributions to the 36th International Cosmic Ray Conference (ICRC 2019)*. 2019, pp. 124–131. arXiv: [1909.09073](https://arxiv.org/abs/1909.09073) [[astro-ph.HE](#)].
- [192] Rasha Abbasi et al. “Density of GeV Muons Measured with IceTop”. In: *PoS ICRC2021 (2021)*, p. 342. DOI: [10.22323/1.395.0342](https://doi.org/10.22323/1.395.0342). arXiv: [2107.09583](https://arxiv.org/abs/2107.09583) [[astro-ph.HE](#)].
- [193] A. G. Bogdanov et al. “Investigation of the properties of the flux and interaction of ultrahigh-energy cosmic rays by the method of local-muon-density spectra”. In: *Phys. Atom. Nucl.* 73 (2010), pp. 1852–1869. DOI: [10.1134/S1063778810110074](https://doi.org/10.1134/S1063778810110074); A. G. Bogdanov et al. “Investigation of very high energy cosmic rays by means of inclined muon bundles”. In: *Astropart. Phys.* 98 (2018), pp. 13–20. DOI: [10.1016/j.astropartphys.2018.01.003](https://doi.org/10.1016/j.astropartphys.2018.01.003).
- [194] J. A. Bellido et al. “Muon content of extensive air showers: Comparison of the energy spectra obtained by the Sydney University Giant Air-shower Recorder and by the Pierre Auger Observatory”. In: *Phys. Rev. D* 98 (2 July 2018), p. 023014. DOI: [10.1103/PhysRevD.98.023014](https://doi.org/10.1103/PhysRevD.98.023014). URL: <https://link.aps.org/doi/10.1103/PhysRevD.98.023014>.
- [195] Flavia Gesualdi et al. “On the muon scale of air showers and its application to the AGASA data”. In: *PoS ICRC2021 (2021)*, p. 473. DOI: [10.22323/1.395.0473](https://doi.org/10.22323/1.395.0473).
- [196] Hans Dembinski et al. “The Muon Puzzle in air showers and its connection to the LHC”. In: *Proceedings of 37th International Cosmic Ray Conference — PoS(ICRC2021)*. Vol. 395. 2021, p. 037. DOI: [10.22323/1.395.0037](https://doi.org/10.22323/1.395.0037).
- [197] Roberto Aloisio et al. “Are Cosmic Rays still a valuable probe of Lorentz Invariance Violations in the Auger era?” In: *Frascati Phys. Ser.* 58 (2014). Ed. by R. Fusco Femiano and G. Mannocchi, p. 274. arXiv: [1408.5213](https://arxiv.org/abs/1408.5213) [[astro-ph.HE](#)].
- [198] Klaus Werner. “Core-Corona Separation in Ultrarelativistic Heavy Ion Collisions”. In: *Phys. Rev. Lett.* 98 (15 Apr. 2007), p. 152301. DOI: [10.1103/PhysRevLett.98.152301](https://doi.org/10.1103/PhysRevLett.98.152301). URL: <https://link.aps.org/doi/10.1103/PhysRevLett.98.152301>.
- [199] Peter Koch, Berndt Müller, and Johann Rafelski. “From strangeness enhancement to quark–gluon plasma discovery”. In: *Int. J. Mod. Phys. A* 32.31 (2017), p. 1730024. DOI: [10.1142/S0217751X17300241](https://doi.org/10.1142/S0217751X17300241). arXiv: [1708.08115](https://arxiv.org/abs/1708.08115) [[nucl-th](#)].
- [200] Jorge Fernandez Soriano et al. “Probing QCD approach to thermal equilibrium with ultrahigh energy cosmic rays”. In: *PoS ICRC2017 (2018)*, p. 342. DOI: [10.22323/1.301.0342](https://doi.org/10.22323/1.301.0342). arXiv: [1811.07728](https://arxiv.org/abs/1811.07728) [[hep-ph](#)].
- [201] *The Pierre Auger Observatory: Contributions to the 36th International Cosmic Ray Conference (ICRC 2019)*. 2019. arXiv: [1909.09073](https://arxiv.org/abs/1909.09073) [[astro-ph.HE](#)].
- [202] Lorenzo Cazon, Ruben Conceição, and Felix Riehn. “Probing the energy spectrum of hadrons in proton air interactions at ultrahigh energies through the fluctuations of the muon content of extensive air showers”. In: *Physics Letters B* 784 (2018), pp. 68–76. ISSN: 0370-2693. DOI: <https://doi.org/10.1016/j.physletb.2018.07.026>. URL: <https://www.sciencedirect.com/science/article/pii/S0370269318305641>.
- [203] P.A. Zyla et al. “Review of Particle Physics - 20. High Energy Soft QCD and Diffraction”. In: *PTEP* 2020.8 (2020), p. 083C01. DOI: [10.1093/ptep/ptaa104](https://doi.org/10.1093/ptep/ptaa104).

- 
- [204] Hans Peter Dembinski. “Computing mean logarithmic mass from muon counts in air shower experiments”. In: *Astropart. Phys.* 102 (2018), pp. 89–94. DOI: [10.1016/j.astropartphys.2018.05.008](https://doi.org/10.1016/j.astropartphys.2018.05.008). arXiv: [1711.05737](https://arxiv.org/abs/1711.05737) [astro-ph.HE].
- [205] Luis A. Anchordoqui et al. “The Forward Physics Facility: Sites, Experiments, and Physics Potential”. In: (Sept. 2021). arXiv: [2109.10905](https://arxiv.org/abs/2109.10905) [hep-ph].
- [206] O. Adriani et al. “Measurements of longitudinal and transverse momentum distributions for neutral pions in the forward-rapidity region with the LHCf detector”. In: *Phys. Rev. D* 94 (3 Aug. 2016), p. 032007. DOI: [10.1103/PhysRevD.94.032007](https://doi.org/10.1103/PhysRevD.94.032007). URL: <https://link.aps.org/doi/10.1103/PhysRevD.94.032007>.
- [207] S. Ostapchenko et al. “Constraining high energy interaction mechanisms by studying forward hadron production at the LHC”. In: *Phys. Rev. D* 94.11 (2016), p. 114026. DOI: [10.1103/PhysRevD.94.114026](https://doi.org/10.1103/PhysRevD.94.114026). arXiv: [1608.07791](https://arxiv.org/abs/1608.07791) [hep-ph].
- [208] Z. Citron et al. “Report from Working Group 5: Future physics opportunities for high-density QCD at the LHC with heavy-ion and proton beams”. In: *CERN Yellow Rep. Monogr.* 7 (2019). Ed. by Andrea Dainese et al., pp. 1159–1410. DOI: [10.23731/CYRM-2019-007.1159](https://doi.org/10.23731/CYRM-2019-007.1159). arXiv: [1812.06772](https://arxiv.org/abs/1812.06772) [hep-ph].
- [209] Á. Pastor-Gutiérrez et al. “Sub-TeV hadronic interaction model differences and their impact on air showers”. In: *European Physical Journal C* 81.4, 369 (Apr. 2021), p. 369. DOI: [10.1140/epjc/s10052-021-09160-2](https://doi.org/10.1140/epjc/s10052-021-09160-2). arXiv: [2104.11034](https://arxiv.org/abs/2104.11034) [astro-ph.HE].
- [210] William Karush. “Minima of functions of several variables with inequalities as side conditions.” PhD thesis. Thesis (S.M.)—University of Chicago, Department of Mathematics, December 1939., 1939.
- [211] H. W. Kuhn and A. W. Tucker. “Nonlinear Programming”. In: *Proceedings of the Second Berkeley Symposium on Mathematical Statistics and Probability*. Berkeley, Calif.: University of California Press, 1951, pp. 481–492. URL: <https://projecteuclid.org/euclid.bsmsp/1200500249>.
- [212] Eric W. Weisstein. *Incomplete Beta Function*. From MathWorld—A Wolfram Web Resource. <https://mathworld.wolfram.com/IncompleteBetaFunction.html>.



# A | Effects of Mixed Compositions

There is no clear mapping from the moments of observables to the fractions making up the composition. In fact, compositions that could reproduce the moments of observables are likely degenerate and therefore not very insightful. Still, the effect of a mixed composition should be taken into account, especially if one intends to interpret the moments of the observables in terms of the CR composition. This appendix consists of three sections where related mappings and projections are discussed, all arising purely from adequately combining composition fractions. The advantage of these mappings is that the compositions are kept implicit, and a subsequent interpretation is only done by comparing moments of observables to one another. For clarity, the following questions are answered in each of the sections, allowing the composition fractions to vary:

- A.1) What are the extreme values of  $\langle \ln A \rangle$  when fixing one of the moments?
- A.2) What are the extreme values of  $\sigma(X_{\max})$  and  $\sigma(R_\mu)/\langle R_\mu \rangle$ ?
- A.3) What are the ranges of values  $\sigma(X_{\max})$  and  $\langle R_\mu \rangle$  can attain when fixing  $\langle X_{\max} \rangle$ ? And what are the ranges of values  $\sigma(R_\mu)/\langle R_\mu \rangle$  and  $\langle X_{\max} \rangle$  can attain when fixing  $\langle R_\mu \rangle$ ?

## A.1 Effect of a Mixed Composition on the Calibration

The effect of a mixed composition on the calibration procedure discussed in Sec. 6.1.1 can be studied by fixing the observable under consideration  $x(f_i)$  to the data  $x_{\text{data}}$ , while letting the fractions of nuclei  $f_i$  making up the composition vary. By varying these fractions, the value of  $\langle \ln A \rangle = \sum_i f_i \ln A_i$  and thus  $z_{\text{mass}}$  could be changed. Through this mechanism we aim to quantify the range of  $\langle \ln A \rangle$  (and thus  $z_{\text{mass}}$ ) values that reproduce the data.

Additional constraints on  $f_i$  arise from the facts that the fractions need to sum to unity and that it is unphysical to have negative fractions. Restricting ourselves to compositions build from nuclei from proton up to iron, including all mass numbers inbetween, we therefore have the set of constraints given by:

$$x(f_i) = x_{\text{data}}, \quad \sum_{i=1}^{56} f_i = 1, \quad f_i \geq 0 \quad \forall i \in \{1, \dots, 56\}. \quad (\text{A.1.1})$$

The effect of a mixed composition can be quantified by finding the extreme values of  $\langle \ln A \rangle$  subject to these constraints. In the case of the average of an observable, the first constraint becomes

$\sum_i f_i \langle O \rangle_i = \langle O \rangle_{\text{data}}$ <sup>1</sup>, making this optimization problem a linear programming problem.

Note that in the case of a strictly linear dependence of the observable on  $\ln A$ , the constraint of reproducing the data becomes  $\langle O \rangle_{\text{data}} = \sum_i f_i \langle O \rangle_i = \sum_i f_i (a \cdot \ln A_i + b) = a \langle \ln A \rangle + b$ , implying that  $\langle \ln A \rangle$  is fixed as well. Therefore, different compositions that reproduce  $\langle O \rangle_{\text{data}}$  will have the same  $\langle \ln A \rangle$ , making this optimization problem irrelevant for that particular case.

Before attempting to solve this linear programming problem, notice that there will only be solutions when  $\langle O \rangle_{\text{data}}$  lies between the most extreme values of  $\langle O \rangle_i$ . This underlines that a mixed composition analysis only makes sense for data that is within the proton to iron range. Given that this condition is satisfied, one can subdivide the components of a mixed composition into two groups: one group where the expected observables are larger than the data,  $\langle O \rangle_i > \langle O \rangle_{\text{data}}$ , and another group where they are smaller,  $\langle O \rangle_i < \langle O \rangle_{\text{data}}$ .<sup>2</sup> To reproduce  $\langle O \rangle_{\text{data}}$ , one therefore needs to compensate a component from one group by components from the other group. In this way, any combination of the components of the two groups could reproduce the data if they appear in a certain ratio.

Generalizing this principle, any mixed composition that reproduces the data can be build from a superposition of such two-component combinations. Associated to each two-component combination is a specific contribution to the average mass  $\langle \ln A \rangle$  of the composition. To then obtain the extremes of  $\langle \ln A \rangle$ , one simply only takes the two-component combination with either the smallest or the largest specific mass contribution. This observation implies that the extremes of  $\langle \ln A \rangle$  correspond to compositions with only two components.

Consequently, these extremes can be found by computing the  $\langle \ln A \rangle$  of all possible two-component combinations that reproduce the observable. The minimum and maximum of these values will be guaranteed to be equal to the minimum and maximum of a mixed composition where all components are allowed to vary. Finding  $\langle \ln A \rangle$  for a possible two-combination follows from solving the same set of constraints, reduced to two components  $i$  and  $j$ :

$$\left. \begin{array}{l} f_i \langle O \rangle_i + f_j \langle O \rangle_j = \langle O \rangle_{\text{data}} \\ f_i + f_j = 1 \end{array} \right\} \implies f_i = \frac{\langle O \rangle_{\text{data}} - \langle O \rangle_j}{\langle O \rangle_i - \langle O \rangle_j} \quad \text{and} \quad f_j = \frac{\langle O \rangle_{\text{data}} - \langle O \rangle_i}{\langle O \rangle_j - \langle O \rangle_i} \quad (\text{A.1.2})$$

with then the average mass given by  $\langle \ln A \rangle = f_i \ln A_i + f_j \ln A_j$ .

In principle one only needs to calculate this for the combinations that contain one component of each of the groups: one component with  $\langle O \rangle_i > \langle O \rangle_{\text{data}}$  and one component with  $\langle O \rangle_i < \langle O \rangle_{\text{data}}$ . If  $\langle O \rangle_k < \langle O \rangle_{\text{data}} < \langle O \rangle_{k+1}$ , this would correspond to  $(56-k) \cdot k$  combinations. However, for practical purposes it is easier to compute  $\langle \ln A \rangle$  for all combinations, which corresponds to  $\binom{56}{2} = 1540$  combinations, and simply verify that the computed fractions are non-negative.

The effect of a mixed composition on the calibration of  $z_{\langle X_{\text{max}} \rangle}$  and  $z_{\langle \ln R_{\mu} \rangle}$  are represented as orange bands in the right plots of Fig. 6.1, corresponding to the Standard Model. These bands can only be computed for  $0 < z_{\text{mass}} < 1$  and are small as expected from the Heitler-Matthews model. Also for the various fireball model scenarios shown in Appendix B the bands are and within the corresponding systematic uncertainties, implying that it is safe to neglect the effect of a mixed composition in the analysis of Sec. 6.2. Apparently, the constraint of reproducing the data is strong enough to not allow much variation in  $\langle \ln A \rangle$ .

---

<sup>1</sup>The average of a mixed composition can be decomposed as a weighted sum of the averages of pure compositions:  $\langle O \rangle = \int O p(O) dO = \int O \sum_i f_i p_i(O) dO = \sum_i f_i \int O p_i(O) dO = \sum_i f_i \langle O \rangle_i$ .

<sup>2</sup>The practically impossible case of  $\langle O \rangle_i = \langle O \rangle_{\text{data}}$  would be part of both groups, but it does not further affect the analysis.

Unfortunately, in the case of the standard deviation of an observable, this procedure becomes significantly more complicated. Instead of being able to replace the first constraint in Eq. A.1.1 by a linear combination of pure composition observables, we are left with  $\sum_i f_i \langle O^2 \rangle_i - (\sum_j f_j \langle O \rangle_j)^2 = \sigma_{\text{data}}^2$ . This results in cross-terms that significantly complicate the optimization problem and is therefore beyond the scope of this study.

## A.2 Extreme Values of $\sigma(X_{\text{max}})$ and $\sigma(R_\mu)/\langle R_\mu \rangle$

The computations of extreme values of the second moments are a bit more involved than the previous discussion since one needs to deal with the aforementioned cross-terms. Instead of a linear programming problem, one is thus left with a quadratic programming problem. A suitable way to solve such a problem is by computing the points satisfying the Karush-Kuhn-Tucker conditions (KKT) [210, 211]:

$$\nabla \mathcal{L} = \nabla f(x^*) + \sum_{j=1}^l \lambda_j \nabla h_j(x^*) + \sum_{i=1}^m \mu_i \nabla g_i(x^*) = 0$$

$$g_i(x^*) \leq 0 \quad \forall i \quad \text{and} \quad h_j(x^*) = 0 \quad \forall j$$

$$\mu_i \geq 0 \quad \forall i$$

$$\sum_{i=1}^m \mu_i g_i(x^*) = 0$$

The first condition requires stationarity of the solution  $x^*$  that minimizes the function  $f$ . The constructed Lagrangian  $\mathcal{L}$  is shifted by the equality  $h_j$  and inequality  $g_i$  constraints, with corresponding multipliers  $\lambda_j$  and  $\mu_i$ . The second condition requires the solution to be primal feasible, i.e. the solution should satisfy the equality and inequality constraints as required by the problem. Notice that these conditions extend the method of Lagrange multipliers by additionally allowing inequality constraints. New are the third and fourth conditions which remove some of the freedom on the Lagrange multipliers  $\mu_i$ , such that the solution lies on the correct side of the inequality constraints. If one wants to maximize  $f$  instead, one needs to flip the sign before the  $\mu_i$ -term in the first condition. Equivalently, one could also change the third condition to  $\mu_i \leq 0$ .

In our problem we want to find the extreme values of  $\sigma(X_{\text{max}})$  and  $\sigma(R_\mu)/\langle R_\mu \rangle$ , which for convenience we will both denote as the observable  $O$ . This optimization problem is subject to the natural constraints on the composition fractions  $\{f_i\}$  of completeness ( $\sum_i f_i = 1$ ) and non-negativity ( $f_i \geq 0$ ). Translating the first KKT condition to our problem we find that the optimal value of the observable  $O$  satisfies

$$\partial_{f_i} \mathcal{L} = \partial_{f_i} O - \mu_i + \lambda = 0 \quad \forall i,$$

where we can require  $\mu_i \geq 0 \quad \forall i$  to minimize  $O$ , or  $\mu_i \leq 0 \quad \forall i$  to maximize  $O$ . Conveniently, this condition allows one to directly solve for the values of  $\mu_i$ :  $\mu_i = \partial_{f_i} O + \lambda$ , for each composition component  $i$ . Due to the strict positivity of the observables of interest, finding the extremes can

be simplified by finding the extremes of their squares. In practice, we thus want to minimize and maximize  $\sigma^2(X_{\max})$  and  $\sigma^2(R_\mu)/\langle R_\mu \rangle^2$ . The corresponding derivatives are given by

$$\partial_{f_i} \sigma^2(X_{\max}) = \partial_{f_i} \left[ \sum_{j=1}^n f_j \langle X_{\max}^2 \rangle_j - \left( \sum_{j=1}^n f_j \langle X_{\max} \rangle_j \right)^2 \right] = \langle X_{\max}^2 \rangle_i - 2 \langle X_{\max} \rangle_i \langle X_{\max} \rangle,$$

and

$$\partial_{f_i} [\sigma^2(R_\mu)/\langle R_\mu \rangle^2] = \partial_{f_i} [\langle R_\mu^2 \rangle / \langle R_\mu \rangle^2 - 1] = \frac{1}{\langle R_\mu \rangle^2} \left( \langle R_\mu^2 \rangle_i - 2 \langle R_\mu \rangle \frac{\langle R_\mu \rangle_i}{\langle R_\mu \rangle} \right),$$

which can be substituted into the first condition to retrieve  $\mu_i$ .

Now for our situation the fourth KKT condition implies that  $\sum_{i=1}^n \mu_i f_i = 0$ , which with the obtained  $\mu_i$  allows us to eliminate  $\lambda$  in both optimization problems:

$$\begin{aligned} 0 = \sum_{i=1}^n \mu_i f_i &= \sum_{i=1}^n f_i [\langle X_{\max}^2 \rangle_i - 2 \langle X_{\max} \rangle_i \langle X_{\max} \rangle + \lambda] = \langle X_{\max}^2 \rangle - 2 \langle X_{\max} \rangle^2 + \lambda \\ &\implies \lambda = 2 \langle X_{\max} \rangle^2 - \langle X_{\max}^2 \rangle, \end{aligned}$$

and

$$\begin{aligned} 0 = \sum_{i=1}^n \mu_i f_i &= \sum_{i=1}^n f_i \left[ \frac{1}{\langle R_\mu \rangle^2} \left( \langle R_\mu^2 \rangle_i - 2 \langle R_\mu \rangle \frac{\langle R_\mu \rangle_i}{\langle R_\mu \rangle} \right) + \lambda \right] = -\frac{\langle R_\mu^2 \rangle}{\langle R_\mu \rangle^2} + \lambda \\ &\implies \lambda = \frac{\langle R_\mu^2 \rangle}{\langle R_\mu \rangle^2}. \end{aligned}$$

Consequently the  $\mu_i$  are given by

$$\mu_i = \langle X_{\max}^2 \rangle_i - \langle X_{\max}^2 \rangle - 2 \langle X_{\max} \rangle (\langle X_{\max} \rangle_i - \langle X_{\max} \rangle),$$

and

$$\mu_i = \frac{1}{\langle R_\mu \rangle^2} \left[ \langle R_\mu^2 \rangle_i + \frac{\langle R_\mu^2 \rangle}{\langle R_\mu \rangle} (\langle R_\mu \rangle - 2 \langle R_\mu \rangle_i) \right].$$

Notice that their dependence on the composition fractions  $\{f_i\}$  are only through the averages  $\langle O \rangle = \sum_{i=1}^n f_i \langle O \rangle_i$  and the average of squares  $\langle O^2 \rangle = \sum_{i=1}^n f_i \langle O^2 \rangle_i$ , where  $O \in \{X_{\max}, R_\mu\}$ . Therefore, there are only two more or less free parameters in  $\mu_i$ , instead of the  $n$  fractions of which the composition is composed.

Now to make further progress, realize that the third KKT condition in combination with the inequality constraints on the fractions require each individual term of the fourth KKT condition  $\sum_i \mu_i f_i = 0$  to vanish. These additional conditions,  $\mu_i f_i = 0 \ \forall i$ , allow us to distinguish cases; either  $f_i = 0$  and  $\mu_i \neq 0$ , or  $f_i \neq 0$  and  $\mu_i = 0$ , indicating whether the component contributes to the composition. Since the previously identified  $\mu_i$  have only 2 free parameters, inconsistencies are likely to arise if there are more than 2 components with  $\mu_i = 0$ . Therefore, the extremes of the observables correspond to compositions with at most 2 non-zero components  $f_i$ .

The remaining calculation of the extremes of observables consists of computing the set of  $\mu_i$  for each combination with one or two non-zero components. The number of non-zero components determines how averages can be expressed in terms of those corresponding to the components. In the case of 1 non-zero component  $f_j$ , we find that the average and average square will be equal to the corresponding value of this component, i.e.,  $\langle O \rangle = \langle O \rangle_j$  and  $\langle O^2 \rangle = \langle O^2 \rangle_j$ . In the case of 2 non-zero components  $f_j$  and  $f_k$ , we know  $\mu_j = 0 = \mu_k$ . These two equations allow us to express the average and average square of the observables in terms of their components:

$$\langle X_{\max} \rangle = \frac{1}{2} \frac{\langle X_{\max}^2 \rangle_k - \langle X_{\max}^2 \rangle_j}{\langle X_{\max} \rangle_k - \langle X_{\max} \rangle_j},$$

$$\langle X_{\max}^2 \rangle = \frac{1}{2} \left( \langle X_{\max}^2 \rangle_j + \langle X_{\max}^2 \rangle_k \right) - \langle X_{\max} \rangle \left[ \langle X_{\max} \rangle_j + \langle X_{\max} \rangle_k - 2 \langle X_{\max} \rangle \right],$$

with  $\langle X_{\max} \rangle$  substituted appropriately in the latter, and

$$\frac{\langle R_{\mu}^2 \rangle}{\langle R_{\mu} \rangle} = \frac{1}{2} \frac{\langle R_{\mu}^2 \rangle_k - \langle R_{\mu}^2 \rangle_j}{\langle R_{\mu} \rangle_k - \langle R_{\mu} \rangle_j},$$

$$\langle R_{\mu} \rangle = \frac{2 \langle R_{\mu} \rangle_j \langle R_{\mu}^2 \rangle_k - 2 \langle R_{\mu} \rangle_k \langle R_{\mu}^2 \rangle_j}{\langle R_{\mu}^2 \rangle_k - \langle R_{\mu}^2 \rangle_j}.$$

These equations allow for direct computations of the sets of  $\mu_i$  for each combination of one and two non-zero components. Each set of  $\mu_i$  for which  $\mu_i \geq 0 \ \forall i$ , in the case of minimization, or  $\mu_i \leq 0 \ \forall i$ , in the case of maximization, are potential composition combinations for the extreme of the observable. A subsequent verification of the non-negativity of  $f_j$  and  $f_k$  in the case of two non-zero components, through e.g.,  $f_j = \frac{\langle O \rangle - \langle O \rangle_k}{\langle O \rangle_j - \langle O \rangle_k}$  and  $f_k = 1 - f_j$ , confirms whether the potential extremes are indeed KKT points. The minimum and maximum values of these KKT points are assured to be the smallest and largest values of the observables that can be attained by varying the composition.

### A.3 Mapping Average Observables to Fluctuations and other Averages

Consistency of the composition interpretation from different observables can be implicitly checked by mapping the data on these observables to one another. These mappings would be based on the physical models (i.e., hadronic interactions as well as the fireball) used in the simulations of EASs. Since the different observables depend differently on the underlying composition, mapping data on one observable to another observable inevitably results in a set of data points, i.e., the mapping is not one-to-one. A subsequent comparison of this set of mapped data points with the data point on the observable itself implicitly shows whether the composition interpretation of the two observables could potentially be consistent.

To make this reasoning more explicit, suppose we have data on both  $\langle X_{\max} \rangle$  and  $\langle R_{\mu} \rangle$ . For a subsequent interpretation one needs to sample these observables with EAS simulations for different CR masses, giving the sets  $\{\langle X_{\max} \rangle_i\}$  and  $\{\langle R_{\mu} \rangle_i\}$  with, e.g.,  $i \in \{p, \text{He}, \text{N}, \text{Si}, \text{Fe}\}$ . A

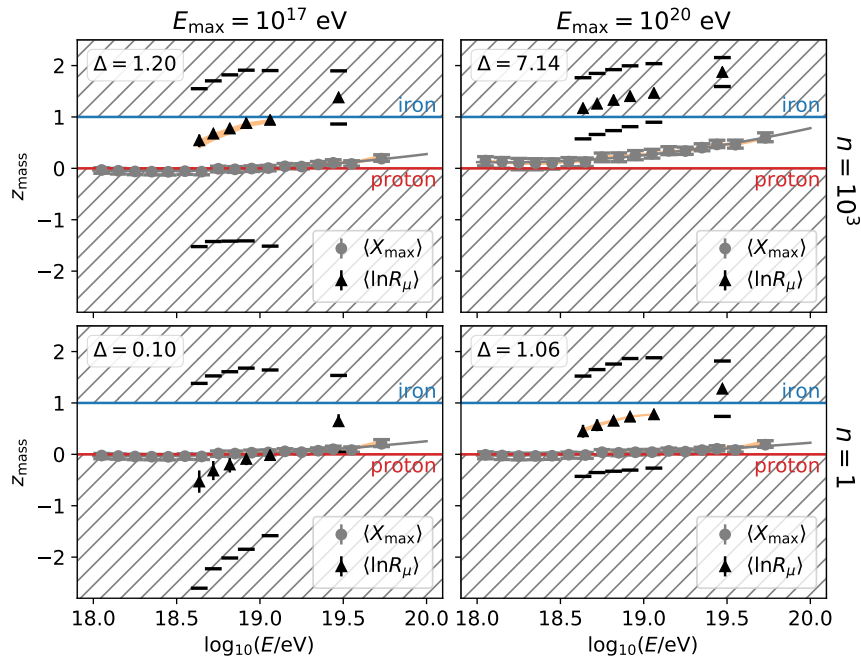
consistent composition requires a single set of  $\{f_i\}$  to simultaneously reproduce the data on both observables:  $\langle X_{\max} \rangle_{\text{data}} = \sum_i f_i \langle X_{\max} \rangle_i$  and  $\langle R_{\mu} \rangle_{\text{data}} = \sum_i f_i \langle R_{\mu} \rangle_i$ . Instead of explicitly solving these  $f_i$ , one can fix one of these observables to the data point and compute how much the other observable is allowed to vary by changing the composition and see whether there is an overlap with the data point.

Since we are dealing with averages in this example, that computation follows the exact same lines as the one described in Appendix A.1: 1) compute  $f_i$  and  $f_j$  as in Eq. A.1.2 for any combination of  $i$  and  $j$ , 2) take only the non-negative fractions, 3) compute the corresponding values of the observable that is being mapped to, 4) find the minimum and maximum of these values. The obtained extremes confine the range of mapped values that correspond to the fixed data point.

While this method relies on the linearity of the observable on the composition, it is also possible to map to the second moments of the same observable. For example, when fixing  $\langle X_{\max} \rangle$  to the data,  $\sigma(X_{\max}) = [\langle X_{\max}^2 \rangle - \langle X_{\max} \rangle_{\text{data}}^2]^{1/2}$  will have its extremes at the same composition that makes  $\langle X_{\max} \rangle$  reach its extremes. Fortunately, the latter is also a linear combination of the underlying composition,  $\langle X_{\max}^2 \rangle = \sum_i f_i \langle X_{\max}^2 \rangle_i$ , and therefore can be computed in the same way as before. The same argument holds for mapping  $\langle R_{\mu} \rangle_{\text{data}}$  to  $\sigma(R_{\mu})/\langle R_{\mu} \rangle = [\langle R_{\mu}^2 \rangle / \langle R_{\mu} \rangle_{\text{data}}^2 - 1]^{1/2}$ . In total we can thus map  $\langle X_{\max} \rangle_{\text{data}}$  to  $\langle R_{\mu} \rangle$  and  $\sigma(X_{\max})$ , and  $\langle R_{\mu} \rangle_{\text{data}}$  to  $\langle X_{\max} \rangle$  and  $\sigma(R_{\mu})/\langle R_{\mu} \rangle$  as shown in Figs. 7.5, 7.6, 7.7 and 7.8.

## B | Additional Figures of $z_{\text{mass}}$ in the Fireball Model

This appendix contains additional plots of  $z_{\text{mass}}$ , intended to give an impression of the impact of a fireball on the mass interpretation of EAS observables. Plots are shown for settings of the fireball-initiation threshold corresponding to the corners of Fig. 6.2 and Fig. 6.3. The fireball-scenarios with settings  $E_{\text{max}} = 10^{20}$  eV and  $n = 10^3$  (top-right plot in the following figures) is close to the Standard Model version. Subsequently, the effect of lowering  $E_{\text{max}}$  can be seen by going to the left and the effect of decreasing  $n$  can be seen by going down. There are three figures per section, each corresponding to a different hadronic interaction model.

B.1 Effect on Tension between  $\langle \ln R_\mu \rangle$  and  $\langle X_{\text{max}} \rangle$ 


**Figure B.1.1:** Effect on the  $z_{\text{mass}}$ -parameters inferred from  $\langle X_{\text{max}} \rangle$  (gray circles) and  $\langle \ln R_\mu \rangle$  (black triangles) in fireball scenarios with different initiation threshold parameters:  $E_{\text{max}} = 10^{17}$  eV (left column),  $E_{\text{max}} = 10^{20}$  eV (right column),  $n = 10^3$  (top row),  $n = 1$  (bottom row). The underlying hadronic interaction model is **QGSJETII-04**. Both statistical (vertical bars) and systematic (brackets) errors are indicated. Also shown are the quadratic fit of  $\langle X_{\text{max}} \rangle$  (gray line) used for the computation of the test statistic  $\Delta$  (inset top left), as well as reference values of  $z$  in the pure proton (red line) and pure iron (blue line) cases. Values in the hatched region are obtained through linear extrapolation and the orange band represents the allowed variation due to possible composition mixtures.

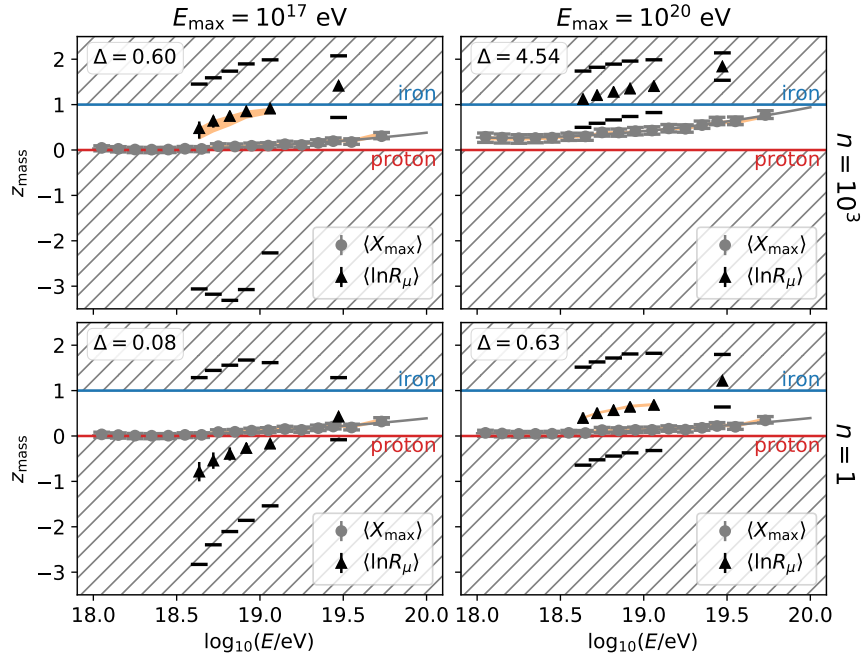


Figure B.1.2: Same as Fig. B.1.1, but then for EPOS-LHC.

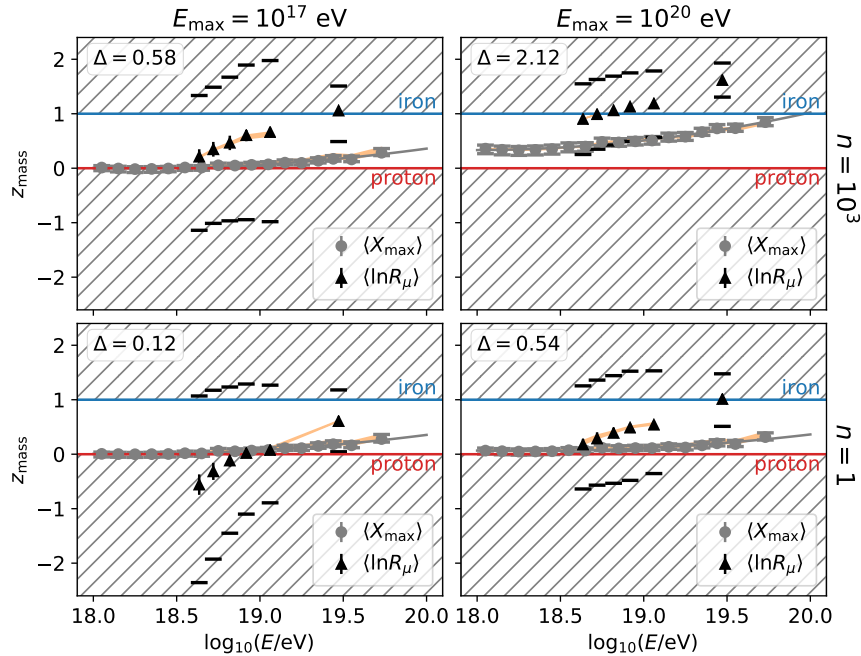
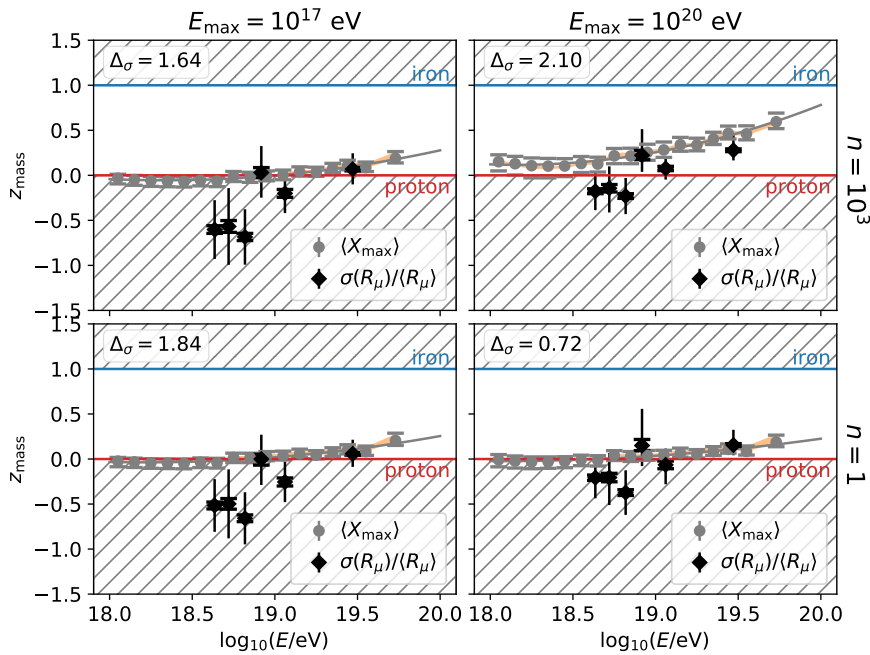


Figure B.1.3: Same as Fig. B.1.1, but then for SIBYLL-2.3C.

B.2 Effect on Tension between  $\sigma(R_\mu)/\langle R_\mu \rangle$  and  $\langle X_{\text{max}} \rangle$ 


**Figure B.2.1:** Effect on the  $z_{\text{mass}}$ -parameters inferred from  $\langle X_{\text{max}} \rangle$  (gray circles) and  $\sigma(R_\mu)/\langle R_\mu \rangle$  (black diamonds) in fireball scenarios with different initiation threshold parameters:  $E_{\text{max}} = 10^{17}$  eV (left column),  $E_{\text{max}} = 10^{20}$  eV (right column),  $n = 10^3$  (top row),  $n = 1$  (bottom row). The underlying hadronic interaction model is **QGSJETII-04**. Both statistical (vertical bars) and systematic (brackets) errors are indicated. Also shown are the quadratic fit of  $\langle X_{\text{max}} \rangle$  (gray line) used for the computation of the test statistic  $\Delta_\sigma$  (inset top left), as well as reference values of  $z$  in the pure proton (red line) and pure iron (blue line) cases. Values in the hatched region are obtained through linear extrapolation and the orange band represents the allowed variation due to possible composition mixtures.

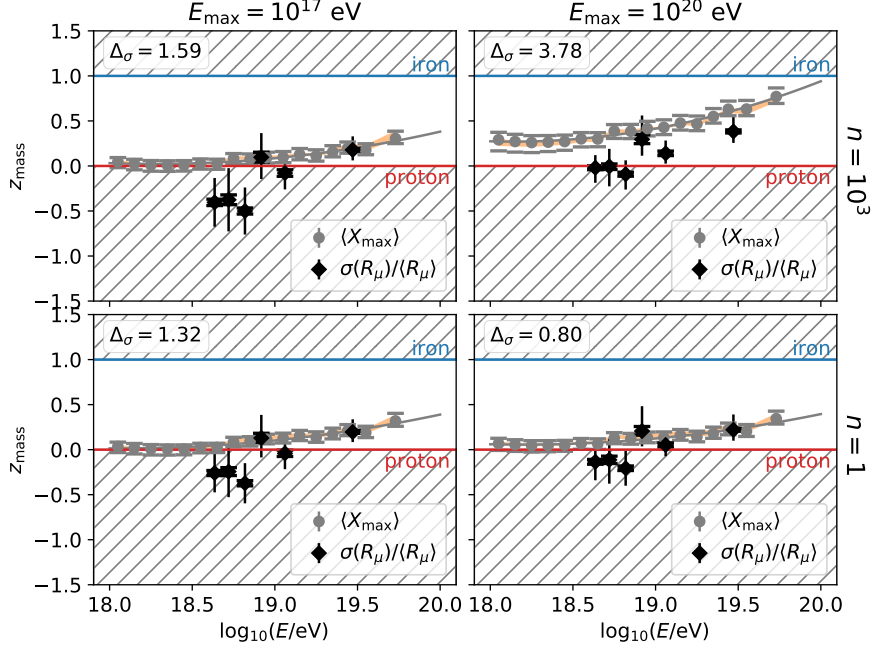


Figure B.2.2: Same as Fig. B.2.1, but then for EPOS-LHC.

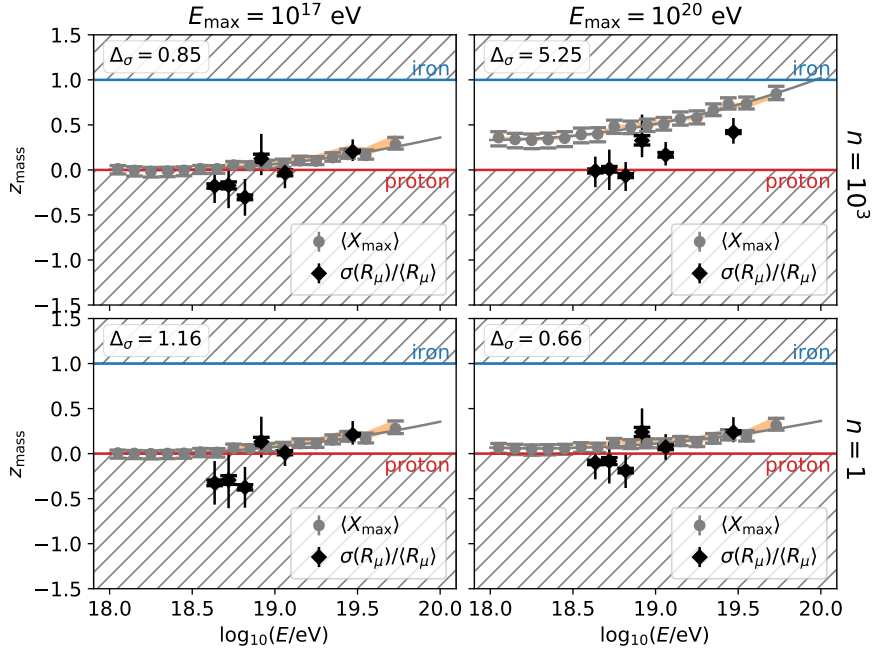


Figure B.2.3: Same as Fig. B.2.1, but then for SIBYLL-2.3C.



## C | List of Symbols for Chapter 8

Here we provide a list of symbols – along with their descriptions – that were used in the derivations of Chapter 8.

- $N_\mu$  *muon number*: the number of muons arriving at the ground. Technically, we use this to be equivalent to the number of muons at the ‘end’ of the shower. Where the end is defined in terms of the critical energy.
- $N_{\text{had}}$  *number of hadronic particles*: the number of hadronic particles in the shower. These particles are assumed to produce muons in a one-to-one ratio at the end of the shower, i.e., one hadronic particle produces one muon.
- $E_0$  *primary energy*: the energy of the primary cosmic ray that produces an air shower at the top of the atmosphere.
- $E_c$  *critical energy*: the energy below which the shower stops. This is analogous to the critical energy of electrons  $E_c^{e.m.} \sim 85$  MeV and pions  $E_c^\pi \sim 20 - 30$  GeV from [81], and can be defined as the energy at which the decay length and interaction length are equal. In our model the critical energy takes on the role of a hard threshold below which all hadronic particles decay to muons.
- $E$  *energy*: usually denotes the energy per particle within a shower. Under our assumptions of an equal division of energy over the secondaries and a fixed multiplicity at each generation, this becomes a direct measure of how far the shower has evolved.
- $k$  *generation*: the number of interactions that occurred since the first interaction of the primary cosmic ray. Under our assumptions of an equal division of energy over the secondaries and a fixed multiplicity at each generation, this becomes a direct measure of how far the shower has evolved. The critical generation  $k_c$  is then the generation at which the energy per particle reaches the critical energy, ending the shower evolution.
- $n_{\text{mult}}$  *multiplicity*: the total number of secondaries produced by an interaction. Note that this includes both hadronic and electromagnetic particles, with a further multiplication by  $r$  to obtain the multiplicity of only the hadronic particles.
- $n_{\text{scale}}$  *scale of power-law multiplicity*: the multiplicity at the energy scale  $E_{\text{scale}}$ , defined as in Eq. 8.10. This parameter is degenerate with  $E_{\text{scale}}$ .

- 
- $E_{\text{scale}}$  *scale of power-law multiplicity*: the energy scale at which the multiplicity is  $n_{\text{scale}}$ , defined as in Eq. 8.10. This parameter is degenerate with  $n_{\text{scale}}$ .
- $b$  *slope of power-law multiplicity*: the logarithmic change of the multiplicity with logarithmic energy, defined as in Eq. 8.10.
- $E_{\text{proj}}$  *projectile energy*: the energy of the projectile in the reference frame of the target. This is equivalent to the energy of the cosmic ray when considering its interaction with stationary air particles.
- $r$  *hadronic energy fraction*: the fraction of the projectile energy (or particles, due to an equal division of energy) that remains in the hadronic component after an interaction. Common subscripts are  $r_{\text{SM}}$  and  $r_{\text{fb}}$ , indicating the fraction in the Standard Model and fireball cases, respectively.
- $r_{\text{eff}}(E)$  *effective hadronic energy fraction*: average of the hadronic energy fraction of Standard Model  $r_{\text{SM}}$  and fireball  $r_{\text{fb}}$  interactions according to the fireball-initiation probability  $p(E)$ , see Eq. 8.1. This average quantifies the fraction of energy that is kept in the hadronic component at the generation parametrized by  $E$ , taking into account that a fraction of the generation produces fireballs.
- $p(E)$  *fireball-initiation probability*: probability of initiating a fireball interaction as parametrized in Eq. 5.3. This probability quantifies the effect that not always the total energy of the collision is available for the production of a fireball state, and therefore the energy-density requirement to produce a fireball may not always be satisfied. At a specific projectile energy thus only a fraction  $p(E)$  of the interactions produce fireballs.
- $E_{\text{min}}$  *minimum energy for producing fireballs*: if the projectile energy is below this energy, no fireballs are produced. Parameter of  $p(E)$  in Eq. 5.3.
- $E_{\text{max}}$  *maximum energy for producing fireballs*: if the projectile energy above this energy, all interactions produce a fireball. Parameter of  $p(E)$  in Eq. 5.3.
- $n$  *energy dependence of fireball probability*: determines how fast the probability of producing fireballs increases with increasing projectile energy;  $n = 1$  is logarithmic,  $n \rightarrow \infty$  approaches a step-function at  $E_{\text{max}}$ . Parameter of  $p(E)$  in Eq. 5.3.
- $\Delta_{\text{disc}}$  *discreteness correction factor*: factor taking into account that fireball interactions produced at higher energies will seep its effect of keeping more energy in the hadronic component deeper into the shower by on average half a generation. This is of order  $\exp(\Delta_{\text{disc}}) \sim \sqrt{r_{\text{fb}}/r_{\text{SM}}} \sim 1.1$  and thus has a 10% effect on the muon number. See Sec. 8.1.1.

# D | Derivation of $N_\mu$ in the Fireball-Extended Heitler-Matthews Model

## D.1 Fireball $N_\mu$ for a Constant Multiplicity

The muon number of Eq. 8.3 requires to solve an integral. For a constant multiplicity we have  $dk/d \log E = -1/\log(n_{\text{mult}})$ . This reduces the integral  $I$  to

$$\log \left( \frac{N_\mu}{E_0/E_c} \right) \equiv I = \frac{1}{\log n_{\text{mult}}} \int_{\log E_c}^{\log E_0} \log \{r_{\text{SM}} + p(E) (r_{\text{fb}} - r_{\text{SM}})\} d \log E, \quad (\text{D.1.1})$$

where  $p(E)$  is given by Eq. 5.3. Assuming the last stages of the shower to follow Standard Model physics, we have  $E_c < E_{\text{min}}$ . For  $E_0$  there remain three regimes:  $E_0 \leq E_{\text{min}}$ ,  $E_{\text{min}} \leq E_0 \leq E_{\text{max}}$ , and  $E_0 \geq E_{\text{max}}$ . In the first case the integrand becomes independent of energy and we get

$$I = \log(E_0/E_c) \frac{\log r_{\text{SM}}}{\log n_{\text{mult}}}, \quad \text{if } E_0 \leq E_{\text{min}}, \quad (\text{D.1.2})$$

in accordance with the Heitler model. For the other two cases the integrand is energy dependent only between  $E_{\text{min}}$  and  $E_{\text{max}}$ .

The contribution to the integral from that range is of the form

$$I'(E') \equiv \frac{1}{\log n_{\text{mult}}} \int_{\log E_{\text{min}}}^{\log E'} \log \left\{ r_{\text{SM}} + \left( \frac{\log(E/E_{\text{min}})}{\log(E_{\text{max}}/E_{\text{min}})} \right)^n (r_{\text{fb}} - r_{\text{SM}}) \right\} d \log E,$$

where  $E'$  will be evaluated at  $E_0$  or  $E_{\text{max}}$  depending on the regime. Making the substitution  $x = \log(E/E_{\text{min}})/\log(E_{\text{max}}/E_{\text{min}})$ , we get

$$I' = \frac{\log(E_{\text{max}}/E_{\text{min}})}{\log n_{\text{mult}}} \int_0^{x'} \log \{r_{\text{SM}} + x^n (r_{\text{fb}} - r_{\text{SM}})\} dx.$$

Integrating by parts gives

$$I' = \frac{\log(E_{\text{max}}/E_{\text{min}})}{\log n_{\text{mult}}} \left[ x' \log \{r_{\text{SM}} + x'^n (r_{\text{fb}} - r_{\text{SM}})\} - n \int_0^{x'} \frac{x^n (r_{\text{fb}} - r_{\text{SM}})}{r_{\text{SM}} + x^n (r_{\text{fb}} - r_{\text{SM}})} dx \right].$$

Making the substitution  $u = (1 - r_{\text{fb}}/r_{\text{SM}})x^n$  in the latter integral gives

$$n \int_0^{x'} \frac{x^n (r_{\text{fb}} - r_{\text{SM}})}{r_{\text{SM}} + x^n (r_{\text{fb}} - r_{\text{SM}})} dx = - \left( 1 - \frac{r_{\text{fb}}}{r_{\text{SM}}} \right)^{-1/n} \int_0^{u'} \frac{u^{1/n}}{1-u} du.$$

The final integral can be expressed in terms of the incomplete beta function  $B(x; a, b)$  or the hypergeometric function  ${}_2F_1(a, b; c; x)$  [212]:

$$\int_0^{u'} \frac{u^{1/n}}{1-u} du = B\left(u'; 1 + \frac{1}{n}, 0\right) = \frac{n}{n+1} (u')^{1+1/n} {}_2F_1\left(1, 1 + \frac{1}{n}; 2 + \frac{1}{n}; u'\right). \quad (\text{D.1.3})$$

Putting this all together, we can express the integral  $I'$  in terms of the hypergeometric function as

$$I'(E') = \frac{\log(E'/E_{\min})}{\log n_{\text{mult}}} \left[ \log \{r_{\text{SM}} + p(E')(r_{\text{fb}} - r_{\text{SM}})\} + \frac{n}{n+1} \left(1 - \frac{r_{\text{fb}}}{r_{\text{SM}}}\right) p(E') {}_2F_1\left(1, 1 + \frac{1}{n}; 2 + \frac{1}{n}; \left(1 - \frac{r_{\text{fb}}}{r_{\text{SM}}}\right) p(E')\right) \right], \quad (\text{D.1.4})$$

where  $p(E') = (\log(E'/E_{\min})/\log(E_{\max}/E_{\min}))^n$ .

For the remaining cases the original integral  $I$  of Eq. D.1.1 thus becomes

$$I = \log(E_{\min}/E_c) \frac{\log r_{\text{SM}}}{\log n_{\text{mult}}} + \begin{cases} I'(E_0), & \text{if } E_{\min} \leq E_0 \leq E_{\max}, \\ I'(E_{\max}) + \log(E_0/E_{\max}) \frac{\log r_{\text{fb}}}{\log n_{\text{mult}}}, & \text{if } E_0 \geq E_{\max}, \end{cases} \quad (\text{D.1.5})$$

with  $I'(E')$  given by Eq. D.1.4. A subsequent exponentiation and multiplication by  $E_0/E_c$  completes the description of the muon number.<sup>1</sup>

## D.2 Fireball $N_\mu$ for a Power-law Multiplicity

The muon number given by Eq. 8.15 depends on the integral

$$I \equiv \frac{-1}{\log(1-b)} \int_{\log E_c}^{\log E_0} \frac{\log \{r_{\text{SM}} + p(E)(r_{\text{fb}} - r_{\text{SM}})\}}{\log(n_{\text{scale}}^{1/b} E/E_{\text{scale}})} d \log E, \quad (\text{D.2.1})$$

which cannot be solved analytically. By adding the integral

$$\epsilon \equiv \frac{-1}{\log(1-b)} \int_{\log E_c}^{\log E_0} \frac{\log r_{\text{SM}} + p(E) \log(r_{\text{fb}}/r_{\text{SM}}) - \log \{r_{\text{SM}} + p(E)(r_{\text{fb}} - r_{\text{SM}})\}}{\log(n_{\text{scale}}^{1/b} E/E_{\text{scale}})} d \log E, \quad (\text{D.2.2})$$

we effectively use a geometric rather than an arithmetic average to obtain an effective  $r$ :

$$I + \epsilon = \frac{-1}{\log(1-b)} \int_{\log E_c}^{\log E_0} \frac{\log r_{\text{SM}} + p(E) \log(r_{\text{fb}}/r_{\text{SM}})}{\log(n_{\text{scale}}^{1/b} E/E_{\text{scale}})} d \log E. \quad (\text{D.2.3})$$

This integral does have an analytic solution, as outlined below.

---

<sup>1</sup>Of course, the effect of discrete interactions still needs to be taken into account following Sec. 8.1.1.

First note that  $p(E)$  introduces three regimes for  $E_0$ , while assuming  $E_c < E_{\min}$ . For  $E_0 \leq E_{\min}$  the integral reduces to the Standard Model case, giving

$$I + \epsilon = \frac{\log r_{\text{SM}}}{\log(1-b)} \log \left[ \frac{\log \left( n_{\text{scale}}^{1/b} E_c / E_{\text{scale}} \right)}{\log \left( n_{\text{scale}}^{1/b} E_0 / E_{\text{scale}} \right)} \right], \quad \text{if } E_0 \leq E_{\min}. \quad (\text{D.2.4})$$

Note that a subsequent exponentiation and a multiplication by  $E_0/E_c$  gives Eq. 8.14.

For the remaining two cases we need to take into account the energy-dependent part of  $p(E)$  between  $E_{\min}$  and  $E_{\max}$ . Over this range we have an integral of the form

$$I'(E') \equiv \int_{\log E_{\min}}^{\log E'} \left( \frac{\log(E/E_{\min})}{\log(E_{\max}/E_{\min})} \right)^n \frac{d \log E}{\log \left( n_{\text{scale}}^{1/b} E / E_{\text{scale}} \right)}.$$

With the consecutive substitutions  $x = \log \left( n_{\text{scale}}^{1/b} E / E_{\text{scale}} \right)$  and  $u = (x_{\min} - x) / x_{\min}$  we get

$$I' \cdot (\log(E_{\max}/E_{\min}))^n = \int_{x_{\min}}^{x'} (x - x_{\min})^n \frac{dx}{x} = -(-x_{\min})^n \int_0^{u'} \frac{u^n}{1-u} du.$$

The last integral has the same form as in Eq. D.1.3 and can thus be expressed in terms of the hypergeometric function  ${}_2F_1(a, b; c; x)$ . Expressing everything back in terms of the energy we find

$$I'(E') = \frac{p(E')}{1+n} \frac{\log(E'/E_{\min})}{\log \left( n_{\text{scale}}^{1/b} E_{\min} / E_{\text{scale}} \right)} {}_2F_1 \left( 1, 1+n; 2+n; \frac{-\log(E'/E_{\min})}{\log \left( n_{\text{scale}}^{1/b} E_{\min} / E_{\text{scale}} \right)} \right), \quad (\text{D.2.5})$$

where  $p(E') = (\log(E'/E_{\min}) / \log(E_{\max}/E_{\min}))^n$ .

The resulting expressions for  $I + \epsilon$  (Eq. D.2.3) for the remaining cases are then given by

$$I + \epsilon = \frac{\log r_{\text{SM}}}{\log(1-b)} \log \left[ \frac{\log \left( n_{\text{scale}}^{1/b} E_c / E_{\text{scale}} \right)}{\log \left( n_{\text{scale}}^{1/b} E_0 / E_{\text{scale}} \right)} \right] - \frac{\log(r_{\text{fb}}/r_{\text{SM}})}{\log(1-b)} I'(E_0), \quad \text{if } E_{\min} \leq E_0 \leq E_{\max}, \quad (\text{D.2.6})$$

and

$$\begin{aligned} I + \epsilon = & \frac{\log r_{\text{SM}}}{\log(1-b)} \log \left[ \frac{\log \left( n_{\text{scale}}^{1/b} E_c / E_{\text{scale}} \right)}{\log \left( n_{\text{scale}}^{1/b} E_{\max} / E_{\text{scale}} \right)} \right] - \frac{\log(r_{\text{fb}}/r_{\text{SM}})}{\log(1-b)} I'(E_{\max}) \\ & + \frac{\log(r_{\text{fb}})}{\log(1-b)} \log \left[ \frac{\log \left( n_{\text{scale}}^{1/b} E_{\max} / E_{\text{scale}} \right)}{\log \left( n_{\text{scale}}^{1/b} E_0 / E_{\text{scale}} \right)} \right], \quad \text{if } E_0 \geq E_{\max}. \end{aligned} \quad (\text{D.2.7})$$

Now if we can show that  $\epsilon$  (Eq. D.2.2) is sufficiently small, we can use  $I + \epsilon$  to accurately approximate the muon number. First notice that due to  $p(E)$  the integrand of  $\epsilon$  is zero outside the

range  $E_{\min} \leq E \leq E_{\max}$ . Therefore,  $\epsilon$  is only non-zero for  $E_0 > E_{\min}$ , and has a constant value above  $E_0 > E_{\max}$ . This effectively reduces the integration limits. Sticking to the non-trivial case of  $E_0 > E_{\min}$ , the integral of Eq. D.2.2 goes from  $\log E_{\min}$  to  $\log E'$ , where  $E' = \min(E_0, E_{\max})$ .

To constrain the remaining  $\epsilon$ , notice that a definite integral is bounded:

$$F = \int_a^b f(x)dx \quad \longrightarrow \quad \min(f(x)) \leq \frac{F}{b-a} \leq \max(f(x)),$$

where the extremes min and max are over the range of the integral. Defining

$$g(E) \equiv \frac{r_{\text{SM}} + p(E)(r_{\text{fb}} - r_{\text{SM}})}{r_{\text{SM}}(r_{\text{fb}}/r_{\text{SM}})^{p(E)}}, \quad (\text{D.2.8})$$

and rewriting the denominator in terms of the multiplicity we find  $\epsilon$  to be bounded by

$$\min \left[ \frac{\log(g(E))}{\log(n_{\text{mult}}(E))} \right] \leq \frac{\log(1-b)}{-b} \frac{\epsilon}{\log(E'/E_{\min})} \leq \max \left[ \frac{\log(g(E))}{\log(n_{\text{mult}}(E))} \right].$$

As pointed out in Sec. 8.2.1, we are restricted to  $b < 1$  because otherwise the multiplicity falls below 1 within a single generation. For all allowed values the factor  $-\log(1-b)/b$  becomes a positive constant.

Since  $\log(n_{\text{mult}}(E)) > 0$ , the lower bound is trivially zero since  $\log(g(E_{\min})) = 0$ . The upper bound is less trivial and depends on  $E'$  as well as the precise multiplicity parameters. However, due to the inequality of arithmetic and geometric means, we know that  $g(E) \geq 1$  and thus  $\log(g(E)) \geq 0$ . Consequently, we know that the upper bound is smaller than the ratio of the maximum of the nominator and the minimum of the denominator. By furthermore extending and fixing the range over which the extremes of these functions are taken to  $E_{\min} \leq E \leq E_{\max}$ , we can again enclose the upper bound from above.

This less stringent constraint thus becomes:

$$0 \leq \epsilon \leq \frac{-b}{\log(1-b)} \log(E'/E_{\min}) \frac{\max[\log(g(E))]}{\min[\log(n_{\text{mult}}(E))]}$$

For a power-law multiplicity,  $\min[\log(n_{\text{mult}}(E))]$  becomes either  $\log(n_{\text{mult}}(E_{\min}))$  or  $\log(n_{\text{mult}}(E_{\max}))$ , depending on the sign of  $b$ . The maximum of  $g$  can be obtained by simply taking the derivative and equating to zero. This gives

$$\max[\log(g(E))] = \log \left( \frac{r_{\text{fb}} - r_{\text{SM}}}{\log(r_{\text{fb}}/r_{\text{SM}})} \right) + \frac{r_{\text{SM}} \log r_{\text{fb}} - r_{\text{fb}} \log r_{\text{SM}}}{r_{\text{fb}} - r_{\text{SM}}} - 1 \quad (\text{D.2.9})$$

Interestingly, the peak of  $\log(g(E))$  is independent of the specific fireball-initiation parameters in  $p(E)$  (Eq. 5.3). A visualization of this fact as well as a comparison between the two effective  $r$ -values is shown in Fig D.2.1.

For realistic values of  $b$ , the multiplicity, and  $E_{\max}/E_{\min}$ , the corresponding factor in the bound on  $\epsilon$  will be of order 1. Then the bound itself will be roughly equal to  $\max[\log(g(E))]$  as given in Eq. D.2.9. For  $r_{\text{SM}} = 0.75$  and  $r_{\text{fb}} = 0.9$  we thus get  $0 \leq \epsilon \leq 0.004$ .

The muon number of Eq. 8.15 is now given by

$$N_\mu \cdot \exp(\epsilon) = \left( \frac{E_0}{E_c} \right) \exp(I + \epsilon + \Delta_{\text{disc}}) \quad (\text{D.2.10})$$

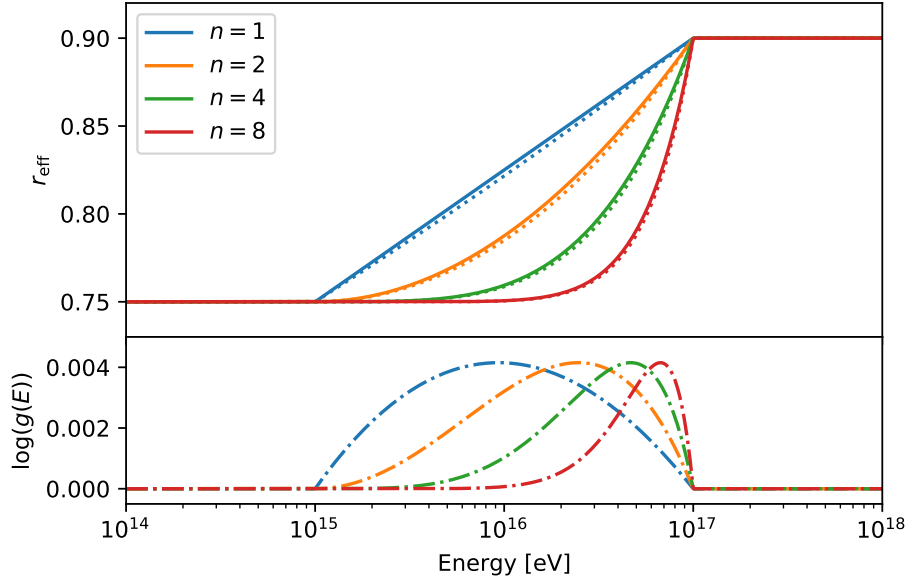


**Figure D.2.1:** Effect of approximating the arithmetically averaged effective  $r$ -value (Eq. 8.1; solid lines) by the geometric average ( $r_{\text{SM}}(r_{\text{fb}}/r_{\text{SM}})^{p(E)}$ ; dotted lines), for various values of  $n$ . The logarithmic difference, defined as  $\log(g(E))$  (Eq. D.2.8; dot-dashed lines) are small and has a maximum independent of  $p(E)$ .

of which the right-hand side can be expressed explicitly in terms  $E_0$  using Eqs. D.2.4, D.2.6, D.2.7 and 8.4, see Eq. 8.16.

From the bound on epsilon, we know that  $1 \leq \exp(\epsilon) \leq 1.004$ . Ignoring this factor means that our approximation overestimates the muon number by (much) less than 1 percent. For the current study this is more than acceptable.



# E | Additional Figures of Fireball-Heitler-Matthews Fits

For clarity we restricted the discussion and plots of Secs. 9.2 and Sec. 9.3 to the EPOS-LHC hadronic interaction model. The conclusions drawn in the main text still hold for the other hadronic models QGSJETII-04 and SIBYLL-2.3D, for which the corresponding figures are shown in this appendix.

## E.1 Fireball-Heitler-Matthews Fits of $\langle N_\mu \rangle$ and $\sigma(N_\mu)/\langle N_\mu \rangle$

This appendix contains the QGSJETII-04 and SIBYLL-2.3D versions of Figs. 9.9 and 9.12, whereas the fit parameters were included in Tables 9.3 and 9.4, respectively.

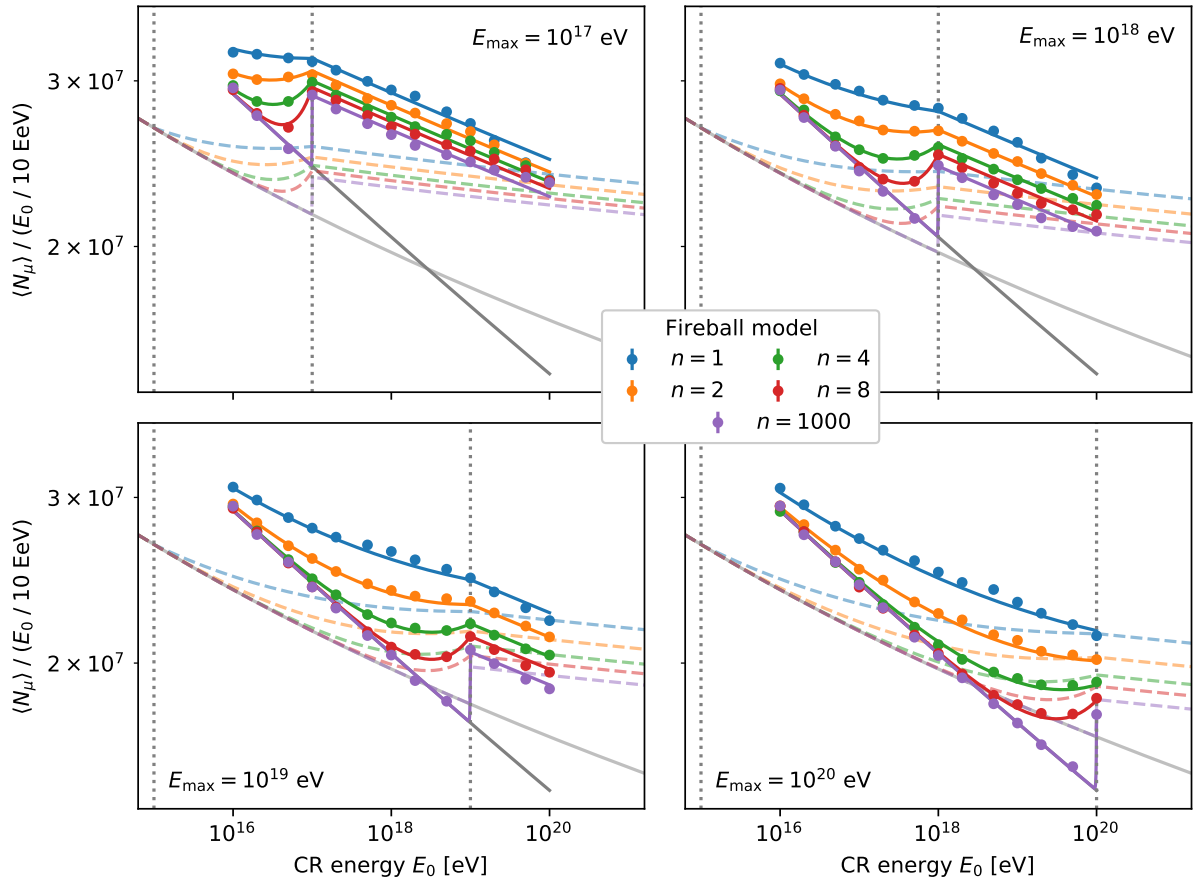


**Figure E.1.1:** Same as Fig. 9.9 but for the QGSJETII-04 hadronic interaction model. The fit parameters are given in Table 9.3.

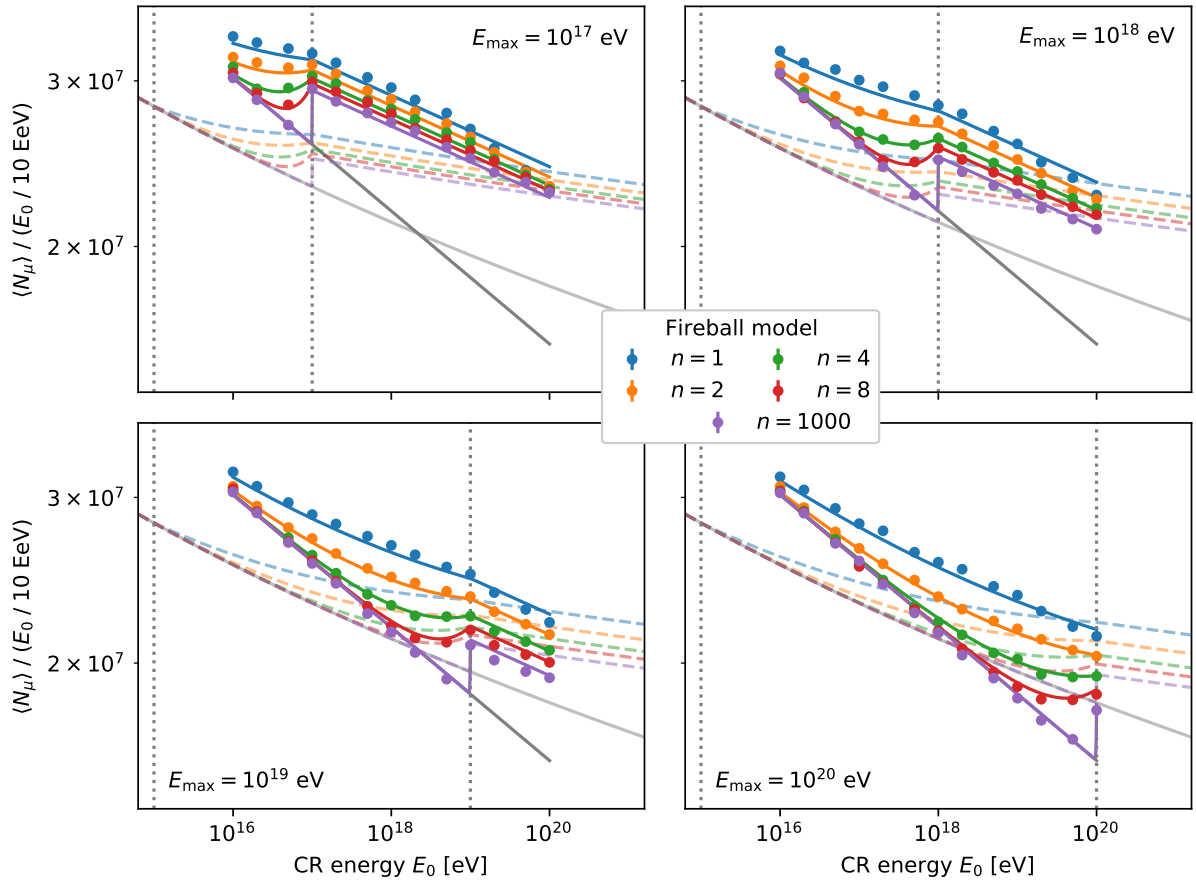


**Figure E.1.2:** Same as Fig. 9.9 but for the SIBYLL-2.3D hadronic interaction model. The fit parameters are given in Table 9.3.

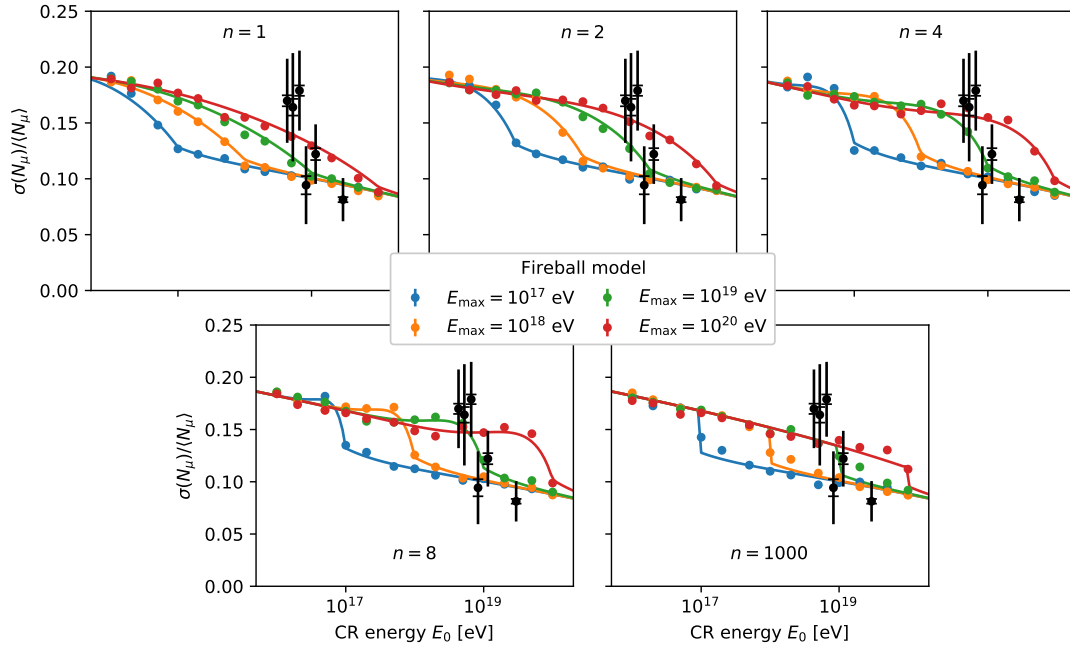


**Figure E.1.3:** Same as Fig. 9.12 but for the QGSJETII-04 hadronic interaction model. The fit parameters are given in Table 9.4.

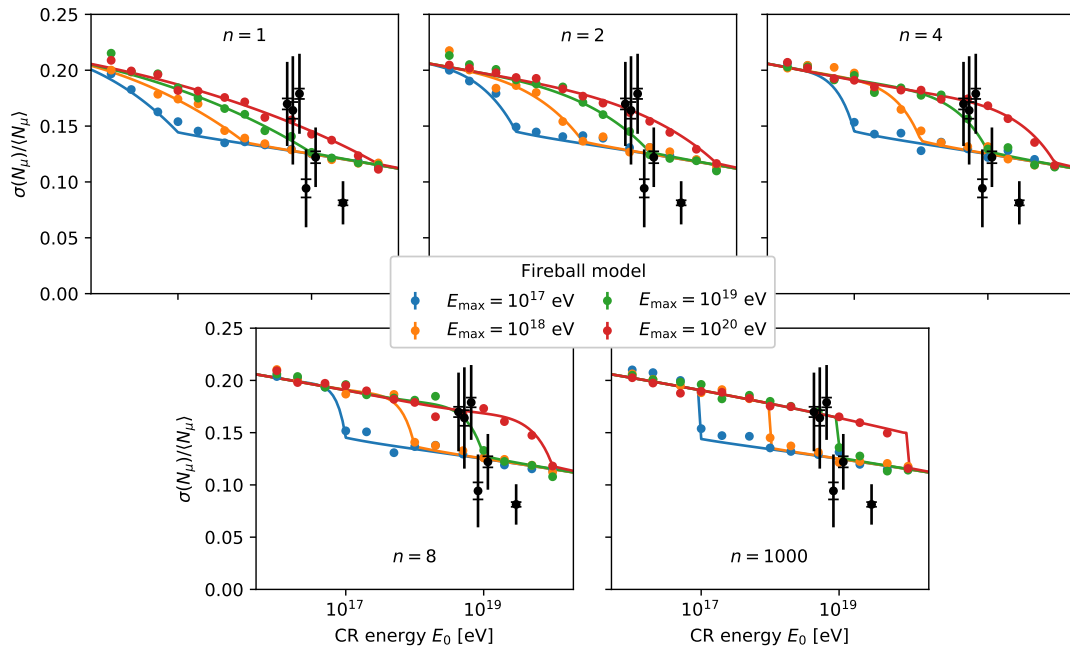


**Figure E.1.4:** Same as Fig. 9.12 but for the SIBYLL-2.3D hadronic interaction model. The fit parameters are given in Table 9.4.

## E.2 Fireball Mass Dependence of $\langle R_\mu \rangle$

This appendix contains the QGSJETII-04 and SIBYLL-2.3D versions of Figs. 9.13.

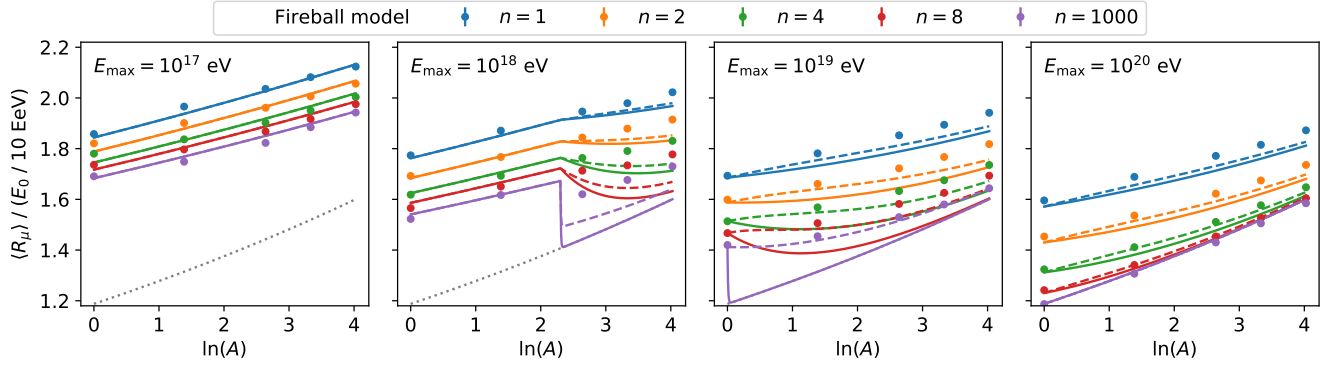


Figure E.2.1: Same as Fig. 9.13 but for the QGSJETII-04 hadronic interaction model.

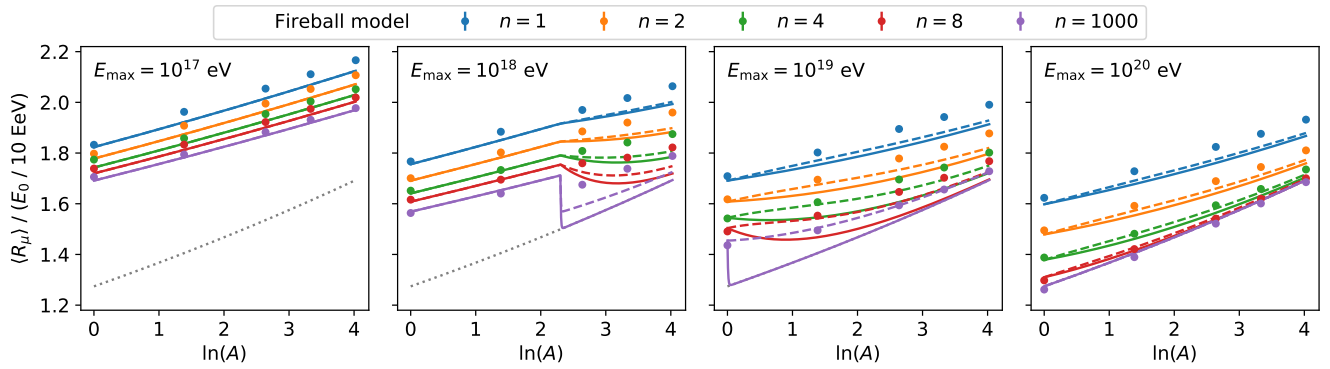


Figure E.2.2: Same as Fig. 9.13 but for the SIBYLL-2.3D hadronic interaction model.

### E.3 Fireball Interpretation of Auger Data

This appendix contains the QGSJETII-04 and SIBYLL-2.3D versions of Figs. 9.15 and 9.16.

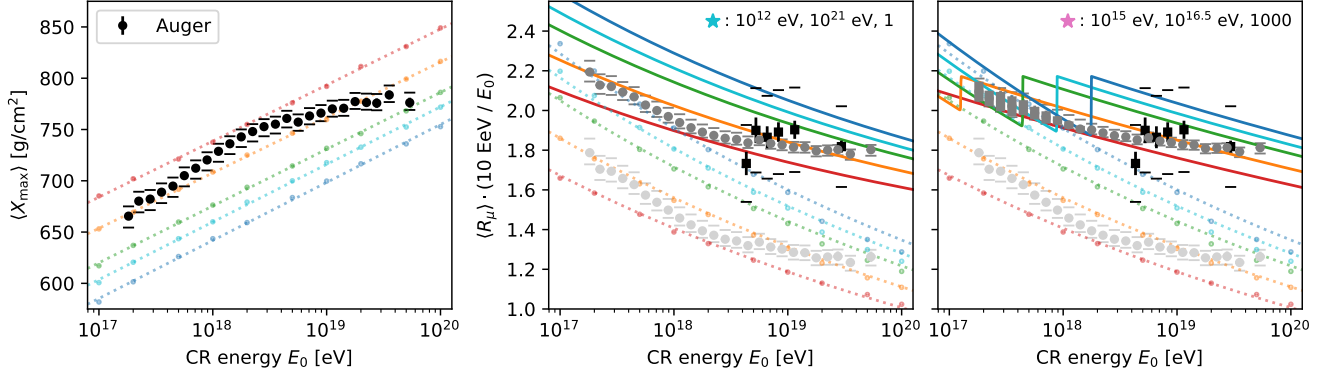


Figure E.3.1: Same as Fig. 9.15 but for the QGSJETII-04 hadronic interaction model.

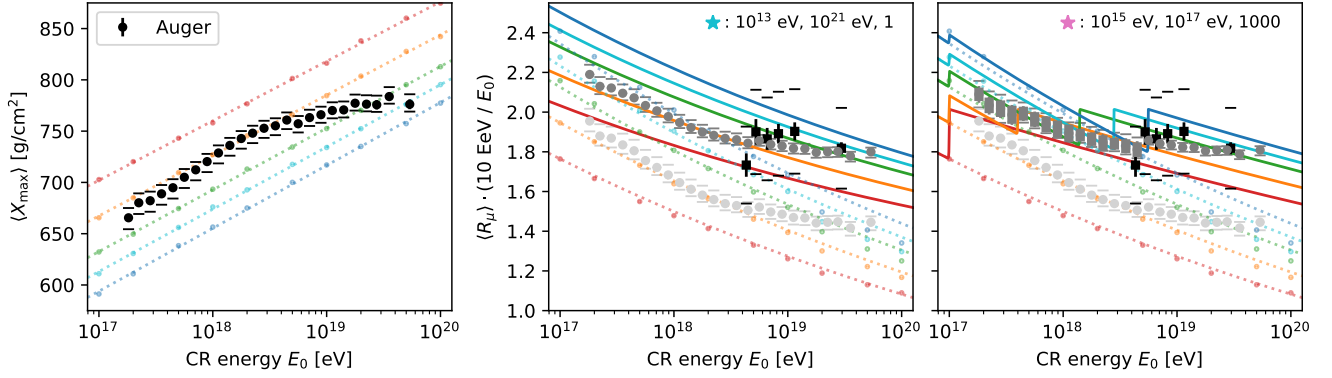


Figure E.3.2: Same as Fig. 9.15 but for the SIBYLL-2.3D hadronic interaction model.

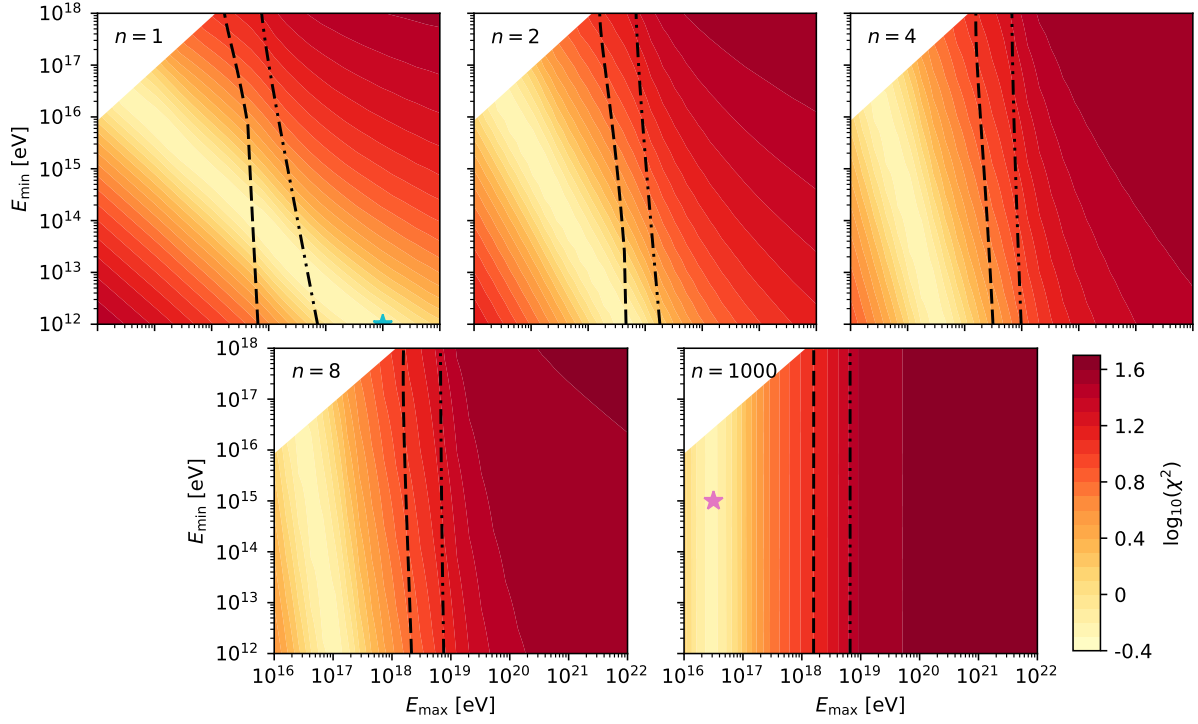


Figure E.3.3: Same as Fig. 9.16 but for the QGSJETII-04 hadronic interaction model.

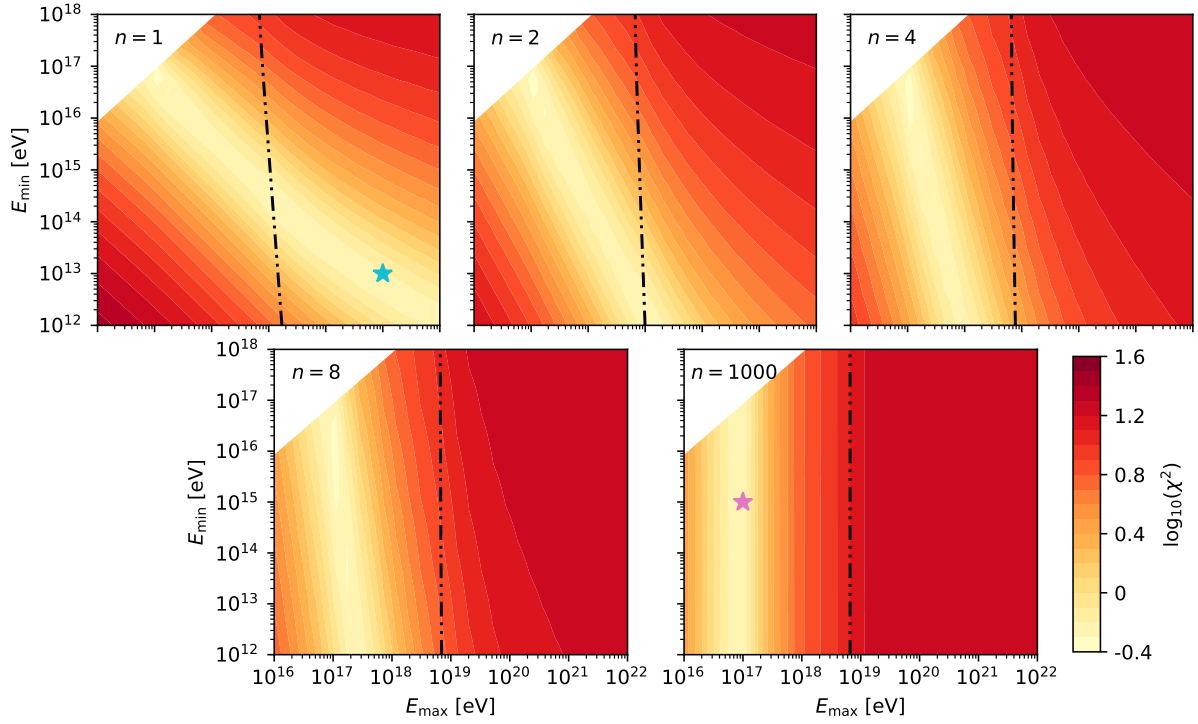


Figure E.3.4: Same as Fig. 9.16 but for the SIBYLL-2.3D hadronic interaction model.